Giuseppe Cocorullo
Felice Crupi
Ernesto Limiti   *Editors*

Proceedings of SIE 2022

53rd Annual Meeting of the Italian Electronics Society

Springer

Lecture Notes in Electrical Engineering 1005

The book series *Lecture Notes in Electrical Engineering* (LNEE) publishes the latest developments in Electrical Engineering—quickly, informally and in high quality. While original research reported in proceedings and monographs has traditionally formed the core of LNEE, we also encourage authors to submit books devoted to supporting student education and professional training in the various fields and applications areas of electrical engineering. The series cover classical and emerging topics concerning:

- Communication Engineering, Information Theory and Networks
- Electronics Engineering and Microelectronics
- Signal, Image and Speech Processing
- Wireless and Mobile Communication
- Circuits and Systems
- Energy Systems, Power Electronics and Electrical Machines
- Electro-optical Engineering
- Instrumentation Engineering
- Avionics Engineering
- Control Systems
- Internet-of-Things and Cybersecurity
- Biomedical Devices, MEMS and NEMS

For general information about this book series, comments or suggestions, please contact leontina.dicecco@springer.com.

To submit a proposal or request further information, please contact the Publishing Editor in your country:

China

Jasmine Dou, Editor (jasmine.dou@springer.com)

India, Japan, Rest of Asia

Swati Meherishi, Editorial Director (Swati.Meherishi@springer.com)

Southeast Asia, Australia, New Zealand

Ramesh Nath Premnath, Editor (ramesh.premnath@springernature.com)

USA, Canada

Michael Luby, Senior Editor (michael.luby@springer.com)

All other Countries

Leontina Di Cecco, Senior Editor (leontina.dicecco@springer.com)

** This series is indexed by EI Compendex and Scopus databases. **

Giuseppe Cocorullo · Felice Crupi ·
Ernesto Limiti
Editors

Proceedings of SIE 2022

53rd Annual Meeting of the Italian
Electronics Society

🖋 Springer

Editors
Giuseppe Cocorullo
DIMES
University of Calabria
Arcavacata, Italy

Felice Crupi
DIMES
University of Calabria
Arcavacata, Italy

Ernesto Limiti
Dipartimento di Ingegneria Elettronica
University of Rome Tor Vergata
Rome, Italy

Preface

This book contains the proceedings of original papers presented at the 53rd Annual Meeting of the Italian Electronics Society (SIE), held in Pizzo (VV), Italy, during September 7–9, 2022. The SIE (formerly the Italian Electronics Group), founded in 2011, is a non-profit association whose institutional aims are the promotion and development of training, research and technology transfer activities in the field of electronics.

The SIE-2022 Annual Meeting included invited lectures involving experts in state-of-the-art topics, oral sessions, round tables, live demonstrations and selected expositions, with the goal of complementing the regular program with emerging topics of particular interest to the Italian Electronics community. The conference received a total of 57 original contributions in the following 7 areas:

- Area 1 - Integrated Circuits and Systems
- Area 2 - Micro- and Nano-Electronic Devices
- Area 3 - Microwave Electronics
- Area 4 - Sensors, Microsystems and Instrumentation
- Area 5 - Optoelectronics and Photonics
- Area 6 - Power Electronics
- Area 7 - Electronic Systems and Applications.

Works submitted to the conference underwent a peer-review process by at least two experts selected by the conference committee. After comprehensive verification of technical content and plagiarism, the conference committee recommended 43 papers be published in this proceedings book.

Contributions in Area 1 focus on time-to-digital converter, precision-scalable multiplier, operational transconductance amplifier and readout electronics. The paper of Area 2 deals with in-memory computing with crosspoint resistive memory. Works of Area 3 include thermal X-parameter modeling of FinFETs, modeling of microstrip structures, harmonic tag sensors, GaN-based mixer for radar, power amplifier for sub-6 5G applications, microwave radars for automotive and GaN-based low-noise amplifiers. The contents of Area 4 papers cover accelerometric system, electrochemical biosensor, IoT unit to monitor water distribution, sensor of volatile organic compounds, ISFET-based NaCl sensor, piezoelectric MEMS transducer, electronics for FLASH radiotherapy, wireless harmonic transponder and hardware for pulse density modulation-to-pulse code modulation conversion. Papers of Area 5 address *pin* photodetectors, fiber Bragg grating, multimodal plastic optical fibers, ultra-long-range LiDAR, biophotonic and microfluidic circuits, surface-enhanced infrared absorption spectroscopy, tunnel junctions vertical-cavity surface-emitting lasers and strain sensor in optical fibers. In Area 6, papers focus on GaN-based resonant converters, charging systems of electrical vehicle fleets, FPGA hardware architecture for space vector pulse width modulation and DC-DC converters. The contents of Area 7 deal with architectures for improving single-event transient fault resilience, deep reinforcement learning for automated driving, learning digital twin for nonlinear dynamical systems, food waste prevention system, manipulation framework

for assistive robotics, monitoring IoT system for phytosanitary products, synthesis of redundant architectures and batteryless soil electrochemical impedance spectroscopy sensor.

Through this book, we aim to provide an overview of latest activities carried out by SIE members across the above research areas. We expect that this book will attract interest in the worldwide Electronics community, while promoting future collaborations.

Finally, we would like to express our sincere thanks to each individual who has contributed toward the publication of these proceedings.

<div style="text-align: right">

Giuseppe Cocorullo
Felice Crupi
Ernesto Limiti

</div>

Organization

Committees

Giuseppe Cocorullo (General Chair)
Ernesto Limiti (General Chair)
Felice Crupi (Conference Co-chair)

Technical Program Committee

Felice Crupi
Carlo Samori
Fernanda Irrera
Giorgio Spiazzi
Giorgio Vannini
Giuseppe Ferri
Luigi Zeni
Riccardo Berta

Local Organizing Committee

Raffaele De Rose
Marco Lanuzza
Giovanni Staino

Contents

Sensors, Microsystems and Instrumentation

Optoelectronics and Photonics

Power Electronics

Electronic Systems and Applications

Integrated Circuits and Systems

High-Resolution, Long-Range Time-to-Digital Converter for SPAD-Based Time-Correlated Single Photon Counting Applications

C. Nonne$^{(\boxtimes)}$, F. Madonini, and F. Villa

Department of Electronics, Information and Bioengineering, Politecnico di Milano, Milan, Italy
`chiara.nonne@polimi.it`

Abstract. Many high precision measurements of time intervals employ Time-of-Flight (ToF) or Time-Correlate Single-Photon Counting (TCSPC) techniques, exploiting SPAD detectors to reveal single photons with high temporal precision.

This work focuses on the design of a Time-to-Digital Converter (TDC) based on a Voltage-Controlled Gated-Ring-Oscillator (GRO).

In particular, it presents high-performance in terms of resolution (31.5 ps LSB, Least Significant Bit) and Full-Scale Range (2 μs FSR), allowing a wide range of applications from Light Detection and Ranging (LiDAR) to Fluorescent Imaging (FLIM). The stability of the TDC to Process, Temperature and Voltage (PVT) variations is assessed through a Phase-Locked-Loop (PLL) providing the control voltage to the GRO. In a SPAD array a single global PLL can be implemented, feeding the in-pixel GROs, which experience approximately the same PVT variations. Post-layout simulations are carried out to disclose, before fabrication, the main challenging design trade-offs, from jitter of the converter to PLL stability and noise. The chip design was realized in a 40 nm CMOS technology.

Keywords: Time measurements · SPAD · Time-of-Flight (ToF) · Time-to-Digital Converter (TDC) · Voltage-Controlled Gated-Ring-Oscillator (VC GRO) · Phase-Locked Loop (PLL) · CMOS 40 nm

1 Introduction

Time Interval Meters (TIMs) are the core block of Time-Correlated Single Photon Counting (TCSPC), which is a photon-efficient statistical sampling technique, where photon arrival times are measured relative to a pulsed laser source and recorded in a histogram over many repeated cycles. Pivotal fields of applications range from Fluorescence Lifetime Imaging Microscopy (FLIM) [1] to Time-of-Flight (ToF) range-finding, including Light Detection and Ranging (LiDAR) [2] and Non-Line-Of-Sight (NLOS) [3].

Continuous advances in Single-Photon Avalanche Diode (SPAD) detectors manufactured in standard CMOS processes have enabled TCSPC measurements to be performed on a single chip by high-performing imaging array. The preferred choice for integrated TIMs is a direct conversion from a time interval to a digital word by means of a Time-to-Digital Converter (TDC).

The timing circuit is the most critical component in this kind of smart SPAD-based pixel sensors in terms of compactness – to maximize the fill factor – low power consumption, and resistance to Process, Voltage and Temperature (PVT) variations across the array. Indeed, these requirements are particularly challenging against TDC's time resolution – quoted in Least Significant Bit (LSB) – and maximum measurable timestamp, i.e., Full-Scale Range (FSR).

Among the reviewed state-of-the art TDC architectures employed in SPAD imaging arrays, the most advantageous designs are based on local high-frequency Ring-Oscillators (ROs), whose clock signal is fed to a counter. By wrapping the delay line in a ring format, ROs reach higher FSRs with respect to Tapped-Delay-Line architectures, while maintaining a compact and low power consuming topology. By means of scaled technologies, LSBs down to few tens of picoseconds can be easily achieved without resorting to more complex Vernier-based architectures [4].

2   TDC Design

Figure 1a. Presents the overall designed architecture. It is based on a compact and reliable Gated RO (GRO) structure, which oscillates at 252 ps only between the beginning of the measurement (START) and the arrival of the first photon (STOP). The GRO output clock signal (OUT0) is fed to a 13-bits ripple counter, to achieve high FSR. The GRO is stabilized against PVT variations by means of a Phase-Locked Loop (PLL). In order to maintain high integrability of the TDC inside a future pixel pitch, as well as limited power consumption, the PLL is placed externally with respect to the TDC and, by means of Vc, it controls in voltage the RO (Voltage-Controlled Ring Oscillator, VCRO).

As depicted in Fig. 1b., to ensure a correct measurement of the time elapsed between *START* and *STOP*, a proper OR-control logic stops and opens the VCRO when the photon arrives, by rising the *RES*-signal and enabling the sampling and saving of the internal VCRO phases (*OUT0–3*) and of the 13 ripple-counter bits (*Q0–12*), through the Readout and Memory (RM) block. Such operation on *OUT0–3* permits a fine division of the VCRO output period (Tos) in eight LSBs of 31.5 ps each, while *Q0–12* bits give the time measurement coarse resolution.

Regarding the ripple counter, in general, such configuration is limited in the high frequency operation: the first Toggle Flip Flop is not sensitive to fast variation of the input Tos. However, the standard C40 static D-type Flip Flops have proven to correctly halve the input clock frequency up to 5 GHz. The frequency division of the VCRO output was successfully post-layout simulated in all five process corners, validating the adoption of such topology to provide the coarse bits *Q0–12*.

The following RM block is equipped with a 13-bits ripple down-counter, identical to the previous one, placed to wait enough time after the GRO opening to let even the last bit (*Q12*) to toggle before sampling *Q0–12*. Indeed, at the rising of the twin counter's last bit (*EoC12*), the 13-bit register samples *Q0–12*. Instead, the sampling of the internal GRO phases is more rapid – at the rising of *EoC0* – to promptly save *OUT0–3* before parasitic capacitor discharging at the VCRO output nodes, by means of a 4-bit register. Both the registers consist in a simple battery of Flip Flops and the decoder is custom-made to convert the 4 bits corresponding to the VCRO sampled phases into 3-bits (*B13- 15*).

Finally, to achieve a consistent timing information from one conversion to the other, an initial condition must be set – i.e., a fixed logical level 0 or 1 at each delay cell output (*OUT0–3*). As it will be clarified later, this happens by differential switching of the *en* signal before the next *START*. With the new measurement, the logic closes the VCRO automatically, by lowering first *en* and then *RES*. The time behavior of the mentioned GRO gating signals is shown in Fig. 2.

Figure 1c. Specifically shows the VCRO block. It consists in four Voltage-Controlled Delay Cells (VCDCs), that achieve a good compromise between a single-cell small delay (*tp*) – i.e., a good TDC resolution – and an oscillation period slow enough to be correctly doubled by the following ripple counter, as well as symmetry when the components are laid out.
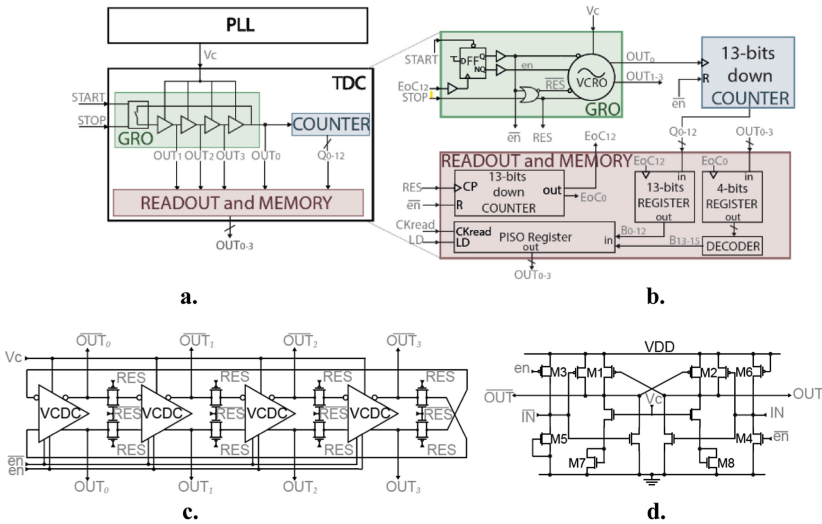
Fig. 1. a. Overall chip architecture, **b.** TDC blocks, **c.** VCRO architecture, **d.** shunt transdiode DCVSL VCDC.
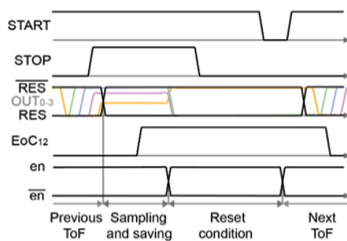
Fig. 2. Time behavior of the gating signals

The VCRO is opened/closed by means of internal Pass Transistor (PT) gate switches. The VCDCs were implemented with a Differential Cascode Voltage Switch Logic

(DCVSL) in Fig. 1d., which enables higher speed performances with respect to Fully-Complementary (FC) CMOS topologies without being penalized for static power consumption. Moreover, the differential structure gives lower sensitivity to disturbances in power supply.

The minimally sized MOS M3 and M4 set the initial condition, while dummy M5 and M6 are placed to ensure layout symmetry. The tunable propagation delay tp is obtained by varying the current injected in the MOS transdiodes M7 and M8, through the change of Vc. The VCRO must provide very accurate and precise tp for each cell. In fact, a highly non-linear and slanting $tp(Vc)$ characteristics would make Tos bounce, mainly because of Vc noise fluctuations and mismatches. Therefore, the cells were sized with a very linear and small $Tos(Vc)$ gain.

The proposed TDC exploits a PLL acting on Vc only, thus the VCRO has to bear open-loop phase noise, whose spectrum, simulated by means of Cadence PSS and PNoise analysis, evidences the dominance of Flicker noise up to 500 kHz far from the carrier frequency. Besides frequency, VCRO noise description in time (i.e., the *jitter*) contributes to TDC precision performance through its standard deviation (σ_jit). Indeed, if the jitter accumulation over the TDC FSR (i.e., the *period jitter*) exceeds one LSB, the TDC resolution is impaired. Therefore, by integrating the VCRO phase noise over a suitable frequency range representative of its operation time, the simulator returns the σ_jit over the FSR. Based on this limitation, in post processing, different combinations of the TDC bits (*B0–15*) coming out from the RM block are selected.

For example, in a long-range modality, the digital information consists in *B0–12* (from all the counter output bits) and *B13* (from the sampling of the first output GRO phase). If we want to use the highest resolution possible, the information comes from *B13–15* (all the internal GRO phases) and *B0–10* (the first eleven bits of the counter). As explained later, such bits selection is limited by the VCRO phase noise and jitter accumulation over the TDC FSR.

3 PLL Design

In order to provide a lock frequency range only limited by the VCRO tuning range, as well as a zero phase-error, a type III-PLL (shown in Fig. 3a.) is here employed. First, the output of a VCRO, which is an exact copy of the one inside the TDC, must be compared to an external precise clock reference in terms of phase and frequency discrepancies. However, whatever component performing such operation is basically blind to VCROs oscillating at 3.97 GHz (i.e., 1/252 ps), thus a frequency division is needed. Acknowledged that the aim of the PLL adopted in this work is to produce the control voltage Vc, rather than a programmable output clock, a 4-bit ripple counter with a divider modulus (M) equal to 16 is employed for such purpose. The output of the divider and the reference period (equal to 252.16 ps = 1/248 MHz) are then fed to the Phase-Frequency Detector (PFD) in Fig. 3b.

With respect to other more common topologies based on Flip Flops, this PFD guarantees a prompt response, generating an output pulse strictly for the duration of the phase error. It is composed by a latch activated at the rising of its earliest input. Thus, when both the inputs are high, both outputs (*UP* and *DW*) are almost instantaneously brought back to zero.
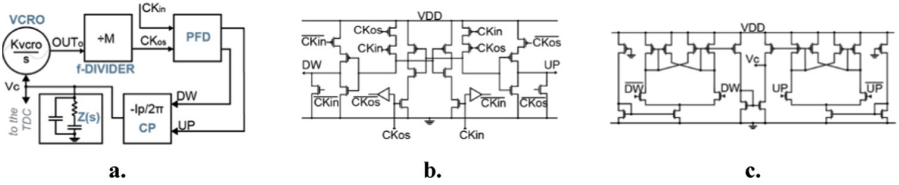
Fig. 3. a. Type-III PLL adopted in this design, **b.** Phase-Frequency Detector, c. Charge Pump

In fact, in our highly scaled and fast technology, the simultaneous activation of *UP* and *DW* signals for a finite amount of time, would expose the control voltage *Vc* to unwanted ripples, besides increasing the power dissipation of the circuit.

The differential and latched approach was adopted also for the Charge Pump (CP) block in Fig. 3c. When a pulse arrives, an unbalance is built-up in the differential stage, thus producing a current pulse that is mirror-transferred to the PLL impedance *Z(s)*. The positive feedback structure in the differential stage allows to speed up the transitions, while the clock feedthrough and the charge injection issues are minimized since the input commutation takes place in a node decoupled from the output.

Finally, the output impedance *Z(s),* integrated inside the loop, was sized to stabilize the PLL and reduce the high-frequency ripples in the control voltage. Its layout is the most critical in terms of area occupation, because of the huge extension of the metal dielectric capacitor. However, such area won't affect the fill factor of a future SPAD array because a single PLL will be employed for all pixels' TDCs and placed in dedicated area external to the pixel array.

The final post-layout transient simulations are carried out giving *CK in* with a finite time-delay in order to let the reference frequency span from 0 Hz to the target 248 MHz and cover the full lock-in range, in the five operating process corners.

Moreover, to deeply assess the contribution of each block to the PLL stability, the loop gain (Gloop) transfer function is modelled using the lumped-element circuit reported in Fig. 4. From the above-mentioned post-layout simulations, the values of *Ip* (i.e., the CP current), impedance singularities included in *Z(s)*, *Kvcro* and *M* are extracted and substituted in the lumped circuit. Thus, the Gloop phase margin evaluated through Bode Criterion. To account for the main sources of variabilities inside the proposed PLL, further analysis on *Z(s)* and *Kvcro* are performed: the global and Montecarlo process variations on the filter, as well as Montecarlo mismatches on *Kvcro* are tested. In such cases, the Gloop plot is minimally perturbed both in the singularities placement and in the dc gain. Such good PLL performances in presence of process and circuit variabilities are due to the small and linear *Kvcro*.

4   Conclusions and References

Table 1 reassumes the main parameters describing the developed TDC, compared to similar architectures integrated inside SPAD-based imaging arrays. This design achieves new values in state-of-the art LSB and FSR, by offering a dual modality operation, while maintaining a restrained increase in average power consumption. Indeed, the scaled performances of the adopted 40 nm CMOS technology allows to feed the 3.97 GHz

VCRO clock (*OUT0*) directly to a ripple counter with high number of bits (13) and thus high FSR, while the sampling of the internal GRO phases enables the fulfillment of the high-resolution requirement. The VCRO differential architecture as well as caring in the layout symmetry guarantee stability of oscillation with respect to mismatches and noise on *Vc* and supply disturbances. The TDC area occupation is slightly worsened with respect to the state-of-the-art reviewed. However, in order to guarantee a good fill factor for a future integration of the TDC in SPAD pixels, there is wide room for layout improvements: for example, by moving the memory logic away from the TDC core component or by furthering refolding the counters' layout. Anyway, the adopted technology node is usable as the bottom tier in a 3D stacking approach, which is another key option for pixel fill factor improvement.
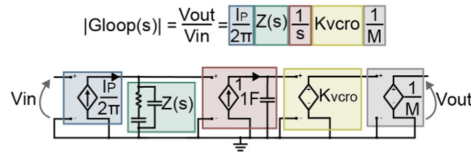
Fig. 4. Lumped electrical model of the PLL and Gloop transfer function.

Table 1. Comparison between this work and other state-of-the-art RO-based TDCs

Ref	This work	[5]	[6]	[7]
Tech. Node	40 nm CMOS	90 nm/40 nm BSI	180 nm CMOS	45 nm/65 nm
Area ($\vec{\mu m}^2$)	747	130	4200	550
LSB (ps)	31.5/126	38	48.8	60
FSR (ns)	520/2000	143	50	1000
Power (μW)	500	NA	300	100

References

1. Henderson, R.K., et al.: no. Ccd (2014)
2. Sesta, V., et al.: Sensors **21**(9) (2021)
3. Faccio, D., et al.: Nat. Rev. Phys. **2**(6), 318–327 (2020)
4. Cheng, Z., et al.: IEEE Trans. Electron Devices **63**(1), 235–251 (2016)
5. Hutchings, S.W., et al.: IEEE J. Solid-State Circuits **54**(11), 2947–2956 (2019)
6. Zhang, C., et al.: IEEE J. Solid-State Circuits **54**(4), 1–15 (2019)
7. Ronchini Ximenes, A., et al.: IEEE J. Solid-State Circuits **54**(11), 3203–3214 (2019)

A Reconfigurable Multiplier/Dot-Product Unit for Precision-Scalable Deep Learning Applications

Luca Urbinati[✉] and Mario R. Casu

Department of Electronics and Telecommunications, Politecnico di Torino,
Torino, Italy
{luca.urbinati,mario.casu}@polito.it

Abstract. Across different Deep Learning (DL) applications or within
the same application but in different phases, bitwidth precision of activa-
tions and weights may vary. Moreover, energy and latency of MAC units
have to be minimized, especially at the edge. Hence, various precision-
scalable MAC units optimized for DL have recently emerged. Our contri-
bution is a new precision-configurable multiplier/dot-product unit based
on a modified Radix-4 Booth signed multiplier with Sum-Together (ST)
mode. Besides 16-bit full precision multiplications, it can be reconfigured
to perform dot products among two 8-bit or four 4-bit sub words of the
input operands without requiring an external adder, thus reducing the
number of cycles of MAC operations. The results of the synthesis in per-
formance, power and area on a 28-nm technology show that our unit (1) is
superior to other state of the art ST multipliers in area ($\approx 35\%$ less) in the
clock frequency range between 100 and 1000 MHz and (2) reduces latency
up to 4x when used to compute a convolutional layer, at the cost of limited
overheads in area ($+10\%$) and power ($+13\%$) compared to a conventional
16-bit Booth multiplier. This unit can play an important role in designing
variable-precision MAC units or DL accelerators for edge devices.

Keywords: Variable-precision multiplier · Precision-Scalable MAC
Unit · Deep Learning

1 Introduction

At the basis of Deep Learning (DL) algorithms are convolutions and matrix
multiplications, which require the computation of many dot products and sim-
ple scalar multiplications between features and weights. These operations are
typically executed by multiply-and-accumulate (MAC) units. In particular, when
running DL applications on edge devices, energy and latency of these MAC units
have to be minimized. This requires reducing the data bit-width to the mini-
mum, while keeping a satisfying level of accuracy. Such minimum data precision
may vary across different applications, but also within the same application in
different phases (e.g. mixed-precision quantization for convolutional layers).

CONFIG	P
16x16 (000b)	A[15:0] x B[15:0]
16x8 (100b)	A[15:0] x B[7:0]
8x8 (010b)	A[15:8] x B[7:0] + A[7:0] x B[15:8]
8x4 (011b)	A[15:8] x B[3:0] + A[7:0] x B[11:8]
4x4 (001b)	A[15:12] x B[3:0] + A[11:8] x B[7:4] + + A[7:4] x B[11:8] + A[3:0] x B[15:12]

(a)   (b)
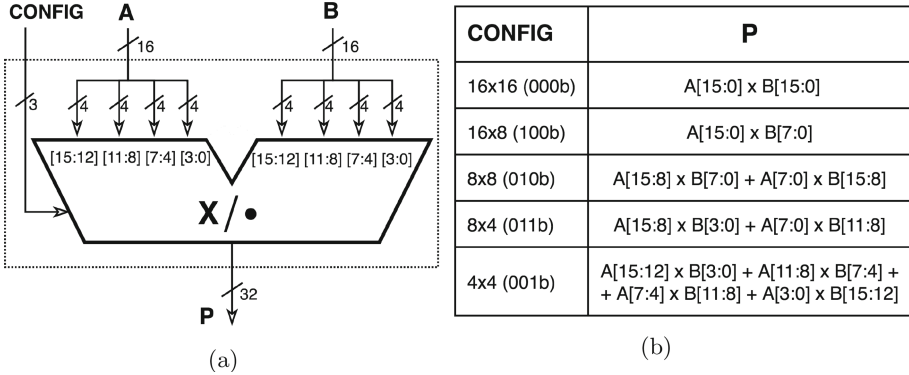
Fig. 1. Outside view of a Multiplier/dot-product unit (a) and its precision configurations (b).

Multipliers with Sum-Together (ST) mode [1] are good candidates to realize precision-scalable MAC units [2–5]. They are special sub-word parallel multipliers that can perform either a multiplication at full precision or a dot-product at lower precision. In particular, they can compute $N = 1, 2, 4$ multiplications/dot-products in parallel among input operands with precision inversely proportional to N (e.g., $16/N$ bits). When used inside MAC units, they reduce the overall latency up to $1/N$ because they save N-1 MAC additions.

In the literature we find different proposals for the implementation of ST multipliers. The design of [2] uses four 16-bit Booth multipliers with a configurable partial products compression array and three configurable 33-bit adders, instead of the usual final adder. The two sub-word parallel dot-product units of [3] comprise of two 17-bit multipliers or four 9-bit multipliers, respectively, followed by a 32-bit adder. The reconfigurable parallel inner product of [4], the ancestor of [5], dynamically composes and decomposes 4 or 8-bit multipliers with a network of combinational logic.

In this context, we propose a new precision-scalable modified Radix-4 Booth signed multiplier with ST mode. Its configuration options are reported in Fig. 1. The main difference with respect to other state of the art (SoA) ST multipliers is that our design does not require a dedicated adder to sum the low-precision products together, but it exploits the normal alignment of partial products as in a standard multiplier (Fig. 2).

The comparison between the SoA ST multipliers and our design in performance, power and area (PPA) on a 28-nm technology shows that, at the cost of limited overhead in area and power compared to a conventional non-ST Booth design, our multiplier/dot-product unit (1) is superior to the other SoA units in the clock frequency range between 100 and 1000 MHz and (2) could reduce latency and energy of convolutional layers when used in MAC units or in variable-precision DL accelerators.

2   Hardware Design

We propose a new precision-configurable Radix-4 Booth signed multiplier with ST mode. The supported configurations are those of Fig. 1(b). The key feature of our multiplier/dot-product unit is the lack of a dedicated external adder to *sum together* the low-precision products during dot-product operations. Instead, such addition comes for free in our design. In fact, our unit exploits the normal alignment of partial products in a standard multiplier, enabling the computation of dot products when two or four scalar inputs are packed in each operand, as shown in Fig. 2. The bits of output P (yellow circles) are obtained by vertically
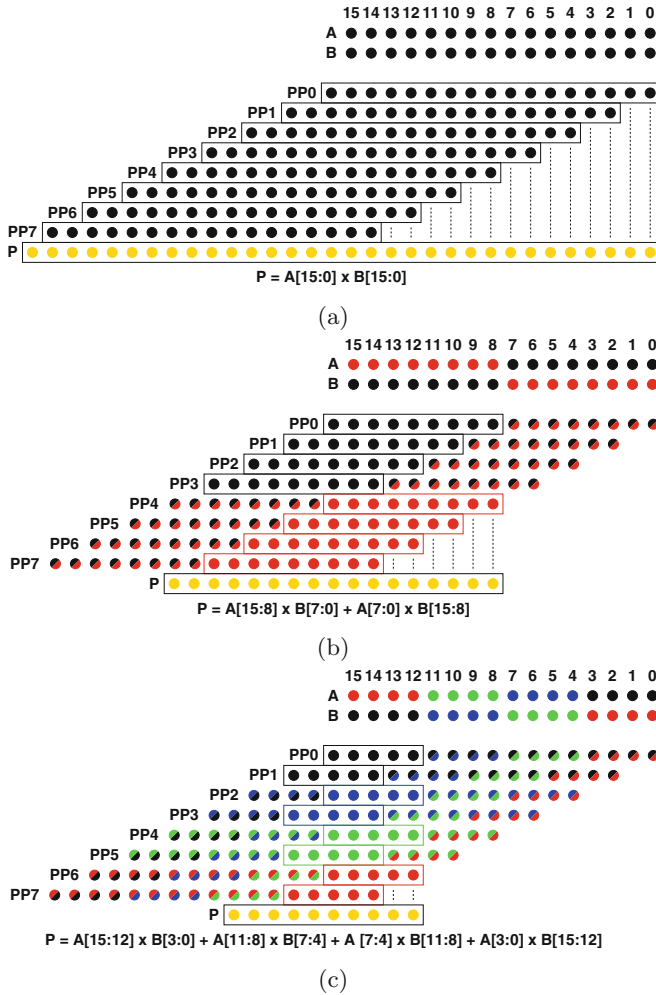
Fig. 2. Alignment of PPi partial products for $CONFIG$ $16 \times 16/16 \times 8$ (a), $8 \times 8/8 \times 4$ (b) and 4×4 (c).
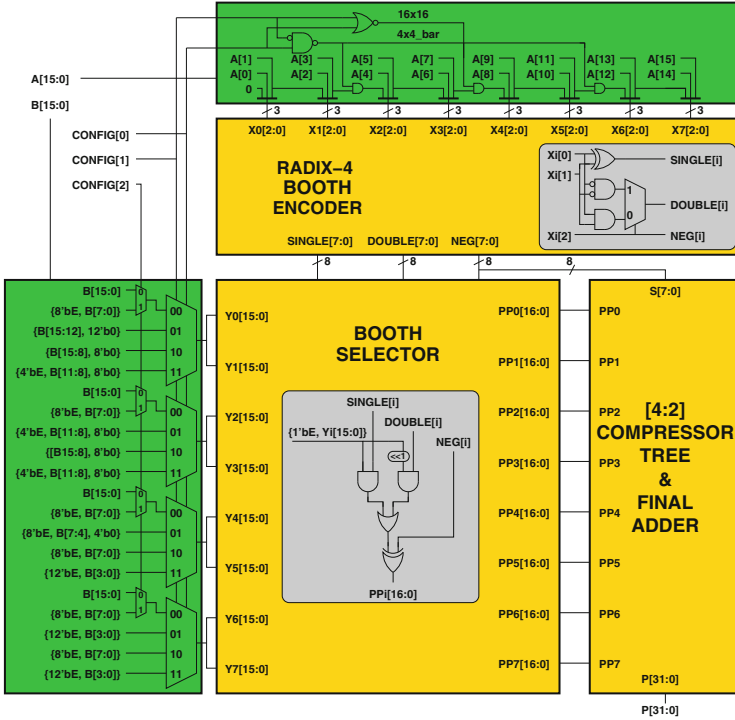
Fig. 3. The design of our Booth ST multiplier.

summing the full-colored circles representing the bits of the eight partial products (PP0-PP7). These full-colored bits are the result of the products of operands with the same color, while the half-colored bits are zeroed as explained below.

In the multiplier architecture shown in Fig. 3, the yellow blocks are the standard components of a Radix-4 Booth multiplier, while the green ones are for precision reconfiguration, for zeroing the half-colored bits of Fig. 2, and for sign extending the inputs in asymmetric configurations, like 16×8 and 8×4, in order to treat them as 16×16 and 8×8. We implement the reduction tree as a Wallace tree with 4:2 compressors, while the final adder is a Carry Propagate Adder with Prefix Network. Regarding the additional logic for reconfigurability, the configuration signal $CONFIG$ controls: 1) how the bits of operand A are properly composed t o form X_0–X_7 input triplets for the encoder; 2) how the sub-words of operand B are arranged and presented to the Y_0–Y_7 inputs of the selector; 3) the number of positions to right-shift the output to the LSB position (Fig. 2).

3   Experimental Results

For a fair comparison, we re-implemented the ideas of the SoA multipliers introduced in Sect. 1, making these minimal adjustments:
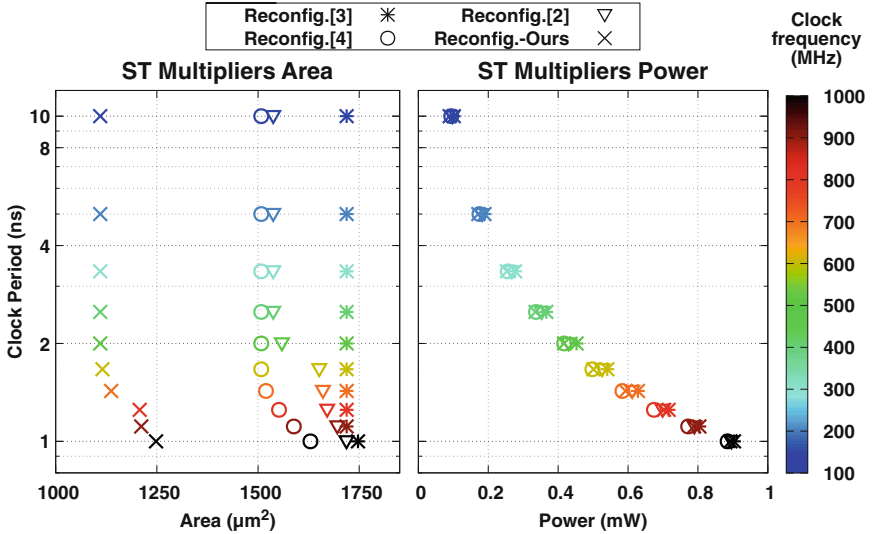
Fig. 4. PPA analysis of the analyzed ST multipliers.

- we standardized their configurations to match those presented in Fig. 1 and we removed all the unnecessary logic that was not necessary to implement the ST multiplier's behavior;
- since the authors of [3] implemented their ST multiplier with a behavioral RTL description, we made the same, but we forced the synthesizer to use a 16-bit Booth multiplier for 16×16/16×8 configurations;
- we right shifted the output of [4] to align it to the LSB because it produces the sum-of-products on higher bit positions, as it happens in our design;
- we added input and output registers to all the ST multipliers, ours included.

We synthesized the designs with Synopsys Design Compiler on a 28-nm technology, varying the clock frequency from 100 to 1000 MHz. The PPA results in the area vs clock period space and power vs clock period space are in Fig. 4(a)–(b), respectively. Our unit is Pareto optimal in area at all frequencies with ≈35% less area than other SoA competitors, while in power all the designs almost overlap each other. A close examination at 1000 MHz is reported in Table 1(a), where ST multipliers are also compared with a conventional non-ST 16-bit Booth multiplier. From this table we find that our Booth multiplier with ST mode consumes +10% of area and +13% of power compared to the baseline version.

In Table 1(b) we show how an ST multiplier could reduce the number of MAC operations and the latency of a convolutional layer, in this case the first of MobileNetV1 and EfficientNet-B0. The theoretical reduction that is possible to achieve is $1/N$ and depends on the precision of activations and weights at which the layer is computed. Finally, it is important to note that we also expect a significant energy saving at lower precisions ($N = 2$ or 4) because energy scales like latency, while power overhead is constant.

Table 1. ST multipliers vs baseline (non-ST 16-bit Booth multiplier) at 1000 MHz (a); theoretical reduction in MAC operations and latency for the first layer of MobileNetV1 and EfficientNet-B0 computed with an ST-multiplier (b).

<table>
<tr><td colspan="3" align="center">(a)</td><td colspan="3" align="center">(b)</td></tr>
<tr><td>Multiplier</td><td>Area [μm^2]</td><td>Power [mW]</td><td>Multiplier</td><td>MAC Ops.</td><td>Latency</td></tr>
<tr><td>Non-reconfig.</td><td>1133</td><td>0.791</td><td>Non-reconfig.</td><td>10.8 M</td><td>1×</td></tr>
<tr><td>Reconfig.-ours</td><td>1248 (+10%)</td><td>0.893 (+13%)</td><td>Reconfig. 16×16/16×8</td><td>10.8 M</td><td>1×</td></tr>
<tr><td>Reconfig.[2]</td><td>1747 (+54%)</td><td>0.903 (+14%)</td><td>Reconfig. 8×8/8×4</td><td>5.4 M</td><td>0.5×</td></tr>
<tr><td>Reconfig.[3]</td><td>1718 (+52%)</td><td>0.896 (+13%)</td><td rowspan="2">Reconfig. 4×4</td><td rowspan="2">2.7 M</td><td rowspan="2">0.25×</td></tr>
<tr><td>Reconfig.[4]</td><td>1629 (+44%)</td><td>0.885 (+12%)</td></tr>
</table>

4   Conclusion

This Booth multiplier with ST mode can play an important role inside precision-scalable MAC units or in variable-precision DL accelerators for edge devices [6] because it supports low-precision configurations which can reduce latency and energy. It also outperforms the SoA alternatives in area with limited reconfigurability overheads against a conventional non-configurable Booth multiplier.

References

1. Camus, V., et al.: Review and benchmarking of precision-scalable multiply-accumulate unit architectures for embedded neural-network processing. IEEE J. Emerg. Sel. Topics Circ. Syst. (JESTCS) **9**(4), 697–711 (2019)
2. Zhang, X., Li, Z., Zheng, Q.: Design of a configurable fixed-point multiplier for digital signal processor. In: Proceedings Asia Pacific Conference on Postgraduate Research in Microelectronics & Electronics (PrimeAsia), pp. 217–220. IEEE, Shanghai (2009)
3. Gautschi, M., et al.: Near-threshold RISC-V core with DSP extensions for scalable IoT endpoint devices. IEEE Trans. Very Large Scale Integr. (VLSI) Syst. **25**(10), 2700–2713 (2017)
4. Lin, R.: Reconfigurable parallel inner product processor architectures. IEEE Trans. Very Large Scale Integr. (VLSI) Syst. **9**(2), 261–272 (2001)
5. Sharma, H., et al.: Bit fusion: bit-level dynamically composable architecture for accelerating deep neural network. In: Proceedings 45th Annual International Symposium on Computer Architecture (ISCA), pp. 764–775. ACM/IEEE (2018)
6. Urbinati, L., Casu, M.R.: A reconfigurable depth-wise convolution module for heterogeneously quantized DNNs. In: Proceedings International Symposium on Circuits and Systems (ISCAS), pp. 128–132. IEEE, Austin (2022)

300-mV Bulk-Driven Three-Stage OTA in 65-nm CMOS

Andrea Ballo[1] , Alfio Dario Grasso[1(✉)] , Salvatore Pennisi[1] ,
and Giovanni Susinni[2]

[1] Dipartmento di Ingegneria Elettrica, Elettronica e Informatica (DIEEI), University of Catania,
Catania, Italy
alfiodario.grasso@unict.it
[2] EDA INDUSTRIES S.P.A, Catania, Italy

Abstract. The paper introduces a bulk-driven operational transconductance amplifier (OTA) suitable for ultra-low-power and ultra-low-voltage applications. The amplifier is made up of three gain stages and features inherent class-AB behavior and precise control of the quiescent current of all transistors. Additionally, positive feedback is exploited for the first stage to enhance its transconductance. The OTA entails a single Miller capacitor for frequency compensation, thus saving area occupation. Implemented in a 65 nm standard CMOS technology, the amplifier occupies an area of $10.6 \cdot 10^{-3}$ mm^2 and is powered from 0.3 V with a total quiescent current equal to 8.5 mA. Experimental measurements show a gain-bandwidth product equal to 1.65 MHz and a phase margin equal to 70° when driving a 50-pF load.

Keywords: Bulk-driven · Class-AB · CMOS analog integrated circuits · Low-voltage · Operational transconductance amplifier

1 Introduction

One of the main trends of current electronics industry is towards the extension of portable devices autonomy through the adoption of low power design techniques. This has reinforced the interest in the development of low-voltage and low-current design approaches for the reduction of the power consumption. Indeed, the reduction of the power consumption allows reducing the battery size (and consequently the overall device volume) for equal lifetime. This latter aspect is crucial for implanted biomedical devices, where low volume of the system is desirable to reduce its invasiveness [1].

Considering the CMOS technology, the most widely adopted methodologies to enable operation of analog circuits below 1-V supplies are subthreshold (or weak inversion) biasing and bulk driving (or body driving) and even a combination of both [2–14].

Among the above-mentioned techniques, bulk-driven stages make wide input ranges possible, even rail to rail. To enable bulk driving, the gate must be biased to form a conduction channel inversion layer and the drain current can be modulated by varying the

bulk voltage through the body effect. Compared to conventional gate-driven circuits, the body-driven ones are characterized by a lower achievable voltage gain, and/or transition frequency, caused by the limited transconductance value, (the body transconductance, g_{mb}, is only about 10–20% of the gate transconductance, g_m).

In order to overcome these limitations, usually met in a traditional body-driven operational transconductance amplifier (OTA), in this paper we exploit positive feedback for the first stage to enhance its equivalent transconductance. Moreover, three cascaded gain stages are adopted to further increase the DC gain and, unlike conventional solutions, a single Miller capacitor is adopted to implement frequency compensation, thus reducing overall area occupation. Finally, class AB operation of the last stage is enabled to increase slew rate performance. The OTA has been fabricated using a 65-nm standard CMOS technology and is capable of working under 0.3-V supply. As compared with other experimentally tested solutions in literature, the OTA offers a significant improvement of the state-of-the-art especially when the area occupation is considered.

2   The Proposed Amplifier

The simplified schematic of the proposed OTA is depicted in Fig. 1. The circuit relies on an input bulk-driven non-tailed differential pair M1-M2. The load is made up by transistors M3 and M4 and resistors R_A and R_B. As demonstrated in [5], the first stage exhibits a fully differential behavior. The bias current of M1-M2 is accurately fixed by the diode-connected transistor M13, whose bulk voltage allows also to set the virtual ground.

The transconductance of the first stage is boosted through the positive feedback obtained by cross connecting the bulk of transistors M3 and M4 respectively to the drain of M4 and M3. The equivalent transconductance is thus equal to

$$G_{mb} = \frac{g_{mb1,2}}{1 - g_{mb3,4}\left(R_{A,B}//r_{o1}\right)} \tag{1}$$

where $g_{mb1,2}$ and $g_{mb3,4}$ is the bulk transconductance of transistors M1-M2 and M3-M4, respectively.
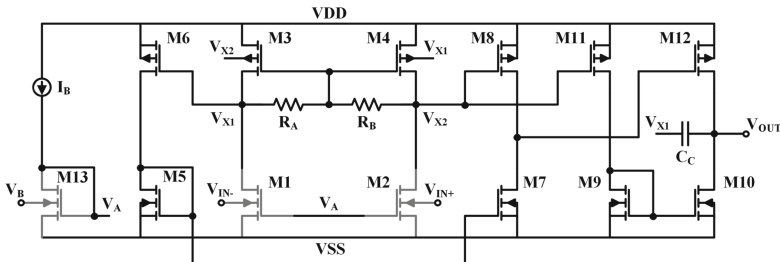
Fig. 1. Simplified schematic of the proposed OTA.

Careful attention must be paid during the design phase in order to guarantee that the denominator of (1) is always positive in all process corners and temperature values [15].

Considering that no current flows through R_A and R_B at DC, the drains of M3-M4 are at the same potential of their gates, i.e., they act as diode-connected transistors. Therefore, transistors M6 and M8 have the same source-gate voltage of M3 and M4, V_{SG}. Similar considerations are valid for the bias current of M6 which adds in conjunction with the current mirror M5-M7 and additional path for the signal.

The last stage is implemented by transistor M12 whose DC current can be again set through the current mirror ratio M8-M12, being the drain of M8 at the same potential of the drain of M4, neglecting systematic offsets. Class-AB operation of the last stage is enabled through M11, whose gate is connected to the output of the first stage, and current mirror M9-M10.

The frequency compensation of the OTA is achieved through the Miller capacitor C_C connected between the output and the drain of M3. Denoting with r_{o1}, r_{o2}, and r_{o3} the output resistance of the first, second and third stage, respectively, with c_{o2} the parasitic capacitance at the output of the second stage and with C_L the loading capacitance (not shown in Fig. 1), the small-signal analysis reveals that the open-loop transfer function can be approximated as

$$A(s) = A_0 \frac{\left(1 + \frac{s}{z_1}\right)}{\left(1 + \frac{s}{p_1}\right)\left(1 + a_1 s + a_2 s^2\right)} \tag{2}$$

where

$$A_0 \approx G_{mb} g_{m6,8} g_{m12} (R_{A,B} // r_{o1}) r_{o2} r_{o3} \tag{3}$$

$$p_1 \approx \frac{1}{g_{m6,8} g_{m12} r_{o2} r_{o3} C_C} \tag{4}$$

$$a_1 \approx \frac{C_L (C_C R_{A,B} + 2 c_{o2} r_{o2})}{2} \tag{5}$$

$$a_2 \approx \frac{C_C C_L c_{o2} R_{A,B} r_{o2}}{2} \tag{6}$$

$$z_1 \approx \frac{g_{m3,4}}{2 C_C} \tag{7}$$

From (3)–(4) the gain-bandwidth product (GBW) is expressed by

$$\omega_{GBW} = A_0 p_1 = \frac{G_{mb}}{C_C} \tag{8}$$

Evaluation of the phase margin, F, yields

$$\Phi = \tan^{-1}\left(\frac{1 - a_2 \omega_{GBW}^2}{a_1 \omega_{GBW}}\right) + \tan^{-1}\left(\frac{\omega_{GBW}}{z_1}\right) \tag{9}$$

Substituting (8) in (9) and solving for C_C allows setting the required value of the Miller capacitor to get the desired value of the phase margin. Table 1 summarizes the transistor aspect ratios and the other circuit parameters. Assuming a load capacitance equal to 50 pF, the required value of the C_C to get a phase margin of 70° is equal to only 470 fF.

Table 1. Transistor aspect ratios and circuit parameters.

Parameter	Value	Parameter	Value	Parameter	Value	Parameter	Value
V_{DD}	300 mV	$(W/L)_6$, $(W/L)_8$	9/0.18	C_L	50 pF	g_{m10}	78.9 μA/V
I_B	1.6 μA	$(W/L)_9$	2.1/0.18	$g_{m1,2}$	25.9 μA/V	g_{m12}	74.7 μA/V
V_B	150 mV	$(W/L)_{10}$	12.6/0.18	$g_{mb1,2}$	7.1 μA/V	r_{o1}	304 kΩ
$(W/L)_1$, $(W/L)_3$	4.2/0.3	$(W/L)_{11}$	9/0.18	$g_{mb3,4}$	3 μA/V	r_{o2}	845 kΩ
$(W/L)_{13}$	4.2/0.3	$(W/L)_{12}$	13.5/0.18	$g_{m3,4}$	7.3 μA/V	r_{o3}	110 kΩ
$(W/L)2$, $(W/L)4$	9/0.18	R_A, R_B	200 kΩ	g_{m7}	14.8 μA/V	c_{o1}	45 fF
$(W/L)5$, $(W/L)7$	0.45/0.18	C_C	470 fF	g_{m8}	16.3 μA/V	c_{o2}	62 fF

3   Experimental Results

The OTA in Fig. 1 has been fabricated using a 65-nm CMOS technology provided by STMicroelectronics. Figure 2a shows the layout of the OTA superimposed to the chip microphotograph. Occupied area is equal to $10.6 \cdot 10^{-3}$ mm^2.

(a)   (b)   (c)
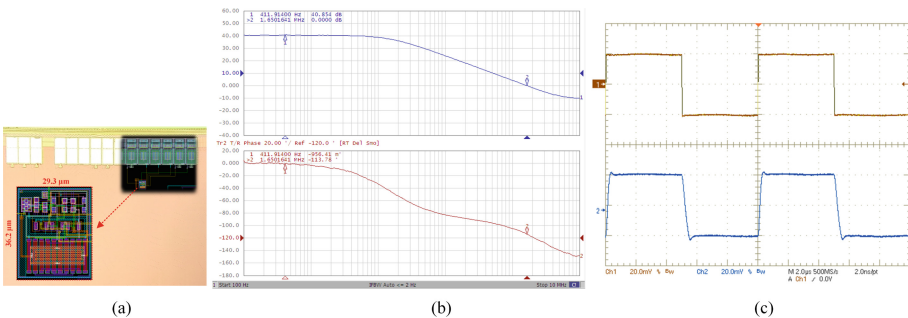
Fig. 2. a): OTA layout and chip microphotograph; b) measured bode diagram in open-loop configuration; c) measured unity-gain step response.

Figures 2b and 2c reports the measured open-loop frequency response and the unity-gain step response of one sample.

Six different samples have been experimentally characterized and the mean value of the main amplifier performance metric are summarized in the last column of Table 2. In the same Table the performance is compared with other recent sub-1-V OTAs. The traditional figures of merit expressions reported at the bottom of Table 2 are adopted to compare the different amplifiers. It can be noted that only solution in [11] shows a higher

than the proposed OTA value of $IFOM_S$ which, however, is a gate-drive OTA and has a 1-V power supply. Regarding, $IFOM_L$, the proposed OTA well compares with the other solutions, being only the value of [9, 12] and [13] higher. When $IFOM_{AS}$ and $IFOM_{AL}$ are considered, the proposed solution exhibits an improvement equal to about 2x and 5x as compared to the other solutions.

Table 2. Summary of measured performance metrics and comparison with other experimentally-tested sub-1-V OTAs.

Ref	[9]	[5]	[11]	[12]	[13]	[14]	This work*
Year	2015	2016	2017	2018	2020	2020	2022
Tech. (nm)	350	180	350	180	180	65	65
Op. Mode**	GD	BD	GD	BD	BD	BD	BD
# stages	3	3	2	2	3	3	3
$Area$ (mm^2)	0.0044	0.0198	0.014	0.0082	0.0098	0.002	0.00106
Supply voltage(V)	1	0.7	0.7	0.3	0.3	0.25	0.3
C_L (pF)	200	20	10	20	30	15	50
DC gain (dB)	129	57	65	63	98.1	70	38
I_{bias} (mA)	0.195	36	27	0.056	0.04333	0.10400	8.5
GBW (MHz)	0.02	3	1	0.0028	0.0031	0.0095	1.65
PM (°)	52	60	60	61	54	88	70.3
SR (V/ms)	0.005	2.8	0.25	0.0071	0.0091	0.002	0.18
$CMRR$ (dB)	70	19	45	72	60	62.5	39.8
$PSRR$ (dB)	184	52	50	62	61	38	44.7
$IFOM_S$ (MHz·pF/µA)[(1)]	20.51	1.67	0.37	1.00	2.15	1.37	9.71
$IFOM_L$ (V/µs·pF/µA)[(2)]	5.13	1.56	0.09	2.54	6.30	0.29	1.06
$IFOM_{AS}$ (MHz·pF/µA·mm^2)[(3)]	4662.00	84.18	26.46	121.95	219.00	685.10	9156.49
$IFOM_{AL}$ (V/µs·pF/µA·mm^2)[(4)]	1165.50	78.56	6.61	309.23	642.86	144.23	998.9

[*] Average values over six samples.

[**]GD: gate-drive; BD: bulk-driven

[(1)] $IFOM_S = \frac{GBW}{I_{bias}} C_L$ [(2)] $IFOM_L = \frac{SR}{I_{bias}} C_L$ [(3)] $IFOM_S = \frac{GBW}{I_{bias} \cdot Area} C_L$ [(4)] $IFOM_L = \frac{SR}{I_{bias} \cdot Area} C_L$

4   Conclusions

A bulk-driven three-stage OTA exploiting positive feedback and a single Miller capacitor has been proposed and experimentally validated. Capable of working under a 0.3-V supply and exhibiting class AB operation, the proposed OTA is a good candidate for area-constrained ultra-low-voltage, ultra-low-power applications, like wireless sensor nodes and implantable biomedical devices.

References

1. Ballo, A., Bottaro, M., Grasso, A.D.: A review of power management integrated circuits for ultrasound-based energy harvesting in implantable medical devices. Appl. Sci. **11**, 2487 (2021)
2. Grasso, A.D., Pennisi, S.: Ultra-low power amplifiers for IoT nodes. In: 2018 25th IEEE International Conference on Electronics, Circuits and Systems (ICECS), pp. 497–500 (2018)
3. Blalock, B.J., Allen, P.E., Rincon-Mora, G.: Designing 1-V op amps using standard digital CMOS technology. IEEE Trans. Circ, Syst. II: Analog Digital Sig. Process. **45**, 769–780 (1998)
4. Raikos, G., Vlassis, S.: 0.8 V bulk-driven operational amplifier. Analog Integr. Circ. Sig. Process. **63**, 425–432 (2010)
5. Cabrera-Bernal, E., Pennisi, S., Grasso, A.D., Torralba, A., Carvajal, R.G.: 0.7-V three-stage class-AB CMOS operational transconductance amplifier. IEEE Trans. Circ. Syst. I: Regul. Pap. **63**, 1807–1815 (2016)
6. Stockstad, T., Yoshizawa, H.: A 0.9-V 0.5-um rail-to-rail CMOS operational amplifier. IEEE J. Solid-State Circ. **37**, 286–292 (2002)
7. Chatterjee, S., Tsividis, Y., Kinget, P.: 0.5-V analog circuit techniques and their application in OTA and filter design. IEEE J. Solid-State Circ. **40**, 2373–2387 (2005)
8. Valero Bernal, M.R., Celma, S., Medrano, N., Calvo, B.: An ultralow-power low-voltage class-AB fully differential OpAmp for long-life autonomous portable equipment. IEEE Trans. Circuits Syst. II Express Briefs **59**, 643–647 (2012)
9. Grasso, A.D., Marano, D., Palumbo, G., Pennisi, S.: Design methodology of subthreshold three-stage CMOS OTAs suitable for ultra-low-power low-area and high driving capability. IEEE Trans. Circuits Syst. I Regul. Pap. **62**, 1453–1462 (2015)
10. Ferreira, L.H.C., Sonkusale, S.R.: A 60-dB Gain OTA Operating at 0.25-V Power Supply in 130-nm Digital CMOS Process. IEEE Trans. Circ. Syst. I: Regul. Pap. **61**, 1609–1617 (2014)
11. Grasso, A.D., Pennisi, S., Scotti, G., Trifiletti, A.: 0.9-V Class-AB Miller OTA in 0.35-mm CMOS with threshold-lowered non-tailed differential pair. IEEE Trans. Circ. Syst. I: Regul. Pap. **64**, 1740–1747 (2017)
12. Kulej, T., Khateb, F.: Design and implementation of sub 0.5-V OTAs in 0.18-μm CMOS. Int. J. Circ. Theory Appli. **46**, 1129–1143 (2018)
13. Kulej, T., Khateb, F.: A 0.3-V 98-dB Rail-to-Rail OTA in $0.18mm CMOS. IEEE Access **8**, 27459–27467 (2020)
14. Woo, K.-C., Yang, B.-D.: A 0.25-V Rail-to-rail three-stage OTA with an enhanced DC gain. IEEE Trans. Circ. Syst. II: Express Briefs **67**, 1179–1183 (2020)
15. Ballo, A., Grasso, A.D., Pennisi, S.: Active load with cross-coupled bulk for high-gain high-CMRR nanometer CMOS differential stages. Int. J. Circuit Theory Appl. **47**, 1700–1704 (2019)

A 0.3 V Three-Stage Body-Driven OTA

Riccardo Della Sala$^{(\boxtimes)}$, Francesco Centurelli, Pietro Monsurrò,
Giuseppe Scotti, and Alessandro Trifiletti

Dipartimento di Ingegneria dell'Informazione Informatica e Statistica,
Università di Roma la Sapienza, Via Eudossiana 18, 00184 Rome, Italy
`riccardo.dellasala@uniroma1.it`

Abstract. This paper presents a 0.3 V rail-to-rail three stage OTA. Due
to the topology of the input stage, to the three gain stages and to sub-
threshold operation, the proposed OTA exhibits high dc gain in spite of
the bulk-driven input. In addition, thanks to the adoption of two fully
differential stages and the usage of an additional local common-mode
feedback (CMFB) loop, the common-mode rejection ratio (CMRR) is
greatly improved with respect to other ULV bulk-driven OTAs. The first
stage is a bulk-driven Arbel-based stage with rail-to-rail input and dou-
bled transconductance gain. The second stage, is gate-driven to enhance
the dc gain. The third stage is again a bulk-driven amplifier and imple-
ments the differential to single-ended conversion through a gate-driven
current mirror. The proposed OTA has been fabricated in a commer-
cial 130 nm CMOS process from STMicroelectronics. Its area is about
0.002 mm^2, and it consumes 30 nW at the supply-voltage of 0.3 V. The
DC gain and unit-gain frequency are about 85 dB and 10 kHz, respec-
tively, with a load capacitance of 35 pF.

Keywords: Bulk-driven OTA · Ultra-low voltage · Three stage
amplifier · Body-biased · Local common mode feedback (LCMFB)

1 Introduction

The ever increasing spreading of Internet-of-Things (IoT) applications demands
for ultra-low power (ULP) and low silicon area integrated circuits to improve
quality and reduce cost of the sensor nodes [1].

Wearable healthcare devices and remote sensors have strongly modified the
way in which medical pathologies are studied and treated [2–6]. In particular,
implanted biomedical electronic devices must receive energy from an external
source or harvest energy from the environment, and the successful implementa-
tion of energy harvesting subsystems is a key factor to enable future electronic
biomedical and IoT devices. Power consumption in the nW range, small area,
and ultra-low supply voltage (ULV) are required to tolerate harvested power
fluctuations or enable direct harvesting in these applications [7]. In this context,
integrated circuits designers have focused on ULP and ULV circuits to improve
power efficiency and the autonomy of portable devices [8]. Since ultra-low power
consumption and supply voltages are needed in this kind of integrated circuits,

Operational Transconductance Amplifiers (OTAs) are among the most challenging blocks for analog designers. In particular the low supply voltage (lower than 0.5V) strongly limits the signal headroom and results in design issues which are very hard to cope with. In fact, achieving rail-to-rail common-mode input range is essential to guarantee a reasonable signal to noise ratio and good linearity performance. From the viewpoint of input common-mode range, body-driven input stages are the preferred ones, even though they exhibit lower gain, limited bandwidth, and worse noise performance [9–15].

Fully digital implementations of OTAs have been recently proposed in [7,14, 16,17]; these OTAs do not require any passive component and are able to operate at supply voltages lower than 0.3V, being very interesting for what concerns area footprint and power consumption. However, the performances of these circuits can be sensitive to process, supply voltage and temperature (PVT) variations and mismatch which are very critical in nanometer CMOS processes [18], and may require suitable calibration strategies to achieve high production yield [19–21].

Indeed, even if bulk-driven OTAs exhibit some drawbacks with respect to gate-driven ones and to digital OTAs, they can be designed to be robust against PVT and mismatch variations.

Another limitation in ULV design is that the use of cascode structures is severely limited, and this implies that achieving large gain is a hard task. Techniques to improve the gain, such as multi-stage amplifiers [22–26], have been proposed in the literature to overcome this issue.

In this work, a 0.3V rail-to-rail three-stage OTA with high DC gain and improved CMRR is presented. The first stage is a bulk-driven Arbel amplifier with a rail-to-rail input. The second stage is gate driven, and both the first and second stages are fully differential to better reject common-mode signals. An additional local CMFB loop is exploited to further enhance CMRR. Differential to single-ended conversion is performed by the last stage which also drives the output load capacitor. The rest of this paper is organized as follows: Sect. 2 describe the proposed OTA and its principle of operation. Section 3 presents the measurement results of the fabricated chip. Finally, conclusions are drawn in Sect. 4.

2   Circuit Description

The proposed OTA topology is reported in Fig. 1. The first and the third stages are body-driven, and their dc operating points are set through gate biasing, whereas the second stage is gate-driven and exploits a body bias approach to set the dc operating point. Denoting as $g_{m_{ni}}$, $g_{mb_{ni}}$ and $g_{ds_{ni}}$ ($g_{m_{pi}}, g_{mb_{pi}}$ and $g_{ds_{pi}}$), the gate and body transconductances and the output conductance of the i-th $NMOS$ ($PMOS$) device respectively, the differential gain is:

$$A_{V_{D_{tot}}} = \prod_{i=1}^{3} A_{V_{D_i}} = 2 \cdot \frac{g_{mb_{n1,2}} + g_{mb_{p1,2}}}{g_{ds_{n1,2}} + g_{ds_{p1,2}}} \frac{g_{m_{n3,4}} + g_{m_{p3,4}}}{g_{ds_{n3,4}} + g_{ds_{p3,4}}} \frac{g_{mb_{n5,6}} + g_{mb_{p5,6}}}{g_{ds_{n5,6}} + g_{ds_{p5,6}}} \quad (1)$$

The first and the second stages are fully differential amplifiers and a CMFB is exploited to reject common mode variations and enhance the CMRR. The
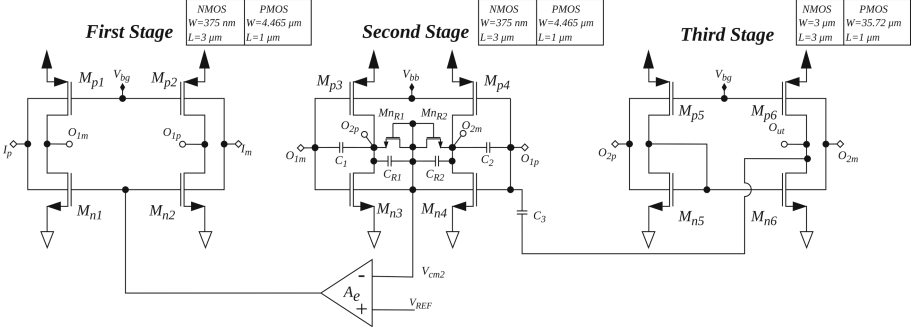
Fig. 1. Proposed OTA Architecture

output common-mode voltage of the second stage is estimated through two large NMOS pseudo-resistors, compared with reference voltage (equal to $V_{DD}/2$), and amplified by an error amplifier A_e whose output voltage is fed back to the first stage to close the feedback loop. To further improve the CMRR performance, an additional local CMFB (closed through the body terminals of M_{n3} and M_{n4}) is used by exploiting an approach similar to the one adopted in [27]. The third stage performs single-ended to differential conversion through transistors M_{n5} and M_{n6} implementing a conventional current mirror which also contributes to enhance the overall CMRR given by:

$$CMRR = \frac{g_{m_{n1,2}}}{g_{ds_{n1,2}} + g_{ds_{p1,2}}} \cdot A_e \cdot \frac{g_{mb_{n3,4}} + g_{mb_{p3,4}}}{g_{ds_{n3,4}} + g_{ds_{p3,4}}} \cdot \frac{g_{m_{n5}}}{g_{ds_{n5,6}} + g_{ds_{p5,6}}} \qquad (2)$$

and results robust under process and mismatch variations. The overall phase margin is assured through the compensation capacitances $C_{1,2,3}$, which provide reverse nested Miller compensation.
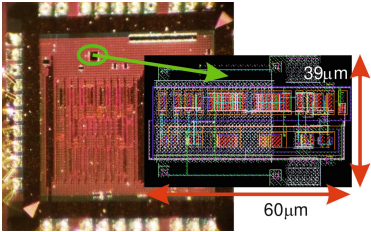
Fig. 2. Chip microphotograph.

Table 1. Monte Carlo mismatch simulations.

	Nominal	μ	σ
A_d [dB]	86.11	85.81	0.64
GBW [kHz]	11.08	10.81	1.12
$m\varphi$ [deg]	58.27	58.05	2.21
SR_{avg} [V/ms]	3.74	3.36	0.45
$CMRR$ [dB]	136.11	57.80	8.73
P_D [nW]	30.00	30.12	4.63
$Offset$ [mV]	0.4m	0.03	11.82

3   Measured Results

The chip microphotograph and the detail with the layout of the proposed OTA are reported in Fig. 2, showing an active area of about $60 \times 39 \ \mu m^2$. Measured

results of the closed-loop non-inverting buffer configuration are shown in Fig. 3(a) (AC response) and Fig. 3(b) (transient response) and are in good agreement with simulations. Main performance parameters are reported in Table 2 and compared with the literature. Table 2 reports the results of Monte Carlo mismatch simulations to show the robustness of the design.

(a)   (b)
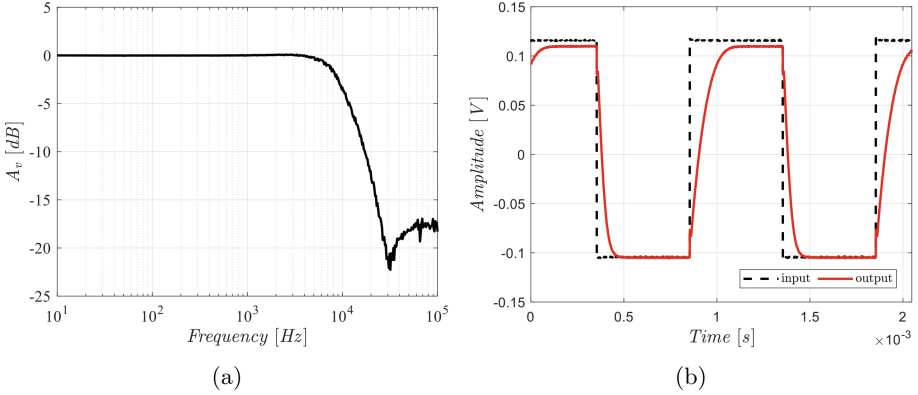
Fig. 3. Measured closed-loop AC response ($GBW = 9.8\ kHz$) a) and measured transient step response ($SR_+ = 2.5\,\text{V/ms}$, $SR_- = 5\,\text{V/ms}$) b).

Table 2. Comparison with the literature.

	This work	[28]	[29]	[23]	[30]
Year	2022	2021	2020	2020	2019
Tech [nm]	130	180	180	180	130
VDD [V]	0.3	0.3	0.3	0.3	0.3
Ad [dB]	86.11	30	64.7	98.1	49.8
CL [pF]	35	150	30	30	2
GBW [kHz]	11.08	0.25	2.96	3.1	9100
mφ [deg]	58.27	90	52	54	76
SRp [$\frac{V}{ms}$]	2.61	–	1.9	14	–
SRm [$\frac{V}{ms}$]	4.86	–	6.4	4.2	–
SRavg [$\frac{V}{ms}$]	3.74	0.085	4.15	9.1	3.8
CMRR [dB]	136.35	41	110	60	–
Pd [nW]	30	2.4	12.6	13	1800
Mode	Body Driven	DIGOTA	Body Driven	Body Driven	Gate Driven
FOM$_s$[$\frac{MHz \cdot pF}{mW}$]	11.5 k	15.89 k	7.05 k	7.15 k	10.11 k

4   Conclusion

In this work we have presented a 0.3V ULV three stage OTA with high dc gain and improved CMRR. Compared with the state of the art, the proposed OTA exhibits very good overall performance and good robustness to both PVT and mismatch variations.

References

1. Alioto, M. (ed.): Enabling the internet of things. Springer, Cham (2017). https://doi.org/10.1007/978-3-319-51482-6
2. Della Sala, R., Centurelli, F., Monsurrò, P., Scotti, G.: Sub-μW front-end low noise amplifier for neural recording applications. In: 2022 17th Conference on Ph. D Research in Microelectronics and Electronics (PRIME), pp. 305–308. IEEE (2022)
3. Silva, R.S., Rodovalho, L.H., Aiello, O., Rodrigues, C.R.: A 1.9 nW, Sub-1 V, 542 pA/V Linear Bulk-Driven OTA with 154 dB CMRR for Bio-Sensing Applications. J. Low Power Electron. Appl. **11**(4), 40 (2021)
4. Pu, X., An, S., Tang, Q., Guo, H., Hu, C.: Wearable triboelectric sensors for biomedical monitoring and human-machine interface. iScience **24**, 102027 (2021)
5. Toledo, P., Crovetti, P.S., Klimach, H.D., Musolino, F., Bampi, S.: Low-Voltage, Low-Area, nW-Power CMOS Digital-Based Biosignal Amplifier. IEEE Access **10**, 44106–44115 (2022)
6. Della Sala, R., Monsurrò, P., Scotti, G., Trifiletti, A.: Area-efficient low-power bandpass Gm-C filter for epileptic seizure detection in 130nm CMOS. In: 2019 26th IEEE International Conference on Electronics, Circuits and Systems (ICECS), pp. 298–301. IEEE (2019)
7. Toledo, P., Crovetti, P., Aiello, O., Alioto, M.: Fully Digital Rail-to-Rail OTA With Sub-1000-μm^2 Area, 250-mV Minimum Supply, and nW Power at 150-pF Load in 180 nm. IEEE Solid-State Circuits Lett. **3**, 474–477 (2020)
8. Grasso, A.D., Pennisi, S.: Ultra-low power amplifiers for IoT nodes. In: 2018 25th IEEE International Conference on Electronics, Circuits and Systems (ICECS), pp. 497–500 (2018)
9. Centurelli, F., Della Sala, R., Monsurrò, P., Scotti, G., Trifiletti, A.: A 0.3 V Rail-to-Rail ultra-low-power OTA with improved bandwidth and slew rate. J. Low Power Electron. Appl. **11**(2), 19 (2021)
10. Centurelli, F., Della Sala, R., Scotti, G., Trifiletti, A.: A 0.3 V, Rail-to-Rail, Ultralow-Power, Non-Tailed, Body-Driven, Sub-Threshold Amplifier. Appl. Sci. **11**(6), 2528 (2021)
11. Centurelli, F., Della Sala, R., Monsurrò, P., Scotti, G., Trifiletti, A.: A novel OTA Architecture exploiting current gain stages to boost bandwidth and slew-rate. Electronics **10**(14), 1638 (2021)
12. Centurelli, F., Della Sala, R., Monsurrò, P., Scotti, G., Trifiletti, A.: A tree-based architecture for high-performance ultra-low-voltage amplifiers. J. Low Power Electron. Appl. **12**(1), 12 (2022)
13. Khateb, F., Kulej, T.: Design and implementation of a 0.3-V differential difference amplifier. IEEE Trans. Circ. Syst. I, **66**(2), 513–523 (2018)
14. Toledo, P., Crovetti, P., Klimach, H., Bampi, S., Aiello, O., Alioto, M.: A 300mV-supply, Sub-nW-power digital-based operational transconductance amplifier. IEEE Trans. Circuits Syst. II **68**(9), 3073–3077 (2021)
15. Della Sala, R., Centurelli, F., Monsurrò, P., Scotti, G.: High-efficiency 0.3V OTA in CMOS 130nm technology using current mirrors with gain. In: 2022 17th Conference on Ph. D Research in Microelectronics and Electronics (PRIME), pp. 69–72. IEEE (2022)
16. Palumbo, G., Scotti, G.: A novel standard-cell-based implementation of the digital OTA suitable for automatic place and route. J. Low Power Electron. Appl. **11**(4), 42 (2021)

17. Centurelli, F., Della Sala, R., Scotti, G.: A standard-cell-based CMFB For fully synthesizable OTAs. J. Low Power Electron. Appl. **12**(2), 27 (2022)
18. Khalid, U., Mastrandrea, A., Olivieri, M.: Novel approaches to quantify failure probability due to process variations in nano-scale CMOS logic. In: 2014 29th International Conference on Microelectronics Proceedings - MIEL 2014, pp. 371–374. IEEE (2014)
19. Toledo, P., Crovetti, P., Klimach, H., Bampi, S.: Dynamic and static calibration of ultra-low-voltage, digital-based operational transconductance amplifiers. Electronics **9**(6), 983 (2020)
20. Della Sala, R., Centurelli, F., Scotti, G.: Enabling ULV fully synthesizable analog circuits: the BA cell, a standard-cell-based building block for analog design. IEEE Trans. Circuits Syst. II **69**, 4689–4693 (2022)
21. Della Sala, R., Centurelli, F., Scotti, G.: A novel differential to single-ended converter for ultra-low-voltage inverter-based OTAs. IEEE Access **10**, 98179–98190 (2022)
22. Abdelfattah, O., Roberts, G.W., Shih, I., Shih, Y.-C.: An ultra-low-voltage CMOS process-insensitive self-biased OTA with rail-to-rail input range. IEEE Trans. Circuits Syst. I Regul. Pap. **62**(10), 2380–2390 (2015)
23. Kulej, T., Khateb, F.: A 0.3-V 98-dB rail-to-rail OTA in 0.18 μ m CMOS. IEEE Access **8**, 27459–27467 (2020)
24. Woo, K-C., Yang, B.-D.: A 0.25-v rail-to-rail three-stage OTA with an enhanced dc gain. IEEE Trans. Circuits Syst. II: Express Briefs **67**, 1179–1183 (2020)
25. Giustolisi, G., Palumbo, G.: Design of three-stage OTA based on settling-time requirements including large and small signal behavior. IEEE Trans. Circuits Syst. I Regul. Pap. **68**(3), 998–1011 (2021)
26. Grasso, A.D., Marano, D., Palumbo, G., Pennisi, S.: Single miller capacitor frequency compensation techniques: theoretical comparison and critical review. Int. J. Circuit Theory Appl. **50**(5), 1462–1486 (2022)
27. Centurelli, F., Della Sala, R., Monsurró, P., Tommasino, P., Trifiletti, A.: An ultra-low-voltage class-ab OTA exploiting local CMFB and body-to-gate interface. AEU - Int. J. Electr. Commun. **145**, 154081 (2022)
28. Toledo, P., Crovetti, P., Aiello, O., Alioto, M.: Design of Digital OTAs with operation down to 0.3 V and NW power for direct harvesting. IEEE Trans. Circ. Syst. I **68**(9), 3693–3706 (2021)
29. Kulej, T., Khateb, F.: A Compact 0.3-V class AB bulk-driven OTA. IEEE Trans. Very Large Scale Integr. VLSI Syst., **28**(1), 224–232 (2019)
30. Lv, L., Zhou, X., Qiao, Z., Li, Q.: Inverter-based subthreshold amplifier techniques and their application in 0.3-V. IEEE J. Solid-State Circuits **54**(5), 1436–1445 (2019)

The 32 Analog Channels Readout for the Long-Flight GAPS Balloon Experiment Tracking System

E. Riceputi[1(✉)], M. Boezio[2], L. Fabris[3], L. Ghislotti[1], P. Lazzaroni[1],
M. Manghisoni[1], L. Ratti[4], V. Re[1], and G. Zampa[2]

[1] Department of Engineering and Applied Sciences,
University of Bergamo, Dalmine, Italy
elisa.riceputi@unibg.it
[2] INFN, Trieste Division, Trieste, Italy
[3] Oak Ridge National Laboratory, Oak Ridge, TN, USA
[4] Department of Electrical, Computer and Biomedical Engineering,
University of Pavia, Pavia, Italy

Abstract. The paper describes the main results of the characterization of the flight ASIC developed for the readout of a lithium-drifted silicon, Si(Li), detector-based tracker. The system aims to detect indirect signatures of dark matter through the identification of low-energy ($<$ 0.25 GeV/n) cosmic-ray antiprotons, antideuterons, and antihelium. This instrument is developed in the frame of the GAPS (General AntiParticle Spectrometer) balloon experiment. The developed electronics consists of a 32-channels mixed-signal ASIC, designed in a commercial 180 nm CMOS technology and an ad-hoc front-end board (FEB). Data from charged particle detection are also reported.

Keywords: CMOS · Readout electronics · Noise · Front-end

1 Introduction

The General AntiParticle Spectrometer (GAPS) is an experiment that is conceived to detect low-energy cosmic ray antinuclei [1]. The experiment consists of a stratospheric balloon with a detection apparatus based on a Time of Flight (ToF) system and on a segmented Si(Li) detectors for particle tracking [2]. A first flight is expected in the austral summer of 2023.

The tracker system is composed of ten layers of 6×6 modules each. The modules are arranged in lines of 6 and every line shares the same low power supply voltage, as schematically reported on the left side of Fig. 1. Each module hosts 4 Si(Li) detectors divided into 8 strips, the ASIC for the readout electronics and the Front-End Board (FEB), see Fig. 1 right side, that implements the connection throughout the ASIC and the detectors and provides low power references and signals between the 6 modules. The ASIC developed for detector readout is a mixed-signal processor that has been produced in a commercial 180 nm CMOS
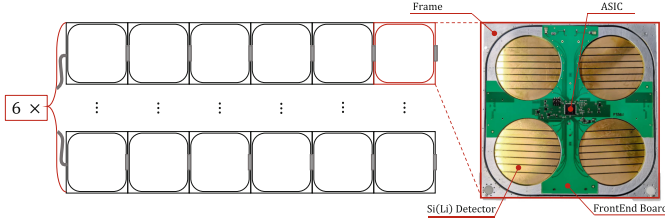
Fig. 1. Schematic of a single layer of the GAPS tracker (left side). Module of the GAPS tracker (right side).
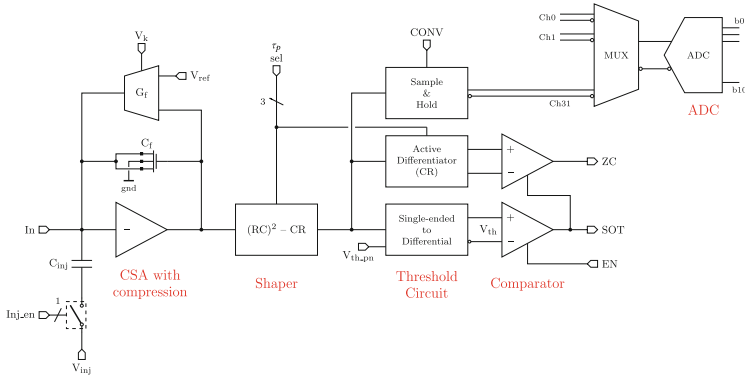
Fig. 2. SLIDER32 analog readout channel schematic.

technology. The device, named SLIDER32 (32 channels Si-Li DEtector Readout ASIC), is comprised of 32 low-noise analog readout channels, an 11-bit SAR ADC and a digital back-end section which is responsible for defining channel settings and to exchange digital information with the data acquisition system (DAQ). The simplified block diagram of the channel is reported in Fig. 2. The electronics have to resolve both X-rays in the range of 20 to 100 keV and charged particles that release in the detectors an energy up to 100 MeV. A resolution of 4 keV FWHM at a strip capacitance of about 40 pF is needed in order to clearly distinguish X-rays from antiprotonic or antideuteronic exotic atoms [1]. To comply with these requirements, the analog conditioning scheme is based on a low-noise charge-sensitive amplifier (CSA) performing dynamic signal compression. This solution takes advantage of the non-linear features of a Metal Oxide Semiconductor (MOS) capacitor in the feedback loop of the CSA [3]. A Krummenacher feedback network provides a continuous reset of the CSA. This architecture was chosen for its capability to compensate for the detector leakage current (5−10 nA per strip). The channel also includes a semi-Gaussian shaper whose output signal peaking time is selectable among eight values in the 0.25−2 μs range, a comparator with a threshold circuit to discriminate the amplified pulses, a single-ended to differential Sample&Hold which provides at the output a signal proportional

to the peak and an active differentiator followed by a zero-crossing circuit that provides a trigger, synchronous with the shaper peaking time, for the S&H. A detailed description of the analog channel is reported in [4]. The readout electronics of the ASIC, which is expected to work at a temperature of $-40\,^\circ$C, need to dissipate less than $10\,$mW/channel to be compatible with the ballooning nature of the experiment.

2 SLIDER32 Performance

The ASIC and FEB have been extensively tested at ambient temperature in a twofold way: by measuring the DC bias conditions of the circuit and by running a purposely developed `Automated validation test`. This procedure performs several types of tests, i.e. noise, pedestal, self trigger, threshold scan, channel input-output characteristic, and waveform scan. The setup implemented for the tests comprises a PC running a Python-based testing program connected to an ALTERA Cyclone V Field Programmable Gate Array (FPGA) via two Universal Serial Bus (USB) cables. An interface board was specifically designed to route the power supplies and the signals through a flex ribbon cable to the FEB. Both the analog and digital bias of the board comes from a Keysight N6705C DC Power analyser. Results obtained from the tests indicate that the ASIC is fully functional and meets the specifications. The most significant outcomes are reported in the following. In Fig. 3a the input-output trans-characteristics of the channel at all the selectable peaking times are reported for a single channel of the ASIC. As expected, the bilinear characteristic of the gain is visible in the graph, with a higher slope for small signals and a lower slope for the rest of the input signal range. Employing a linear interpolation in the low energy range, the gain of the channel at that peaking time is extracted. Figure 3b shows a magnification of the same plot at a peaking time setting of $0.98\,\mu$s: the evaluated gain, $1.06\,$ADU/keV, is consistent with post-layout simulations.

One of the most interesting outcomes of the test activity is relevant to the noise performance at $-40\,^\circ$C. The figure of merit commonly used for this purpose is the Equivalent Noise Charge (ENC) evaluated as the width of the distribution at half maximum (FWHM). The Equivalent Noise Energy (ENE) FWHM, expressed in keV, is calculated from measurements of ENC using the following expression:

$$FWHM = 2.35 \times \varepsilon \times \frac{ENC}{q} \tag{1}$$

where ε is the ionization energy of silicon and q is the elementary charge. The noise is measured at the output of the ADC (ENC extracted from the variance of the distribution of the output values, as shown in Fig. 4a, divided by the gain of the channel). Figure 4b reports the FWHM as a function of the peaking time measured in two different conditions, namely with and without an input capacitance of $40\,$pF that emulates the detector capacitance. As expected, noise measurements for channels with the capacitance are higher with respect

(a)   (b)
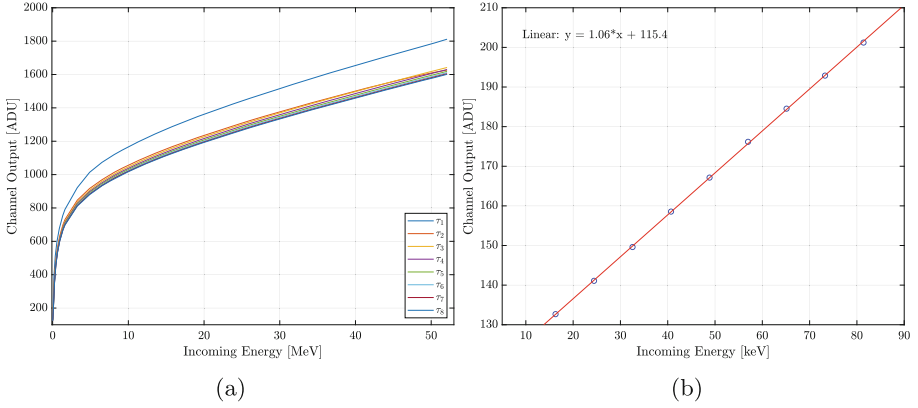
Fig. 3. (a) Channel Output as a function of the Incoming Energy of one channel at different peaking times: the bilinear behavior of the derived gain, typical of the dynamic compression of the signal implemented in the channel, is clearly visible. The value at output of the channel is expressed in Analog Digital Units (ADU). (b) Channel Output as a function of the Incoming Energy in the linear high gain region for one channel at a peaking time of $0.98\,\mu$s.

to channels with no capacitance, but in line with the experiment requirements, in particular for peaking times in the $0.5-1.5\,\mu$s range.

To properly verify the behavior of the entire acquisition chain, data from a fully assembled module were evaluated. In particular, the purpose of this activity is to detect the charge released in the detector by cosmic relativistic muons.

(a)   (b)
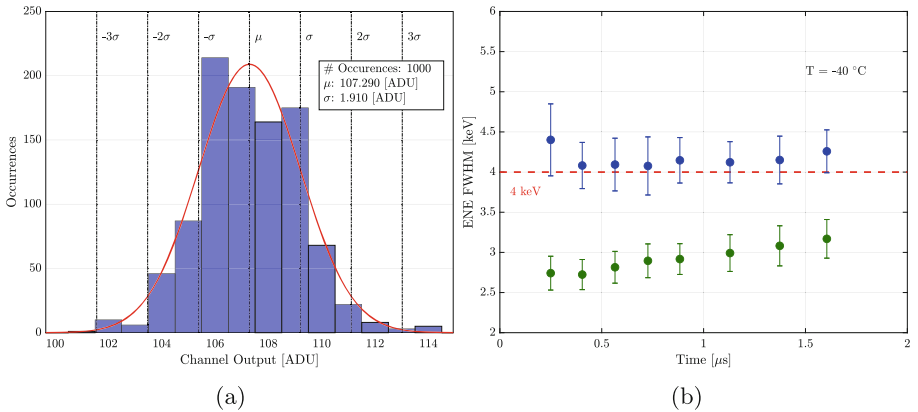
Fig. 4. (a) Pedestal plot: distribution of values measured at the output of the channel without injecting charge. (b) ENE FWHM as a function of the peaking time for channels with a $40\,$pF capacitance connected at the input (blue dots) and channels without it (green dots).

(a)   (b)
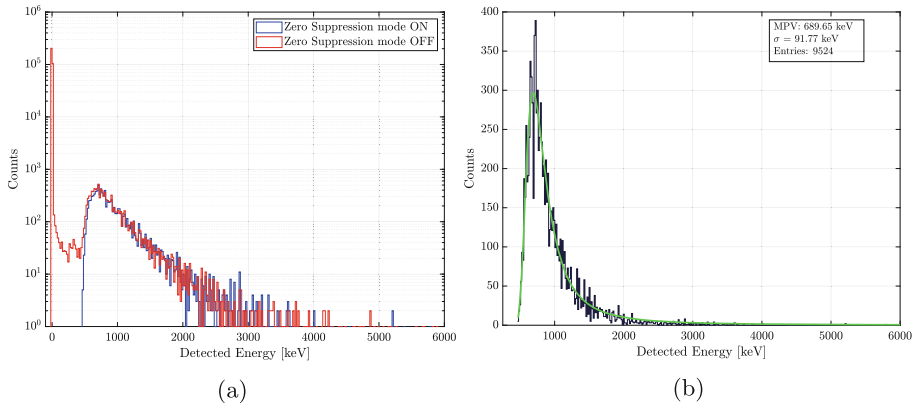
Fig. 5. (a) Comparison between an acquisition in Self-Tigger mode with the Zero-Suppression functionality activated (red line) and without this feature (blue line). (b) Data acquired in Zero-Suppression mode (black line) fitted with a Landau distribution (green line), which shows a peak at 689.65 keV.

The same setup used for the characterisation of the FEBs was implemented for these tests with the addition of a CAEN HiVolta high voltage power supply to provide the –250 V biasing voltage to the Si(Li) detectors. Figure 5a shows the result of the acquisition performed for a duration of 1 h with the ASIC operated in Self-Trigger mode. The blue histogram represents the measurement carried out with the Zero Suppression (ZS) feature activated. The latter represents an operating mode where the output of the channel, sampled by the ADC, can be read with the dedicated procedure only if the Signal Over Threshold (SOT) comparator fires. The threshold, above which the SOT triggers the acquisition chain, is set to ≈450 keV, to prevent natural radioactivity and electronic noise from affecting the acquisitions. The two measurements are consistent with each other, the only difference being that, for the zero-suppressed data, the pedestal peak (that represents the noise) is not present, as expected. The distribution of the detected muons is fairly consistent with data acquired with the same type of detector (Si(Li)), with discrete electronics in [5]. As reported in Fig. 5b, the distribution of the detected cosmic muon is well fitted with a Landau distribution with the most probable value peaked in ≈690 keV.

3   Conclusions

The paper discusses the performance of the SLIDER32 ASIC developed for the GAPS experiment. The analog low-noise channel exhibits the typical bilinear response associated with the dynamic compression of the signal used to cope with the large energy range requirements. The focus is on the noise performance, which meets the specifications of the experiment, i.e. ∼4 keV FWHM, especially for long peaking times (up to 1.5 μs). Results from cosmic muon detection demonstrate that Self-Trigger and Zero-Suppression modes work correctly,

especially for incoming particles with energy above 450 keV. Further studies are ongoing in order to verify the functionality of the system also for lower energies: an optimum target can be a threshold of 20 keV. The achievement of this target is of utmost importance for detecting X-rays from different sources (i.e. 22 keV and 88 keV from ^{108}Cd and 59.54 keV from ^{241}Am) for the calibration of the system. A goal threshold of 20 keV is also fundamental for the identification of part of the X-rays from the de-excitation of the exotic atom and therefore for the identification of the antinuclei and the achievement of the scientific objectives of the experiment.

References

1. Aramaki, T., et al.: Antideuteron sensitivity for the GAPS experiment. Astropart. Phys. **74**, 6–13 (2016)
2. Aramaki, T., et al.: Development of large format Si(Li) detectors for the GAPS dark matter experiment. Nucl. Instrum. Methods Phys. Res. A **682**, 90–96 (2012)
3. Manghisoni, M., Comotti, D., Gaioni, L., Ratti, L., Re, V.: Dynamic compression of the signal in a charge sensitive amplifier: from concept to design. IEEE Trans. Nucl. Sci. **62**(5), 2318–2326 (2015)
4. Manghisoni, M., Re, V., Riceputi, E., Sonzogni, M., Ratti, L., Fabris, L.: Low-noise analog channel for the readout of the Si(Li) detector of the gaps experiment. IEEE Trans. Nucl. Sci. **68**(11), 2661–2669 (2021)
5. Rogers, F., et al.: Large-area Si(Li) detectors for X-ray spectrometry and particle tracking in the GAPS experiment. J. Instrumentation **14**(10), P10009 (2019)

Micro- and Nano-electronic Devices

In-Memory Computing with Crosspoint Resistive Memory Arrays for Machine Learning

Saverio Ricci[✉], Piergiulio Mannocci, Matteo Farronato, and Daniele Ielmini

Dipartimento di Elettronica, Informazione e Bioingegneria (DEIB), Politecnico di Milano, Milano, Italy
saverio.ricci@polimi.it

Abstract. Memristor-based hardware accelerators play a crucial role in achieving energy-efficient big data processing and artificial intelligence, overcoming the limitations of traditional von Neumann architectures. Resistive-switching memories (RRAMs) combine a simple two terminal structure with the possibility of tuning the device conductance. When organized in matrices, they are able to perform analog Matrix-Vector-Multiplication (MVM) between the conductance matrix encoded using the RRAMs and the input voltage in one operation. In this work, we present forming-free RRAMs as suitable elements to overcome the common forming initialization problem of the crossbar, thus enabling large scale crossbar implementation. A fully memristive architecture optimized for MVMs in implemented to demonstrate experimental eigenvalue/eigenvector calculation according to the power-iteration algorithm, with a fast convergence within about 10 iterations to the correct solution. Finally, Principal Component Analysis of the Wine dataset is proposed to support forming-free crosspoint arrays for accelerating advanced machine learning, showing a 99% accuracy comparable to a floating-point implementation.

Keywords: Resistive switching memory (RRAM) · Forming · Matrix-vector multiplication · Principal component analysis · In-memory computing

1 Introduction

In memory computing (IMC) appears as one of the most promising candidates to improve the performance and energy efficiency of computation [1–4], thanks to its suppressed data movement [1, 5] and inherent parallelism [6, 7]. This new computational paradigm takes advantage of emerging memory technologies, such as the resistive switching memory (RRAM), which allow for unique features, such as analogue programmability, good scaling and back-end-of-line integration [1, 2]. These devices, in fact, can execute matrix-vector-multiplications (MVM) [4–7], backbone of most machine learning and scientific computing algorithm, in parallel within the crosspoint array configuration, by summing the currents according to the Kirchhoff's law and multiplying voltage and conductance by the Ohm's law in just one operation [1–3]. In this work we proposed novel forming-free RRAMs to overcome the common initialization problems of the devices and enable

large passive crossbar fabrication [2, 5, 6]. The electrical characterization highlights a good programmability both with the current and the reset amplitude, with analog-grade programmability between 1 µS and 500 µS. The analogue tuning precision is tested using an 8 × 8 crossbar to compute several MVMs and power iterations. Finally, a fully memristive architecture is implemented to tackle the Wine dataset classification [5], mapping the covariance matrix in the RRAM crossbar, and extracting the principal component using the power iteration and deflation. The results of the Principal Component Analysis (PCA) show a clustering accuracy comparable to a 64-bit floating point processor, with a 98.99% overlap of the projected datasets, thus supporting RRAMs for high-efficiency, low-power hardware accelerators for machine learning applications.

2   Electrical Characterization of the RRAMs

RRAMs are two-terminal devices made by an oxide layer sandwiched between two metals [1–3]. The conductance can be tuned by externally applied voltage pulses to locally change the oxygen vacancy concentration inside the oxide and create a conductive path responsible for the electrical properties [2, 5]. The bottom electrode (BE) is usually made in platinum, adopted as Schottky-type materials since it is inert with respect to the oxide interface [2], while titanium can act as good top electrode (TE) material for oxygen scavenging, thus leading to the formation of a thin vacancy-rich oxygen exchange layer [6]. By applying a positive voltage to the TE, the oxygen vacancies migrate and reallocate inside the oxide layer to form a vacancy-based conductive channel, which dictates a low resistance state (LRS). The sudden decrease of resistance, known as set transition, is commonly limited by a compliance (I_{CC}) current to prevent permanent breakdown during the set operation. During the reset, the application of a negative voltage induces a vacancy migration toward the opposite direction, thus reducing the conductivity of the channel to a high resistive state (HRS). One of the most critical aspects for RRAM is the forming operation, the first breakdown process which creates a conductive path in the device, which usually requires large voltages able to disturb and damage other devices in the passive crossbar [2, 6]. With the aim of fabricating a device which eliminates the need of the forming initialization, here we proposed a forming-free RRAM based on Pt/1.5 nm HfO_2/Ti/Au stack [6]. Figure 1(a) reports the cycling behavior of the devices. The red dashed line stands for the reset initialization, which brings the device from the 957 µS LRS to an HRS <1 µS. Set and reset operations are thus possible, showing a butterfly-like hysteresis which is increasingly wider with I_{CC}. The conductance values reached during the set transition, in Fig. 1(b), linearly depend on the I_{CC} while the HRS is independent. The gradual behavior of the response during the reset suggests the possibility of controlling the device state by controlling the reset voltage during the sweep, as visible in Fig. 1(c), where the device is gradually reset and the hysteresis curves gradually move from the LRS to the HRS. Considering the states achieved at different amplitude, in Fig. 1(d), the conductance spreads over 4 order of magnitudes from several mS to a few µS. The exponential behavior suggests an Arrhenius-like behavior based on activation energy of the oxygen vacancy migration [1, 2].
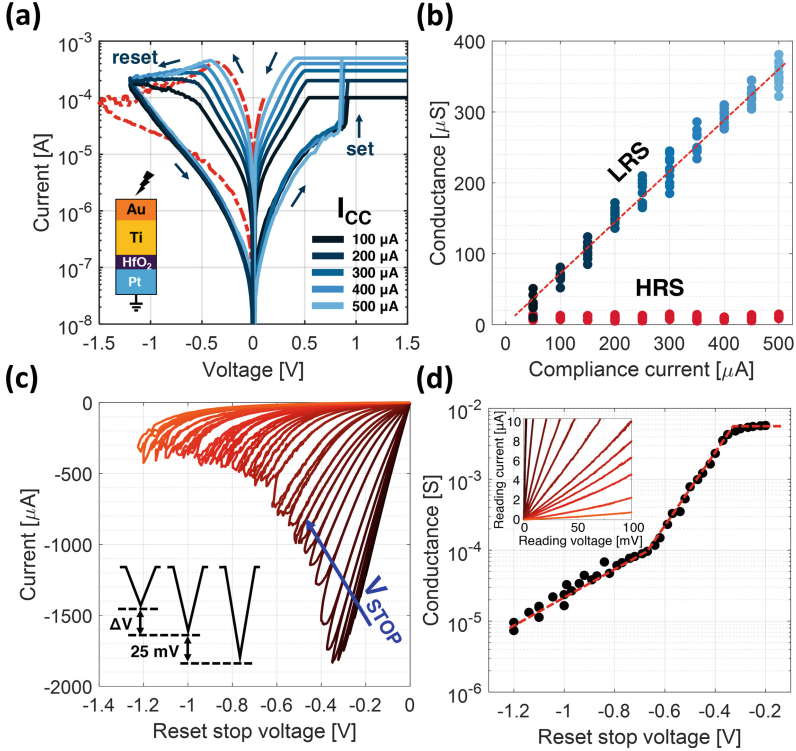
Fig. 1. Quasi-static characterization of a single RRAM. a) Reset initialization (red dashed lines) and I–V curves at different I_{CC}. Increasing the I_{CC} the different hysteresis curves have wider windows. b) Linear dependence of the conductance states (LRS) reached choosing different I_{CC}. c) Subsequent I–V reset sweeps stopped at different amplitudes (V_{stop}). The difference between two sweeps is 25 mV. d) Conductance states as a function of V_{stop}. In the inset, an insight of the I–V curves between 0 and 100 mV to highlight the linear response.

The electrical response, highlighted in the insight of Fig. 1(d), has a good linearity between 0 and 100 mV, the voltage window adopted in this work for the experiments. A 32×32 forming-free RRAM-based crossbar is presented in Fig. 2(a) together with the initial state on an 8×8 matrix used for the experiments, in Fig. 2(b), where the values spread between 1 μS and 100 μS. A suitable program and verify algorithm is used to program the devices till a desired target, for example the one visible in Fig. 2(c), by increasing the I_{CC} to make the device more conductive or resetting the devices with proper amplitude and decrease the values. The programmed crossbar encodes the covariance matrix associated to the Wine dataset, which will be later user for the PCA. Figure 2(d) summarizes the result of the programming for 4 different devices. When the algorithm runs the first time, all the matrix is programmed with an average number of operations between 20 and 50. After each cycle, a full read of the matrix is performed. For most of the devices the conductance value remains stable during the programming of other devices inside the array, as shown by the orange curve or the light blue one. Other

devices, instead, spontaneously change their conductance possibly due to instability or programming disturb within the array, as for the red curve and the blue one. Additional cycles are thus required to completely program the array, 1 more for the blue and two for the red device.
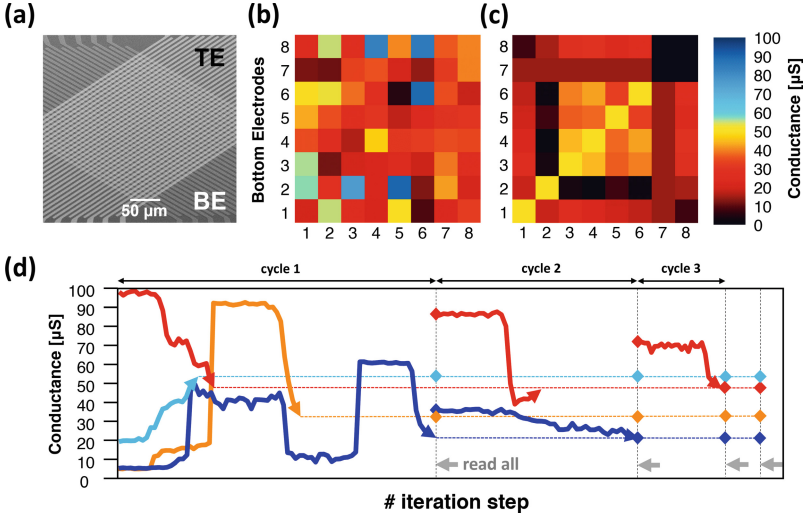
Fig. 2. Program and verify algorithm for array programming. a) SEM image of a 32×32 crossbar with orthogonal TEs and BEs. b) Initial conductance state of the 8×8 matrix used in this work. The values spread between $1\,\mu S$ and $100\,\mu S$. c) Desired target conductance matrix for the power iteration demonstration. The values are between $1\,\mu S$ and $50\,\mu S$. d) Evolution of 4 RRAMs during the program and verify algorithm. Some devices require additional programming cycles since they were modified in the previous operations (blue and red curves).

3   Power Iteration and Principal Component Analysis

To support the use of the RRAMs for in-memory computing, in this section we demonstrate MVM operations and their use in the power iteration algorithm [7, 8], a method used to compute the eigenvectors (or principal components, PCs) of a matrix by performing multiple MVMs. Figure 3(a) sketches the working principle of the algorithm. For a given matrix, an arbitrary input voltage is used to perform the MVM and the correspondent current result, which is linked to the eigenvector, is properly normalized and used to feed again the matrix [8]. At each iteration, the output currents (the red arrow in the example) get closer to the convergence values (the blue arrow), which stand for the largest eigenvector. In Fig. 3(b) a possible implementation for the memristive architecture. The output currents, result of the MVM between the conductance matrix encoded with the RRAMs and the input voltages, are collected and converted in voltages through transimpedance amplifiers. Before proceeding with a new iteration of the algorithm, the voltages are normalized to ensure the values are below the 100 mV maximum value [6]. To overcome the absence of negative conductances, the mathematical matrix was

properly scaled and shifted to contain only positive values between 1 µS and 50 µS. Deflation technique [6, 7] is adopted to compute the real current values as the difference between the current considering the offset (due to the shift to have only positive conductance) and the offset current alone. To do this, additional row and column (BE7 and TE7 in Fig. 2(c)) are added to the initial matrix. The current with offset is evaluated with the MVM where TE7 and TE8 are not biased. The offset current instead is retrieved biasing only the TE7. Doing this, the real current can be computed, and the result is presented in Fig. 3(c). The convergence is ensured in less than 10 iteration steps with an accuracy of 99% at the 20th step.
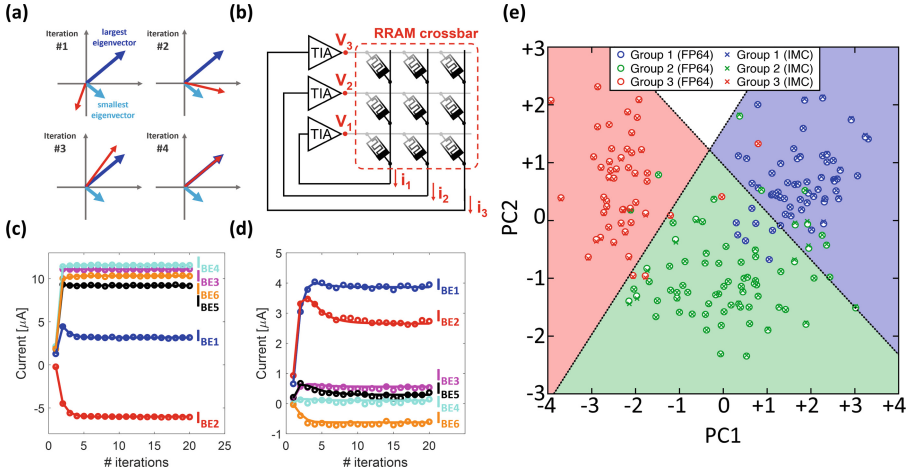
Fig. 3. Power Iteration algorithm. a) Visual sketch of the operation principle of the Power iteration on a 2×2 matrix. The two components are placed in the cartesian plane and, at each iteration, a test vector (in red) gets closer to the largest eigenvector. b) Equivalent circuit of a fully memristive accelerator for the Power Iteration. The product between the voltages (V_{input}) and the conductances is performed and the currents (I_{output}) are then converted using TIAs and the new voltage normalized to not overcome the maximum working voltage (100 mV). c) Result of the Power Iteration to compute the first eigenvector (PC1). The current values reach the convergence in less than 10 iterations. d) Extraction of the second eigenvector (PC2) with a convergence ensured in less than 15 iterations. e) Result of the PCA and visual clustering of the dataset. The IMC has a 98.99% overlap with the FP64 result.

The second PC is computed with a similar procedure of the PC1 but adding an additional row and column (BE8 and TE8) to consider the presence of the PC1. When now the MVM is executed, the current has inside the contribute of the offset, due to the shift, and the one of the PC1. Thus, by also eliminating the effect of the first eigenvector (biasing only the TE8) the system is allowed to converge to the second eigenvector [6–8], which is the dominant one since the first has been eliminated. By projecting the Wine dataset onto the PCs, the dataset dimensionality is reduced, thus enabling data clustering and classification with an accuracy of 99%, equal to that obtained using the FP64.

4   Conclusion

We presented a forming-free RRAM device based on ultrathin HfO_2 layer as promising candidate for large-scale, passive RRAM crossbars. The proposed forming-free RRAMs allow to avoid the forming initialization usually responsible for disturbances and failures of other devices in the crossbar and the analog-grade programmability makes them extremely promising candidate for hardware accelerators. We show in situ MVM, power iteration for eigenvector computation and PCA for Wine dataset clustering. The analog architecture reached 98.99% of accuracy in clustering and recognition, thus supporting the forming-free RRAM array for accurate acceleration of machine learning by in-memory computing.

References

1. Yang, J.J., Strukov, D.B., Stewart, D.R.: Memristive devices for computing. Nat. Nanotechnol. **8**(1), 13–24 (2013). https://doi.org/10.1038/nnano.2012.240
2. Kim, H., Mahmoodi, M.R., Nili, H., Strukov, D.B.: 4K-memristor analog-grade passive crossbar circuit. Nat. Commun. **12**(1), 5198 (2021)
3. Milano, G., et al.: In materia reservoir computing with a fully memristive architecture based on self-organizing nanowire networks. Nat. Mater. **21**(2), 195–202 (2022)
4. Pedretti, G., Mannocci, P., Li, C., Sun, Z., Strachan, J.P., Ielmini, D.: Redundancy and analog slicing for precise in-memory machine learning—Part II: applications and benchmark. IEEE Trans. Electron Devices **68**(9), 4379–4383 (2021)
5. Wang, R., et al.: Implementing in-situ self-organizing maps with memristor crossbar arrays for data mining and optimization. Nat. Commun. **13**, 2289 (2022)
6. Ricci, S., Mannocci, P., Farronato, M., Hashemkhani, S., Ielmini, D.: Forming-free resistive switching memory crosspoint arrays for in-memory machine learning. Adv. Intell. Syst. **4**, 2200053 (2022)
7. Mannocci, P., et al.: In-Memory principal component analysis by crosspoint array of resistive switching memory: a new hardware approach for energy-efficient data analysis in edge computing. IEEE Nanatechnol. Mag. **16**(2), 4–13 (2022)
8. Jolliffe, I.: Principal component analysis. In: Encyclopedia of Statistics in Behavioral Science, p. bsa501. John Wiley & Sons, Ltd., Chichester, October 2005

Microwave Electronics

Multi-bias Thermal X-Parameter Model for Efficient Physics-Based FinFET Simulation in RF CAD Tools

Eva Catoggio[(✉)], Simona Donati Guerrieri, Chiara Ramella, and Fabrizio Bonani

Politecnico di Torino, Torino, Italy
{eva.catoggio,simona.donati,chiara.ramella,fabrizio.bonani}@polito.it

Abstract. In this contribution we present a physics-based multi-bias thermal X-parameter model for a 54 nm Si FinFET transistor. The model is extracted directly in the frequency domain through an in-house developed Technology CAD tool providing Large-Signal analysis using the Harmonic Balance algorithm. Such an approach allows for accurate modeling of parasitic and thermal effects, which are particularly critical in FinFETs, especially in multi-finger devices, due to their peculiar 3D geometry. The X-parameter approach is then exploited to translate the physics-based model into a numerically efficiency parameterized electro-thermal black-box model that can then be adopted for circuit design within EDA tools. Thus, once coupled with an appropriate thermal impedance, it can provide accurate analysis of the device dynamic self-heating. To demonstrate this, we report the analysis of the device, matched at the output for maximum power, at 70 GHz in pulsed mode operation, testing different bias points from class A to class B.

Keywords: X-parameters · Thermal modeling · TCAD · FinFET modeling

1 Introduction

FinFET technology represents a potential key enabling technology for the integration of RF and digital circuits into a single chip in millimeter-wave phased arrays [11,12]. The peculiar 3D geometry of FinFET transistors, together with the need to use multi-finger structures to achieve proper power levels, calls for accurate physics-based simulations to properly account for all parasitic and thermal effects [13]. This can be effectively addressed by Technology CAD (TCAD) tools embedding Large-Signal (LS) analysis capability. However, TCAD simulations are very time-consuming, while RF designers need reliable and numerically efficient device models that can be implemented into the commercial RF CAD tools they use for circuit design.
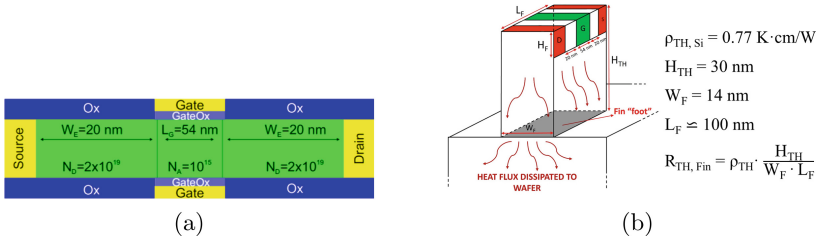
Fig. 1. FinFET device: (a) 2D cross-section of the fin used for TCAD simulations and (b) fin structure used for the fin thermal resistance calculation.

In [7,8] we demonstrated how X-parameters (Xpar) extracted from accurate LS TCAD simulations, can be effectively exploited to obtain an accurate yet efficient parameterized device model, straightforward to be imported into RF CAD tools. The Xpar model can be parameterized as a function of one or more physical (e.g., doping [2]) or electrical (e.g., bias conditions) parameters. Furthermore, temperature (T)-dependent simulations yield a T-dependent Xpar (T-Xpar) model. In this work we present a multi-bias, T-Xpar model of a 54 nm Si FinFET [6], extracted from TCAD LS simulations. The model is adopted to demonstrate a FinFET-based power amplifier (PA) working in pulsed operation, sweeping the bias conditions from class A to class B. The PA self-heating is simulated by coupling the T-Xpar model to a simple thermal-RC circuit.

2   TCAD Approach and Xpar Model

The adopted TCAD is an in-house developed 2D (planar-3D) drift-diffusion code including different temperature-dependent models [3,6,10,14], e.g. for mobility and thermionic emission in hetero-structures. The developed simulator is able to perform both Large-Signal (LS) and perturbative Small-Signal Large-Signal (SS-LS) simulations exploiting the Harmonic Balance technique and allowing for the X-parameter extraction, as detailed in [7].

The case study is a FinFET device with 54 nm gate-length. The simulated structure is the individual fin, Fig. 1 (a), of a multi-finger device with 10 fingers, each featuring 30 fins of 25 nm height and 14 nm width. LS TCAD analysis was carried out at 70 GHz, with 50 Ω termination at both input and output ports (unmatched), and including 10 harmonics to account for all nonlinearities and to avoid aliasing. The device is assumed isothermal. A temperature-dependent X-parameter model [5,9] was extracted at 2 different gate voltages, namely at 0.675 V corresponding to class A and at 0.5 V corresponding to class B, and at 3 different temperatures, namely 300 K, 340 K and 380 K.
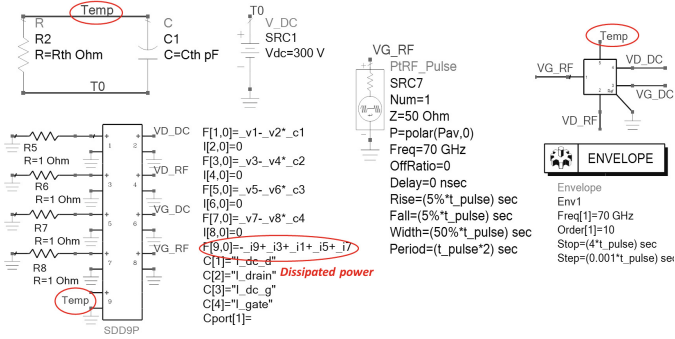
Fig. 2. ADS setup for Envelope PA analysis in pulsed operation.

The T-Xpar model is imported into Keysight ADS as an X-parameter file, with a unique gate contact and a fictitious DC voltage port for the temperature, as shown in Fig. 2 [3]. Since X-parameters are instantaneous, for the *dynamic self-heating analysis* [1] the device is coupled to an external lumped RC thermal impedance, through which heat is dissipated towards a heat sink kept at $T_0 = 300$ K. The thermal resistance $R_{th} = 1$ K/μW was calculated paralleling 30 fins, which individual thermal resistance is computed as shown in Fig. 1(b), while the thermal capacitance is sized to yield a thermal time constant of $15\,\mu$s (10 KHz thermal cut-off). The thermal impedance is used to compute the device temperature as a function of the instantaneous dissipated power through a Symbolically Defined Device (SDDs), which is fed back to the Xpar model to achieve a coupled electro-thermal model, as show in Fig. 2, reporting the simulation set-up: the device input port is terminated on $50\,\Omega$, while the drain port is loaded with the optimum load for power at 70 GHz, $Z_{opt} = (53 + j6)\,\Omega$. The bias conditions are varied from class A to class B. The input is pulsed (50% duty cycle, 5% rise/fall time), adopting the Envelope simulation to capture the thermal dynamics.

3   Results

In Fig. 3 we report the analysis of the pulsed power amplifier. When sweeping the gate bias from class A to class B, the available input power is changed to keep the same output power in all cases. Figure 3-top shows the predicted T vs. P_{out} for 3 different pulse lengths, chosen to be, respectively, below (5 ms), close to (50 μs) and above (0.5 μs) the thermal cut-off, while Fig. 3-bottom shows the temperature variation as a function of time. We can notice the expected opposite
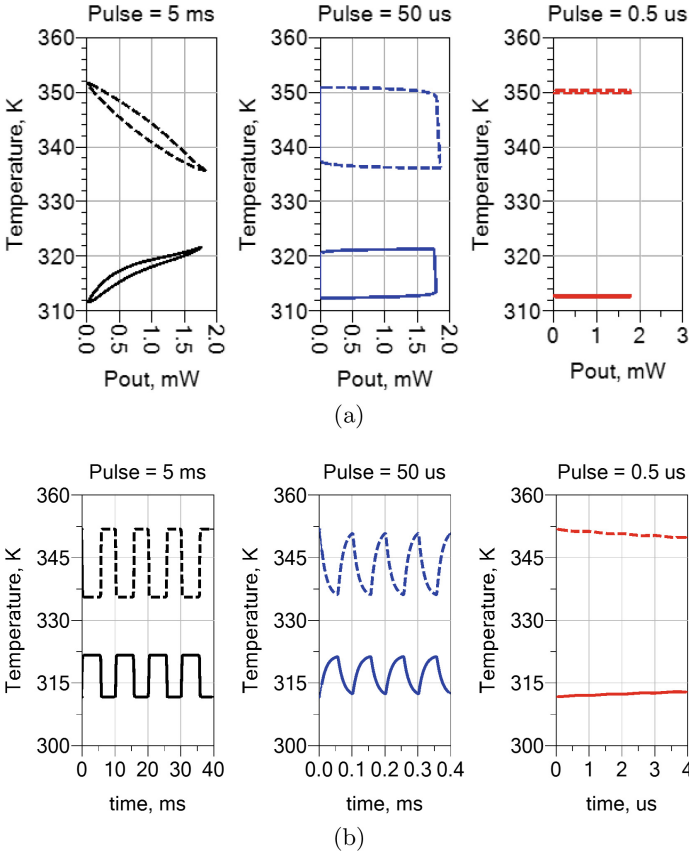
Fig. 3. Results of the pulsed mode analysis of the matched FinFET in class A (dashed lines) and class B (solid lines): (a) dynamic temperature variation as a function of the output power over the pulse cycle and (b) temperature variation over the cycle for the 3 different pulse durations.

behavior of the class A and B stages: the former is hotter when the pulse is off, while the latter gets cooler. The thermal shunt, though, makes temperature variations to be quenched by increasing the pulse speed. Figure 4 reports the output power variation vs. (normalized) time, highlighting the capability of the T-Xpar model of predicting the P_{out} thermal dispersion. It is worth noticing that this analysis would not be possible adopting a mere X-par model extracted at 300 K. Finally, Fig. 5 shows that the implemented model can continuously interpolate among the X-par data both in terms of temperature and gate bias.
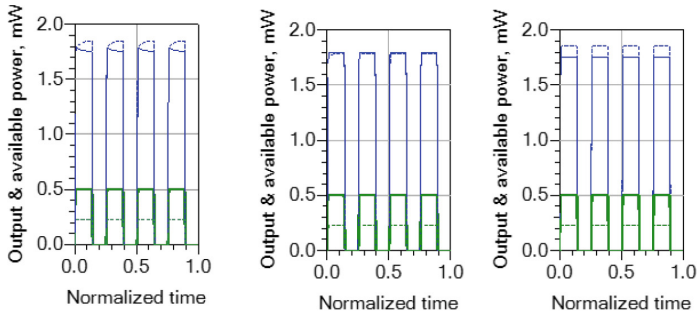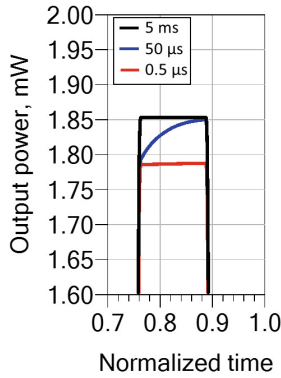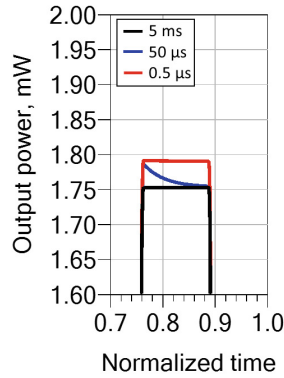
Fig. 4. Results of the pulsed mode analysis of the matched FinFET: (a) output power variation over the cycle in class A (dashed lines) and class B (solid lines) and (b) detailed view of the output power behavior in the ON state for the 3 different pulse durations.
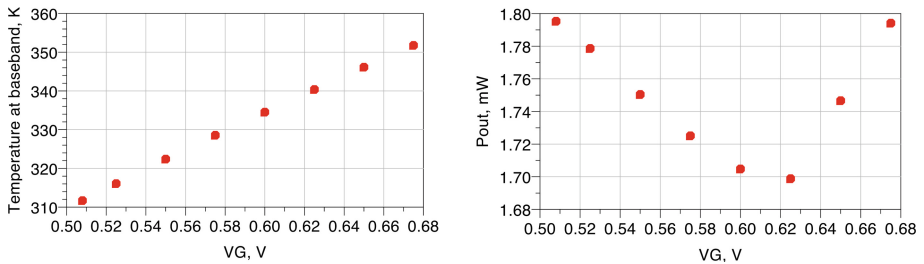
Fig. 5. Results of the pulsed mode analysis of the matched FinFET: (left) temperature at baseband and (right) output power at the RF envelope at different gate bias voltages, from class A to class B, for a pulse length of 0.5 μs.

4   Conclusions

An efficient multi-bias thermal model of a 54 nm Si FinFET device is presented. The model is directly extracted from Large-Signal TCAD simulations via the X-parameters approach. The model is then coupled to a thermal impedance to achieve an electro-thermal model capable of predicting the device dynamic self-heating. Exploiting the Envelope analysis, we demonstrated the effect of self-heating in pulsed operating conditions, highlighting the different role of thermal memory in class A and class B cases.

References

1. Bonani, F., Donati Guerrieri, S., Camarchia, V., Cappelluti, F., Ghione, G., Pirola, M.: When self-consistency makes a difference. IEEE Microwave Mag. (2008). https://doi.org/10.1109/mmm.2008.927638
2. Bughio, A.M., Donati Guerrieri, S., Bonani, F., Ghione, G.: Physics-based modeling of FinFET RF variability. In: 11th European Microwave Integrated Circuits Conference, EuMIC (2016). https://doi.org/10.1109/eumic.2016.7777534
3. Catoggio, E., Donati Guerrieri, S., Bonani, F., Ghione, G.: Efficient TCAD temperature-dependent large-signal simulation of a FinFET power amplifier. In: 16th European Microwave Integrated Circuits Conference, EuMIC (2021). https://doi.org/10.23919/eumic50153.2022.9783235
4. Catoggio, E., Donati Guerrieri, S., Bonani, F., Ghione, G.: TCAD-based dynamic thermal X-parameters for PA Self-Heating Analysis. In: 17th European Microwave Integrated Circuits Conference, EuMIC (2022). https://doi.org/10.23919/EuMIC54520.2022.9923459
5. Catoggio, E., Donati Guerrieri, S., Ramella, C., Bonani, F.: Thermal modeling of RF FinFET PAs through temperature-dependent X-parameters extracted from physics-based simulations. In: International Workshop on Integrated Nonlinear Microwave and Millimetre-Wave Circuits, INMMiC (2022). https://doi.org/10.1109/INMMiC54248.2022.9762142
6. Catoggio, E., Donati Guerrieri, S., Bonani, F.: Efficient TCAD thermal analysis of semiconductor devices. IEEE Tran. Electron Dev. (2021). https://doi.org/10.1109/ted.2021.3076753
7. Donati Guerrieri, S., Bonani, F., Ghione, G.: Linking X parameters to physical simulations for design-oriented large-signal device variability modeling. IEEE Int. Microw. Symp. IMS 2019 (2019). https://doi.org/10.1109/mwsym.2019.8700869
8. Donati Guerrieri, S., Ramella, C., Bonani, F., Ghione, G.: Efficient sensitivity and variability analysis of nonlinear microwave stages through concurrent TCAD and EM modeling. IEEE J. Multiscale Multiphys. Comput. Tech. (2019). https://doi.org/10.1109/jmmct.2019.2962083
9. Gillespie, S.J., Root, D.E., Marcu, M., Aaen, P.H.: Electrothermal X-Parameters for dynamic modeling of RF and microwave power transistors. In: 13th European Microwave Integrated Circuits Conference, EuMIC (2018). https://doi.org/10.23919/eumic.2018.8539893
10. Prasad, C.: A review of self-heating effects in advanced CMOS technologies. IEEE Tran. Electron Dev. (2019). https://doi.org/10.1109/ted.2019.2943744

11. Raskin, J.P.: FinFET versus UTBB SOI – a RF perspective. In: European Solid State Device Research Conference, ESSDERC (2015). https://doi.org/10.1109/essderc.2015.7324719
12. Scholten, A., et al.: Experimental assessment of self-heating in SOI FinFETs. In: IEEE International Electron Devices Meeting, IEDM (2009). https://doi.org/10.1109/iedm.2009.5424362
13. Uchida, K., Takahashi, T.: Thermal-aware CMOS: Challenges for future technology and design evolutions. In: European Solid-State Device Research Conference, ESSDERC (2016). https://doi.org/10.1109/essderc.2016.7599609
14. Venkateswarlu, S., Sudarsanan, A., Singh, S.G., Nayak, K.: Ambient temperature-induced device self-heating effects on multi-fin si n-FinFET performance. IEEE Tran. Electron Dev. (2018). https://doi.org/10.1109/ted.2018.2834979

Parameterized Surrogate Models of Microstrip Structures for Electromagnetic-Based Power Amplifier Design and Statistical Analysis

Chiara Ramella[✉], Alessandro Zanco, Marco De Stefano, Tommaso Bradde, Stefano Grivet-Talocia, and Marco Pirola

DET, Politecnico di Torino, 10129 Torino, Italy
`chiara.ramella@polito.it`

Abstract. Integrated circuits operating in the millimetre-wave range require careful electromagnetic optimization of the passive networks to properly account for crosstalk and radiative effects, but also accurate and reliable statistical analysis to assess the impact of process induced variability on chip yield. These two requirements are typically computationally incompatible, since the simulation time required by electromagnetic analysis is too high to allow for multi-trial Monte Carlo statistical analysis. This work presents a parameterized surrogate approach to model the passive networks that allows for an efficient yet accurate electromagnetic-based variability analysis of microwave circuits. As a case study, we report the statistical analysis of a GaN/Si device at 28 GHz evaluating the impact of statistical variations of the matching network, under concurrent variation of two technological parameters, on device performance.

Keywords: Parameterized behavioral models · Process induced variability · Electromagnetic simulation · MMIC statistical analysis

1 Introduction

The adoption of higher frequency bands for both microwave telecommunication and radar systems [1,3,7,15] poses new challenges in the design of monolithic integrated circuits (MMIC) in terms of electromagnetic (EM) coupling, stability issues and sensitivity to process variations, that could instead be neglected, or greatly simplified, at lower frequencies. The high cut-off frequency of the active devices together with the relatively low gain and output power achievable with single transistors/stages makes high-frequency MMICs densely integrated, with unavoidable EM coupling between adjacent structures [11,13], hence making EM-based analysis and optimization a crucial design step.

At the same time, process induced variability (PIV) is a growing concern. Active devices capable of operating at millimetre-wave should feature very short

gate-lengths, but such technologies are typically less mature and thus affected by larger technological variation. On the other hand, the effect of devices' reactive parasitics become significant at high frequency, hence making the design of the matching networks increasingly challenging and the device performance much more sensitive to load variations. Both aspects increase the impact of PIV on yield, which may drop well below 50%, hence requiring a PIV-aware design approach [9].

Statistical analysis typically relies on the Monte Carlo (MC) approach, requiring accurate but also computationally efficient models for both the active devices and the passive networks [2,5,8]. Focusing on passives, to achieve accurate and reliable statistical results, an EM-based approach must be pursued, as it ensures a direct link between physical process parameters and network performance [4]. However, EM simulations are extremely time-consuming, even when resorting to planar-3D analysis for microstrip structure. Data arrays with several thousands of points should in fact be manipulated to achieve reasonable accuracy, requiring hours of simulation even on multi-core computers. This still widely limit the use of EM simulations in MMIC statistical analysis.

In [12] we proposed a parameterized reduced-order behavioral model as an efficient yet highly accurate approach for EM-based MMIC statistical analysis: few EM simulations, at properly chosen sets of parameter values, are enough to extract a mathematical model of the networks's scattering matrix [6], then translated into an equivalent SPICE circuit [14] to be used within any RF CAD tools. As a case study, we consider the output matching network (OMN) of a commercial GaN/Si HEMT transistor for power amplifier (PA) applications at 28 GHz, presenting in [12] the statistical analysis of its small-signal matching performance. In this work we extend the analysis to the large-signal performance of the matched transistor, confirming model accuracy and showing the impact of OMN variations on the most relevant PA performance.

2   Modeling Approach and Case Study

The EM-simulated S-matrix of the network to be modeled is approximated with a rational barycentric function of the form [6]:

$$\mathbf{S}(j\omega, \boldsymbol{\vartheta}) = \frac{\sum_n \mathbf{R}_n(\boldsymbol{\vartheta})\varphi_n(j\omega)}{\sum_n r_n(\boldsymbol{\vartheta})\varphi_n(j\omega)} \tag{1}$$

The basis functions $\varphi_n(j\omega)$ are used to model the frequency dependence of the S-parameters and are represented by a set of N stable poles q_n [16]:

$$\varphi(j\omega) = \begin{cases} 1 & \text{for } n = 0 \\ \dfrac{1}{j\omega - q_n} & \text{for } n = 1, \dots, N \end{cases} \tag{2}$$

The coefficients are functions of the technological parameters θ_i, through Chebyshev polynomials basis functions ξ_l:

$$\mathbf{R}_n(\boldsymbol{\vartheta}) = \sum_l \mathbf{R}_{ln}\xi_l(\boldsymbol{\vartheta}) \quad \text{and} \quad r_n(\boldsymbol{\vartheta}) = \sum_l r_{ln}\xi_l(\boldsymbol{\vartheta}) \tag{3}$$

As a case study, we consider a $6 \times 100\,\mu\mathrm{m}$ GaN/Si HEMT device matched at output for maximum power at $28\,\mathrm{GHz}$. The adopted technology is the 100-nm process from OMMIC [3]. The device is biased in shallow (25%) class AB and the optimum drain termination is $Z_{Lopt} \approx (6 + j11)\,\Omega$, allowing for an output power in excess of $31.7\,\mathrm{dBm}$ with associated gain and efficiency better than $8.8\,\mathrm{dB}$ and 44%, respectively. The matching network, shown in Fig. 1, transforms the standard $50\,\Omega$ load into Z_{Lopt} on a broad frequency range. The network is EM simulated in the $18\,\mathrm{GHz}$-$38\,\mathrm{GHz}$ range with $100\,\mathrm{MHz}$ frequency sampling: the simulation time is roughly $15\,\mathrm{min}$, thus incompatible with a MC analysis, which would demand several days.
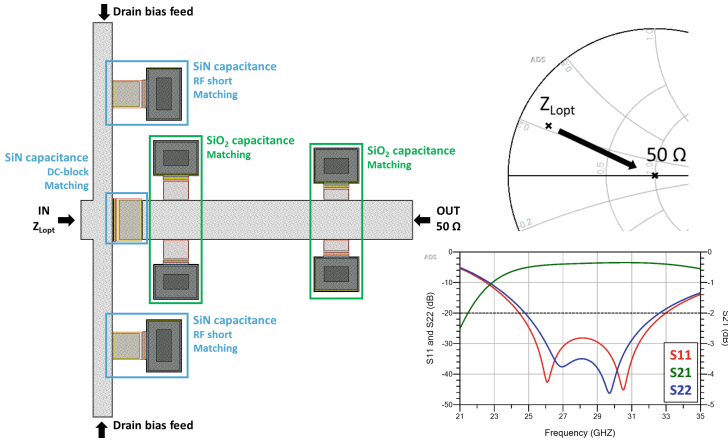
Fig. 1. Output matching network layout and matching performance.

The considered variable parameters are the dielectric layer thicknesses for the two types of MIM capacitors (SiN and SiO_2) available in the process: based on the available statistical data, we assume a relative variance σ of 5% for the nitride thickness and 3% for the oxide thickness. The parameter space boundaries are set to $\pm\sigma$ for both parameters: a deliberately reduced limit with respect to the classical $\pm 3\sigma$ to assess the model extrapolation capabilities under larger variations during MC analysis. Only 10 EM simulations were required to extract the model coefficients with residual error less than 10^{-3} [14]. As detailed in [12], the model demonstrates remarkable robustness against port impedance change, maintaining an accuracy within $4 \cdot 10^{-3}$ when simulating the S-parameters with Z_{Lopt}^* at the input port.

3   Results

The large-signal performance of the matched device is analyzed under continuous-wave excitation in the $25\,\mathrm{GHz}$ to $31\,\mathrm{GHz}$ range (1 GHz step), sweeping the input power from small-signal to saturation. The comparison between

EM simulations (black lines) and model predictions (red symbols) are reported in the following figures: Fig. 2-top reports the performance at saturation over frequency for nominal (solid/circles) and two random (dash/crosses) parameter values. The accuracy is very good, as confirmed by the results shown in Fig. 2-bottom, reporting the rms errors at 10 randomly selected test points. The maximum errors in predicting the output power, drain efficiency and gain are lower than 0.28 dB, 2.3% points and 0.31 dB, respectively.

(a) Output power   (b) Efficiency   (c) Power gain

(d) Output power   (e) Efficiency   (f) Power gain
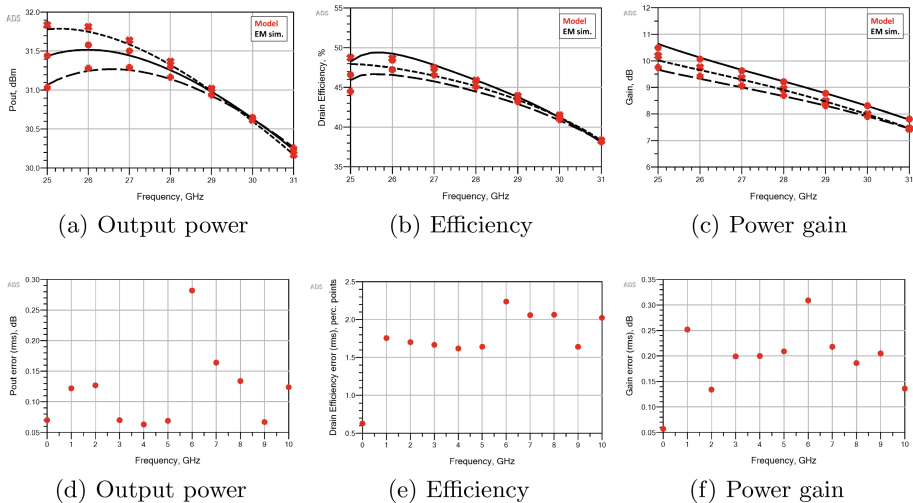
Fig. 2. Model accuracy: (top) comparison between EM simulations and model predictions and (bottom) rms error.

Figure 3 illustrates the extrapolation capabilities of the model. Figure 3(a) reports the output power at extrapolated parameter values, namely $+3\sigma$ (solid/circles) and -3σ (dash/crosses): the agreement with EM simulations is still excellent. Figure 3(b) shows instead the output power at second (solid/circles) and third (dash/crosses) harmonics. Considering the small absolute value of these quantities, the agreement is still good. Remarkably, as detailed in Fig. 3(c), the proposed model extrapolates in frequency much better that any other built-in ADS extrapolation algorithms applied to narrow-band (18 GHz-38 GHz) EM simulations (blue curves).

Figure 4 reports the results of a 500-trial Monte Carlo simulation with uncorrelated variations of the two parameters, both featuring a gaussian distribution with σ relative variance. Except for gain, affected by constant symmetrical spread at all power levels, PIV most affects the performance at saturation where up to 1 dB of power/gain spread and 6% points of efficiency spread can be observed in the lower portion of the band. The dissipated power density, which determines the device temperature [10], is also reported in Fig. 5: at high power levels the spread reaches 250 mW/mm.

(a) Saturated power at $\pm 3\sigma$ (b) Saturated power at 2nd and 3rd harmonics   (c) Power at 2nd harmonic
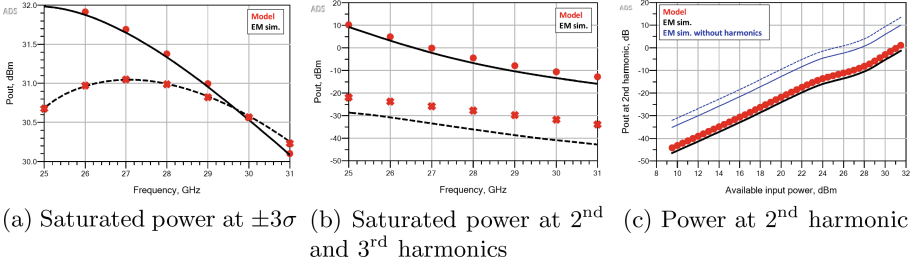
Fig. 3. Results at extrapolated (a) parameters and (b)-(c) frequency values.

(a) Output power   (b) Drain efficiency   (c) Power gain

(d) Output power   (e) Drain efficiency   (f) Power gain
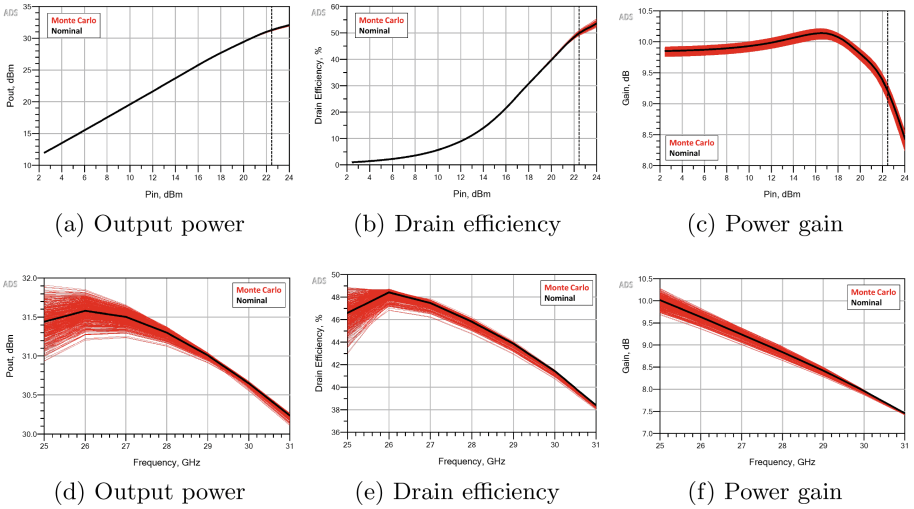
Fig. 4. Statistical analysis results.

(a)   (b)
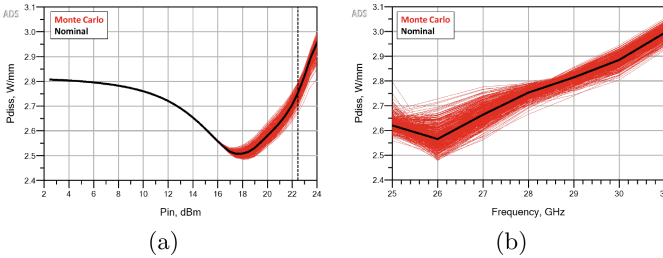
Fig. 5. Statistical analysis results: dissipated power density.

References

1. Bao, M., et al.: A 24–28-GHz Doherty power amplifier with 4-W output power and 32% PAE at 6-dB OPBO in 150-nm GaN Technology. IEEE Microw. Wireless Compon. Lett. **31**(6), 752–755 (2021). https://doi.org/10.1109/LMWC.2021.3063868
2. Beleniotis, P., et al.: Statistical modeling of GaN hemts by direct transfer of variations to model parameters. In: EuMIC (2021). https://doi.org/10.23919/EuMIC50153.2022.9783780
3. Cidronali, A., et al.: System level analysis of Millimetre-wave GaN-based MIMO radar for detection of micro unmanned aerial vehicles. PIERS-Spring (2019). https://doi.org/10.1109/PIERS-Spring46901.2019.9017681
4. Donati Guerrieri, S., et al.: Efficient sensitivity and variability analysis of nonlinear microwave stages through concurrent TCAD and EM modeling. IEEE J. Multiscale Multiphys. Comput. Tech. **4**, 356–363 (2019). https://doi.org/10.1109/JMMCT.2019.2962083
5. Donati Guerrieri, S., et al.: Bridging the gap between physical and circuit analysis for variability-aware microwave design: modeling approaches. Electronics **11**(6), 860 (2022). https://doi.org/10.3390/electronics11060860
6. Grivet-Talocia, S., Trinchero, R.: Behavioral, parameterized, and broadband modeling of wired interconnects with internal discontinuities. IEEE Trans. Electromagn. Compat. **60**(1), 77–85 (2018). https://doi.org/10.1109/TEMC.2017.2723629
7. Ishikawa, R., et al.: A 28-GHz-Band GaN HEMT MMIC doherty power amplifier designed by load resistance division adjustment. In: EuMIC (2021). https://doi.org/10.23919/EuMIC50153.2022.9783948
8. Manfredi, P., Canavero, F.G.: Efficient statistical simulation of microwave devices via stochastic testing-based circuit equivalents of nonlinear components. IEEE Trans. Microw. Theory Techn. **63**(5), 1502–1511 (2015). https://doi.org/10.1109/TMTT.2015.2417855
9. Mao, S., et al.: A yield-improvement method for millimeter-wave GaN MMIC power amplifier design based on load-pull analysis. IEEE Trans. Microw. Theory Techn. 69(8), 3883–3895 (2021). https://doi.org/10.1109/TMTT.2021.3088499
10. Ramella, C., et al.: Thermal-aware GaN/Si MMIC design for space applications. In: COMCAS (2019). https://doi.org/10.1109/COMCAS44984.2019.8958104
11. Ramella, C., et al.: Electro-magnetic Crosstalk Effects in a Millimeter-wave MMIC Stacked Cell. In: INMMiC (2020). https://doi.org/10.1109/INMMiC46721.2020.9160341
12. Ramella, C., et al.: Efficient EM-based variability analysis of passive microwave structures through parameterized reduced-order behavioral models. In: EuMIC (2022). https://doi.org/10.23919/EuMIC54520.2022.9922958
13. Sangwan, V., et al.: High-frequency electromagnetic simulation and optimization for GaN-HEMT power amplifier IC. IEEE Trans. Electromagn. Compat. **61**(2), 564–571 (2019). https://doi.org/10.1109/TEMC.2018.2820202
14. Triverio, P., et al.: A parameterized macromodeling strategy with uniform stability test. IEEE Trans. Adv. Packag. **32**(1), 205–215 (2009). https://doi.org/10.1109/TADVP.2008.2007913

15. Wohlert, D., et al.: 8-watt linear three-stage GaN Doherty power amplifier for 28 GHz 5G applications. In: BCICTS (2019). https://doi.org/10.1109/BCICTS45179.2019.8972750
16. Zanco, A., et al.: Uniformly stable parameterized macromodeling through positive definite basis functions. IEEE Trans. Compon. Packag. Manuf. Technol. **10**(11), 1782–1794 (2020). https://doi.org/10.1109/TCPMT.2020.3012275

Zero-Power Harmonic Tag Sensors Based on Orthogonally Polarized Waves

Valentina Palazzi[ID], Giulia Orecchini[ID], Giacomo Schiavolini,
Giordano Cicioni[ID], Raffaele Salvati[ID], Guendalina Simoncini[ID],
Paolo Mezzanotte[ID], Luca Roselli[ID], and Federico Alimenti[(✉)][ID]

Department of Engineering, University Perugia, Perugia, Italy
`federico.alimenti@unipg.it`

Abstract. This paper investigates, for the first time, the feasibility of harmonic tag sensors based on orthogonally polarized waves. The main tag building blocks (circular and dual polarization antennas, Schottky diode frequency doubler and phase shifter) are designed, implemented with standard PCBs technology and materials, and experimentally characterized. Finally a proof-of-concept of the whole system operating at $1.04/2.08$ GHz is proposed and validated in laboratory. The system can recover the encoded phase regardless the interrogation distance.

Keywords: Harmonic transponders · Harmonic radars · Orthogonal polarization transmission · RFID sensors

1 Introduction

Batteryless sensor tags are key devices enabling the Internet-of-Things (IoT) revolution [1]. Among various approaches, harmonic tags have emerged because they are simple, low-cost and easy to detect with moderate interrogation power levels [2]. Due to their simplicity, harmonic tags have been implemented on cellulose-based (i.e. paper) substrates [3] mainly for logistic applications, reaching record reading distances [4].

Tags based on varactor or Schottky diodes were originally used in harmonic radar systems [5], and further developed to exploit the intermodulation communication principle [6,7]. Another way to encode sensor data in harmonic tags is based on the polarization diversity principle [8]. When interrogated by a carrier, the tag generates a harmonic signal that is split and transmitted back to the reader in two orthogonal polarization. The phase or the amplitude of one polarization can be altered with respect to the other as a function of the encoded information. Such an information is finally reconstructed by the reader using a dual polarization antenna and two vector receivers. This approach is promising since it is simple, robust and distance independent.

Although the polarization diversity method was proposed and patented several years ago, no physical demonstrators were developed yet. Purpose of this
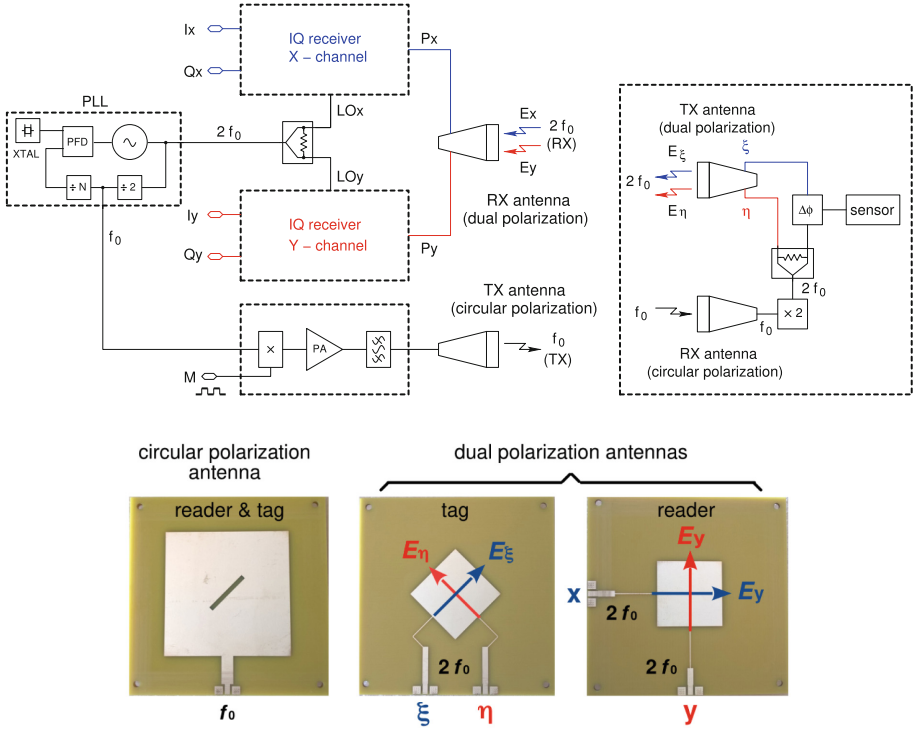
Fig. 1. Block diagram of the harmonic wireless sensor based on orthogonally polarized waves (top panels). Reader (top left) and tag (top right). Fabricated antennas prototypes (bottom panels). Circular polarized patch antenna operating at f_0 used in both reader and tag (bottom left). Dual polarization square patch antennas operating at $2f_0$ adopted in the tag (bottom center) and in the reader (bottom right).

paper is to provide, for the first time, an experimental validation of harmonic sensor tags based on orthogonally polarized waves, thus investigating their practical feasibility. Devices of this type could be used, due to simplicity and robustness, in smart agriculture applications [9] or in extreme environments, like industrial ones or those encountered during planetary exploration missions.

2   System Overview

The proposed harmonic wireless sensor system is shown in Fig. 1, and is composed of a reader (top left) and a tag (to right). According to theory [8], the tag receives a carrier at frequency f_0 (fundamental) and generates two equal signals at $2f_0$ (second harmonic), by means of a frequency doubler and a power splitter. The first signal component is not altered and acts as a reference (red path). The second signal component, instead, goes through a phase shifter that is actuated

by an electrical, micromechanical or microfluidic sensor (blue path). The sensor information is thus encoded as the phase difference $\Delta\phi$ between these two paths, and the corresponding signals are transmitted back to the reader using two orthogonal polarization. The reader can finally recover $\Delta\phi$ with two vector (IQ) receivers tuned at $2\,f_0$, one for each polarization.

Antennas play a key role in the proposed system: the fabricated prototypes are shown in the bottom panels of Fig. 1. The reader-to-tag link at $f_0 = 1.04\,\mathrm{GHz}$ is done with a circular polarization antenna. In this way the tag can be rotated with respect to the reader, keeping the frequency doubler input power almost constant. The tag-to-reader link at $2\,f_0 = 2.08\,\mathrm{GHz}$, instead, is based on dual polarization antennas. The square patches shown in the figure have a cross polarization better that $20\,\mathrm{dB}$; in such a way reference and encoded signals can be combined and separated without significant loss of information. The tag antenna is aligned so that the ξ and η axes are rotated by $\pi/4$ with respect to the x and y axes of the reader antenna (see figure). For example, if the central antenna is excited with two in-phase signals of the same amplitude, a vertical polarized wave is generated, and this is detected by the y-port of the reader antenna.

3   Materials and Methods

The present study is based on prototyping and experimental verification. Tag and antennas are physically implemented by using standard PCB manufacturing processes and low-cost FR4 substrate materials of various thickness. For the design phases, commerical CAD tools, nonlinear (harmonic balance) circuit solvers, and 3D electromagnetic simulations are adopted.

The validation of the overall system does not exploit two vector receivers, but a simple spectrum analyzer. Such an instrument is adopted to measure the received power at the x and y (dual polarization) reader antenna outputs (see bottom panel of Fig. 1). These powers, P_x and P_y, can be modeled according to the equations (11)-(16) of [8]. We get:

$$P_x = \frac{V_0^2}{2R_0} \left[\sin^2\theta + \left(\frac{E_\eta}{E_\xi}\right)^2 \cos^2\theta + 2\frac{E_\eta}{E_\xi}\sin\theta\cos\theta\cos\Delta\phi \right] \tag{1}$$

$$P_y = \frac{V_0^2}{2R_0} \left[\cos^2\theta + \left(\frac{E_\eta}{E_\xi}\right)^2 \sin^2\theta - 2\frac{E_\eta}{E_\xi}\sin\theta\cos\theta\cos\Delta\phi \right] \tag{2}$$

Such a model assumes that the dual polarization antennas of reader and tag are aligned (same axis) and rotated by θ. The phase shift between the two polarization is $\Delta\phi = \phi_\xi - \phi_\eta$, the received amplitude V_0, while $R_0 = 50\,\Omega$ is the spectrum analyzer input impedance. Now, if the tag is designed so that $E_\eta/E_\xi = 1$ (ideal balance between its η and ξ ports) and the dual polarization antennas are rotated by $\theta = \pi/4$, the P_x/P_y ratio becomes:

$$\frac{P_x}{P_y} = \frac{1 + \cos\Delta\phi}{1 + \sin\Delta\phi} = \tan^2\left(\frac{\Delta\phi}{2}\right) \tag{3}$$
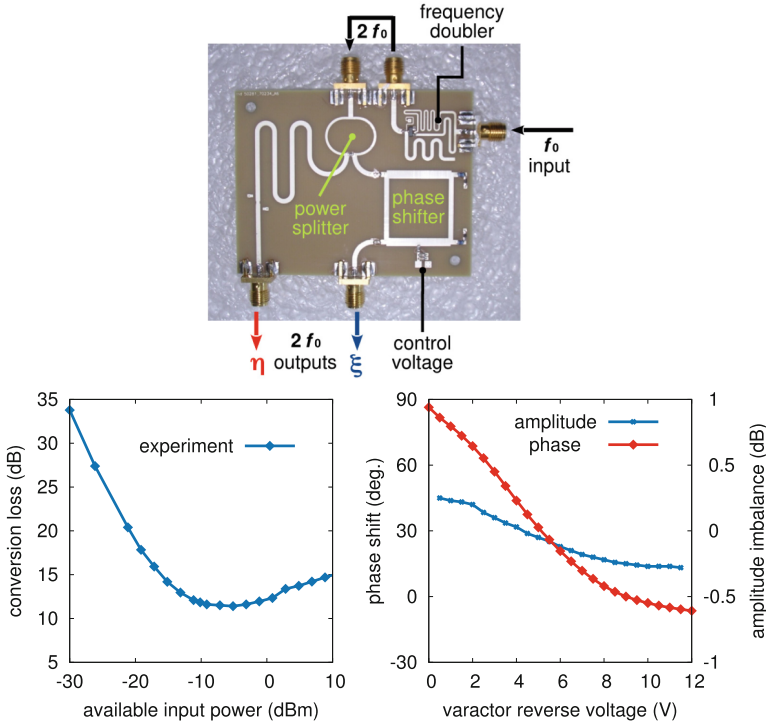
Fig. 2. Implemented harmonic tag exploiting the orthogonally polarized waves concept (top) and experimental characterization of the harmonic tag: frequency doubler conversion loss (bottom left), phase shift versus the varactor voltage (bottom right).

4   Results

In a first step, the main building blocks of the proposed system have been fabricated and experimentally characterized as standalone devices. The realized antennas, on which the polarization diversity principle relies, are shown in Fig. 1. All these devices are proved to be tuned at the design frequencies, with a $|S_{11}|$ of about -20 dB (coaxial adapter including). A cross polarization better than 20 dB is measured for both the dual polarization antennas. Figure 2 illustrates the implemented harmonic tag prototype that includes a Schottky diode frequency doubler, a Wilkinson power splitter and a reflection-type phase shifter. The frequency doubler uses the HSMS-2850 diode, and features a conversion loss better than 34 dB for an input power greater than -30 dBm (bottom panel, left). The phase shifter is based on two identical SMV-1234 varactor diodes, that are used to program a known $\Delta\phi$ as a function of a control voltage. The phase control capability of the whole tag is shown in the right bottom panel of the same figure. The phase shift between ξ and η outputs can be controlled from 87 to $-7°$ applying a reverse voltage in the range 0–12 V. The measured amplitude imbalance is within ±0.25 dB in the same voltage range.
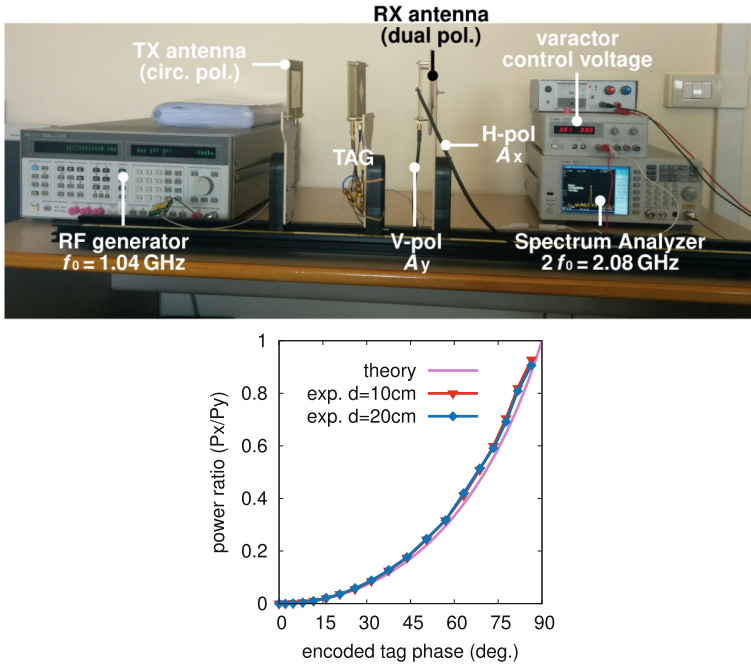
Fig. 3. Physical demonstrator of the harmonic wireless sensor system based on orthogonally polarized waves (top panel). Received power ratio P_x/P_y versus the phase shift $\Delta\phi$ programmed on the tag by means of the varactor voltage. Comparison between theory and experiments at 10 and 20 cm distances (bottom panel).

A proof-of-concept of the harmonic wireless sensor system based on the polarization diversity principle is finally tested with the experimental setup of Fig. 3. The reader transmitter is based on a laboratory RF signal generator (HP-8664A), whereas the received signals powers on x and y polarization are measured with a spectrum analyzer (Agilent N9320B). The illuminating power is 0 dBm at 1.04 GHz (fundamental) while the spectrum analyzer is tuned at 2.08 GHz (second harmonic). The antennas are aligned on a guide and share the same axis. Interrogation distances of 10 and 20 cm are considered: in these condition the second harmonic power received by the reader are -41 and -56 dBm respectively. The power ratio P_x/P_y is then recorded as a function of $\Delta\phi$ and compared to (3). The bottom panel of Fig. 3 depicts the obtained results: the agreement between model and experiments is within 7% at both distances, meaning that the reader can recover $\Delta\phi$ with a small error. A final comparison with the state-of-the-art is given in Table 1.

Table 1. Comparison with the State-of-the-Art

Ref.	freq. (MHz)	onboard battery	sensing capability	number of bit	TX power (dBm)	reading range (cm)	tag sens. (dBm)
[10]	860	no	no	96 (*)	n.a.	n.a.	−15
this work	1040 2080	no	yes	6 (+)	0	20	−20

(*) Serially transmitted code according to Gen-2 UHF RFID standard
(+) Equivalent number of bit estimated by system considerations

5   Conclusions

This work demonstrates that a harmonic tag using the orthogonally polarization wave transmission is feasible, robust and low-cost. A system prototype is implemented at 1.04/2.08 GHz can precisely recover the encoded phase information at both 10 and 20-cm distances, with a 0 dBm illumination. The proposed experiment constitutes the base for further developments of the system.

References

1. Mezzanotte, P., Palazzi, V., Alimenti, F., Roselli, L.: Innovative RFID sensors for internet of things applications. IEEE J. Microwaves **1**(1), 55–65 (2021)
2. Rasilainen, K., Ilvonen, J., Lehtovuori, A., Hannula, J.M., Viikari, V.: On design and evaluation of harmonic transponders. IEEE Trans. Antennas Propag. **63**(1), 15–23 (2015)
3. Mariotti, C., et al.: Modeling and characterization of copper tape microstrips on paper substrate and application to 24 GHz branch-line couplers. In: 43rd European Microwave Conference, pp. 794–797. Nuremberg, Germany (2013)
4. Palazzi, V., Alimenti, F., Kalialakis, C., Mezzanotte, P., Georgiadis, A., Roselli, L.: Highly integrable paper-based harmonic transponder for low-power and long-range IoT applications. IEEE Antennas Wirel. Propag. Lett. **16**, 3196–3199 (2017)
5. Colpitts, B., Boiteau, G.: Harmonic radar transceiver design: miniature miniature tags for insect tracking. IEEE Trans. Antennas Propag. **52**(11), 2825–2832 (2004)
6. Viikari, V., Seppa, H., Kim, D.W.: Intermodulation read-out principle for passive wireless sensors. IEEE Trans. Microwave Theory Techn. **59**(4), 1025–1031 (2011)
7. Song, J., Viikari, V., Pesonen, N., Marttila, I., Seppa, H.: Optimization of wireless sensors based on intermodulation communication. IEEE Trans. Microwave Theory Techn. **61**(9), 3446–3452 (2013)
8. Alimenti, F., Roselli, L.: Theory of zero-power RFID sensors based on harmonic generation and orthogonally polarized antennas. Progress Electromagn. Res. **134**, 337–357 (2013)
9. Palazzi, V., Gelati, F., Vaglioni, U., Alimenti, F., Mezzanotte, P., Roselli, L.: Leaf-compatible autonomous RFID-based wireless temperature sensors for precision agriculture. In: IEEE Topical Conference on Wireless Sensors and Sensor Networks (WiSNet), pp. 1–4. Orlando, FL, USA (2019)
10. Ruander, J.H., Khuda, I., Kildal, P.S., Orlenius, C.: Measurements of RFID tag sensitivity in reverberation chamber. IEEE Antennas Wirel. Propag. Lett. **10**, 1345–1348 (2011)

Analysis of a Single-Ended GaN-Based Drain-Pumped Mixer for Radar Applications

Lorenzo Pagnini$^{(\boxtimes)}$, Giovanni Collodi , and Alessandro Cidronali

Department of Information Engineering, University of Florence, Florence, Italy
{lorenzo.pagnini,giovanni.collodi,alessandro.cidronali}@unifi.it

Abstract. The aim of the present paper consists of a deep analysis concerning the impact of the GaN HEMT technology. Two methods of analysis were implemented. The first one is based on the time-varying power series approach which is based on simple measure of the I/V characteristics, thus allowing for experimental-based predictions without the need of manufacturing the mixer. The device I/V characteristics and the relative derivatives were extracted in a dynamic way as to avoid the dispersion phenomena to which the GaN technology is affected. The second method is based on the harmonic-balance analysis of a designed GaN HEMT DP mixer operating in S-band, whose relative simulations were performed by means of a commercial CAD. The analyzes was repeated for different local-oscillator power levels (P_{LO}) as to capture the CL and IIP3 behaviors when the $P_{LO} > 10\,\text{dBm}$. Both the analysis methods show improvements at high P_{LO}. In particular, the IIP3 reveals a peak for $P_{LO} \approx 21\,\text{dBm}$ caused by a sweet spot of the output third-order intermodulation products (IMP3) occurring at the same P_{LO}.

Keywords: GaN · Drain-pumped · Power-series

1 Introduction

In the literature, with regards to the radar applications, resistive mixers are mainly taken into consideration thanks to their intrinsic capability of showing great linearity. Modern radar systems are based on multiple transmitter and receiver modules architecture. In the latter the critical functional block consists of the low noise amplifier (LNA). Their presence has the purpose to reduce the noise figure (NF) of the whole receiver chain, which is as a consequence of the high CL showed by the resistive mixers. Recently, a gate-pumped mixer was experimentally proven to provide high linearity when implemented in GaN HEMT technology and driven with high P_{LO} [1]. Moreover, such a topology provides conversion gain (CG) as the input signal is injected at the gate side and the output signal is measured at the drain side, while keeping the drain bias such as to operate in the flat region of the I/V output characteristics. However, the input power combiner losses aggravate the general NF. Furthermore,

the proximity between the RF and LO signal frequencies as required for radar applications makes the isolation difficult.

Moving from this recent evidence, the idea was to inject the pump at the GaN HEMT drain side, thus obtaining a drain-pumped mixer. This improves the isolation performance and the absence of the input power combiner leads to better performances in terms of NF [2,3]. The RF signal path is the same as for the gate-pumped topology, and for this reason it is expected to show better performances in terms of CL with respect to the resistive counterparts. Furthermore, in [4] a field-effect-based DP mixer was shown to increase both the CL and the IIP3 when the P_{LO} increases up to 10 dBm.

To the author's knowledge, this is the first work exploring the GaN HEMT technology impact on the DP performances.

For this purpose, an analysis technique based on the time-varying power series approach was performed. In literature it is widely known that this approach is capable of providing accurate predictions on field-effect transistors IMP3, but the preliminary extraction of the device intrinsic and extrinsic parameters is a very challenging task [5], which makes the technique scarcely used. However, recently the time-varying power-series analysis developed on the basis of the only device I/V characteristics was found to be suitable for the comparison between the linearity performances of two gate-pumped mixers in different technology [1]. In this work the same analysis was adapted for the DP topology, for which behavioral predictions of conversion and linearity performances were carried out. Unlike the harmonic-balance algorithm, this analysis is able to get deep inside the device mixing process, thus providing qualitative explanations about the mixer operation. Furthermore, the experimental nature of such analysis potentially provides more concreteness to the results than using the model alone.
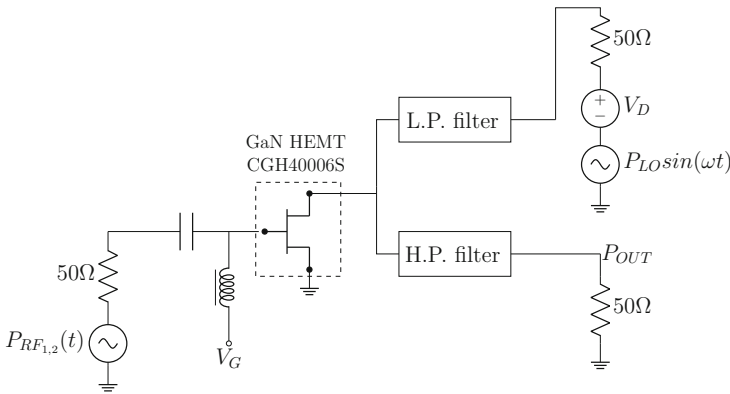
Fig. 1. Conceptual schematic used for the analysis of the drain-pumped mixer

2   Analysis

2.1   Method 1: Time-Varying Power Series Analysis

Dominant Contributions to the CL and IMP3 of the GaN HEMT DP Mixer

It is well known in the literature that the most important contributions in general field-effect transistor applications come from the device drain-current [5,6]. For the purpose of identifying the main contributions to the CL and IMP3 of the DP mixer, we assume the time-varying small signal drain current expansion in Taylor's series as follows:

$$
\begin{aligned}
i_d(v_g, v_d) =& g_m v_g + g_{ds} v_d + \\
& g_{m2} v_g^2 + g_{d2} v_d^2 + \\
& g_{m1d1} v_g v_d + g_{m3} v_g^3 + \\
& g_{m2d1} v_g^2 v_d + g_{m1d2} v_g v_d^2 + g_{d3} v_d^3,
\end{aligned}
\tag{1}
$$

where the time dependence of all coefficients due to the LO pump has been dropped, to simplify the notation.

The work in this subsection relies on the time-varying Volterra series approach [7]. In [4] it was shown that the device transconductance is the main contribution to the DP mixer operation. In this work we inherit these results, being a first insight in the subject. The mixer has the purpose of operating in a receiver chain in S band, however as a first approximation there is no reason for the device reactive components to affect the CL and IMP3 behavior with respect to the P_{LO}, thus they have been neglected.

As to separate the linear and the third-order contributions of the drain current in 1, that give contributions to CL and IMP3 respectively, we make the assumption that the equivalent device input stage does not present nonlinear elements, making the input signal v_g only composed by its first order mixing product voltage.

Thus we obtain:

$$
i_{d1}(t) = g_m(t) v_{g1}(t)
\tag{2}
$$

and

$$
i_{d3}(t) = g_{m3}(t) v_{g1}(t)^3
\tag{3}
$$

The left sides of the Eqs. 2 and 3 contain the main device contributions to the mixer CG and IMP3, that are the ones at $\omega_{IF} = \omega_{RF_1} - \omega_{LO}$ and $\omega_{IF_{IMP3}} = 2\omega_{RF_1} - \omega_{RF_2} - \omega_{LO}$, respectively. It is worth noting that, being the two spectrum side specular, only one spectrum side was considered for the analysis as to simplify the notation. By translating to the frequency domain,

thus applying the matrix form of the convolution product to the expressions 2 and 3, we are able to extract the terms of our interest:

$$I_d(\omega_{IF}) \approx G_{m_{-1}} V_{g1}(\omega_{RF_1}) \tag{4}$$

and

$$I_{d3}(\omega_{IF_{IMP3}}) \approx G_{m3_{-1}} V_{g1}^{(3)}(2\omega_{RF_1} - \omega_{RF_2}) \tag{5}$$

where $G_{m\alpha_k}$ is the component of the $\mathbf{G_{m\alpha}}$ conversion matrix corresponding to the k-th Fourier coefficient of the $g_{m\alpha}(t)$ waveform.

Equation 4 and Eq. 5 reveal the $G_{m_{-1}}$ and the $G_{m3_{-1}}$ to be the coefficients governing the CL and IMP3, respectively.
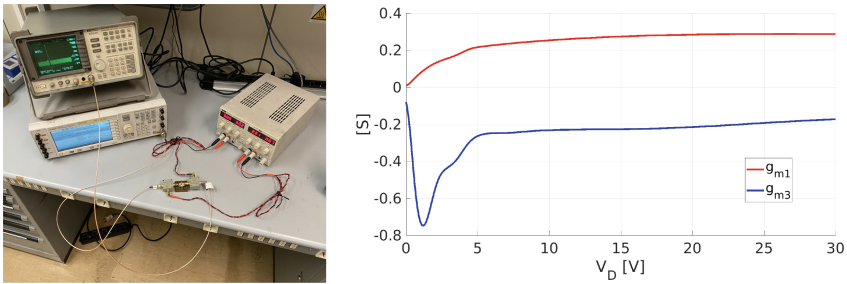
Fig. 2. On the left: the experimental setup for the $g_m(V_D)$ and $g_{m3}(V_D)$ extraction. On the right: the extracted $g_m(V_D)$ and $g_{m3}(V_D)$ evolutions.

Coefficients Extraction Procedure

In this section the procedure for the extraction of the coefficients $G_{m_{-1}}$ and $G_{m3_{-1}}$ of Eqs. 4 and 5 is illustrated. The measures were carried out on a test circuit containing the stand-alone device with a proper set of bias-T, as it is shown in the left of Fig. 2. For this task the device under characterization is the Cree GaN HEMT CGH60004S. Firstly the drain bias-dependent transconductance and its derivatives have been extracted, while the bias voltage was kept fixed where the transconductance peaks, about $-1.6\,\mathrm{V}$. This extraction procedure is dynamic as to avoid traps and self-heating effects and follows the one explained in [6]. A low-frequency tone has been injected at the device gate side by means of a signal generator, and the power of the first and third harmonics has been measured for different drain-bias values at the device drain side by means of a spectrum analyzer. The application of the nonlinear current method then leads to the extraction of $g_m(V_D)$ and $g_{m3}(V_D)$, whose evolutions are shown at the right side of Fig. 2.
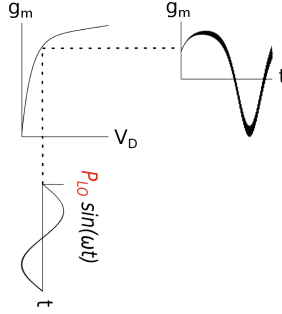
Fig. 3. The algorithm for the transconductance time-varying waveform extraction. The figure illustrates the case for the $g_m(t)$ extraction, but the procedure is the same also for the $g_{m3}(t)$ extraction.

Under the assumption of perfectly LO matching, the $P_{LO}(t)$ at the device drain side is the same signal as the one injected at the LO side of the circuit, shown in Fig. 1. This allows for the application of the algorithm illustrated on the Fig. 3, from which the time-varying waveform were extracted. The figure illustrates the case for the $g_m(t)$ extraction, but the procedure is the same also for the $g_{m3}(t)$ extraction. Knowing the time-varying waveforms, the analytical Fourier coefficient extraction $G_{m_{-1}}$ and $G_{m3_{-1}}$ was straightforward. For each extracted curve, the algorithm was repeated as the P_{LO} changed.

2.2 Method 2: Harmonic-Balance Analysis

A DP mixer operating in S-band was designed and simulated by means the commercial CAD ADS. The conceptual schematic shown in Fig. 1 was the first step of the design. Subsequently, the MOMENTUM software was used with the aim of designing and electromagnetically simulating the whole circuit layout. The S-parameters of the whole layout were then imported at the schematic level and used for the harmonic-balance simulations of the DP mixer.

3 Results

The results of both the analyzes are shown in Fig. 4. The $G_{m_{-1}}$ coefficient governs directly the CL form of the DP mixer, as shown on the left of Fig. 4. Both the experimental-based and the model-based analyzes predict the CL to keep decreasing for high P_{LO}. The harmonic-balance algorithm predicts the CL to reach 0 dB.

The $G_{m3_{-1}}$ instead governs the IMP3 of the DP mixer, which reveals a sweet-spot for $P_{LO} \approx 21.7$ dBm. The sweet-spot is confirmed by the IIP3 fom predicted with the harmonic-balance algorithm, showing a peak at the same P_{LO} level.
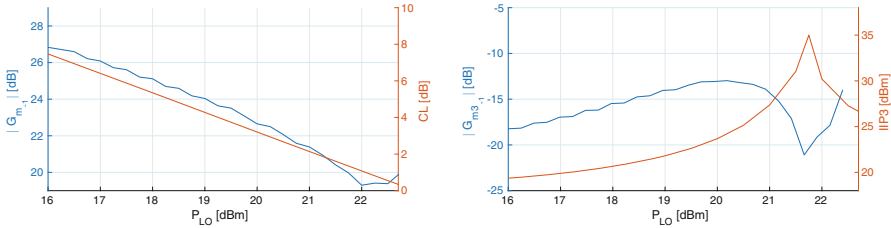
Fig. 4. On the left: comparison between the Fourier coefficient governing the CL of the DP mixer and the harmonic-balance simulated CL of the DP mixer. On the right: comparison between the Fourier coefficient governing the IMP3 of the DP mixer and the harmonic-balance simulated IIP3 of the DP mixer.

4   Conclusions

The present paper investigates, for the first time, the impact of the GaN HEMT technology on DP mixer performances. An experimental analysis based on a measured GaN HEMT device was carried out. In addition, the harmonic balance simulation of the device model has been carried out introducing the electromagnetic simulation of the whole circuit layout (including DC). Both the results predict improvements of the CL and the linearity when the mixer is driven with high P_{LO}. Thus, the present work lays concrete foundations for further investigations on the subject.

References

1. Cidronali, A., Pagnini, L., Collodi, G., Passafiume, M.: A highly linear Ka-Band GaN-on-Si active balanced mixer for radar applications. IEEE Trans. Circuits Syst. I Regular Papers (2022). https://doi.org/10.1109/TCSI.2022.3193960
2. Gunnarsson, S.E., Wadefalk, N., Angelov, I., Zirath, H., Kallfass, I., Leuther, A.: A G-band (140–220 GHz) microstrip MMIC mixer operating in both resistive and drain-pumped mode. In: IEEE MTT-S International Microwave Symposium Digest 2008, pp. 407–410 (2008)
3. Shiba, S., et al.: An F-band fundamental mixer using 75-nm InP HEMTs for precise spectrum analysis. In: European Microwave Integrated Circuit Conference 2013, pp. 137–140 (2013)
4. Ellinger, F., et al.: 30–40-GHz drain-pumped passive-mixer MMIC fabricated on VLSI SOI CMOS technology. IEEE Trans. Microw. Theory Tech. **52**(5), 1382–1391 (2004)
5. Pedro, J.C., Perez, J.: Accurate simulation of GaAs MESFET's intermodulation distortion using a new drain-source current model. IEEE Trans. Microw. Theory Tech. **42**(1), 25–33 (1994)
6. Maas, S.A., Crosmun, A.: Modeling the gate I/V characteristic of a GaAs MESFET for Volterra-series analysis. IEEE Trans. Microw. Theory Tech. **37**(7), 1134–1136 (1989)
7. Carvalho, N.B., Pedro, J.C.: Intermodulation Distortion in Microwave and Wireless Circuits, Artech (2003)

A Broadband Doherty Power Amplifier for Sub-6 5G Applications

Mohammad Shahmordi[1], Sayyed-Hossein Javid-Hosseini[1], Vahid Nayyeri[1], Rocco Giofrè[2], and Paolo Colantonio[2(✉)]

[1] School of Advanced Technologies, Iran University of Science and Technology, Tehran, Iran
nayyeri@iust.ac.ir
[2] Electronic Engineering Department, University of Rome Tor Vergata, Rome, Italy
paolo.colantonio@uniroma2.it

Abstract. In this contribution, a workflow procedure adopted to design a Doherty Power Amplifier (DPA) for broadband Sub-6 5G frequency applications is presented. The approach developed accounts for loading effects of the auxiliary amplifier on the main amplifiers in back-off condition. Moreover, an improved version of optimum region (as opposed to optimum point) in the load and source pulling analysis is introduced. As proof of concept, a symmetric DPA is designed, fabricated and tested. The measurements showed a working frequency band from 3.3 to 3.9 GHz (aimed at n78 band of 5G-NR), a minimum peak output power of 36 W, with a drain efficiency between 48% and 53.22% at peak power, and 34.6%–44.5% at 6 dB of back-off while the transistor maintained a minimum gain of 5.4 dB.

Keywords: Power amplifiers · Doherty amplifiers · GaN · 5G

1 Introduction

The complexity of modern modulation schemes calls for more accurate procedures in designing RF power amplifiers. The narrow margins defined by today standards call for unprecedented levels of performance. Furthermore, due to the increasing signal envelope variations, the classic amplifier configurations show poor performance in terms of efficiency. In fact, the variation of signal's envelope effectively changes its power, and in modern modulations this variation can be quite sever, with the peak power more than 8 times greater than signal's average power. In this context, the Doherty Power Amplifier (DPA) [1,2] is one of the topologies well suited for modulations with varying envelope. Several techniques have been also reported to extend the operative bandwidth of DPA or to improve its performance [3–7]. In a traditional DPA design, a quarter wavelength transmission line is used to implement the active load modulation concept, i.e., to change the load value perceived by one device (referred as Main amplifier) when a second device (referred as Auxiliary amplifier) starts to deliver

output power [8,9]. It is usually assumed that the main and auxiliary amplifiers do not see each other, and as a result have no direct loading effect on one another. Moreover, it is assumed that at back-off, i.e., when the auxiliary is off, the main amplifier sees a load of R_L. As the power increases and the auxiliary amplifiers starts to produce power, the load seen by the main is pulled toward $R_L/2$. Both of these assumptions are somewhat correct at peak, but erroneous at back-off. In the back-off, the auxiliary amplifier along with its corresponding circuitry have a serious loading effect on the main amplifier. In this work, we have devised a procedural workflow to account for this loading effect and take it into account when designing the main power amplifier. In addition to this novel development, we have also used an improved version of optimum region (as opposed to optimum point) in the load and source pulling. In order to validate the proposed approach, a DPA was realized in a hybrid version, based on Wolfspeed CG2H40025F devices, and fabricated on two different substrates. Most of the design is on RT/duroid 5880 whereas the output matching network of the transistors is fabricated on AD1000. The amplifier showed a working frequency bandwidth of 600 MHz, from 3.3 to 3.9 GHz (n78 channel of 5G-NR). In this frequency band, amplifier has at least 36 W of saturated output power, 48% drain efficiency at peak and 34.6% at back-off.

2   Design Procedure

The design approach consists in the following steps:

– design of auxiliary amplifier output matching network
– accounts for the auxiliary loading effects in back-off condition to design the main output matching network
– apply post-matching impedance transformation to finally match the overall DPA to the standard 50 Ω impedance [10,11].

The auxiliary amplifier is biased in class C while the main one is biased in class AB. Both amplifiers use the same CG2H40025F transistor but with different drain voltage, while transformer-less load modulated (TLLM) architecture [12] were also considered. Moreover, since post-matching approach has been considered, the amplifiers have been matched to a 5 Ω load and then using a real to real impedance transformer, the 5 Ω is converted to 50 Ω.

2.1   Auxiliary Amplifier

In order to design the auxiliary amplifier, a preliminary load pull analysis has been performed in the class C biasing condition, considering for the active device the biasing voltages V_{DD}=32 V and $V_{GG} = -4.6$ V (I_D=0). For each frequency in a broader range, e.g. from 3 GHz to 4.2 GHz, contour curves for efficiency (PAE) and output power (Pout) are acquired on the Smith chart, identifying a minimum acceptable level, resulting in this case in a PAE greater than 65 % and Pout greater than 44.5 dBm, respectively. The common region where both
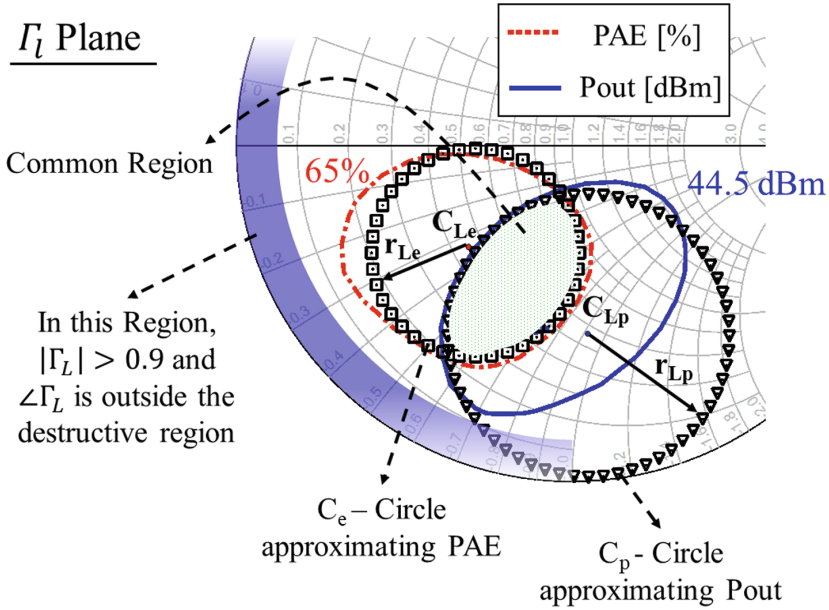
Fig. 1. Example of load-pull result, where the PAE and Pout contours have been approximated with arcs from two circles.

conditions are fulfilled has been identified by defining the two "circles", as for example reported in Fig. 1).

Instead of choosing a single optimum impedance value, the entire common region between the PAE and Pout contours is used as simulation goal, so relaxing the constraints allowing an increase of bandwidth while reducing the complexity in the output matching network design. Furthermore, the effects of second harmonic load termination have been analysed, identifying a reliable region (shadow blue region shown in Fig. 1) for these impedances. Starting from the information on optimum region for fundamental and second harmonic, the optimization process for the design of the output matching network has been performed. Figure 2(left) shows the matching network structure for the auxiliary output network, while in Fig. 2(right) are reported the resulting impedance trajectories.

2.2 Main Amplifier

A similar approach to identify the optimum regions for the main device has been adopted for peak power and 6 dB of back-off, obtaining the results depicted in Fig. 3(left).

Since the output impedance of the auxiliary amplifier in its off condition could affect the operation of the main amplifier, the former behaviour has been extracted under back-off power condition in the entire bandwidth and considered
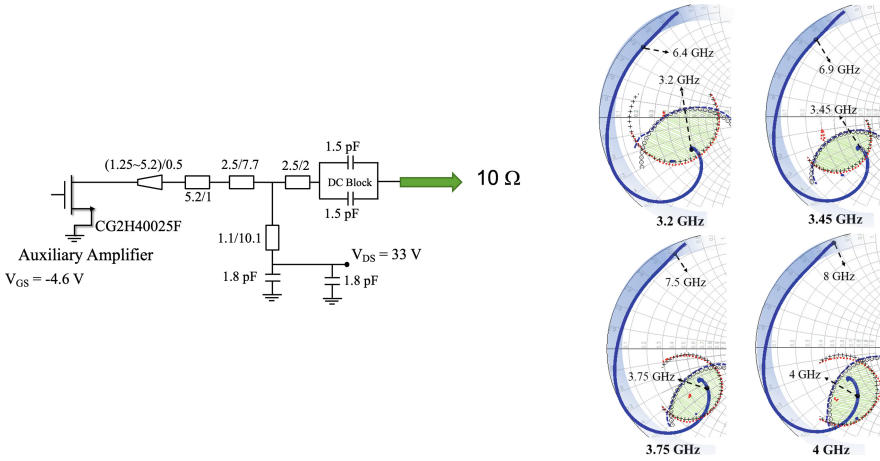
Fig. 2. Structure of the auxiliary output matching network and the resulting synthesised loading trajectory.
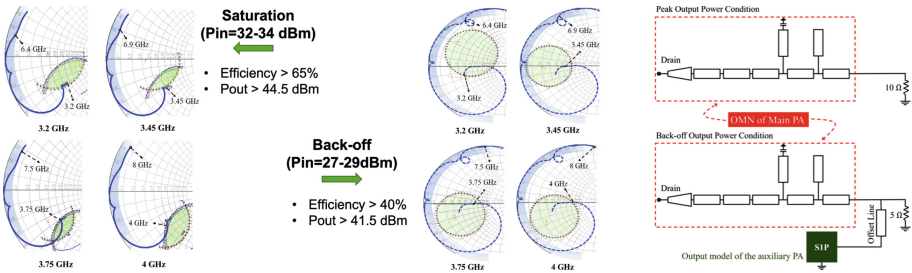
Fig. 3. Left: Load pull optimum regions identified for the main device. Right: Design approach adopted for the main device output network.

when designing the output matching network of the latter, as schematically shown in Fig. 3(right).

3   Realization and Measurement Results

The two designed structures have been finally integrated in the overall schematic, as shown in Fig. 4, where at the input a Gysel combiner has been considered.

The small- and large-signal measured performance are reported in Fig. 5.

The amplifier operates in the frequency band of 3.3–3.9 GHz, which results in a fractional bandwidth of 16.7%. It achieved a saturated output power of 36 W while maintaining a drain efficiency of 48–53% in the peak and 35–45% in the 6 dB back-off power.
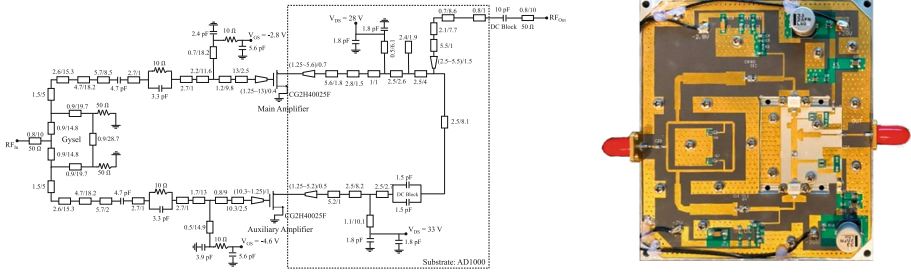
Fig. 4. Left: Schematic of the designed DPA. Right: Photo of the realized DPA.
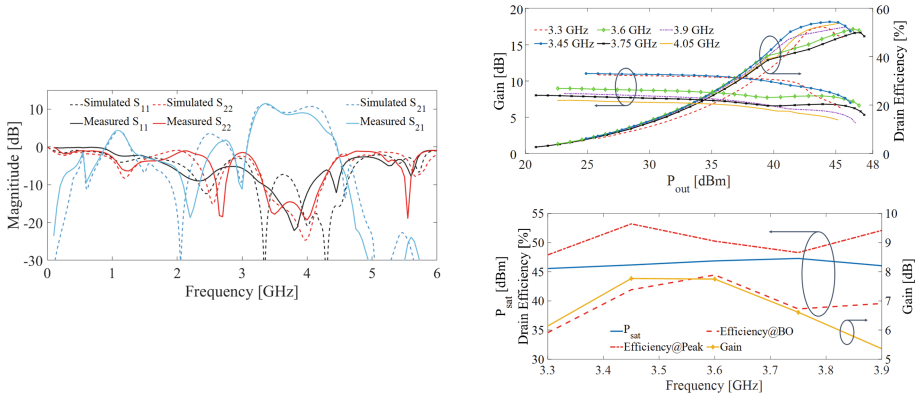
Fig. 5. Small signal (left) and large signal (right) measurement of the realized DPA, in the biasing condition: $V_{DD,Main} = 28\,\mathrm{V}$ - $I_{D,Main} = 220\,\mathrm{mA}$, $V_{DD,Aux} = 32\,\mathrm{V}$ - $V_{GG,Aux} = -9\,\mathrm{V}$.

References

1. Doherty, W.H.: A new high efficiency power amplifier for modulated waves. Proc. Inst. Radio Eng. **24**(9), 1163–1182 (1936)
2. Iwamoto, M., et al.: An extended Doherty amplifier with high efficiency over a wide power range. In: 2001 IEEE MTT-S International Microwave Sympsoium Digest (Cat. No. 01CH37157), vol. 2. Phoenix, AZ, USA: IEEE, pp. 931–934 (2001). [Online]. http://ieeexplore.ieee.org/document/967044/
3. Sun, G., Jansen, R.: Broadband doherty power amplifier via real frequency technique. IEEE Trans. Microwave Theory Techn. **60**(1), 99–111 (2012). http://ieeexplore.ieee.org/document/6084840/
4. Chen, S., Wang, G., Cheng, Z., Xue, Q.: A bandwidth enhanced doherty power amplifier with a compact output combiner. IEEE Microw. Wirel. Compon. Lett. **26**(6), 434–436 (2016). http://ieeexplore.ieee.org/document/7465688/
5. Rafati, S., Nayyeri, V., Soleimani, M.: A 100-W Doherty power amplifier with super-octave bandwidth. IEEE Trans. Circuits Syst. II Exp. Briefs **67**(6), 1009–D1013 (2020). [Online]. https://ieeexplore.ieee.org/document/8765596/

6. Fang, X. H., Cheng, K.-K. M.: Extension of high-efficiency range of doherty amplifier by using complex combining load. IEEE Trans. Microw. Theory nd Techn. 62(9), 2038–2047(2014). [Online]. http://ieeexplore.ieee.org/document/6850081/

7. Camarchia, V., et al.: A design strategy for AM/PM Compensation in GaN doherty power amplifiers. IEEE Access **5**, 22 244–22 251 (2017). [Online]. https://ieeexplore.ieee.org/document/8057734/

8. Colantonio, P., Giannini, F., Giofrè, R., Piazzon, L.: The AB-C doherty power amplifier. Part I: theory. Int. J. RF Microw. Comput. Aided Eng. **19**(3), 293–306 (2009) (ISSN: 1096-4290)

9. Colantonio, P., Giannini, F., Giofrè, R., Piazzon, L.: The AB-C doherty power amplifier. Part II: validation. Int. J. RF Microw. Comput. Aided Eng. **9**(3), 307–316 (2009) (ISSN: 1096-4290)

10. Pang, J., He, S., Dai, Z., Huang, C., Peng, J., You, J.: Design of a Post-matching asymmetric doherty power amplifier for broadband applications. IEEE Microw. Wirel. Compon. Lett. **26**(1), 52–54 (2016). [Online]. http://ieeexplore.ieee.org/document/7358163/

11. Zhou, X. Y., Zheng, S.Y., Chan, W.S., Chen, S., Ho, D.: Broadband efficiency-enhanced mutually coupled harmonic postmatching doherty power amplifier," IEEE Trans. Circuits Syst. I: Regul. Papers **64**(7), 1758–1771 (2017). [Online]. http://ieeexplore.ieee.org/document/7862117/

12. Akbarpour, M., Helaoui, M., Ghannouchi, F.M.: A Transformer- less load-modulated (TLLM) architecture for efficient wideband power amplifiers. IEEE Trans. Microw. Theory Techn. **60**(9,) 2863–2874 (2012). [Online]. http://ieeexplore.ieee.org/document/6236239/

Microwave Radars for Automotive In-Cabin Detection

Emanuele Cardillo[1](✉), Luigi Ferro[1], Changzhi Li[2], and Alina Caddemi[1]

[1] Department of Engineering, University of Messina, Messina, Italy
ecardillo@unime.it

[2] Department of Electrical and Computer Engineering, Texas Tech University, Lubbock, TX, USA

Abstract. Modern cars are complex systems where the passenger safety and comfort are high on the list of the requirements. To this aim, the chance to control the car infotainment system without any contacts represents an advanced feature with a great potential in different applications. In this contribution, a 24 GHz Doppler radar system was specifically designed to investigate the features and current challenges related to the in-cabin detection topic and in detail concerning the radar capability to control the touch-free infotainment system. A case study concerning the contactless adjustment of the car audio system was demonstrated first by identifying the right gesture by exploiting the micro-Doppler analysis and subsequently by extracting the desired volume level from the real fingers' aperture. To measure the fingers' aperture, the radar feature to detect movements in the range of millimeters and below was exploited. Moreover, the phase and amplitude imbalance between the two receiving channels was estimated and corrected. Exploiting radars to enable such a kind of features might pave the way to the next generation of advanced cars where the passengers will be able to comfortably control different infotainment systems.

Keywords: Radar · Automotive · In-cabin detection · Gesture recognition · Micro-Doppler signature · Safety

1 Introduction

Since the production of the first car, the World is assisting to an exponential increase of the electronic devices within the vehicle aimed at enhancing the safety and comfort of the passengers.

Compact radars represent both one of the most employed, e.g., for the task of autonomous mobility, and most promising technologies for the in-cabin sensing [1].

Among the main advantages, radar-based sensing exhibits compact dimensions and consequently high level of integration with the car, together with high spatial resolution, immunity to different light conditions and limited privacy concerns [2–5].

Between the most interesting and challenging features which are available or will be available in modern cars, three different areas of interest stand out and deserve particular interest. They concern:

a)   passenger presence detection;
b)   inattentive driver behavior identification;
c)   Touch-Free Infotainment System Control

The effective passenger detection is a widely investigated topic, particularly due to the great interest for the baby presence detection. In the literature, different works show radars employed to understand if a baby is being left in a car, thus providing an alert for the car driver or a relative/friend [6].

The identification of inattentive driver behaviors is crucial for the driver and passenger safety. Frequently, characteristic movements of the head can be associated with inattentive behaviors. Different researchers tried to identify such a kind of movements by exploiting radar systems, i.e., without any contact or discomfort for the user, to activate emergency procedures for preventing the danger [7].

The case c) represents the main subject of this contribution. The car has plenty of conventional and touch-based buttons that might represent a serious risk for the driver and passenger safety. Indeed, they may distract the driver thus creating potential dangers.

Developing a radar-based touch-free infotainment control system would provide an effective way to control the different car services, enhancing the passenger safety.

In this contribution, a 24 GHz Doppler radar system was specifically designed to investigate the features and current challenges related to the in-cabin detection topic. It is composed of a microwave front-end, a low-frequency amplification board both realized in-house and a microcontroller-based control and elaboration board. A case study was analyzed to investigate the possibility of enabling the touch-free car audio system control. In detail, the feasibility of the accurate volume adjustment was tested by extracting the micro-Doppler signature associated with the finger movements, i.e., extending/reducing the distance between fingers proportionally to the desired audio level. Unfortunately, all quadrature direct-conversion receivers are affected by the signal deterioration due to the in-phase/quadrature (IQ) mismatch, which generates mirrored signals and destroys the orthogonality of the demodulated data [8].

Therefore, the phase and amplitude imbalance between two channels were estimated and corrected. In the next section, the radar system is described and the results of the measurements shown and commented.

2   Touch-Free Infotainment System Control

In order to investigate and demonstrate the radar capability to control the car infotainment system, a 24 GHz radar board, based on the Infineon BGT24MTR11 was designed and realized by means of in-house facilities, i.e., by exploiting the microwave circuit board plotter LPKF ProtoMat S103. In Fig. 1, it is possible to observe the microwave front-end, including the two microstrip transmitting and receiving antennas.

The radar is configured in Doppler mode, thus the demodulated in-phase $s_I(t)$ and quadrature $s_Q(t)$ signals at the output of the transceiver are represented by the expression reported in Eq. 1.1 and Eq. 1.2.

$$s_I(t) = \cos\left(\Delta\phi \pm \frac{4\pi x(t)}{\lambda}\right) \tag{1.1}$$
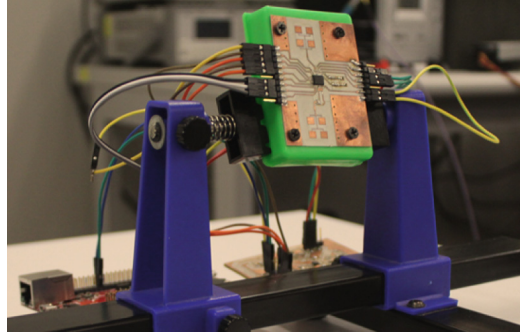
Fig. 1. Picture of the in-house realized radar system.

$$s_Q(t) = \sin\left(\Delta\phi \pm \frac{4\pi x(t)}{\lambda}\right) \tag{1.2}$$

where $\Delta\phi$ is the residual phase, λ is the wavelength and $x(t)$ is the target displacement.

The two low-frequency channels are cascaded with the amplification board which provides two levels of gain, which can be selected according to the application. A microcontroller board set the system operating mode and main parameters and has the task to send the raw data to the computer for the next elaboration steps.

From the phase of the reconstructed complex demodulated signal, it is possible to accurately extract the displacement of the target. Moreover, a short-time Fourier transform (STFT) can be exploited to have a representation of the Doppler components with respect to the time. These two radar features enable the gesture recognition and consequently the contactless control of the infotainment system.

The capability to control without contact the infotainment system was tested by analyzing the case study of the car audio system control. In detail, the first step has the purpose to recognize the gesture associated with the audio level regulation. It is graphically depicted in Fig. 2. The finger movement consists in extending/reducing the fingers distance proportionally to the desired audio level.
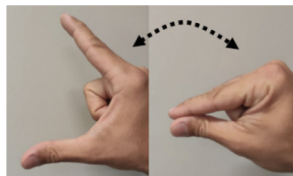
Fig. 2. Movement of fingers associated to the audio level.

This gesture can be recognized by extracting the associated characteristic micro-Doppler signature. The result of the gesture detection is reported in Fig. 3a. In detail, the positive Doppler strips represent the increase of the finger distance due to the index finger approaching radar and a reduction of the distance between radar and index finger.

In the same way, negative Doppler strips represent the decrease of the finger distance due to the index finger moving away from radar.

However, mirrored signals appear nearby the Doppler strips of interest, thus making the detection more challenging. As anticipated, this is due the signal orthogonality deterioration arising from the IQ mismatch.

With the purpose to improve the quality of the detection, the phase and amplitude imbalance between the two channels was estimated by computing the equation of the ellipse associated with every couple of sampled data, and then corrected by employing the Gram-Schmidt transformation [9, 10]. The results of the IQ imbalance correction on the micro-Doppler are shown in Fig. 3b, where the positive and negative strips are clearly visible.

(a)

(b)
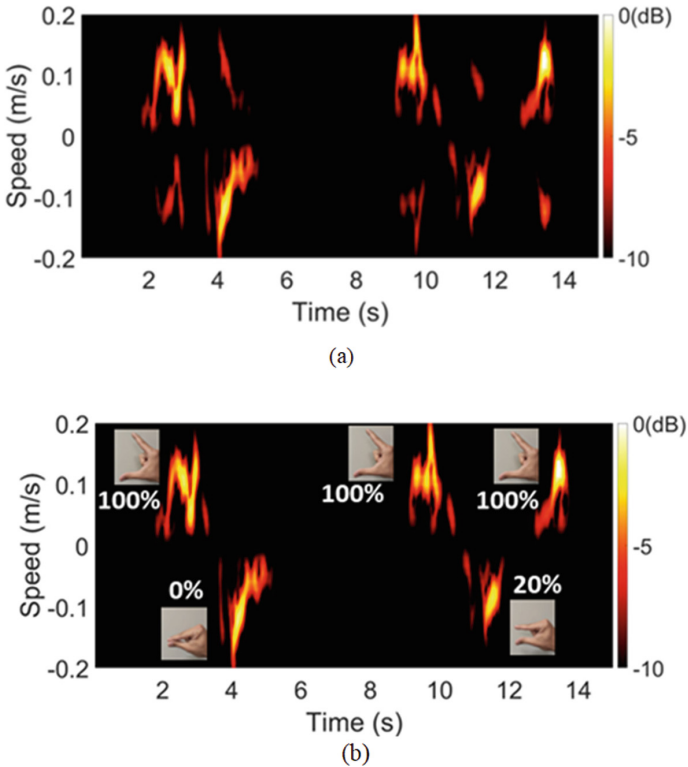
Fig. 3. Measured micro-Doppler signature (a) before and (b) after the IQ imbalance correction.

After the first step of gesture recognition, the next goal consisted in measuring the displacement due to the finger motion. This task was accomplished by extracting the phase of the signal after the downconversion stage and computing the related range shift. By exploiting the radar features, this step can be accomplished in a robust and accurate way, while preserving the user privacy.

Figure 4a shows the displacement related with a total aperture of the fingers, which can be associated with an audio level increase up to 100%.

Thereafter, three consecutive movements were tested in order to verify the radar capability to regulate the audio level. In Fig. 4b, a total aperture of the fingers, a partial contraction to 20% and finally a 100% aperture are shown.
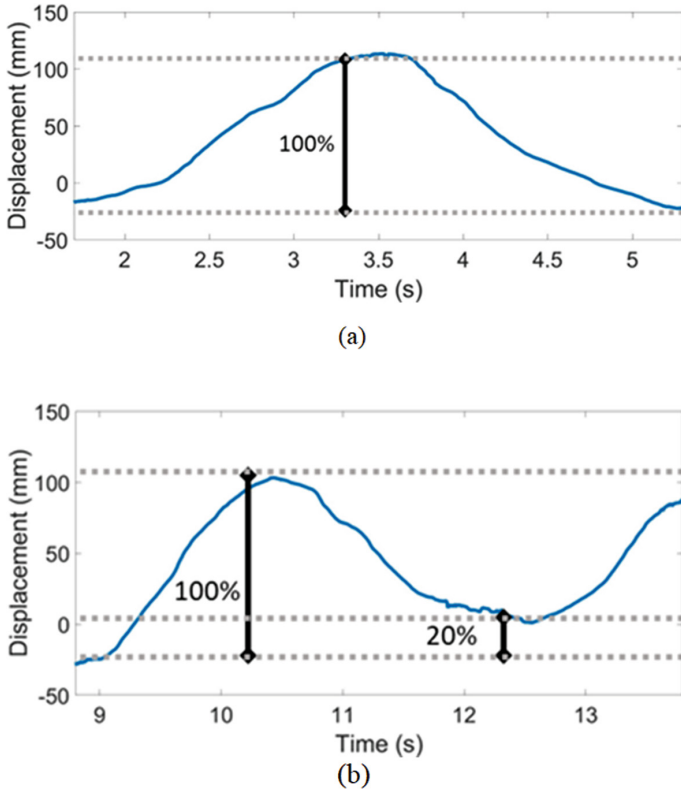
Fig. 4. Measured displacements related to different finger apertures. a) 0% to 100%. b) 0% to 100% to 20% to 100%.

By associating the extension of the fingers to the audio level percentage, it is possible to control the audio system, accordingly. However, even though the measurement of the displacement is correct, due to the random relative movement between the hand and the radar, the precise measurement of the 100% level at the end of the measuring time in Fig. 3b is not properly accomplished. An error equal to 12.75% was estimated for the second 100% level measurement.

Avoiding the effects of random body motion represents one of the main challenges to be faced to enable the next generation of advanced cars where the passengers will be able to comfortably control different infotainment systems.

3 Conclusions

In this contribution the task of the car infotainment system control without any contacts has been investigated. By means of a 24 GHz Doppler radar system, a case study concerning the contactless regulation of the car audio system was investigated by identifying the right gesture and by extracting the desired volume level from the real aperture of fingers.

The reported preliminary results are encouraging for the next research in the field of the in-cabin automotive radar detection.

References

1. Dandu, K., et al.: 2.2 high-performance and small form-factor mm-Wave CMOS radars for automotive and industrial sensing in 76-to-81 GHz and 57-to-64 GHz Bands. In: IEEE International Solid- State Circuits Conference (ISSCC), San Francisco, CA, USA, pp. 39–41 (2021)
2. Cardillo, E., et al.: Head motion and eyes blinking detection: a mm-Wave radar for assisting people with neurodegenerative disorders. In: 50th European Microwave Conference (EuMC), pp. 925–928. The Netherlands, Utrecht (2021)
3. Cardillo, E., Li, C., Caddemi, A.: Heating, ventilation, and air conditioning control by range-doppler and micro-doppler radar sensor. In: 18th European Radar Conference (EuRAD), 2022, London, U.K, pp. 21–24 (2021)
4. Cardillo, E., Ferro, L.: Multi-frequency analysis of microwave and millimeter-wave radars for ship collision avoidance. In: Microwave Mediterranean Symposium (MMS), Pizzo Calabro, Italy, pp. 1–4 (2022)
5. Zhu, C., et al.: Testing of passive intermodulation based on an ultrawideband dual-carrier nulling. IEEE Trans. Microw. Theory Techn. **70**(8), 4017–4025 (2022)
6. Caddemi, A., Cardillo, E.: Automotive anti-abandon systems: a millimeter-wave radar sensor for the detection of child presence. In: 14th International Conference on Advanced Technologies, Systems and Services in Telecommunications (TELSIKS), Nis, Serbia, pp. 94–97 (2019)
7. Ding, C., et al.: Inattentive driving behavior detection based on portable FMCW radar. IEEE Trans. Microw. Theory Tech. **67**(10), 4031–4041 (2019)
8. Rodriguez, D., Li, C.: Sensitivity and distortion analysis of a 125-GHz interferometry radar for submicrometer motion sensing applications. IEEE Trans. Microw. Theory Tech. **67**(12), 5384–5395 (2019)
9. Singh, A., et al.: Data-based quadrature imbalance compensation for a CW doppler radar system. IEEE Trans. Microw. Theory Tech. **61**(4), 1718–1724 (2013)
10. Park, B., Yamada, S., Lubecke, V.: Measurement method for imbalance factors in direct-conversion quadrature radar systems. IEEE Microw. Wirel. Comp. Lett. **17**(5), 403–405 (2007)

Low-Noise Amplifiers in Gallium Nitride for Robust and Highly Linear Ka-Band SATCOM

Patrick Ettore Longhi(✉) 🄳, Lorenzo Pace 🄳, Walter Ciccognani 🄳, Sergio Colangeli 🄳, and Ernesto Limiti 🄳

E.E. Department, Università di Roma "Tor Vergata", 0013 Roma, Italy
longhi@ing.uniroma2.it

Abstract. Recently, within the framework of a project funded by the European Space Agency, two concept demonstrators in OMMIC's industrial-grade GaN HEMT technology on a Silicon substrate have been developed. The first test vehicle is an ultra Low-Noise Amplifier (LNA), realized in OMMIC's 60-nm GaN HEMT technology, demonstrating state-of-the-art 1.2 dB Noise Figure, in the 26–32 GHz bandwidth. The second test vehicle is a Medium Level Amplifier (MLA), realized in OMMIC's 100-nm GaN HEMT technology, providing +31 dBm Output Third Order Intercept point (OTOI). Both performances compare very well with recently published material.

Keywords: Gallium nitride · Low-noise amplifier · Ka-band · Third order intercept point · High linearity

1 Introduction

Gallium Nitride (GaN) is gaining considerable interest in the Space community due to some advantages respect to other low-noise and high frequency technologies (mainly Gallum Arsenide) for the reasons explained in the following. GaN is a wide-bandgap material compared to GaAs, more than twice; this results in a breakdown voltage field much higher, by about one order of magnitude. Moreover, GaN supports smaller circuits for a given frequency and power levels, allowing higher power densities and efficiencies. As consequence of the above feature, GaN is capable to withstand strong signals without degradation or breakup. Finally, thermal conductivity of the GaN is more than three times the thermal conductivity of the GaAs.

In this contribution, we highlight the design solutions and preliminary characterization of two circuits: a robust low-noise amplifier (LNA) and a medium-level amplifier (MLA). The main design goals are minimizing LNA's Noise Figure and more than + 30 dBm OTOI in the MLA. The targeted bandwidth is Ka-band, and more particularly 27–31 GHz for SATCOM applications.

2 Circuit Design

The two circuits are designed to fulfil the following key requirements. Ka-band operation and more in particular 27 to 31 GHz. The LNA shall feature ultra low-nosie behaviour (NF 1.5 dB) while the MLA is oriented towards high-linearity (OTOI + 30 dBm). Another feature is to minimize DC power consumption so the circuits can represent an attractive solution for a 1-to-1 replacement of existing GaAs counterparts. 30 mW and 50 mW are the requested PDC of the LNA and MLA respectively.

2.1 Technology Selection

The most suitable MMIC technology is selected considering the following requirements and recommendations, which are listed not necessarily in order of importance.

In order to produce acceptable gain level at ka-band, parameters such as gate length, f_T and f_{MAX} are evaluated. Equally, Noise Performance, evaluated by NF_{min} at operating frequency is also of interest. Power handling requirements, evaluated by power density at 30 GHz and breakdown voltage V_{BGD} and to be addressed since the MLA has to deliver acceptable linearity performance. Finally, Technology maturity level; possibly a Space-level technology given the target application.

A scouting of foundry processes that are capable of providing low-noise performance for Ka-band (27–31 GHz) operation, and capable of handling RF signals in the order of +20 dBm are provided in the following: OMMIC'S D01GH, a 100 nm GaN HEMT on Si process that is under evaluation for Space application [1]. UMS GH10 process is a 100 nm GaN HEMT on SiC optimized to produce low noise, wideband and medium power amplifier MMICs operating up to 55 GHz. WIN foundry NP-15 GaN on SiC process leverages an advanced materials design with electron-beam defined 0.15 µm gates and a qualified 150 mm manufacturing infrastructure to obtain a high volume, ultra-high-performance technology platform. The process is targeted for Power amplifiers through 35 GHz as well as Switch and LNA functionalities. Fraunhofer Institute for Applied Solid State Physics - IAF offers the GaN10 HEMT process in grounded coplanar waveguide on 3-inch SiC substrates for operation up to W-band. A summary table of these technologies key electrical requirements is reported in Table 1.

Table 1. Key electrical parameters of benchmarked GaN technologies

Parameter	OMMIC D01GH	UMS GH10	WIN NP15	IAF GAN10
f_T (GHz)	100	80	35	80
f_{MAX} (GHz)	180	130	120	190
NF_{min} @ 30 GHz	1.4	1.7	2.3	1.4
$g_{m,max}$ (mS/mm)	400	400	435	350
I_{DSS} (mA/mm)	1200	500	990	1300
V_{BGD} (V)	40	50	60	40
Technology	GaN/Si	GaN/SiC	GaN/SiC	GaN/SiC

OMMIC's D01GH is selected for this research project since it combines interesting electrical performance, in conjunction with production grade technology. Moreover, it is grown on a Silicon substrate and therefore immune to export or production issues suffered by Silicon Carbide (SiC) epitaxy.

2.2 Topology Selection

The topology is selected to fulfil the electrical requirements briefly expressed at the beginning of Sect. 1. The critical requirements are low-noise behaviour for the LNA, high-linearity for the MLA and finally reduced PDC for both circuits. Several topologies are investigated and evaluated. Four circuit topologies are evaluated, these are: single-ended, distributed, cascode, and balanced. The PROs and CONs of each circuit topology is reported in Table 2.

Table 2. Performance evaluation of the considered circuit topologies

Feature	Critical	Single ended	Cascode	Balanced	Distributed
Noise	Yes	Excellent	Very good	Average	Average
Bandwidth	No	Average	Very good	Very good	Excellent
Gain	Yes	Good	Very good	Average	Good
DC power	Yes	Excellent	Average	Average	Poor
Return loss	No	Average	Good	Very good	Very good
Size	No	Small	Medium	Large	Large
Linearity	Yes	Good	Excellent	Very good	Good

We opted for the single-ended topology since it combines low-noise behaviour in conjunction with linearity at reduced PDC request. Other topologies experience some drawbacks. For example, the cascode topology requires practically double drain voltage value that is halved across the two transistors. The other circuit topologies (balanced and distributed) require many transistors which in turn severely affects the power consumption of the circuit.

2.3 Circuit Synthesis

A 3-stage topology is selected for both circuits to obtain the prescribed 20 dB gain level. The transistor size is optimized to account to trade-off between contrasting goals of power consumption, linearity, and robustness. The first parameter entails the use of smaller transistors while the latter parameters would require the use of larger transistors. A $4 \times 20\,\mu m$ transistor biased at $V_D = 5V$ and I_D 125 mA/mm is selected for the overall LNA and the first stage of the MLA. The final stages of the MLA employ larger transistors, 4×30 and $4 \times 40\,\mu m$ transistors. To improve the Noise Figure of the LNA we opted to insert a 60-nm gate length transistor in the first stage. The stages are reactively

matched. Dissipative elements (resistors) are placed ion the bias lines to enhance stability and reduce low-frequency gain. The value of the gate resistor is maximized to protect the first stage from detrimental overdrive effects [2]. Source degenerative feedback is applied to obtain good noise and signal match at the input over the operating bandwidth [3]. The input termination of the LNA is selected for optimum noise condition (Γ_{OPT}) while a source and load pull of the finals stage device of the MLA shows that the optimum load impedance for linearity is $20 + 45 \cdot j\ \Omega$, yielding more than 31 dBm OTOI at 30 GHz.

3   Circuit Characterization and Benchmarking

The two circuits are characterized to verify their compliance respect to the key requirements listed at the beginning of Sect. 1. The two circuits microphotographs are shown in Fig. 1. Chip size is 3 mm × 2 mm in both cases. All test reported in the following sections are performed at the nominal Drain voltage set to +5V for both circuits. The drain current for the LNA is 30 mA and 45 mA for the MLA.
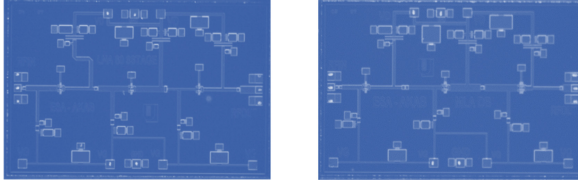
Fig. 1. GaN Ka-band 60-nm LNA (left) and 100-nm MLA (right). Size is 3 mm × 2 mm.

3.1   Linear and Noise Characterization

Figure 2 depicts the two amplifiers gain and Noise Figure characterization in the operating bandwidth 27–31 GHz. In both cases the target gain is average +20 dB while the 60-nm NF is better than the MLA counterpart.
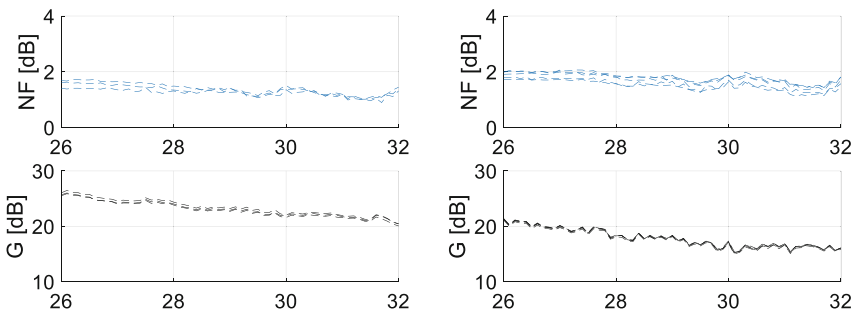
Fig. 2. Gain and NF of GaN Ka-band 60-nm LNA (left) and 100-nm MLA (right). 3 samples per type.

The gain is greater than 20 dB for the 60-nm LNA and greater than 19 dB for the MLA. The NF of the 60-nm LNA is around 1.4 dB in band while the MLA's NF is 1.8 dB typical. The gain slope is corrected at system level by adding a gain equalizer.

3.2 Nonlinear Characterization

Figure 3 reports the nonlinear characterization of the 60-nm LNA and MLA. The left plot contains the LNA's NF 10 sweeps stress test at 29 GHz while the right graph reports the MLA two-tone test.
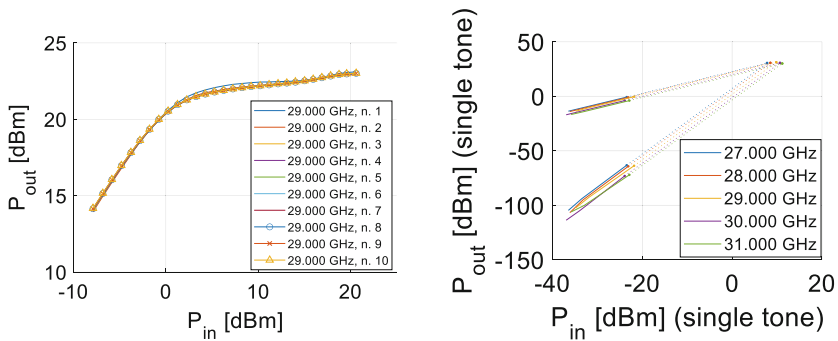
Fig. 3. CW stress of GaN Ka-band 60-nm LNA (left) and OTOI of 100-nm MLA (right).

The LNA is subject up to +22 dBm input power without showing significant degradation after 10 sweeps while the MLA demonstrates an OTOI in excess of 30 dBm.

3.3 Benchmarking

Table 3 reports the electrical performance of similar circuits reported in the open literature. The two MMICs here presented compare well against other contribution reported in open literature. The LNA provides excellent NF, while the MLA excellent OTOI in conjunction with reduced DC power consumption.

Table 3. State-of-the-art LNA Ka-band GaN MMICs.

Ref	Tech	BW (GHz)	Gain (dB)	NF (dB)	OTOI (dBm)	PDC (mW)
[4]	GaN-on-Si 100	33–38	26	2.0	28.4	540
[2]	GaN-on-SiC 150	27–29	20	4.0	N/R	800
[5]	GaN-on-SiC 40	30–40	25	1.5	20	100
[6]	GaN-on-Si 100	22–30	13	1.5	N/R	720
[7]	GaN-on-Si 100	18–31	22	1.9	28	280
[8]	GaN-on-Si 100	26–34	20	1.6	N/R	720
[9]	GaN-on-Si 100	34–38	30	2.4	N/R	325
t.w. LNA	GaN-on-Si 60	26–32	23	1.3	26	150
t.w. MLA	GaN-on-Si 100	26–32	20	1.7	30.5	225

4   Conclusions

Design solutions of a pair of Low-Noise Amplifiers operating at Ka-band are given. The 60-nm version exhibits excellent Noise Fig. (1.3 dB) in conjunction with robustness (+21 dBm CW). The 60-nm version exhibits excellent linearity, in terms of OTOI (+30.5 dBm) in conjunction with reduced power consumption (only 225 mW).

References

1. Colangeli, S., et al.: Linear characterization and modeling of GaN-on-Si HEMT technologies with 100 nm and 60 nm gate lengths. Electron **10**, 1–16 (2021). https://doi.org/10.3390/electronics10020134
2. Suijker, E.M., et al.: Robust AlGaN/GaN low noise amplifier MMICs for C-, Ku- and Ka-band space applications. In: Technical Digest - IEEE Compound Semiconductor Integrated Circuit Symposium, CSIC. pp. 1–4. IEEE (2009). https://doi.org/10.1109/csics.2009.5315640
3. Longhi, P.E., Pace, L., Colangeli, S., Ciccognani, W., Limiti, E.: Novel design charts for optimum source degeneration trade-off in conjugately matched multistage low-noise amplifiers. IEEE Trans. Microw. Theory Tech. **69**, 2531–2540 (2021). https://doi.org/10.1109/TMTT.2021.3068285
4. Florian, C., Traverso, P.A., Santarelli, A.: A Ka-Band MMIC LNA in GaN-on-Si 100-nm technology for high dynamic range radar receivers. IEEE Microw. Wirel. Components Lett. **31**, 161–164 (2021). https://doi.org/10.1109/LMWC.2020.3047152
5. Micovic, M., et al.: Ka-Band LNA MMIC's Realized in Fmax > 580 GHz GaN HEMT Technology. In: 2016 IEEE Compound Semiconductor Integrated Circuit Symposium (CSICS). pp. 1–4. IEEE (2016). https://doi.org/10.1109/CSICS.2016.7751051
6. Tong, X., Wang, R., Zhang, S., Xu, J., Zheng, P., Chen, F.X.: Degradation of Ka-Band GaN LNA under high-input power stress: experimental and theoretical insights. IEEE Trans. Electron Devices. **66**, 5091–5096 (2019). https://doi.org/10.1109/TED.2019.2947311
7. Tong, X., Zhang, S., Zheng, P., Xu, J., Shi, X.: 18–31 GHz GaN MMIC LNA using a 0.1 um T-gate HEMT process. In: 2018 22nd International Microwave and Radar Conference (MIKON). pp. 500–503. IEEE (2018). https://doi.org/10.23919/MIKON.2018.8405269

8. CGY2250UH: 26-34 GHz GaN LOW NOISE AMPLIFIER, OMMIC Product Catalogue. https://www.ommic.com/product_lna/?ref=CGY2250UH
9. Pace, L., et al.: Design and validation of 100 nm GaN-On-Si Ka-Band LNA based on custom noise and small signal models. Electronics **9**, 150 (2020). https://doi.org/10.3390/electronics9010150

Sensors, Microsystems and Instrumentation

Accelerometric System Based on a Fully FDM 3D Printed Sensor

Gianluca Barile(✉) 🄳, Laura Iacoboni, Vincenzo Stornelli 🄳, and Giuseppe Ferri 🄳

Department of Industrial and Information Engineering, University of L'Aquila, 67100 L'Aquila, Italy
gianluca.barile@univaq.it

Abstract. In this manuscript, the authors propose an accelerometric system whose sensing element is fully fabricated via FDM 3D printing process. Exploiting the inherent features of the additive manufacturing fabrication, such as the possibility of implementing intricate shapes, and the peculiar features of the FDM process such as the possibility to extrude different materials at the same time, it is here shown how to realize a fully functioning three axis capacitive accelerometer that requires no post processing at the end of the fabrication. In this manuscript the electronic interface used to convert differential capacitance to voltage variations is also described. Measurements conducted on a single axis, showing a natural frequency for the sensor of 4 Hz and a quality factor of 6.33 are reported. System DC characteristic shows a maximum linearity error of 6.2% and a sensitivity of 1.22 mV/V, with a minimum detectable acceleration of 0.5 g.

Keywords: Accelerometer · Additive manufacturing · FDM · 3D printing

1 Introduction

In recent years, accelerometers have become extremely widespread devices [1]. Probably, the main reason behind this fact is that the determination of the acceleration to which a system is subjected, is a fundamental requirement in the monitoring and control of many phenomena, since, from the acceleration, it is possible to also obtain information about position and speed. Capacitive and differential capacitive accelerometers rely on the exploitation of a mobile mass to vary an electrical capacitance, acting as a mass-spring system [2].

3D printing technology is a useful tool for rapid prototyping of devices and systems [3, 4]. In particular, the FDM/FFF category features a wide variety of materials available among which the relatively novel electrically conductive filaments [5]. There are several manuscripts in the literature featuring 3D printed sensors and 3D printed electronics: many of them propose a peculiar sensor shape which is then printed and metallized via chemical procedures, while others use 3D printing to fabricate a specifically shaped substrate that is then post processed, given the need to deposit the actual conductors and traces. Other manuscripts show the use of a pseudo-3D printing approach based

on conductive silicone. This approach employs a CNC motion platform to deposit liquid silicone that however is cumbersome to shape and needs to dry before depositing successive layers. Moreover, it is not easy to print intricate and detailed shapes [6–9].

This work aims at demonstrating the feasibility of a fully 3D printed sensor fabricated via a multi-material FDM process. The used sensor shape is taken from [6], where the authors used a mix of SLA 3D printing and wet metallization. Although FDM/FFF technology is in general less accurate than the SLA one, it gives many more degrees of freedom such as modifying the proof mass weight without reshaping the sensor, the possibility of minimizing parasitic elements by accurately using conductive material where needed, and the possibility to use water soluble supports so to avoid the need of removing them by hand and therefore minimizing the post processing phase.

The manuscript is divided as follows: Sect. 2 shows the sensor design, its equivalent model, the fabrication process in terms of materials and printing technology, and an overview of the electronic readout interface; Sect. 3 gives the main measurement results. Finally, Sect. 4 gives some conclusions.

2   Materials and Methods

2.1   Transducer Design

The shape of the transducer here proposed is taken from [6] and is suitably modified so to take advantage of the FDM multi material fabrication process. It is shown in Fig. 1: as visible it consists of a chassis where a moving mass is fixed onto via insulating springs. The mass is free to move in each of the three dimensions. Differently from [6] where the actual conductivity was achieved via a chemical post processing stage, in a FDM process it is possible to assign a specific property to each of the surfaces of the object. Indeed, see Fig. 1a and Fig. 1b, all the conductive surfaces are reported in black, whereas the insulating ones are reported in white. Another advantage with respect to other additive manufacturing processes, is the possibility of designing true differential capacitive sensors for each axis. This means that each of the three central conductors are insulated from each other (Fig. 2a), so achieving a reduced cross-axis coupling. The electrical equivalent model of the sensor is shown in Fig. 2b.

(a)   (b)
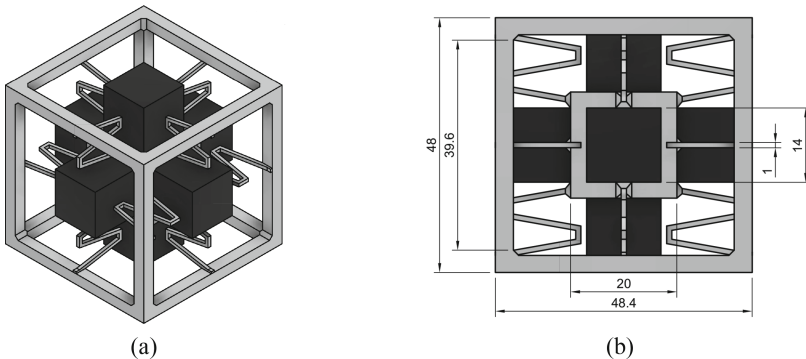
Fig. 1. The proposed transducer (a) shape and (b) dimensions.
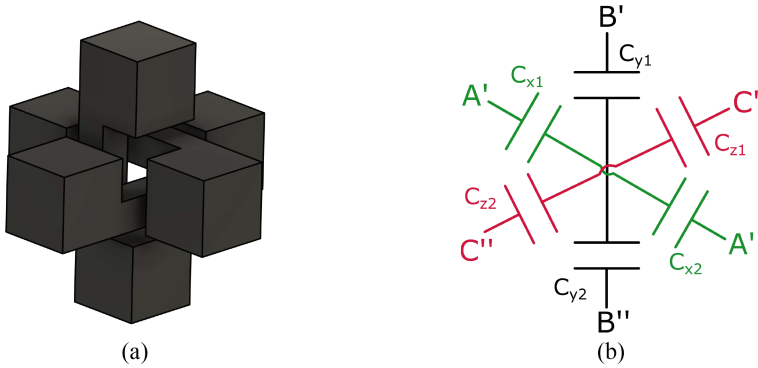
Fig. 2. (a) Shape of the central conductors; (b) electrical equivalent model of the sensor.

2.2 Fabrication Process

The sensor was manufactured using a mix of Proto Pasta Conductive filament to implement conductive surfaces, generic polylactic acid (PLA) for the insulating surfaces and water-soluble polyvinyl alcohol (PVA) to implement the supports (see Fig. 3).

The printing setup is shown in Fig. 4a. The printer is a Tips 3DPRN LAB1 that features a single extruder with a 0.4 mm nozzle diameter. To achieve the multi material feature the Mosaic Palette+ was paired with the printer (Fig. 4b). Specifically, the Palette+ acts as a filament multiplexer allowing to assign specific features to specific surfaces of the object. Based on the g-code of the printer, the Palette+ takes multiple materials as an input and produces a calibrated stream of multi material output so to make sure that the specific material is deposited at the correct location of the object. An example of the output filament is shown in Fig. 4b. Figure 4c shows the manufacturing process few layers after the start of the print, where the different deposited materials are visible. Electrical contacts were embedded into the sensor during the printing process. The result, shown in Fig. 4d, is a triaxial accelerometer featuring true differential capacitors for each of them, where the fixed plates of the capacitors are implemented via copper plates.
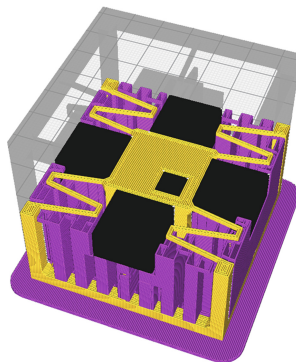
Fig. 3. Material choice for each surface: in yellow the insulating structures, in black the conductive ones and in purple soluble supports are highlighted.
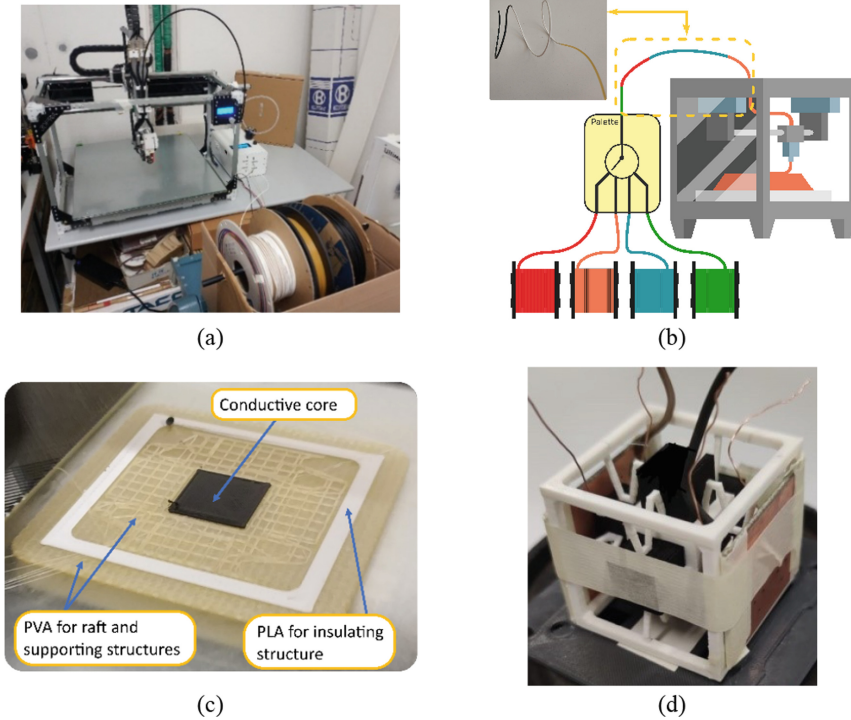
Fig. 4. (a) Printing setup; (b) Palette + working principle; (c) Palette + output filament example.

2.3 Electronic Readout Interface

Amongst the many available techniques, the differential capacitance readout was carried out using a custom designed interface based on the autobalanced bridge structure [10–12]. Figure 5 shows the electronic interface schematic: the sensor is placed along a branch of the bridge, while the other one hosts a reference impedance together with a variable resistor suitably driven by a feedback voltage. The feedback network, based on a synchronous modulation/demodulation technique, makes sure that the bridge remains balanced, i.e., $V_a = V_b$. The capacitance variation and the output voltage are linked by the linear relationship $V_{ctrl} = 10[\text{V}]x$, where $x = (C_1 - C_2)/(C_1 + C_2)$.

3 Measurement Results

Measurements were conducted using the following setup: mechanical stimuli were produced by a loudspeaker connected to a suitable driver. The fabricated sensor was fixed to this platform together with an ADXL345 used as a reference accelerometer. The output of the interface was recorded via an oscilloscope. Measurements were carried out on a single axis, both small signal sinusoidal response as well as step response were investigated.
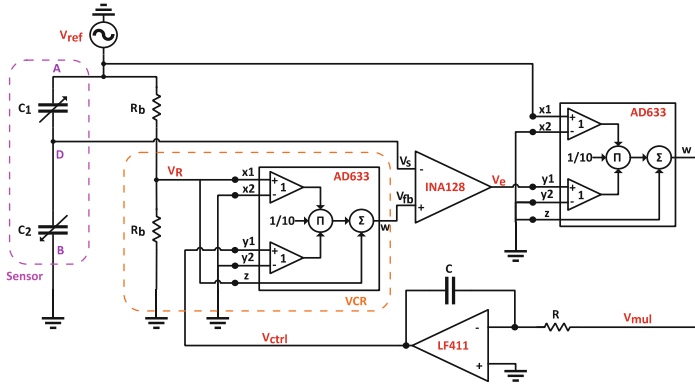
Fig. 5. Electronic interface schematic.

Figure 6a shows the linearity and sensitivity of the interface at different sinusoidal input frequencies and amplitudes. Results are given in Table 1: sensitivity decreases as the frequency raises, proving the very low natural frequency of the sensor. Maximum linearity error remains below 6.5% whereas the resolution of the sensor is 0.5 g.

Figure 6b shows the step response of the sensor: a step input with an amplitude of ± 1 g was used for this test; the output of the proposed sensor was compared with the reference accelerometer. By analyzing the sensor decay time, supposing a mass-spring-damper model, it is possible to extract some meaningful data reported in Table 2. Interestingly, the natural frequency of the sensor is equal to 4 Hz, which confirms the small signal behavior previously reported.
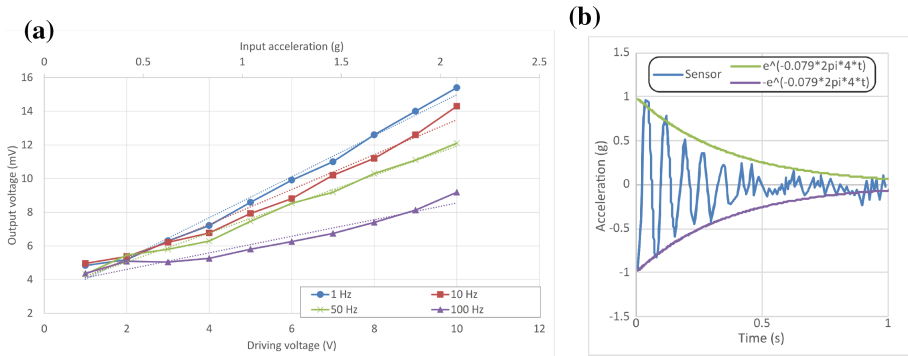
Fig. 6. (a) Sensor output as a function of the frequency and the amplitude of the input oscillation, (b) step response of the sensor.

Table 1. Small signal linearity and sensitivity results.

Frequency (Hz)	Sensitivity (mV/V)	Linearity error (%)
1	1.22	6.24
10	1.03	6.23
50	0.86	6.67
100	0.5	8.11

Table 2. Sensor main parameters.

Magnitude	Relationship	Value
Decay rate	$\delta = ln\frac{x(t2)}{x(t1)}$	0.5
Damping coefficient	$\zeta = \frac{\delta}{2\pi}$	0.079
Quality factor	$Q = \frac{1}{2\zeta}$	6.33
Natural frequency	-	$\cong 4$ Hz

4   Conclusions

In this manuscript a 3-axis accelerometric system with a fully FDM 3D printed transducer was analyzed and proposed. Measurements have shown that proposed approach can be valuable given the many degrees of freedom that it is possible to exploit. This allows to design and fabricate fully ah-hoc sensors for each specific application, in terms of mechanical, electrical, and chemical properties. Moreover, the aforementioned features are achievable with negligible costs and time to production.

References

1. Niu, W., et al.: Summary of research status and application of MEMS accelerometers. J. Comput. Commun. **6**(12), 215–221 (2018)
2. Mohammed, Z., Elfadel, M., Rasras, M.: Monolithic multi degree of freedom (MDoF) capacitive MEMS accelerometers. Micromachines **9**(11), 602 (2018)
3. Bagheri, A., Jin, J.: Photopolymerization in 3D Printing. ACS Appl. Polym. Mater. **1**(4), 593–611 (2019)
4. Tino, R., et al.: COVID-19 and the role of 3D printing in medicine. 3D Printing Med. **6**(1), 11 (2020)
5. Kwok, S.W., et al.: Electrically conductive filament for 3D-printed circuits and sensors. Appl. Mater. Today **9**, 167–175 (2017)
6. Zega, V., et al.: The first 3D-printed and wet-metallized three-axis accelerometer with differential capacitive sensing. IEEE Sensors J. **19**, 9131–9138 (2019)
7. Macdonald, E., et al.: 3d printing for the rapid prototyping of structural electronics. IEEE Access **2**, 234–242 (2014)

8. Leoni, A., Stornelli, V., Pantoli, L.: A low-cost portable spherical directional anemometer for fixed points measurement. Sens. Actuators, A **280**, 543–551 (2018)

9. Leoni, A., Barile, G., Ferri, G., Stornelli, V.: Analysis and development technique of a fully 3D-printed differential capacitive anemometric sensor. IEEE Sensors J. **22**, 19439–19454 (2022)

10. Barile, G., et al.: A standard CMOS bridge-based analog interface for differential capacitive sensors. In: 2017 13th Conference on Ph.D. Research in Microelectronics and Electronics (PRIME), pp. 281–284 (2017)

11. Barile, G., et al.: A VCII-based stray insensitive analog interface for differential capacitance sensors. Sensors **19**(16) (2019)

12. Safari, L., et al.: New current mode wheatstone bridge topologies with intrinsic linearity. In: 2018 14th Conference on PhD Research in Microelectronics and Electronics (PRIME), pp 9–12 (2018)

An Electrochemical Biosensor for the Detection of Bacteriophage of *Lactococcus Lactis*

Stefano Bonaldo[1(✉)], Erica Cretaio[2], Elisabetta Pasqualotto[2], Matteo Scaramuzza[3], Lara Franchin[1], Sara Poggi[1], and Alessandro Paccagnella[1]

[1] Department of Information Engineering, University of Padova, 35131 Padova, Italy
stefano.bonaldo@dei.unipd.it
[2] ARCADIA, 35132 Padova, Italy
[3] ARC-Centro Ricerche Applicate, 35132 Padova, Italy

Abstract. The bacterial activity of *Lactococcus lactis* is exploited in the dairy industry for the fermentation of milk. However, the spreading of phages of *L. lactis* prevents the proper lactic fermentation, causing economic losses and waste. This work aims to explore an electrochemical detection method for the fast and reliable monitoring of the presence of the *L. lactis* phages. The detection is based on electrochemical biosensor with live *L. lactis* bacteria covering the sensor electrodes, whose electrical response is measured by electrochemical impedance spectroscopy (EIS). Solutions contaminated by phages induce bacteria lysis, clearly reducing the bacteria coverage over the electrodes and leading to evident parametrical shifts in the charge transfer resistance. Screen-printed and interdigitated sensors were tested to identify the most stable electrode suitable to work with the lab solutions. Experimental measurements with laboratory contaminated ideal samples show that the screen-printed sensors with gold and silver electrodes have great stability, reproducibility, and detection capability. Electrochemical results evidence great decreases of the charge transfer resistance in phages contaminated sensors in lab environments, paving the basis for the development of a new electrochemical biosensor capable of detecting the *L. lactis* phages.

Keywords: Electrochemical biosensor · Phage · *Lactococcus lactis* · Electrochemical impedance spectroscopy · Charge transfer resistance

1 Introduction

The rapid and accurate detection of pathogens in the food industry is of great interest to prevent the spreading of the contamination with consequent food waste and/or low-quality products on the market [1]. In particular, the dairy industry requires a continuous monitoring of the presence of dangerous pathogens along the production chain. *Lactococcus lactis* is a lactic acid bacterium directly involved in the milk fermentation process. Hence, the proliferation of the *L. lactis* bacteriophages in the milk lots is one of the major concerns for the dairy sector since their presence prevents the proper lactic fermentation, thus leading to inevitable waste of the contaminated products and to economic losses. The conventional methods used to detect foodborne pathogens are often

time consuming and expensive, as they require trained personnel and the use of micro-biological laboratories [2]. Instead, electrochemical biosensors offer a fast and cheap pathogen detection, allowing to rapidly isolate the contaminated lots and proceed with sanitation protocols [3]. In the last years, different electrochemical biosensing methods have been proposed for dairy industry applications, such as the monitoring of the presence of lactate in milk [4] and the quantification of antibiotic in milk [5, 6]. Usually, the phages have been typically applied as recognition element [7, 8], but only few works have explored biosensing approaches for the detection of the phages [9, 10].

In this work, we proposed an electrochemical detection method suitable for monitoring the *L. lactis* phages through electrochemical impedance spectroscopy (EIS) measurements. The most stable electrode configuration was selected and successfully tested with ideal laboratory solutions, exploiting a layer of bacteria deposited at the electrode surface as sensing element. When phages are present the bacteria undergo lysis, hence lowering the electrode coverage and leading to electrical shifts of the charge transfer resistance. Altogether, our results provided a solid starting point for a novel cost-effective approach for the bacteriophages detection with great sensitivity and timely response for the agri-food sector, as the method is also promising for the detection of other types of phages.

2 Materials and Methods

2.1 Chemicals and Biological Elements

In all the experiments, the chemicals were of analytical grade. The water was filtered and de-ionized to ultrapure Milli-Q water. The M17 broth, purchased from HiMedia Laboratories, was used as culture medium for the *Lactococcus lactis* dissolved in MilliQ water. Phages were stored in a specific phage buffer prepared with 100 mM NaCl, 8 mM $MgSO_4$, and 50 mM Tris-HCl at pH 7.5. The *L. lactis* growth was evaluated by measuring the optical density (OD) of solutions placed in proper cuvettes through the spectrophotometer ONDA, model UV-30 SCAN, at 30 °C at the wavelength of 600 nm, corresponding to the absorbance peak of the *L. lactis* bacteria. The redox couple $Fe(CN)_6^{3-}/Fe(CN)_6^{4-}$, for brevity FeCN, composed by potassium hexacyanoferrate III ($K_3[Fe(CN)_6]$) and potassium hexacyanoferrate II ($K_4[Fe(CN)_6]$) trihydrate, was prepared at 10 mM by dissolving the potassium hexacyanoferrate III and potassium hexacyanoferrate II directly in the M17 broth.

2.2 Devices and Test Conditions

The selected biosensors for the tests were based respectively on screen-printed electrodes (DPRC223AT) and interdigitated electrodes (PW-IDEAU100) by Metrohm DropSens (Spain). The DRP electrodes were screen-printed on a ceramic substrate (34 × 10 × 0.5 mm), with a conventional three-electrode configuration based on working, counter, and reference electrodes. The working electrode disk has a diameter of 1.6 mm. The working and counter electrodes were made of gold, and the pseudo-reference electrode

was made of silver. Meanwhile, the INTD electrodes were produced on a transparent flexible plastic substrate (22.8 × 7 × 0.175 mm), with a two-electrode configuration made of gold with a finger width and an interdigit gap of 100 µm. An external Ag/AgCl electrode was used as reference. A hermetic customized 3D-printed cell was used as electrochemical cell to remove problems related to solution contamination and evaporation.

The biosensors were electrically characterized by using the Electrochemical Impedance Spectroscopy (EIS). The redox standard potential E_0 with a solution 10 mM FeCN in M17 was obtained through preliminary Cyclic Voltammetry (CV) measurements. The EIS measurements were performed using a two-electrodes configuration in a frequency range between 1 Hz and 100 kHz. The peak-to-peak amplitude of the ac signal was 0.01 V, while the dc bias was deduced from the preliminary CV measurements as $V_{DC} = 0.091$ V for the DRP electrodes and $V_{DC} = 0.05$ V for the INTD electrodes. The EIS responses were fitted through the equivalent electric circuit based on a modified Randles' cell, substituting the Warburg element with a constant phase element.

3   Experimental Results and Discussion

3.1   Electrodes Stability and Device-to-Device Variability

To identify the most suitable electrodes for the application, we tested the stability and the reproducibility of the screen-printed electrodes (DRP) and the interdigitated electrodes (INTD). Firstly, we evaluated the influence of the cleaning procedure, performed by rinsing the surface with MilliQ water and drying at room temperature. These tests highlighted the superior stability of DRP sensors, for the limited effects produced by subsequent rinses, with respect to INTD electrodes.

We also studied the time-stability and the device-to-device variability of the electrodes by performing EIS measurements with 10 mM FeCN in M17 solution every 30 min, following the complete evolution of the R_{ct} values over a period of 150 min. Both cases present a gradual shift in time – DRP R_{ct} increases of 20% while INTD decreases of 47% after 150 min. However, the sensor-to-sensor variation, represented by the 1σ standard deviation, suggests that the DRP electrodes have a much better device-to-device variability when the time-stability is considered (Fig. 1a). Instead, the INTD electrodes (Fig. 1b) present a variability higher than one order of magnitude with respect to DRPs, which may be attributed to random working area shifts during the hand-assembly of the electrochemical cells.

Overall, the DRP electrodes proved to have a high stability and device-to-device repeatability, while the INTDs evidence more variability in the responses.

3.2   Detection of Bacterial Growth

In this section, we present the experimental results for the growth detection of the *L. lactis*. The bacterial solutions were prepared by adding 1200 µL of *L. lactis* to 3000 µL of 20 mM FeCN in M17, and to 1800 µL of M17 to obtain a 10 mM FeCN in M17 solution with *L. lactis* (LL). The negative control solutions (NC) were prepared using 3000 µL
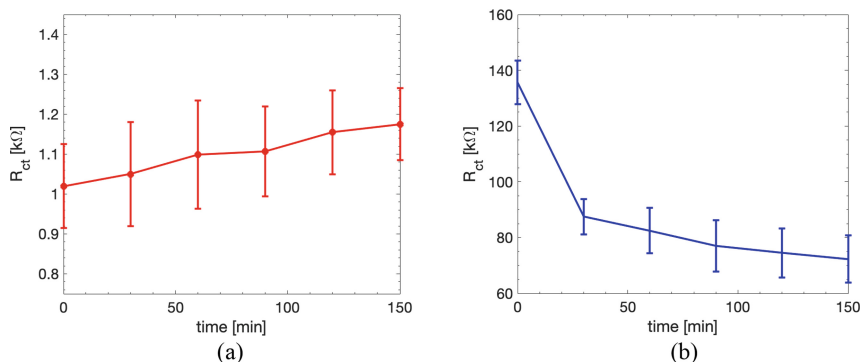
Fig. 1. The R_{ct} values retrieved from the EIS responses with 10 mM of FeCN as a function of the time for (a) the DRP electrodes and (b) the INTD electrodes.

of 20 mM FeCN in M17 and 3000 µL of M17. We studied the EIS response in presence of *L. lactis* over an observation period of 150 min, following the bacterial growth every 30 min, on both DRP and INTD sensors to identify the best configuration. After each measurement, the sensors were rinsed in MilliQ and a new solution drop of 90 mL was deposited to avoid the bacteria death due to lack of nourishment in the lower deposition layers on the surface. A waiting time of 15 min was required to allow the precipitation of the bacteria in solution on the electrode surface before each measurement.

Figure 2 reports the EIS response of the sensors for NC and for LL at the time 0 min, 90 min and 150 min for DRP and INTD electrodes. The starting time of the experiment is considered from the first performed measurement, without the previous 15-min stabilization time. For DRP sensors, the Nyquist diagram of Fig. 2(a) shows an evident variation of EIS curves at 150 min for *L. lactis*, while the NC curves are practically stable along all the observation time. Instead, the results for INTD electrodes (Fig. 2b) shows a high decrease of R_{ct} after the first measurement, but almost no differences among the EIS signals of NC and LL over time. Considering these results, we chose to select the DRP sensors for this application, as they grant an effective detection of the bacterial presence and proliferation on the electrode.

3.3 Phage Detection in Ideal Solution

The bacteriophages were stored at −20 °C in the phage buffer, whose composition was described in Sect. 2.1. Contaminated solutions were prepared with the phage solution at a phage concentration of 10^7 PFU/mL. The solution of *L. lactis* contaminated by the phages was obtained by adding 480 µL of bacteriophages in phage buffer to 1200 µL of *L. lactis*, to 3000 µL of 20 mM FeCN in M17, and to 1320 µL of M17.

Figure 3a shows the absorbance measurement of DRP sensors prepared with the *L. lactis* alone (LL) and with solution of *L. lactis* contaminated by the phages (PG). Up until 120 min, the LL and PG curves nicely overlap each other since the bacteria are growing in both the solutions. Yet, if the test time further increases, a more evident shift appears between the curves reaching a final difference of 0.25 at 270 min, meaning that the phages in PG started their lytic activity which decreases the number of bacteria
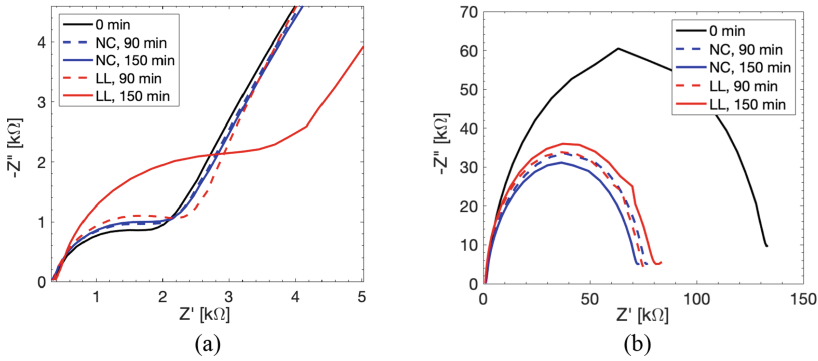
Fig. 2. (a), (b) The Nyquist diagram of the EIS responses obtained with 10 mM FeCN in M17 solution without (NC) and with (LL) *L. lactis* for the DRP and INTD electrodes, respectively.

cells with respect to LL. The differences between PG and LL sensors appear also when considering the R_{ct} value over time (Fig. 3b). The curves are similar for the LL and PG sensors at the beginning and at intermediate times. At 270 min, the LL curve increases to 2.2 kΩ, while the PG value reaches 1.65 kΩ. This difference is consistent with the absorbance results, and it is due the phages presence which reduces the electrode surface bacterial coverage, decreasing the R_{ct} value over time.
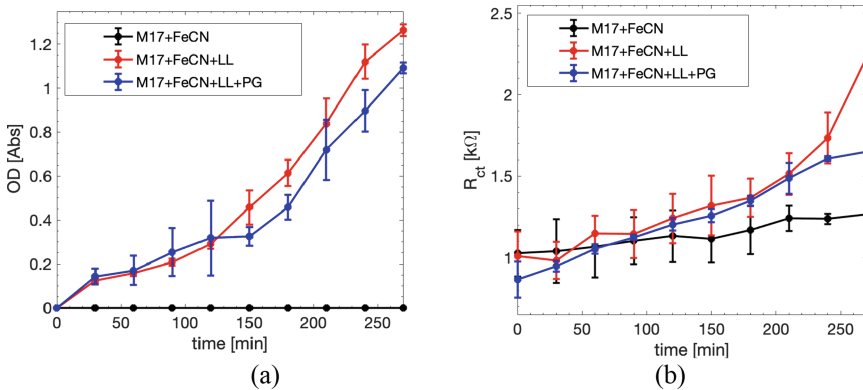
Fig. 3. Test of the LL and PG solutions in ideal laboratory conditions. (a) Optical absorbance as a function of the time. (b) Charge transfer resistance R_{ct} extrapolated by the EIS measurements.

Hence, the detection principle is based on a differential measurement. By looking at the electrochemical signal of a non-contaminated reference solution, the test solution is evaluated through comparison. The significantly lower shift of the electrical parameters than the reference solution leads to detect and quantify the presence of bacteriophages in the sample. The different behavior of the LL and PG curves allows to distinguish a contaminated ideal solution from a phage-free ideal sample, effectively detecting the phages presence in less than 5 h from the phage inoculation time.

4 Conclusions

In this work, we have electrochemically tested two different electrodes configurations in ideal solutions to propose a new electrochemical biosensor capable of detecting the *L. lactis* bacteriophages. The interdigitated sensors showed an acceptable stability over time, but the experimental measurements evidenced a high device-to-device variation and a low sensitivity to the bacterial growth on the electrode surface. Meanwhile, the screen-printed electrodes presented a high time-stability and a low device-to-device variation, guaranteeing highly repeatable and stable measurements. The bacterial growth on the electrode surface showed evident increases of charge transfer resistance. On the other hand, the phages infection inhibited the bacterial growth, leading to significantly lower shifts of the electrical parameters. The biosensor was tested in ideal solutions for a contamination of 10^7 PFU/mL of phages yielding promising results in less than 5 h. Future work will aim to increase the detection sensitivity and to validate the method with more complex non-ideal solutions and with milk solutions, and studying its application to other types of phages.

References

1. Garneau, J., et al.: Bacteriophages of lactic acid bacteria and their impact on milk fermentations. Microb. Cell. Fact. **10**(1), S20 (2011)
2. Del Rio, B., et al.: Multiplex PCR for the detection and identification of dairy bacteriophages in milk. Food Microbiol. **24**(1), 75–81 (2007)
3. Kalyani, N., et al.: On-site sensing of pesticides using point-of-care biosensors: a review. Environ. Chem. Lett. **19**, 345–354 (2021)
4. Rathee, K., et al.: Biosensors based on electrochemical lactate detection: a comprehensive review. Biochem. Biophys. Rep. **5**, 35–54 (2016)
5. Rosati, G., et al.: Silver nanoparticles inkjet-printed flexible biosensor for rapid label-free antibiotic detection in milk. Sens. Actuat. B Chem. **280**, 280–289 (2019)
6. Rinken, T., et al.: Determination of antibiotic residues and their interaction in milk with lactate biosensor. J. Biochem. Biophys. Methods **66**(1–3), 13–21 (2006)
7. García-Anaya, M.C., et al.: Phages as biocontrol agents in dairy products. Trends Food Sci. Technol. **95**, 10–20 (2020)
8. Chai, Y., et al.: Rapid and Sensitive Detection of Salmonella Typhimurium on Eggshells by Using Wireless Biosensors. J. Food Prot. **75**(4), 631–636 (2012)
9. Garcìa-Aljaro, C., et al.: On-chip impedimetric detection of bacteriophages in dairy samples. Biosens. Bioelectron. **24**(6), 1712–1716 (2009)
10. Rosati, G., et al.: A plug, print & play inkjet printing and impedance-based biosensing technology operating through a smartphone for clinical diagnostics. Biosens. Bioelectron. **196**, 113737 (2022)

Modular IoT Unit to Monitor Water Distribution with an Impedance Leak Sensor

Christian Riboldi, Daniele M. Crafa, and Marco Carminati[✉]

Dipartimento di Elettronica, Informazione e Bioingegneria, Politecnico di Milano, Milano, Italy
`marco1.carminati@polimi.it`

Abstract. We present an electronic IoT system leveraging non-intrusive sensors able to measure water flow rate (with ultrasonic transducers) and detect leaks in distribution pipelines (with electrodes measuring soil impedance). Underground units can communicate with a central node (powered by a battery and a solar panel on the surface with the radio antenna) by means of the same four sensing electrodes as demonstrated here. Low dissipation (below 1 mWh) is achieved. The electronic design and validation of a demonstrator are here reported.

Keywords: Water leakage · Wireless sensors networks · Low-power · Impedance detection · Ultrasonic flow meter

1 Introduction

Water is a fundamental resource for mankind and its optimized handling is a priority for a sustainable society. One of the major problems affecting water distribution networks is water leakage (on average at 40% in Italy). We have proposed [1] an approach based on the measurement of impedance between couples of band electrodes applied along the pipe to detect water leaks that alter the humidity of the terrain around the underground pipe.

In this work we present a complete electronic network composed of a surface part (with a wireless connection of the main node to a gateway through LoRaWAN) and an underground part composed of remote nodes connected to the central unit by means of the metal electrodes running on the pipe, serving for both sensing, power and data transmission. In this way, the number of nodes requiring access to the surface (for solar panel, antenna and for replacement of the battery or sensors, such as electrochemical ones requiring periodic maintenance) is reduced. In addition to leak monitoring, flow rate, pressure and temperature of water are measured by the central unit in this demonstrator. However, different parameters (such as pH, conductivity and solid deposits fouling the inner pipe surface could be measured as well [2]).

The two main sensor types here validated - impedance electrodes and clamp-on ultrasonic transducers - are contactless and do not require drilling of the pipe. Thus, they preserve its integrity (and max. pressure rating) and pave the way to retrofitting old pipelines, that are already installed, by simply attaching the sensors where needed.

2 Circuit Design and Realization

2.1 Central Unit

The block diagram in Fig. 1 describes the central unit architecture. It is powered by 6 V–1.3 Ah seal lead acid (SLA) battery which is charged by a compact solar panel through a custom circuit. The measurement of flow rate is carried out by a couple of time-of-flight (TOF) clamp-on flow meters, whose working principle is based on the fact that when an ultrasonic pulse propagates through the flowing medium, its travel time will vary with the fluid velocity. The Ultrasonic Flow Converter (UFC) used to perform the flow measurement is an AS6040 which contains a 22 ps resolution Time to Digital Converter (TDC) and a 18 V programmable charge pump to correctly drive the piezoelectric clamp-on transducer (resonating at 1 MHz). Each transducer can work both in transmission and reception. When the switches of the respective transducer are open, a buffer fed through a charge pump allows to correctly drive the transducer. During the receive phase, the switches are closed and a programmable gain amplifier (PGA) amplifies the signal generated by the piezoelectric transducer by direct piezoelectric effect. A zero-cross detector generates the trigger signal that stops the TDC. The same chip allows to measure water temperature by exploiting the TDC to measure the discharge time of a capacitor on a PT1000 sensor. The temperature measurement cold also be obtained by estimating the speed of sound in the water using the TOF values. Pressure is acquired through a transducer with non-ratiometric voltage output. A 433 MHz LoRa module sends the data collected by the sensors to a gateway that is connected to a LoRaWAN Network Server which provides one output to an online dashboard and one via WebSocket protocol. An ultra-low-power RS485 transceiver is used to communicate with the remote unit containing the circuitry for leak detection. All components have been chosen with the same power supply voltage in order to use a single very efficient buck converter with a low quiescent current. A Python application has been developed in order to exchange data between the PC and the unit through USB interface or by entering the access token to establish the Web-Soket connection with the LoRaWAN server.

2.2 Sensing Unit

The sensing unit is divided in three different electronic boards (Fig. 2) which have been implemented on four PCBs in order to minimize the overall circuit area. The Lock-In board performs the impedance measurement with an analog scheme. The Lock-In chain is composed of a first stage based on a DDS generating a sinusoidal current signal with programmable frequency and amplitude. This signal is then converted into a voltage signal, amplified, and band-pass filtered (to remove the spurious harmonics) by means of a fifth order active filter. At this point, the obtained signal reaches two parallel branches: the first one consists of the impedance conversion stage into a voltage signal with an
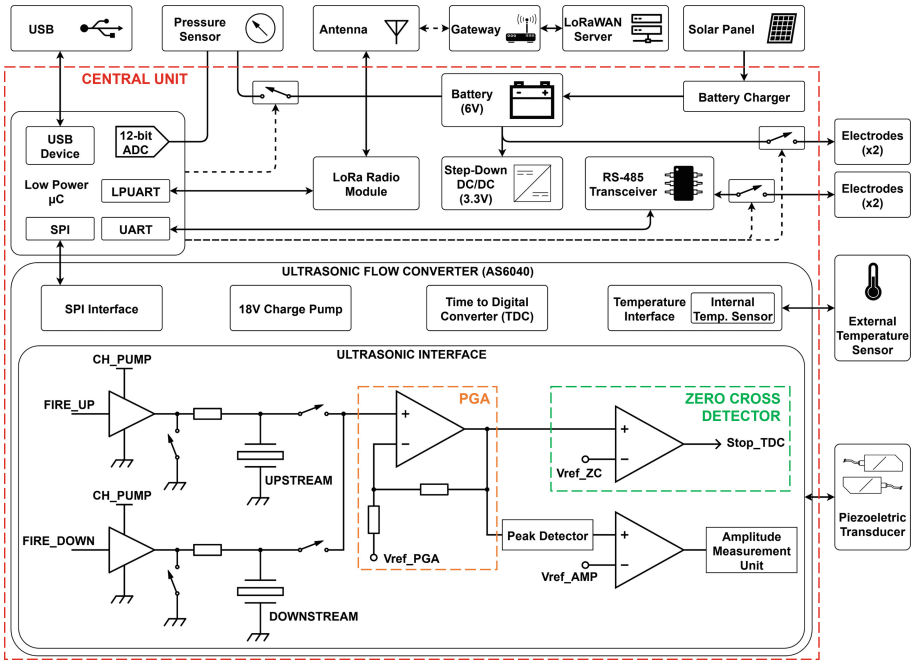
Fig. 1. Central unit block diagram featuring off-the-shelf discrete components.

amplitude function of the electrodes impedance, while the second one corresponds to the rephasing stage which generates the reference signal for the analog multiplication. Then, the obtained signals reach an analog multiplier (AD835 by Analog Devices), downstream of which a conditioning stage which depends on the impedance of the electrodes. At the same time, it adapts this voltage to the input FSR of the microcontroller ADC. The control board manages the entire sensing unit by means of a microcontroller of the Ultra-Low-Power family STM32L4 by ST Microelectronics, which has an internal 12-bit ADC used to digitize the output voltage of the Lock-In board. This board also presents the transceiver used for communication with the central unit and the circuit controlling the power supply of the Lock-In board (which has been implemented by means of bistable relays to reduce static dissipation). The power supply board generates the voltages needed by the electronic. During the measurement phase, the sensing unit is powered by two supercapacitors connected in series providing a dual supply voltage, which are re-charged during the low-power mode of the sensor (when no measurement is per-formed) by means of a BJT based circuit connected to the central unit battery. In this way the electrodes can only be connected to the Lock-In board during the measurement, preventing the load impedance from affecting the measurements.
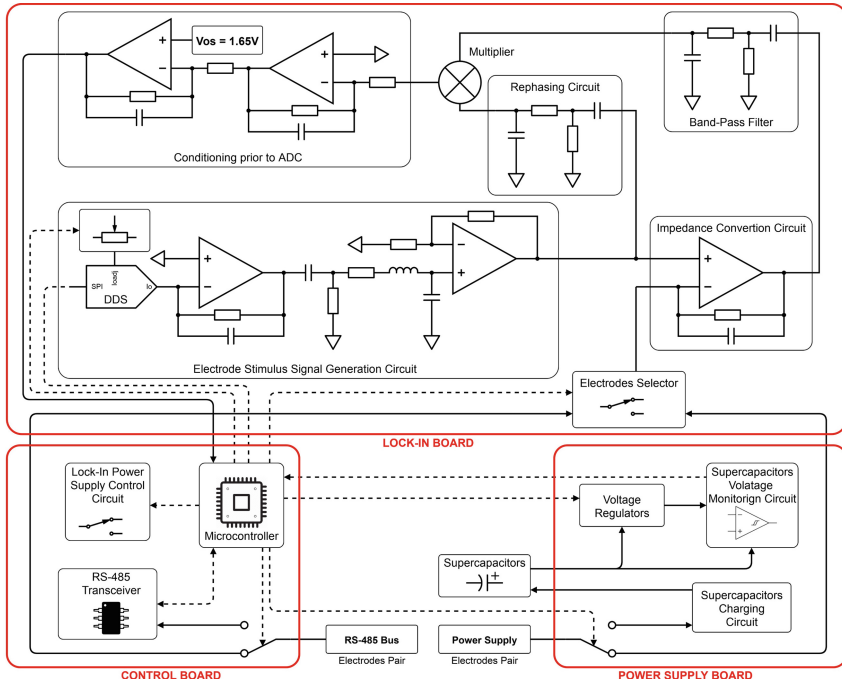
Fig. 2. Architecture of remote unit containing the impedance leakage sensor.

3 Experimental Results

3.1 Central Unit

A hydraulic circuit for laboratory tests and validation of the units was built with PVC pipes (of 90 m diameter), a valve, and a 60 l tank containing an immersion pump that generates an estimated maximum flow rate of 22 m/h. In sleep mode the battery cur-rent absorbed by the central unit is 30 μA, while during the measurement it is ~1 mA. By acquiring and transmitting measurements from each transducer every hour, the average power consumption is 340.8 μWh. In order to validate the results of the flow meter, a comparison was made with the commercial RIELS RIF600P using the same transducers and performing the same measurement cycle. The results show that the performance is very similar, but it is possible to notice that, when the pump is off, the RIF600Pa cross-correlation algorithm to obtain the TOF difference. This problem does not occur in the Zero Crossing Detection method used by the AS6040 however, it has been experimentally verified that it is necessary to perform the average on at least 40 time-of-flight samples in order to recognize a Gaussian distribution in TOF values and obtain a stable flow rate measurement. The AS6040 integrates an amplitude measurement unit (Fig. 1) which in this case is used by an algorithm to detect air bubbles and to correctly adjust the gain of suffers of an error known as Zero Flow Error. This is likely due to the use of a cross-correlation algorithm to obtain the TOF difference. This problem does not occur in the Zero Crossing Detection method used by the AS6040 however, it has been

experimentally verified that it is necessary to perform the average on at least 40 time-of-flight samples in order to recognize a Gaussian distribution in TOF values and obtain a stable flow rate measurement. The AS6040 integrates an amplitude measurement unit (Fig. 1) which in this case is used by an algorithm to detect air bubbles and to correctly adjust the gain of the PGA in order to obtain an amplitude signal from 200 mV to 400 mV (Fig. 3).
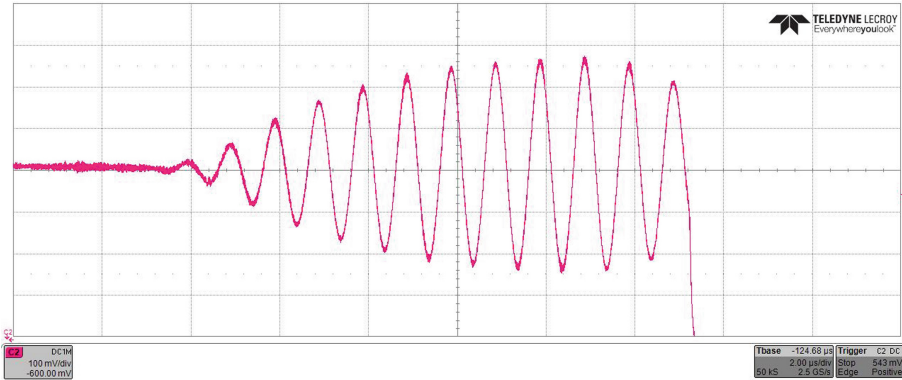
Fig. 3. Oscilloscope acquisition (100 mV/div vertical scale and 2 μs/div horizontal one) of the PGA (gain = 5) output signal during the receive phase at the maximum flow rate.

3.2 Sensing Unit

In order to validate the results of the Lock-In amplifier some known pure resistive reference impedances were measured at various frequencies and with a quite large stimulation signal for the electrodes (in order to increase the SNR of the signal). The obtained measurements are shown in Fig. 4, where it is possible to notice that the Lock-In amplifier cannot perform measurements using stimulation signal at frequency larger than 4 MHz. However, the resulting accuracy is quite good with just 5.3% of relative error on the absolute value of the measured impedance, while the standard deviation of the measure is excellent (in fact the error bars are not even visible in the graph) with just 0.02% considering a 50.1 Ω test resistor. These results were achieved by implementing the over-sampling acquisition technique for the microcontroller ADC, which allows to improve a lot the SNR of the samples by removing the noise affecting the Lock-In amplifier output. The power consumption of the sensor during a measurement is also small. In fact, even if the current absorbed from the two superca-pacitors (shown in Fig. 5) results to be large (about 35 mA from the negative supply I_{-VC}, and roughly 45 mA from the positive supply I_{+VC}), the measurement lasts only 5.5 s thus leading to a total energy (obtained by integrating the current curve over the measurement time) of 982.79 μWh for each measurement. Then, considering to perform a leakage test every 12 h, the daily energy consumption due to the measurements is about 1.97 mWh/day. When the leakage sensor does not perform any measurement, it enters a low-power operating mode, during which only the microcontroller is turned on. In this operating mode the overall

current absorbed from the two supercapacitors is about 1.5 mA, therefore the overall daily energy consumption considering this mode lasts for almost 24 h a day (since the measurement duration is only 5.5 s) is roughly 603.97 mWh/day. Hence the leakage sensor is not as low-power as the central unit, but this energy can be provided by a notebook-sized solar panel.
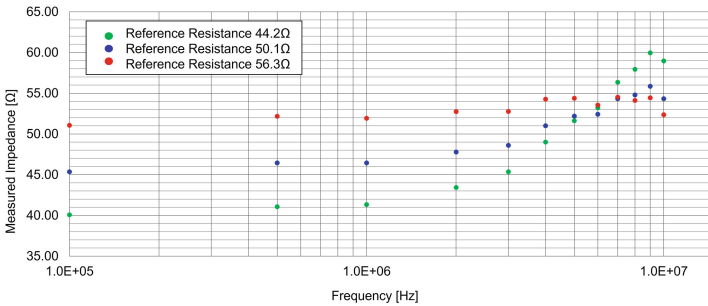
Fig. 4. Impedance measurements performed during the leak sensor test.
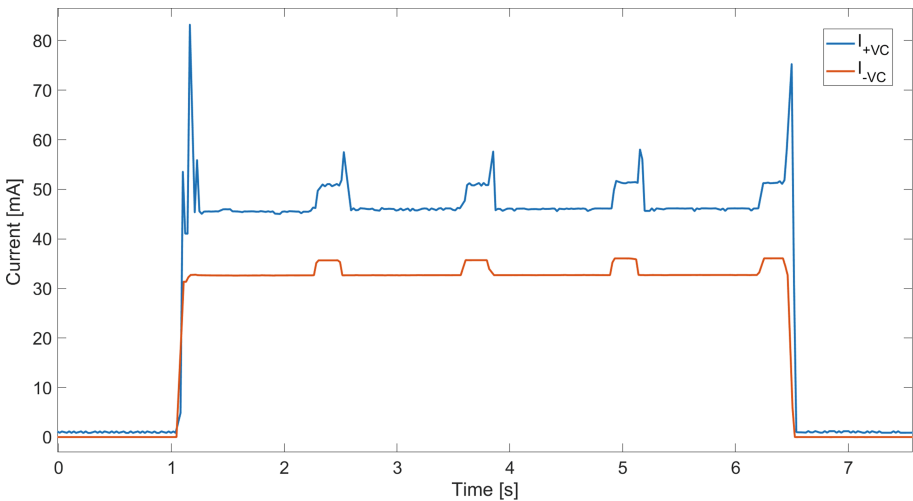
Fig. 5. Recording of the remote unit current absorption during an acquisition of 4 impedance measurements across four electrode couples lasting 5.5 s.

4   Conclusions

We have presented an energy autonomous electronic unit able to communicate with other nodes by means of longitudinal conductors (at least 4) applied on the pipe to detect small (~1 L) water leaks. Simulations have shown that the maximum length of a sensing segment is ~ 10 m, since the relative impedance change decreases by increasing the

electrodes length. We envision that such a system could be installed with a density of about 1 unit/km (mostly set by the radio range and budget constraints) thus monitoring segments of $\pm$ 10 m of pipe in the most critical points of the water distribution network. Specific sensors (of water quality and quantity) can be installed depending on the network topology and condition. Anyway, thanks to its low-power design (100 times better than [2]), the battery and the solar panel are very compact (few cm^2, as the boards) thus minimizing the unit bulkiness.

References

1. D'Adda, I., Battaglin, G., Carminati, M.: Low-cost flexible pipe sheath for multi-parameter monitoring of water distribution. In: Proceeding of IEEE ISCAS (2021)
2. Carminati, M., et al.: A self-powered wireless water quality sensing network enabling smart monitoring of biological and chemical stability in supply systems. Sensors 1125 (2020)

AuNP-Coated Cotton as VOC Sensor for Disease Detection from Breath

Silvia Casalinuovo[1(✉)] , Alessio Buzzin[1] , Daniela Caschera[2] ,
Simone Quaranta[2] , Fulvio Federici[2] , Laura Zortea[3] , Andrea Brotzu[3] ,
Stefano Natali[3] , Donatella Puglisi[4] , Giampiero de Cesare[1] ,
and Domenico Caputo[1]

[1] Department of Information Engineering, Electronics and Telecommunications,
Sapienza University of Rome, Rome, Italy
`silvia.casalinuovo@uniroma1.it`

[2] Institute for the Study of Nanostructured Materials (ISMN), National Research Council,
Rome, Italy

[3] Department of Chemical Engineering, Materials and Environment,
Sapienza University of Rome, Rome, Italy

[4] Department of Physics, Chemistry and Biology (IFM), Linköping University, Linköping,
Sweden

Abstract. The COVID-19 pandemic outbreak, declared in March 2020, has led to several behavioral changes in the general population, such as social distancing and mask usage among others. Furthermore, the sanitary emergency has stressed health system weaknesses in terms of disease prevention, diagnosis, and cure. Thus, smart technologies allowing for early and quick detection of diseases are called for. In this framework, the development of point-of-care devices can provide new solutions for sanitary emergencies management. This work focuses on the development of useful tools for early disease diagnosis based on nanomaterials on cotton substrates, to obtain a low-cost and easy-to-use detector of breath volatiles as disease markers. Specifically, we report encouraging experimental results concerning acetone detection through impedance measurements. Such findings can pave the way to the implementation of VOCs (Volatile Organic Compounds) sensors into smart and user friendly diagnostic devices.

Keywords: Gold nanoparticle (AuNP) · Acetone · Volatile Organic Compound (VOC) · Cotton · Impedance sensor

1 Introduction

According to WHO Director-General, Dr. Tedros Adhanom Ghebreyesus, "All countries should pay particular attention to diagnostics, to promote better health, keep their populations safe, and serve the vulnerable". Hence, investments in point of care (POC) devices are intended to play a strategic role for improving health care protocols [1]. Particularly, new diagnostic and therapeutic approaches are required in order to address the Pandora's box effect brought about by the SARS CoV-2 virus [2–4]. Since diagnosis

usually relies on several time-consuming steps (symptom manifestation, observation, and medical testing), revealing health conditions through a quick method based on a quantitative/qualitative detection of volatile organic compounds (VOCs) is an intriguing challenge [5]. Currently, mass spectrometry/gas chromatography (MS/GC) is the benchmark technique for VOCs identification. However, it presents drawbacks such as high costs, time/energy consumption and the need for skilled professionals [6]. Conversely, sensor-based techniques, being highly sensitive, low cost and easy-to-use in compact systems [7], have a great potential in early diagnosis of diseases [8]. Here, we propose a nanomaterial-based chemoresistive sensor as a promising alternative to traditional diagnostic tools.

2   AuNP-Coated Cotton as VOC Detector

Among the wide range of substrates suitable for sensor integration, cotton fabric possesses numerous advantages over other state-of-the-art solutions. Indeed, cotton is flexible, inexpensive and more eco-friendly with respect to silicon and/or plastic chips [9]. To obtain a chemoresistive system, capable of changing its electrical resistance when exposed to the target analytes (and proportionally to analyte's amount), two metal electrodes were considered, in a sandwich configuration, and gold nanoparticles (AuNPs) were studied as VOC-sensible element. The use of AuNP is justified by their well-known ability to promote fast response and recovery times, parts per billion (ppb) detection limits and the usage on both rigid and flexible materials [10].

2.1   Target: VOCs

VOCs are chemicals originating from cellular metabolic activity and are able to diffuse into different body fluids due to their small size and volatility [5]. Therefore, VOCs are considered as informative biomarkers reflecting any changes stemming from a pathophysiological state (cancer, renal/intestinal/neurological diseases, diabetes) [11]. Recent studies have identified a total of 1764 VOCs with the following distribution: 34% in breath, 20% in skin, 15% in feces, 14% in saliva, 11% in urine, 6% in blood [12]. The present research work focuses on breathborne VOCs. Among many chemical substances, our interest has been focusing on acetone as one of the most widely used and non-toxic. Moreover, as it originates from decarboxylation of acetoacetate and oxidation of isopropanol [13], it can be considered as an indicator of various diseases (diabetic, lung cancer, liver disease, heart failure) [14, 15].

2.2   Materials and Methods

Figure 1a shows the synthesis/deposition steps involved in the sensor fabrication. AuNPs were synthesized from a polyvinylpyrrolidone (PVP) aqueous solution (1) [16]. PVP served as both surfactant/reducing agent. Tetrachloroauric acid ($HAuCl_4$) was added as gold precursor (2) obtaining a violet solution after 20 min of magnetic stirring. Subsequently, AuNPs were deposited by dipping a (2.5·5) cm^2 cotton sample into the gold nanoparticle solution (3). The result is depicted in Fig. 1.
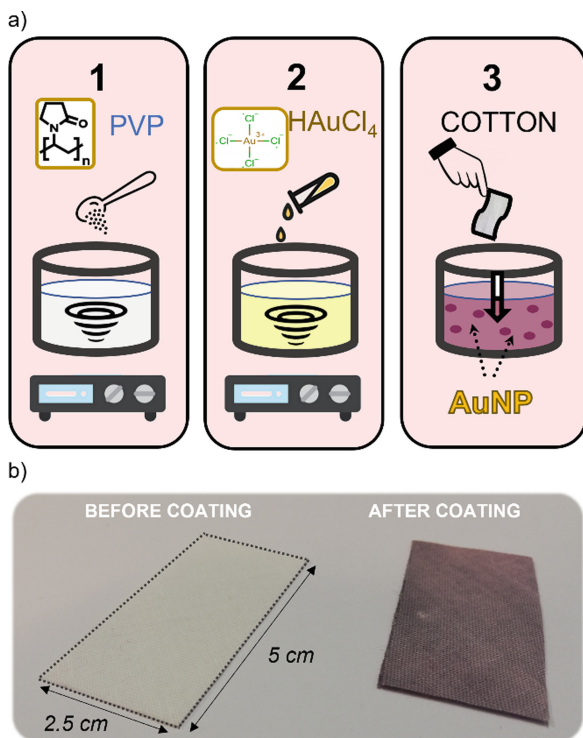
Fig. 1. (a) Illustration of AuNP synthesis/deposition steps (1, 2, 3) to obtain a AuNP-coated cotton sample. (b) Picture of two cotton samples, before (left) and after (right) AuNP coating.

2.3 Results and Discussion

Optical and electrical characterizations were carried out to confirm the correct process flow for the sensor fabrication, to demonstrate the AuNPs transfer on the cotton surface and to acknowledge their VOC detection capabilities. Figure 2 reports three optical absorbance tests for pristine cotton, AuNP-coated cotton and AuNP solution, carried out in the visible spectrum using a V-660 Jasco UV spectrophotometer. The AuNP solution shows an absorption peak centered at about 550 nm and corresponding to an estimated gold nanoparticles average size of approximately 20 nm [17]. A similar peak, only slightly shifted from the original position, was observed for the AuNP-coated cotton. In the case of pristine cotton, no peaks were present, demonstrating that AuNPs were successfully transferred, without evident agglomeration, from the solution to the sample through the dipping process.
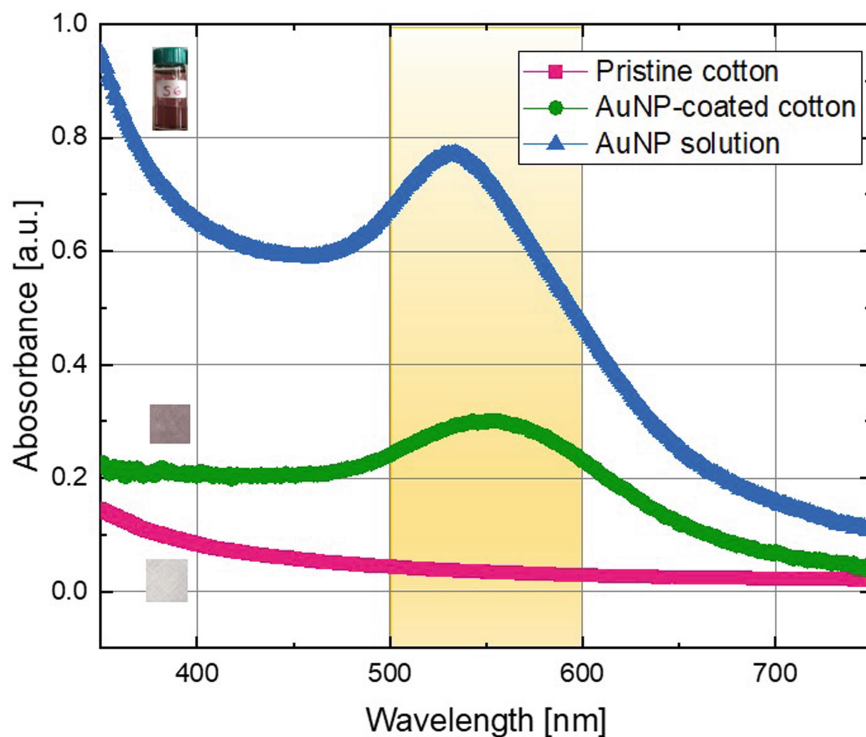
Fig. 2. Optical characterization in the UV-visible range of pristine cotton, AuNP-coated cotton and AuNP solution.

AuNP-functionalized cotton was electrically characterized by impedance spectroscopy (EIS) in the 1 Hz–1 MHz frequency range by means of a combined potentiostat/galvanostat/ZRA by Gamry (Reference 3000). In the reported test, a 40% acetone solution diluted in deionized water was sprayed over the sample to evaluate VOC impact on its complex (resistance and reactance) electrical properties. The cotton sample was connected to the measuring equipment using crocodile cables on two metal electrodes, in a two-electrode/sandwich configuration (see Fig. 3a). Two (5·5) cm^2 glass slides secured the sample in place and in contact with the electrodes. The entire setup was put in a Faraday cage to avoid electromagnetic interferences. Preliminary results are reported in Fig. 3b. As the inset shows, a resistance variation of about two orders of magnitude (from 10^8 Ω to 10^6 Ω) was observed after spraying acetone on the sample in the whole investigated frequency range. The changes in both impedance's real and imaginary parts can be ascribed to gold nanoparticles capability of absorbing organic molecules (i.e. acetone) on their surface, hence leading to a relevant change in the electrical features of the system.
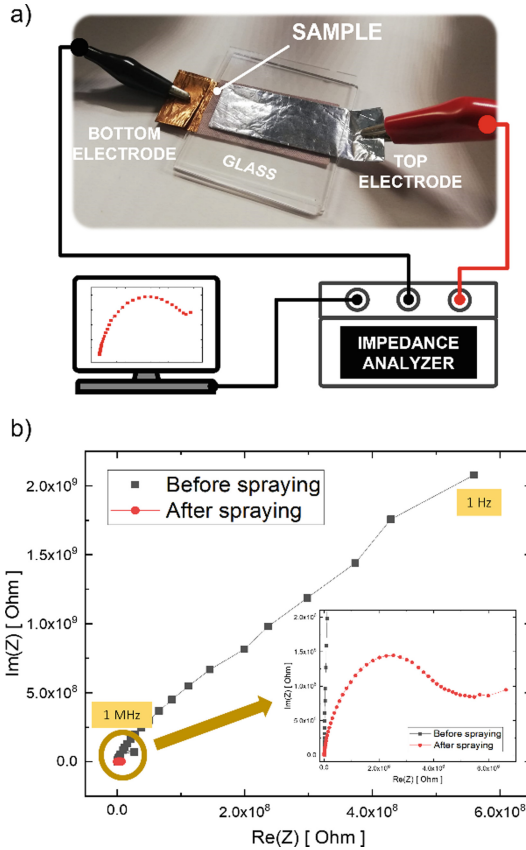
Fig. 3. (a) Experimental EIS setup for analyzing AuNP-coated cotton as acetone detector in the 1 Hz–1 MHz frequency range. (b) Nyquist plot of the AuNP-coated cotton sample before and after spraying a 40% acetone solution.

3   Conclusions

This work presents preliminary results on a new concept of health-wise VOC sensors applied on AuNP-functionalized cotton fabric. Specifically, gold nanoparticles were synthesized by taking advantage of PVP as reductant and surfactant agent and were transferred on a cotton substrate by dip-coating. Electrical measurements pointed out a remarkable (two-order of magnitude) sensor impedance variation due to acetone adsorption. Our preliminary results encourage other sets of measurements to assure the repeatability, stability and reusability of the proposed sensor. Surely, the next step foresees the design of a miniaturized electronic circuit for impedance analysis, the identification of a list of volatiles useful for a certain disease diagnosis, and further investigation for the functionalization of the AuNP for a selective probe detection. Our study can be seen as a response to the healthcare system's demand to urgently invest in new, cheaper and more effective point-of-care devices.

References

1. WHO publishes new Essential Diagnostics List and urges countries to prioritize investments in testing (2021). https://www.who.int/news/item/29-01-2021-who-publishes-new-essential-diagnostics-list-and-urges-countries-to-prioritize-investments-in-testing

2. Basu, S., et al.: Impact of lockdown due to COVID-19 outbreak: lifestyle changes and public health concerns in India. Int. J. Indian Psychol. **8**(2), 1385–1411 (2020)

3. Buzzin, A., DomènechGil, G., Fraschetti, E., Giovine, E., Puglisi, D., Caputo, D.: Assessing the consequences of prolonged usage of disposable face masks. Sci. Rep. **12**, 16796 (2022). https://doi.org/10.1038/s41598-022-20692-9

4. Mbunge, E., Akinnuwesi, B., Fashoto, S.G., Metfula, A.S., Mashwama, P.: A critical review of emerging technologies for tackling COVID-19 pandemic. Human Behav. Emerg. Technol. **3**(1), 25–39 (2021)

5. Davis, C., Pleil, J., Beauchamp, J.: Breathborne Biomarkers and the Human Volatilome. 2nd edn. Elsevier, Amsterdam (2020)

6. Lubes, G., Goodarzi, M.: GC–MS based metabolomics used for the identification of cancer volatile organic compounds as biomarkers. J. Pharm. Biomed. Anal. **147**, 313–322 (2018)

7. Laschuk, N.O., et al.: Rational design of a material for rapid colorimetric Fe2+ detection. Mater. Des. **107**, 18–25 (2016)

8. Broza, Y.Y., Vishinkin, R., Barash, O., Nakhleh, M.K., Haick, H.: Synergy between nanomaterials and volatile organic compounds for non-invasive medical evaluation. Chem. Soc. Rev. **47**(13), 4781–4859 (2018)

9. Mukherjee, A., Rosenwaks, Y.: Recent advances in silicon FET devices for gas and volatile organic compound sensing. Chemosensors **9**(9), 260 (2021)

10. Nakhleh, M.K., Broza, Y.Y., Haick, H.: Monolayer-capped gold nanoparticles for disease detection from breath. Nanomedicine **9**(13), 1991–2002 (2014)

11. Das, S., Pal, S., Mitra, M.: Significance of exhaled breath test in clinical diagnosis: a special focus on the detection of diabetes mellitus. J. Med. Biol. Eng. **36**(5), 605–624 (2016)

12. Broza, Y.Y., Mochalski, P., Ruzsanyi, V., Amann, A., Haick, H.: Hybrid volatolomics and disease detection. Angew. Chem. Int. Ed. **54**(38), 11036–11048 (2015)

13. Ruzsányi, V., Kalapos, M.P.: Breath acetone as a potential marker in clinical practice. J. Breath Res. **11**(2), 024002 (2017)

14. MarcondesBraga, F.G., Batista, G.L., Bacal, F., Gutz, I.: Exhaled breath analysis in heart failure. Curr. Heart Fail. Rep. **13**(4), 166–171 (2016)

15. Van den Velde, S., Nevens, F., van Steenberghe, D., Quirynen, M.: GC–MS analysis of breath odor compounds in liver patients. J. Chromatogr. B **875**(2), 344–348 (2008)

16. Chan, K.L., Fawcett, D., Poinern, G.E.J.: Gold nanoparticle treated textile-based materials for potential use as wearable sensors. Int. J. Sci. **2**(05), 82–89 (2016)

17. Caschera, D., Federici, F., Zane, D., Focanti, F., Curulli, A., Padeletti, G.: Gold nanoparticles modified GC electrodes: electrochemical behaviour dependence of different neurotransmitters and molecules of biological interest on the particles size and shape. J. Nanopart. Res. **11**(8), 1925–1936 (2009)

Modelling and Design of an ISFET-Based NaCl Sensor for Cystic Fibrosis Diagnosis and Management

Annabella la Grasta, Martino De Carlo, Francesco Dell'Olio[(✉)], and Vittorio M. N. Passaro

Department of Electrical and Information Engineering, Polytechnic University of Bari, Bari, Italy
`francesco.dellolio@poliba.it`

Abstract. Ion-Sensitive Field-Effect Transistors (ISFETs) are widely used for detecting various target analytes in chemical and biological solutions. Although they have been mainly used for pH sensing, in this paper investigations of the device for NaCl sensing, with Hafnium Oxide (HfO_2) as high-k insulator, are discussed for the diagnosis and analysis of cystic fibrosis. Our findings have proven the necessity of using an Ion-Selective Membrane, made up of Polyvinil Chloride (PVC), to improve the sensibility of ISFET with respect to other ions than hydrogen. The achieved results have demonstrated the possibility to substitute the traditional test to diagnose the cystic fibrosis with the designed sensor, avoiding committing errors during the execution of the same test.

Keywords: ISFET · Cystic fibrosis · NaCl sensing · Ion-selective membrane

1 Introduction

Chemical sensors and biosensors are strongly demanded due to their wide range of potential uses in fields as disparate as healthcare and agriculture, to the environment and the food industry, to lab-on-a-chip technology. In the realm of pH sensing, ion sensitive field-effect transistors (ISFET) have shown to be an effective and promising sensing technology. ISFETs were first conceived by Bergveld in 1970 for pH sensing, but now they are widely utilized to detect other types of biomolecules (enzymes, antibodies, and proteins) [1].

The paper reports on a properly designed ISFET intended for Sodium Chloride (NaCl) sensing with reference to an important clinical case, the cystic fibrosis, a disease due to mutations in the cystic fibrosis transmembrane regulator (CFTR) gene, characterized by an accumulation of salts on the surface of the skin. The purpose of the designed device is the evaluation of the pharmacological treatments' effectiveness, optimizing the clinical trial, and the prediction of false positives, avoiding diagnostic errors associated with performing the traditional sweat test.

2 Clinical Case

Sweat is an important part of the diagnostic process for a wide range of diseases since it is a synthesis of human physiological activity.

Produced by the sweat glands, perspiration is the primary vehicle for salt to travel through the body. Sweat that evaporates to the skin's surface is somewhat salty in healthy people. In healthy persons, the sweat that evaporates to the surface of the skin has a little salty taste.

People who suffer from cystic fibrosis have a mutation in a gene that codes for a chloride-conducting transmembrane channel called CFTR, which regulates the transport of water and some salts inside and outside cells. Because of this mutation, the epithelial tissue is unable to reabsorb the chloride, which results in insufficient absorption of sodium from the ducts. This disease is recognized as the source of salty sweat due to an excess of sodium chloride ($[NaCl] > 70$ mol/m^3) in perspiration [2].

3 ISFET Operating Principle and Modelling

The Ion-Sensitive Field-Effect Transistor, or ISFET, is a solid-state potentiometric FET-based sensor. Its structure is very similar to that of a MOSFET [3], but it is modified with respect to the latter by replacing the metal oxide with a reference electrode, which is typically an Ag/AgCl, in such a way as to expose the gate directly to the electrolyte solution. The functionality of this device is derived from the fact that the insulator acts as a sensing film. As a result, the insulator can generate a potential at the interface with the solution, which is dependent on the concentration of ions in the solution itself. Because of this, the drain current in the semiconductor changes.

ISFET may be described by taking into consideration two neighboring domains, which are referred to as the semiconductor domain and the electrolyte domain. In reference to one major theory, named as "Site-Binding", the operating principle is derived from the chemical reaction that takes place between gate oxide and electrolytic solution [3, 4].

According to this first theory, the insulating surface has hydroxyl groups (HfOH groups, in the case of Hafnium Oxide) that may donate or take protons through two processes, protonation (1) and deprotonation (2), respectively, depending on the concentration of hydrogen ions (H^+) in the electrolyte [5]:

$$HfOH + H^+ \iff HfOH_2^+, \, K_+ = \frac{[HfOH][H^+]_S}{[HfOH_2^+]} \tag{1}$$

$$HfOH \iff HfO^- + H^+, \, K_- = \frac{[HfO^-][H^+]_S}{[HfOH]} \tag{2}$$
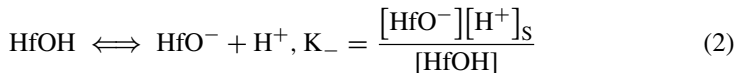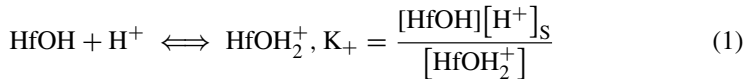
Because of this, the oxide layer, which was initially neutral, will transform into a charged surface, which may include positively or negatively charged sites. As a result, the charge on the surface will be determined by the proportion of one kind of charged site that is predominant over the other.

For the purposes of simulation, it has been considered that the net surface charge is affected by the concentration of protons at the insulator surface, which is denoted by the notation $[H_S^+]$. According to the Boltzmann equation, this concentration is related to the concentration of protons found within the electrolyte bulk, which is denoted by $[H_B^+]$:

$$[H_S^+] = [H_B^+]\exp\left(\frac{-q\psi_0}{kT}\right) \tag{3}$$

where ψ_0 is the surface potential, k is the Boltzmann's constant and T is the absolute temperature of the device.

From the last, the equation of surface charge density (σ_0) can be derived:

$$\sigma_0 = qN_S \frac{[H_S^+]^2 - K_aK_b}{[H_S^+]^2 + K_b[H_S^+] + K_aK_b} \tag{4}$$

where N_S represents the density of surface sites per unit area, K_a and K_b are the dissociation constants for deprotonation and protonation reactions, respectively.

In addition to H^+ and OH^- ions, the electrolyte also includes the existence of other kinds of anions and cations. These anions and cations are the ones that, via a process known as surface complexation, combine to create ion pairs with surface sites or groups that have opposing charges. At this point, known that in the case of cystic fibrosis, the major effects are caused by the adsorption of negative ions, that is chloride, Cl^-, a modified version of the earlier Site-Binding model needs to be considered (6), which consequently produces a variation in the Boltzmann Eq. (7) [5]:

$$HfOH_2^+ + Cl^- \iff HfOHCl^- \tag{5}$$

$$[Cl_S^+] = [Cl_B^+]\exp\left(\frac{-q\psi_0}{kT}\right) \tag{6}$$

Equation (8) shows the role of activity of Cl^- ions at the oxide surface in determining the surface charge density [4]:

$$\sigma_0 = qN_S \frac{[H_S^+]^2[H_B^+] - K_aK_b[H_B^+] - K_c[Cl_S^-][H_S^+]^2}{[H_S^+]^2[H_B^+] + K_aK_b[H_B^+] + K_c[Cl_S^-][H_S^+]^2 + K_b[H_S^+][H_B^+]} \tag{7}$$

Since the additional reaction is produced by the combination of two elementary reactions, which results in an exchange of ions, the resulting reaction constant, K_c is not strictly speaking a dissociation constant, and it is a dimensionless quantity.

When ISFETs are modified to be chemically sensitive to ions other than H^+, an Ion-Selective Membrane, also known as an ISM, may be modeled, and put in various locations, such as above the oxide layer [6, 7]. In our study, we have considered an ISM made of Polyvinil Chloride (PVC) in such a way to better filter the flux of Cl^- ions from the electrolyte. This is achieved by using a selectivity coefficient, K_i, which is defined as the ratio between the concentration on the up side and on the down side of the boundary considered ($c_{i,u}$ and $c_{i,d}$ respectively):

$$K_i = \frac{c_{i,u}}{c_{i,d}} \tag{8}$$

The selectivity coefficient is to be interpreted as a multiplicative coefficient that reduces the weight of the terms characterizing the interfering ions.

4 Numerical Results

The device has been modelled and designed using the Finite Element Method (FEM), considering two adjacent domains: the semiconductor domain and the electrolyte domain (see Fig. 1).

As shown in Fig. 2a, we calculated the drain-source current, I_{DS}, dependence on the drain-source voltage, V_{DS}, for two values of the Cl^- ions concentration, c_0; as expected, I_{DS} increases as V_{DS} increases, as typical for an ISFET. For the two values of c_0, 50 mol/m^3 and 80 mol/m^3, the saturation current exhibits a difference ΔI_{DS} of 3.8 μA.

Then, we have expressed the drain-source current, I_{DS}, as a function of the concentration value, c_0, with a fixed value of the drain-source voltage, V_{DS} (see Fig. 2b).

Assuming a minimum-detectable change in current, min(ΔI_{DS}), of 0.5 nA [7], it is possible to obtain a corresponding minimum detectable change in concentration, min(Δc_0), of 0.004 mol/m^3.
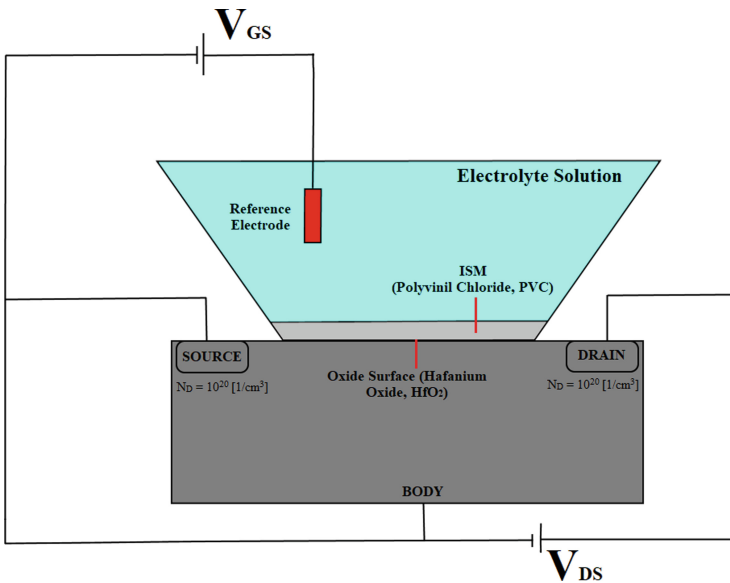
Fig. 1. Schematic diagram of ISFET for NaCl sensing
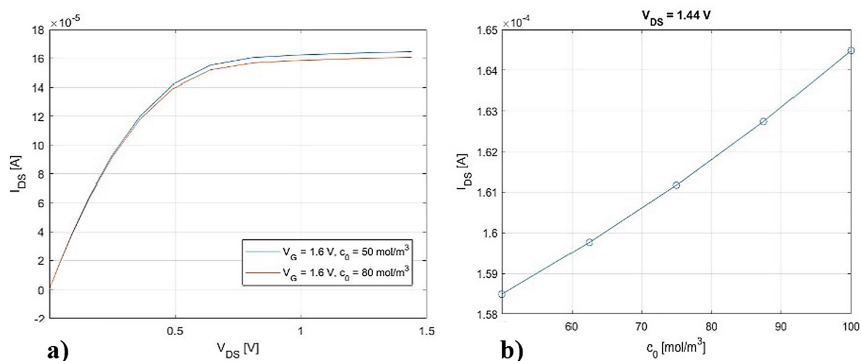
Fig. 2. a) Drain-source current VS drain-source voltage for two different [NaCl] values; b) I_{DS} / $c0$ curve with a fixed value of V_{DS} for the ISFET-based NaCl sensor

5 Conclusions

The achieved results are promising towards the development of an ISFET-based NaCl sensor useful in the context of point-of-care diagnosis and management of cystic fibrosis and have paved the way for the development of a compact and portable technology, replacing traditional diagnostic techniques. This is confirmed by the value of sensitivity derived for the same, equal to 1.2×10^{-7} Am^3/mol.

References

1. Lee, C., et al.: Ion-sensitive field-effect transistor for biological sensing. Sensors **9**, 7111–7131 (2009). https://doi.org/10.3390/s90907111
2. Hall, S.K., et al.: Sweat sodium and chloride concentrations-essential criteria for the diagnosis of cystic fibrosis in adults. Ann. Clin. Biochem. **27**, 318–320 (1990). https://doi.org/10.1016/j.jpeds.2008.05.005
3. Sinha, S., Pal, T.: A comprehensive review of FET-based pH sensors: materials, fabrication technologies, and modeling. Electrochem. Sci. Adv. **2**(5), 2100147 (2021). https://doi.org/10.1002/elsa.202100147
4. Mele, L.J., Palestri, P., Selmi, L.: General approach to model the surface charge induced by multiple surface chemical reactions in potentiometric FET sensors. IEEE Trans. Electron Dev. **67**(3), 1149–1156 (2020). https://doi.org/10.1109/TED.2020.2964062
5. Tarasov, A., et al.: Understanding the electrolyte background for biochemical sensing with ion-sensitive field-effect transistors. ACS Nano **6**(10), 9291–9298 (2012). https://doi.org/10.1021/nn303795r
6. Mele, L.J., et al.: Modeling selectivity and cross-sensitivity in membrane-based potentiometric sensors. In: 2020 Joint International EUROSOI Workshop and International Conference on Ultimate Integration on Silicon (2020). https://doi.org/10.1109/EUROSOI-ULIS49407.2020.9365285
7. Birrell, S.J., Hummel, J.W.: Membrane selection and ISFET configuration evaluation for soil nitrate sensing. Trans. ASAE. **43**(2), 197 (2000). https://doi.org/10.13031/2013.2694

Flexural Plate Wave Piezoelectric MEMS Transducer for Cell Alignment in Aqueous Solution

Alessandro Nastro[1]($\boxtimes$) , Marco Baù[1] , Marco Ferrari[1] , Libor Rufer[2] ,
Skandar Basrour[2] , and Vittorio Ferrari[1]

[1] Department of Information Engineering, University of Brescia, 25123 Brescia, Italy
`alessandro.nastro@unibs.it`
[2] CNRS, Grenoble INP, TIMA, University Grenoble Alpes, 38000 Grenoble, France

Abstract. In this work, the possibility to align cells dispersed in water by means of standing flexural plate waves (FPWs) in an underlying substrate has been explored by designing and fabricating a piezoelectric MEMS transducer. The MEMS exhibits a 6x6 mm^2 cavity etched out in a silicon substrate forming a volume where cells dispersed in liquid can be steered under electronic control. The diaphragm of the cavity is composed of silicon (Si) and an aluminum nitride (AlN) layer. The generation of FPWs of the A_0 mode in the diaphragm is achieved by applying proper excitation voltages to two metal interdigital transducers (IDTs). In turn, acoustic waves are transferred in the liquid, generating a one-dimensional acoustic field pattern thus steering and trapping the dispersed cells in distinct positions. The MEMS device has been fabricated by using the PiezoMUMPs process and experimentally tested by exploiting a tailored front-end circuit. The cavity has been loaded with inert fibroblasts cells with an approximate diameter of 15 μm dispersed in demineralized water with a concentration in the order of 10^5 cells/ml. By properly driving two IDTs, lines of cells spaced by half wavelength $\lambda/2 = 56$ μm have been achieved at 12.5 MHz, in good agreement with theoretical expectations.

Keywords: Cell alignment · Acoustic waves · Flexural plate waves · MEMS · Piezoelectric · PiezoMUMPs · Transducer

1 Introduction

Tissue engineering is a promising technique to build functional bio-constructs that restore, maintain, or improve damaged tissues [1]. For instance, a self-adaptive multifunctional hydrogel-base tissue has been engineered to achieve self-healing properties and injectability for dynamic regulation of wound microenvironment [2]. However, the key step in tissue engineering is the recreation, with adequate patterning resolution, of extracellular matrix components for the proper fulfilment of cells biological functions [3]. In [4] a tissue-engineered scale model of the human left ventricle has been made by employing a cellular patterning technique based on scaffolds to promote anisotropic myocardial tissue genesis. In [5] an extracellular matrix microarray platform for the

culture of patterned cells has been developed as a medical diagnostic tool to study the differentiation in response to a multitude of microenvironments. The main issue in achieving proper cellular patterning is to develop intercellular forces employing external stimuli and fields without altering cells integrity [6]. To overcome this issue a valid solution is represented by acoustophoresis, i.e. the use of acoustic forces to handle particles and cells in microfluidic systems, since it is a label-free, noncontact and non-invasive technique compatible with biological applications [7–9]. In this context, the present work proposes a piezoelectric MEMS transducer that is able to generate standing flexural plate waves (FPWs) in an underlying substrate to align cells in aqueous solutions. The paper is organized as follows: flexural plate wave piezoelectric MEMS transducer (Sect. 2), experimental results (Sect. 3) and conclusions (Sect. 4).

2   Flexural Plate Wave Piezoelectric MEMS Transducer

The possibility to align cells dispersed in water by means of Lamb waves in an underlying substrate has been explored by designing and fabricating a dedicated piezoelectric MEMS device. Figure 1a,b show the top and bottom schematic views of the developed device, respectively. The proposed MEMS embeds a 6x6 mm^2 cavity etched out in a 400 µm-thick silicon substrate forming a volume where cells dispersed in liquid can be aligned. The diaphragm of the cavity is composed of 10 µm-thick silicon layer and 0.5 µm-thick aluminum nitride (AlN) piezoelectric layer which can be electrically actuated by means of 1 µm-thick metal interdigital transducers (IDTs). Each IDT is composed of two interleaved comb-shaped arrays of twenty equally spaced fingers with pitch $p = 112$ µm. The generation of standing flexural plate waves (FPWs) of the A_0 mode in the diaphragm is achieved by applying sinusoidal excitation voltages to two IDTs disposed symmetrically with respect to the centre of the device.

Fig. 1. Top (**a**) and bottom (**b**) schematic view of the proposed piezoelectric MEMS device.

In turn, acoustic waves are transferred in the liquid thus generating a one-dimensional (1D) acoustic field pattern in which pressure nodes are located at half the acoustic wavelength $\lambda/2 = 56$ µm.
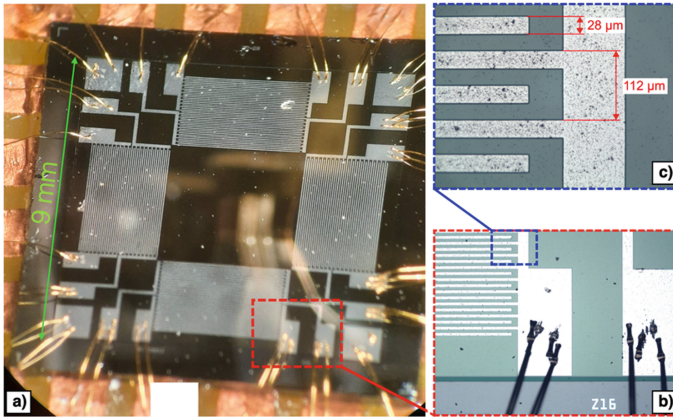
Fig. 2. Bottom view of the fabricated piezoelectric MEMS device (**a**). Enlarged image of the comb-shaped arrays terminals (**b, c**).

The cells dispersed in the liquid are thus steered and trapped in distinct positions by developed acoustic forces. The bottom view of the piezoelectric MEMS device fabricated with the MEMSCAP PiezoMUMPs process is shown in Fig. 2a. Enlarged images of the comb-shaped array terminals are shown in Fig.2b, c. The layout of the device has been designed to create a general-purpose platform exploitable in different applications such as for driving mechanical vortexes in aqueous solution droplets [10] or for tuning electrically the resonance of an acoustic transducer [11, 12]. Specifically, the design of the device has been carried out considering the optimal acoustic-fluidic coupling between the liquid and the diaphragm occurring when the wavelengths of the A_0 mode in the diaphragm and the longitudinal wave in water are equal which theoretically happens at the excitation frequency of 13.3 MHz. In such a case, cells in the liquid are expected to be trapped by acoustic forces along a regular pattern with a gap of $\lambda/2 = 56\,\mu m$.

3   Experimental Results

To experimentally validate cell alignment dispersed in water with 1D acoustic field pattern, the MEMS has been tested developing a custom front-end electronic circuit and Fig. 3 shows the corresponding block diagram. The sinusoidal excitation signals have been generated by employing a circuit based on the AD9959 direct digital synthesizer (DDS). The DDS channels CH0 and CH1 generate two sinusoidal signals $v_{s0}(t)$ and $v_{s1}(t)$ with fine frequency tuning, same peak amplitude of 250 mV and zero relative phase shift. The signals $v_{s0}(t)$ and $v_{s1}(t)$ have been amplified with a voltage gain A = 40 up to a peak level of 10 V and fed to drive the IDT1 and IDT3 up to 15 MHz.

The MEMS device has been fixed on a printed circuit board (PCB), connected to the front-end circuit and placed under optical microscope as shown in Fig. 4a,b, respectively. The cavity has been loaded with inert fibroblast cells with an approximate diameter d_p of $15\,\mu m$ dispersed in demineralized water with a concentration in the order of 10^5 cells/ml. Figure 5a shows a picture taken at the optical microscope of the cells in water when no
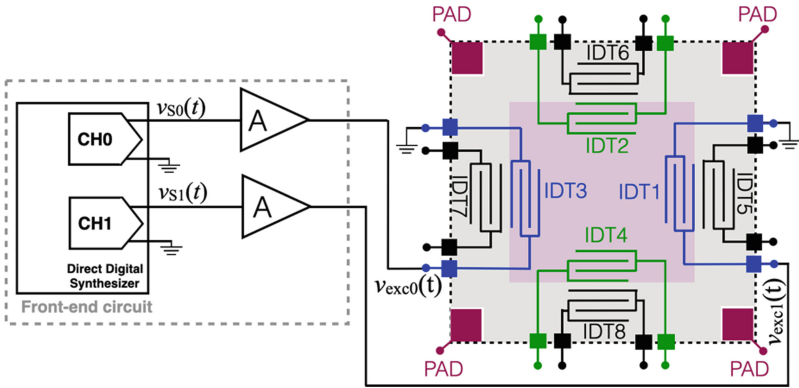
Fig. 3. Block diagram of the front-end circuit adopted to drive IDT1 and IDT3 for generating the 1D acoustic field patterning.

excitation signal is applied to the device. By driving IDT1 and IDT3, and finely tuning the excitation frequency, cell alignment has been successfully achieved within the expected frequency range, as shown in Fig. 5b. Specifically, Fig. 5b evidences a nominal spacing between two adjacent lines of cells of 56 µm which corresponds to half the acoustic wavelength $\lambda/2$ by applying an excitation frequency of 12.5 MHz, in good agreement with theoretical expectations.
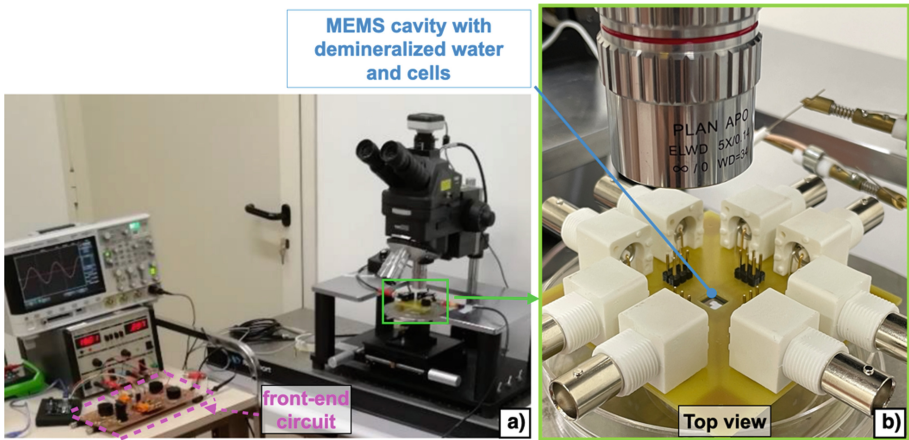
Fig. 4. Experimental setup (**a**) employed to test the piezoelectric MEMS device. Enlarged image of the MEMS cavity placed under the optical microscope (**b**).

The experimental results confirm that the proposed piezoelectric MEMS device can be effectively employed for the generation of 1D acoustic field pattern to align microparticles or cells dispersed in a liquid.
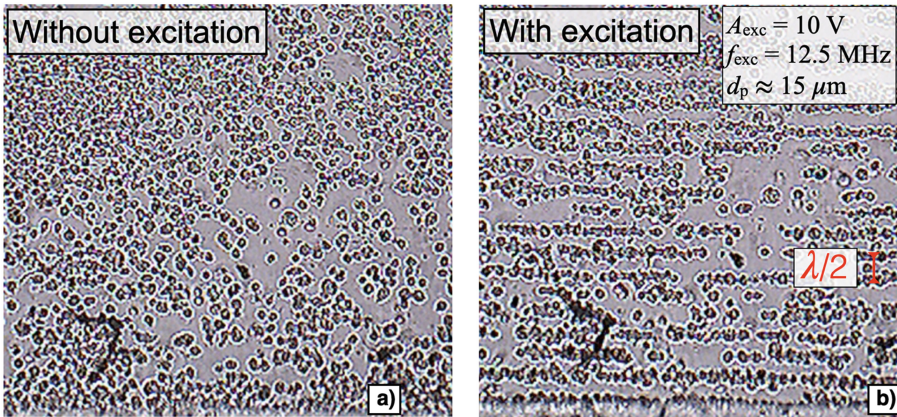
Fig. 5. Images of inert fibroblasts cells dispersed in demineralized water placed in the cavity of the MEMS device without (**a**) and with (**b**) electrical excitation.

4   Conclusions

This work has presented a flexural plate wave piezoelectric MEMS transducer to align cells in aqueous solutions. The MEMS device has been fabricated with the PiezoMUMPs technology developed by MEMSCAP employing AlN piezoelectric and doped silicon layers to realize the diaphragm. A 6x6 mm^2 cavity has been etched out in the silicon substrate to steer and contain cells dispersed in aqueous solution. The exploitation of FPWs of the A_0 mode in the diaphragm has been achieved by exploiting the inverse piezoelectric effect and applying sinusoidal excitation voltages to two metal IDTs disposed symmetrically with respect to the centre of the device thus generating a on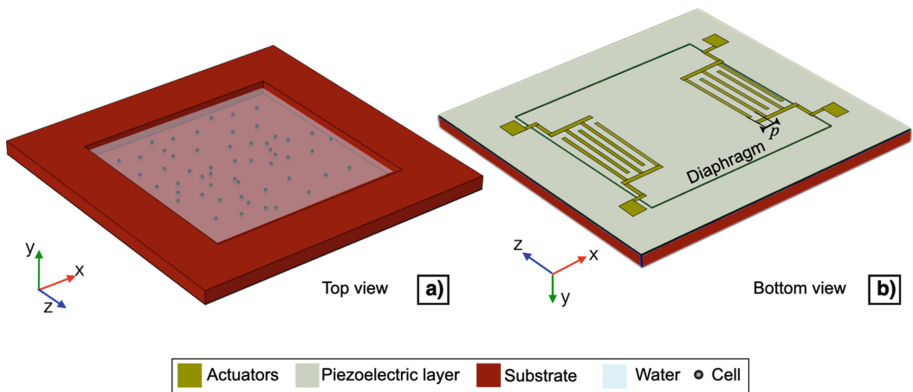e dimensional (1D) acoustic field pattern in which pressure nodes are located at half the acoustic wavelength. A tailored DDS-based front-end electronic circuit has been developed to drive a couple of IDTs up to 15 MHz. The cavity has been loaded with inert fibroblast cells with an approximate diameter d_p of 15 µm and dispersed in demineralized water. By applying the sinusoidal excitation signals with same peak amplitude of 10 V and zero phase shift between them at the excitation frequency of 12.5 MHz, cells have been correctly aligned. Specifically, the distance between two consecutive lines of cells has been estimated optically and it is equal to 56 µm, i.e., half the acoustic wavelength, thus demonstrating that the proposed MEMS device is able to properly generate 1D acoustic field pattern to align cells or microparticles in aqueous solution.

References

1. Guilak, F., Butler, D.L., Goldstein, S.A., Baaijens, F.P.: Biomechanics and mechanobiology in functional tissue engineering. J. Biomech. 27; **47**(9), 1933–40 (2014). https://doi.org/10.1016/j.jbiomech.2014.04.019
2. Shao, Z., Yin, T., Jiang, J., He, Y., Xiang, T., Zhou, S.: Wound microenvironment self-adaptive hydrogel with efficient angiogenesis for promoting diabetic wound healing. Bioact. Mater. **20**, 561–573 (2023). https://doi.org/10.1016/j.bioactmat.2022.06.018

3. Song, K., Wang, Z., Liu, R., Chen, G., Liu, L.: Microfabrication-based three-dimensional (3-D) extracellular matrix microenvironments for cancer and other diseases. Int. J. Mol. Sci. 21; **19**(4), 935 (2018). https://doi.org/10.3390/ijms19040935

4. MacQueen, L.A., et al.: A tissue-engineered scale model of the heart ventricle. Nat. Biomed. Eng. **2**(12), 930–941 (2018). https://doi.org/10.1038/s41551-018-0271-5

5. Flaim, C.J., Chien, S., Bhatia, S.N.: An extracellular matrix microarray for probing cellular differentiation. Nat. Methods **2**(2), 119–125 (2005). https://doi.org/10.1038/nmeth736

6. Kanafusa, S., Maspero, U., Petersen, M.A., Galindo, F.G.: Influence of pulsed electric field-assisted dehydration on the volatile compounds of basil leaves. IFSET. 77 (2022). https://doi.org/10.1016/j.ifset.2022.102979

7. Qian, J., Ren, J., Huang, W., Lam, R.H.W., Lee, J.E-Y.: Acoustically driven manipulation of microparticles and cells on a detachable surface micromachined silicon chip. IEEE Sens. J. **21**(10), 11999–12008 (2021). https://doi.org/10.1109/JSEN.2021.3065694

8. Burguillos, M.A., et al.: Microchannel acoustophoresis does not impact survival or function of microglia, Leukocytes or tumor cells. Plos One. **8**(5) (2013). https://doi.org/10.1371/journal.pone.0064233

9. Sehgal, P., Kirby, B.J.: Separation of 300 and 100 nm particles in fabry-perot acoustofluidic resonators. Anal. Chem. **89**(22), 12192–12200 (2017). https://doi.org/10.1021/acs.analchem.7b02858

10. Nastro, A., Baù, M., Ferrari, M., Ferrari, V.: Piezoelectric MEMS for sensors, actuators and energy harvesting. In: Di Francia, G., Di Natale, C. (eds.) Sensors and Microsystems: Proceedings of AISEM 2021 – In Memory of Arnaldo D'Amico, pp. 264–270. Springer International Publishing, Cham (2023). https://doi.org/10.1007/978-3-031-08136-1_41

11. Nastro, A., Ferrari, M., Rufer, L., Basrour, S., Ferrari, V.: Piezoelectric MEMS acoustic transducer with electrically-tunable resonant frequency. Micromachines **13**, 96 (2022). https://doi.org/10.3390/mi13010096

12. Nastro, A., Ferrari, M., Rufer, L., Basrour, S., Ferrari, V.: Piezoelectric micromachined acoustic transducer with electrically-tunable resonant frequency. In: 20th International Conference on Solid-State Sensors, Actuators and Microsystems & Eurosensors XXXIII (TRANSDUCERS & EUROSENSORS XXXIII), pp. 1905–1908 (2019). https://doi.org/10.1109/TRANSDUCERS.2019.8808488

Development of VOCs Sensor Based on Synthetic Zeolite Layers

G. Oliva, A. S. Fiorillo[✉], and S. A. Pullano

BATS Lab, Department of Health Sciences, "Magna Græcia" University of Catanzaro, Catanzaro, Italy
nino@unicz.it

Abstract. Endogenous or exogenous process byproducts include a wide range of chemicals, which can be used as promising candidate biomarkers for systemic diseases. Among them, Volatile Organic Compounds (VOCs) expressed in biological fluids could be evaluated through non-invasive techniques for the diagnosis and follow-up of a pathological condition (e.g., inflammatory process, neoplasia, etc.). Among VOCs contained in biological fluids, propionic and succinic acids are involved in important inflammatory processes. The development of a reliable, non-invasive sensor for the rapid quantification of VOCs is thus a topic of interest, especially for the screening of large populations. To this end, we investigated synthetic zeolite as a nanoporous adsorbing layer for the development of a VOCs sensor. Zeolite type 4A has been used as it provides a large surface/area ratio, a well-defined porosity, and considerable ion-exchange capabilities. A detection system based on a photoionization system has been investigated. The quantification of VOCs was evaluated by analyzing the emission profiles during the desorption process, which is strongly influenced by the environmental parameters such as temperature. Results evidenced that the joint use of a zeolite layer and a photoionization system is able to detect and quantify the presence of propionic acid respect to the succinic, since the latter is poorly physically adsorbed in the layer. The overall device is thus able to detect and quantify specific VOCs trapped inside the zeolite layer with a linear relation between the desorbed molecules and the sample concentration.

Keywords: Zeolite · Adsorption process · Nanoporous materials · Sensor application

1 Introduction

The non-invasive detection of molecules for health monitoring is a topic of interest for early diagnosis and follow-up of different diseases [1, 2]. Specific volatile organic compounds (VOCs) can be related to the onset of a pathological condition. Thus, VOCs are emerging as a new category of biomarkers for different diseases (e.g., hepatocarcinoma, prostate cancer, lung cancer etc.). Among non-invasive biological samples, saliva could provide precious information about systemic diseases that directly or indirectly affect the salivary glands, causing alterations in its composition [3]. In fact, VOCs may

reflect metabolic changes due to endogenous processes (e.g., inflammation, necrosis, and alteration of the microbiota) or exogenous processes (e.g., contamination, drugs, diet, etc.) [4, 5]. Literature evidenced as specific molecules, normally expressed in the saliva, are up- or down-regulated in patients affected by neoplasia [6, 7]. Specifically, succinic and propionic acids are involved in different metabolic processes, so they can be considered as non-invasive candidate biomarkers (for prostate cancer, oral squamous cell carcinoma, hepatocarcinoma) [8].

In biomedical field, synthetic zeolite represents an advanced material for the development of sensors for the detection of specific molecules [9, 10]. Zeolites include a wide range of porous crystalline aluminosilicates (both natural and synthetic), consisting of tetrahedral units formed by $[SiO_4]^{4-}$ and $[AlO_4]^{5-}$ with non-linear oxygen bridges (Si-O-Al), forming an open crystalline structure and interconnected channels. The metal cations inside the structure and the Si/Al ratio determines the zeolite type, while Al atoms make the outer structure negatively charged. These characteristics result in high surface/area ratio, ionic exchange capability, chemical/physical adsorption, thermal stability, which make them interesting in a wide range of applications [11-14]. The tridimensional structure of zeolite, as its large contact area, allows selective adsorption of molecules, both in liquid and gas state.

Hereafter, a nanoporous layer made of zeolite 4A was investigated for the adsorption of succinic and propionic acids [14-16]. The realization of the adsorbent layer includes the deposition of a mixture of zeolite/vegetable oil deposited on silicon wafer obtaining a thin nanoporous layer. The analysis of VOCs through a photoionization system was used to evaluate the emissive profiles during the desorption process of molecules physically adsorbed inside the layer [17-19]. The goal of this work is to develop a zeolite-based sensor capable of discriminate the presence of two or more VOCs in a biological medium.

2 Materials and Methods

Zeolite 4A in form of powder is characterized by a cubic grains form with an average size of 450 nm, a density more than 700 mg/ml, pH less than 11.00, a Si/Al ratio of 1 and the presence of mobile sodium cation. The building units of zeolites are $[SiO_4]^{4-}$ and $[AlO_4]^{5-}$ tetrahedra connected by oxygen bridges, resulting in a three-dimensional structure composed of interconnected pores and channels. In the purely siliceous structure within the lattice, the TO_4 (T = Si) units consist of one silicon atom connected to four oxygen atoms to the adjacent tetrahedra. However, the presence of Aluminum (trivalent) in the silica structure with charge $+ 3$, whose tetrahedron is $[AlO_2]^-$, makes the zeolite structure negatively charged [9, 14]. The α-cage consists of apertures of 4 Å and a central cavity with a diameter of 11.4 Å [11].

Zeolite is widely employed in different application exploiting its ion exchange and catalytic properties. One of the interesting characteristics of the zeolite respect to other nanoporous materials is its high adsorption capacity, making it ideal for applications as molecular sieves [13, 16]. Zeolite type 4A was kindly furnished by UOP-Honeywell, Reggio Calabria, Italy. Before being used, zeolite powder was dehydrated at 250 °C for 2 h.

Soybean oil was chosen for its low smoke point (130 °C), low viscosity (3.4–10-5 m^2/s), and for its low flash point (254 °C). It is composed by 55.4% of 9,12-octadecadienoic acid, 26.3% of 9-octadecenoic acid, 12.8% of hexadecanoic acid, 4.2% of octadecanoic acid, and 1.3% of 12-octadecenoic acid. A mixture of 65% w/w of zeolite 4A, and 35% w/w of soybean oil was prepared using homogenizer (Ultra-Turrax). Then, it was deposited on silicon substrate by spin coating technique at 6500 rpm for 60 s. The sample was then annealed at 150 °C for 5 h to release of the volatiles present in the compound and the formation of a carbon matrix that ensures adhesion to the silicon substrate, obtaining a layer with a thickness of 20 μm. The Succinic and propionic acids are organic compounds consisting of a carboxyl group (-COOH), which is a hydroxyl group (-OH) bound to a carbonyl group (C = O). They are defined as Short Chain Fatty Acids. Specifically, succinic acid ($C_4H_6O_4$) has a molar weight of 118.09 g/mol and crystalline structure with the major dimension of about 5.2 Å, while propionic acid ($C_3H_6O_2$) has a molar weight of 74.08 g/mol and crystalline structure with the major dimension of about 3.6 Å.

One ml of acid sample was placed onto the layer for 1 h and subsequently rinsed with deionized water and dried under nitrogen flow (see Fig. 1). The adsorption capabilities of the thin zeolite layer was investigated by the analysis of emissive profiles evaluated by a photoionization system (MiniRae 3000) in a temperature-controlled environment. The detection system (Fig. 2) has a high-energy UV lamp (10.6 eV at 120 nm).
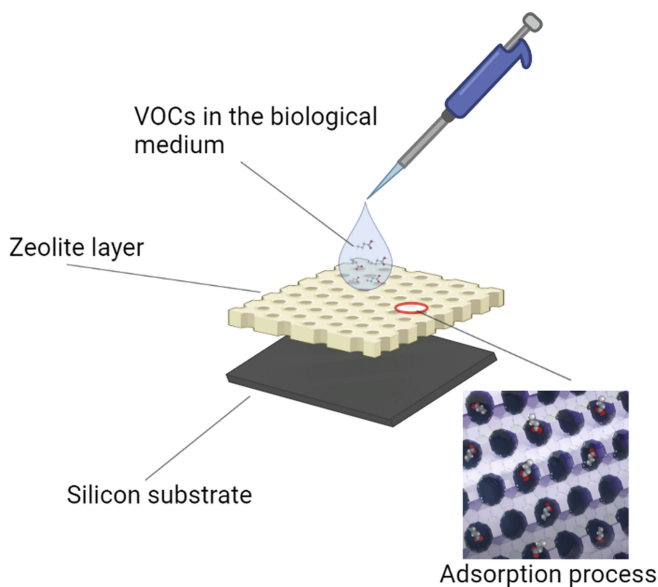
Fig. 1. Representation of adsorption processes based on zeolite. The zeolite layer acts as a molecular sieve, allowing the physical entrapment of molecule inside the pores.

The interaction of UV light with the molecule can cause the removal of electron resulting in the generation of a positively charged ion which in turn generate an electric current. The number of ionized molecules is proportional to the concentration of VOCs in the sample. The PID MiniRae 3000 allow to conduct measurements in a range from 0.1 ppm to 15000 ppm with a resolution of 0.1 ppm.
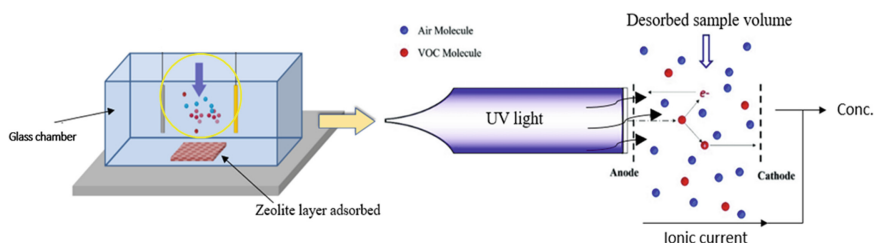
Fig. 2. Schematic zeolite-based system during desorption process. The low molecular weight molecules desorbed inside the analysis chamber are detected by a photoionization system.

Quantification of VOCs was evaluated by analyzing the emission profiles during desorption process, which is strongly influenced by the environmental temperatures. Emissive profiles were performed in a glass chamber of size 7x8x2 cm with an upper exit hole of 0.4 cm in diameter. Afterwards, the chamber containing the layer was maintained at 100 °C for the analysis. The emissive profile was evaluated for 300 s. using the photoionization system.

3   Results and Discussion

Firstly, the emission profile of zeolite sample was evaluated to define a background emission level. As reported in Fig. 3a no VOCs were desorbed form the sample before the analysis. After the adsorption process of a solution of succinic acid (50% v/v), emissive profile evidenced a desorption level as reported in Fig. 3b. Considering that the molecule of succinic acid is bigger than that of the pore, the emission level can be considered residual and due to molecules localized on the surface. Considering propionic acid (Fig. 3c and d), higher desorption levels were evidenced at different concentrations since the dimension of propionic acid molecule is compatible with that of pore. Propionic acid molecules can thus be trapped inside the cavities, acting as a selective adsorbing layer. In addition, it was evidenced that desorption profile and dynamics is specific of each molecule. The relation between the peak of emission (ppm) and the concentration (% v/v) evidenced a linear trend (see Fig. 3e) and higher reproducibility of emission profile over multiple adsorption cycles.
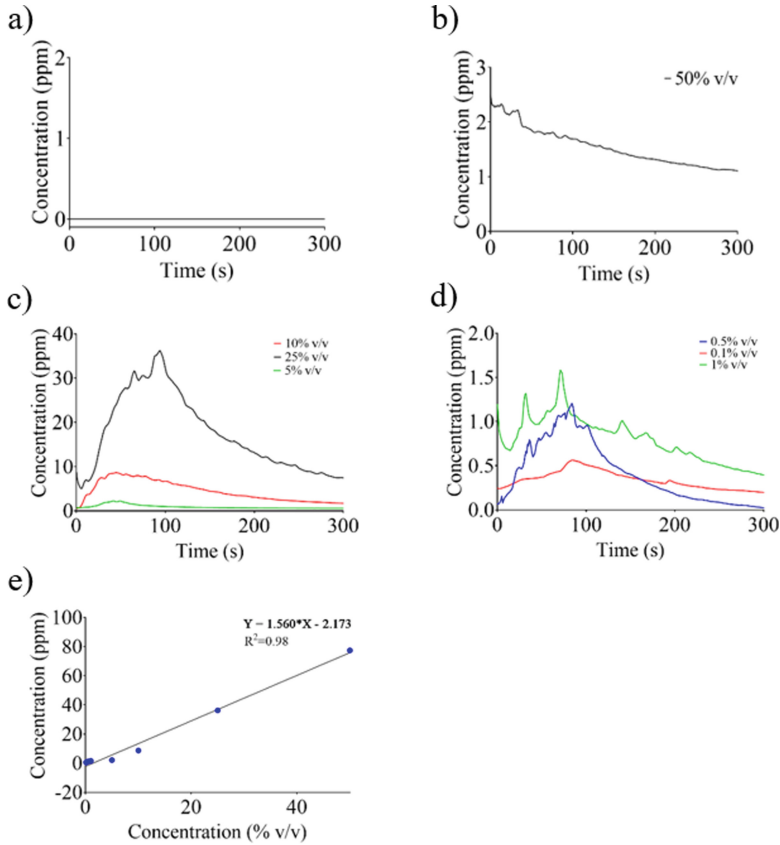
Fig. 3. a) Zeolite layer background emission profile; b) Emission profile of succinic acid (50% v/v). c) Emission profiles of propionic acid at 25%, 10%, and 5% v/v. d) Emission profiles of propionic acid at 1%, 0.5%, and 0.1%. e) Emission peak concentration (ppm) vs. sample concentration (% v/v).

4   Conclusion

The development of a device for the quantification of VOCs is a topic of interest, especially for the rapid and non-invasive screening of specific diseases, enhancing the diagnosis even at an early stage. The use of zeolite as nanoporous layer together with a detection system based on photoionization was investigated for the detection of VOCs. The aim is to highlight the adsorbing capabilities of zeolite towards succinic and propionic acid molecules, and the possibility of fabricating a device for biological sample analysis (e.g., urine, saliva etc.). The desorption characteristics of the nanoporous layers were evaluated in terms of emission profile. It has been evidenced that the type of interactions between zeolite layer and specific molecules is based on physical process. Results obtained evidenced that emissive profiles provide information about trapped molecules, and that the zeolite layer can be selective for specific molecules. Moreover, a linear trend is evidenced between the number of desorbed molecules and the concentration of the

analyzed sample. The overall device is thus able to detect and quantify specific VOCs trapped inside the zeolite cavities, results in a promising sensing technique.

References

1. Da Costa, B.R.B., Spinosa De Martinis, B.: Analysis of urinary VOCs using mass spectrometric methods to diagnose cancer: a review. Clin. Mass Spectrom. **18**, 27–37 (2020)
2. Di Lena, M., Porcelli, F., Altomare, D.F.: Volatile organic compounds as new biomarkers for colorectal cancer: a review. Colorectal Dis. J. **18**(7), 654–663 (2016)
3. Amann, A., et al.: The human volatilome: volatile organic compounds (VOCs) in exhaled breath, skin emanations, urine, feces and saliva. J. Breath Res. **8**(3), 17 (2014)
4. Gaude, E., et al.: Targeted breath analysis: exogenous volatile organic compounds (EVOC) as metabolic pathway-specific probes. J. Breath Res. **13**(3), 032001 (2019)
5. Arakawa, T., Viet Dao, D., Mitsubayashi, K.: Biosensors and chemical sensors for healthcare monitoring: a review. IEEJ Trans. **17**(5), 626–636 (2022)
6. Shigeyama, H., Wang, T., Ichinose, M., Ansai, T., Lee, S-W.: Identification of volatile metabolites in human saliva from patients with oral squamous cell carcinoma via zeolite-based thin-film microextraction coupled with GC–MS. J. Chromatogr. B. Anal. Technol. Biomed. Life Sci. **1104**, 49−58 (2019)
7. Milanowski, M., Pomastowski, P., Ligor, T., Buszewski, B.: Saliva – volatile biomarkers and profiles. Crit. Rev. Anal. Chem. **47**(3), 251–266 (2017). https://doi.org/10.1080/10408347.2016.1266925
8. Broza, Y.Y., Vishinkin, R., Barash, O., Nakhleh, M.K., Haick, H.: Synergy between nanomaterials and volatile organic compounds for non-invasive medical evaluation. Chem. Soc. Rev. **47**, 4781–4859 (2018)
9. Tyagi, D., Bhattacharyya, K.: Synthesis of porous materials. In: Tyagi, A.K., Ningthoujam, R.S. (eds.) Handbook on Synthesis Strategies for Advanced Materials. IIMS, pp. 189–227. Springer, Singapore (2022). https://doi.org/10.1007/978-981-16-1803-1_6
10. Fiorillo, A.S., Tiriolo, R., Pullano, S.A.: Absorption of Urea into zeolite layer integrated with microelectronic circuits. IEEE Trans. Nanotechnol. **14**(2), 214–217 (2015)
11. Pullano, S.A., et al.: Antireflection properties of composite zeolite gold nanoparticles film. Electron. Lett. **54**(6), 370–372 (2018)
12. Stetsenko, M., Pullano, S.A., Margitych, T., et al.: Antireflection enhancement by composite nanoporous zeolite 3a–carbon thin film. Nanomaterials **9**, 1641 (2019)
13. Oliva, G., Bianco, M.G., Fiorillo, A.S., Pullano, S.A.: Anti-reflective zeolite coating for implantable bioelectronic devices. Bioengineering **9**, 404 (2022)
14. Pullano, S.A., Falcone, F., Critello, C.D., Bianco, M.G., Menniti, M., Fiorillo, A.S.: An affordable fabrication of a zeolite-based capacitor for gas sensing. Sensors **20**(7), 2143 (2020)
15. Oliva, G., Fiorillo, A.S.: Detection of volatile organic compounds adsorbed onto zeolite layers. In: International Symposium on Medical Measurements and Applications (MeMeA) Proceedings, IEEE, Messina, Italy (2022)
16. de Pietre, M.K., Freitas, J.C.C.: Fundamental studies on zeolite–adsorbate interactions: designing a better aluminosilicate adsorbent for pollutants' removal. Environ. Earth Sci. **81**(1), 1–22 (2021). https://doi.org/10.1007/s12665-021-10130-w
17. Agbroko, S.O., Covington, J.: A novel, low-cost, portable PID sensor for the detection of volatile organic compounds. Sens. Actuators, B Chem. **275**, 10–15 (2018)
18. Di Natale, C., et al.: Lung cancer identification by the analysis of breath by means of an array of non-selective gas sensors. Biosens. Bioelectron. **18**(10), 1209–1218 (2003)
19. Szulczyński, B., Gębicki, J.: Currently commercially available chemical sensors employed for detection of volatile organic compounds in outdoor and indoor air. Environments **4**(1), 21 (2017)

Toward Single-Pulse Monitoring for FLASH Radiotherapy

Sara Pettinato[1,2]([✉]), Marco Girolami[2], Maria Cristina Rossi[3], Daniele Barettin[1], and Stefano Salvatori[1,2]

[1] Faculty of Engineering, Università Degli Studi "Niccolò Cusano", 00166 Rome, Italy
sara.pettinato@unicusano.it

[2] Istituto di Struttura Della Materia, Consiglio Nazionale Delle Ricerche, Montelibretti, Italy

[3] Department of Industrial, Electronic and Mechanical Engineering, Università Degli Studi Roma Tre, Rome, Italy

Abstract. FLASH radiotherapy is an emerging technique that uses high dose rates (~40 Gy/s) and high dose-per-pulse values (~1 Gy/pulse) by delivering the total dose in a single session, resulting in significantly shorter treatment times and safeguarding healthy tissues. In this field, single-pulse dose measurements appear critical for understanding the tissue-radiation interaction when high-intensity pulses and high dose rates are involved. In this work, we describe a compact high-precision electronics coupled to a diamond dosimeter for pulse-by-pulse monitoring of electron packets emitted by medical LINACs. The front-end can be used with a full scale up to tens of nC. Therefore, in the case of detectors with a sensitivity around 1 nC/Gy, the system is able to acquire doses up to tens of Gy/pulse, as required in FLASH. The detection prototype was characterized in the lab, emulating charge-pulses up to 30 nC. An excellent linearity was observed in the wide range 40 fC – 30 nC with a readout error lower than $\pm 0.5\%$. In addition, the diamond dosimeter irradiated by electron-packets generated by a medical LINAC was connected to the realized electronics for field-tests. Experimental results demonstrate that the proposed detection system is able to monitor the intensity of individual pulses, confirming the wide versatility of the proposed electronics also to meet the FLASH therapy requirements.

Keywords: Gated-integrator · Pulse-by-pulse monitoring · CVD-diamond · Dosimeter · Radiation therapy · FLASH therapy

1 Introduction

Radiation therapy (RT) is a physical therapy that uses high-energy ionizing radiation to damage the DNA of cancer cells, causing apoptosis and necrosis, thereby blocking their proliferation [1]. Radiation-induced damage to the surrounding healthy tissues is one of the major drawbacks in RT. Favaudon et al. [2] illustrated a new promising technology, named FLASH therapy, in which ultrahigh dose-rate (DR) electron pulses are effective against tumor cells but causing little damage to healthy tissues.

Single crystal diamonds grown by chemical vapor deposition technique (scCVD-diamonds) are widely used for the fabrication of radiation and particle detectors [3–5]. In addition, due to its physicochemical properties (e.g. tissue equivalence and radiation hardness, to cite a few), scCVD-diamond is an elective material for radiation-dosimetry purposes, especially for the fabrication of dosimeters with very small dimensions [6]. Diamond dosimeters are now a mature technology and commercially available devices are widely used in clinical routine by health physicists [7]. Recently, Marinelli et al. designed and realized a novel diamond-based Schottky diode detector matching the requirements of FLASH-RT [8].

Single-pulse dose measurements are critical for understanding the interaction between the tissue and the radiation when high-intensity pulses and high DRs are involved as in FLASH-RT. In our research works, we already demonstrated that scCVD-diamond dosimeters coupled to a specifically designed gated-integrating electronics are effective for single-pulse monitoring of the current signals generated by the detector under high-energy photons or electrons irradiation [9, 10]. The designed electronics easily allows adapting the dynamics of the front-end to the specific detector signal, allowing the use of the developed instrument also for high-intensity impinging radiation. In this work, we upgraded the electronics for pulse-by-pulse monitoring of charge packets up to tens of nC having a duration of few microseconds. Experimental results highlight the system capability also to process signals generated by dosimeters irradiated by high-intensity electron packets, as those used in FLASH-RT.

2 Experimental Results and Discussion

2.1 Front-End

Figure 1 reports the schematic of the realized front-end. The prototype is based on the precision switched integrator transimpedance amplifier IVC102. The component integrates a low-noise op-amp, three high quality capacitors, and two low leakage FET switches for reset and hold functions. As outlined in [11], for the digital timing/control circuit, a specifically programmed microcontroller was used to generate the HOLD and RESET signals indicated in Fig. 1. An inverting amplifier (based on the LT1995) has been inserted at the output of the IVC102, adapting the integrator output dynamics to that of the 12-bit ADC embedded into the microcontroller. Depending on the position of the jumpers (see the table reported in Fig. 1), the electronics can be used with a full scale up to either 300 pC or 30 nC. Therefore, in the case of detectors with a sensitivity of 1 nC/Gy, the system is able to integrate pulses up to 30 Gy/pulse. It is worth to note that the non-inverting input of the LT1995 is biased at about 100 mV by means of the REF200 100 μA current reference. Despite to a slight decrease of the output dynamics, this assures the possibility to correctly convert the input pulses also in presence of relatively high offset and leakage currents of the detector.

When the IVC102 input voltage is greater than 200 μA, the on-resistance of about 1500 Ω of the S1 MOS-switch integrated into the device creates a voltage difference able to forward-bias the internal ESD protection diodes. Therefore, for more intense signals, J1 allows to directly connect the detector to the inverting input of the IVC102. With this solution, input current peaks up to 5 mA (as specified in the IVC102 datasheet) can be acquired. Obviously, in this case also a large enough external C_{EXT} capacitor is necessary. For example, with C_{EXT} equal to a few nF, the system would be able to integrate peaks up to tens of nC/pulse, of the order of those used in FLASH-RT [2]. As reported in the schematic, in this work the front-end was equipped with a 2.2 nF polyester capacitor allowing the IVC102 to integrate charge pulses up to 30 nC.

F.S.	J1a	J1b	J2	J3
0.3 nC	closed	opened	opened	opened
30 nC	opened	closed	closed	closed
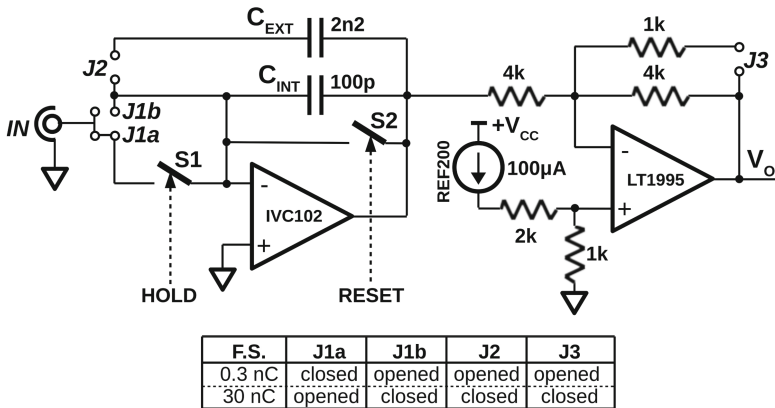
Fig. 1. Simplified schematic of the realized front-end for conditioning of charge-pulses up to 30 nC. The table summarizes the jumper positions according to the desired full scale.

2.2 In-Lab Characterizations

Impulsive signals generated with a precision programmable current source Keithley 6221 were used to fully characterize the realized prototype. Figure 2 illustrates the example of a pulse used during the tests (amplitude 8 mA, duration 4 μs, and repetition frequency 360 Hz). The signal reproduces what is normally generated by a medical LINAC [11]: duration of 4 μs, delayed by about 12 μs with respect to the sync signal.

Lab-tests were conducted by emulating the pulse amplitudes generated by a detector from 10 nA to 7.5 mA, i.e. charge-packets per pulse in the range 40 fC – 30 nC. Figure 3 shows the results obtained by selecting the integrating capacitor $C_{INT} = 100$ pF (blue dots) and $C_{INT} \| C_{EXT} = 2.3$ nF (red diamonds). In addition to the wide input dynamics, an excellent linearity is observed with readout errors of approximately $\pm 0.1\%$ between 10 pC and 300 pC (C_{INT}) and $\pm 0.5\%$ between 1 nC and 30 nC ($C_{INT} \| C_{EXT}$).
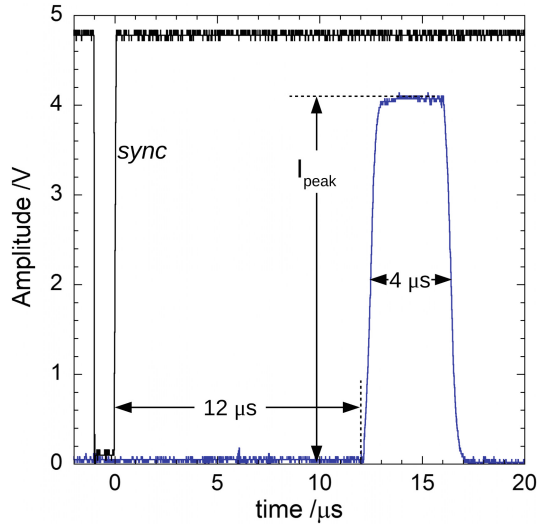
Fig. 2. Example of a current-pulse generated by the Keithley 6221 used for lab-tests.
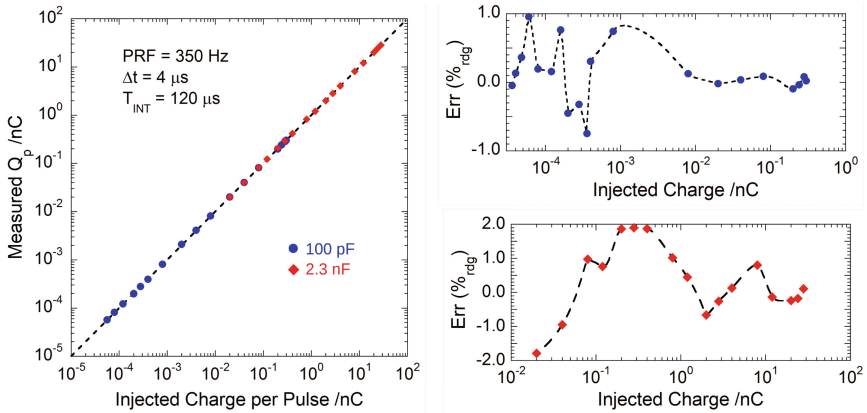
Fig. 3. Measured charge versus the injected charge packets for C_{INT} equal to 100 pF (blue dots) and 2.3 nF (red diamonds). On the right the percentage of the reading error for the two C_{INT}.

2.3 Preliminary Field-Tests

Field-tests were performed with an in-lab-made scCVD-diamond dosimeter [10] irradiated by electrons generated by a Clinac iX (by Varian) at different energies for a fixed DR of 10 Gy/min. The Clinac iX generates pulses at a pulse repetition frequency of 180 Hz when operating with electron beams. Figure 4 shows the experimental results of a 1 s acquisition for each energy. It can be clearly seen that the system is able to monitor the intensity of individual pulses. Significantly, how the LINAC works: in order to keep the released dose stable, a number of pulses are suppressed depending on the energy.
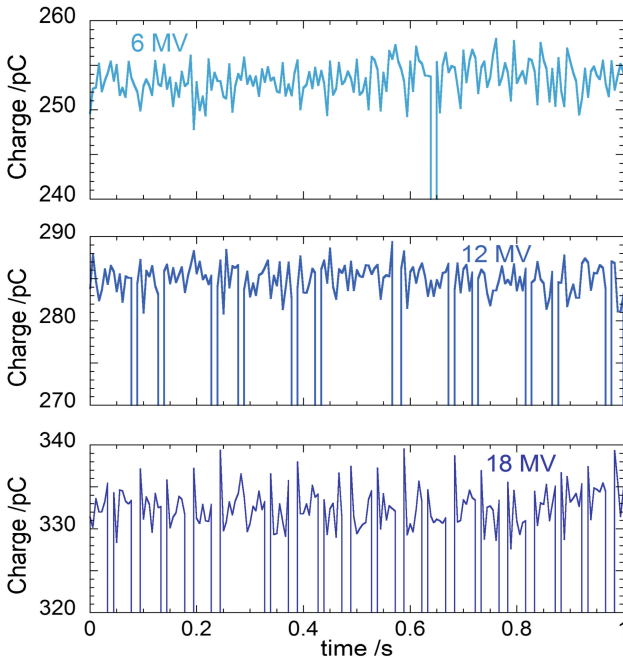
Fig. 4. Example of acquisitions of charge-per-pulse collected under electron irradiation at different energies.

The firmware of the microcontroller was adapted to calculate the cumulative charge values acquired at different doses. Experimental results obtained at the three electron energies are reported in Fig. 5. Dotted line represents the best fit linear regression line of data with a slope of (298 ± 4) nC/Gy in good agreement with the sensitivity obtained for the same detector irradiated by high-energy photons emitted by the Clinac iX [9].

The topic addressed in this work appears crucial for modern radiotherapy techniques. Indeed, single-pulse dose measurements become critical for understanding the mechanisms related to tissue-radiation interaction, especially for high-intensity pulses involved in the emerging FLASH radiotherapy technique. The experimental results confirm the wide versatility of the proposed electronics coupled with a diamond detector, which can be easily adapted to the intensity, amplitude and repetition frequency of the pulses. Work is in progress to validate the proposed detection system for high-intensity electron beams generated by LINACs specifically developed for FLASH-RT.
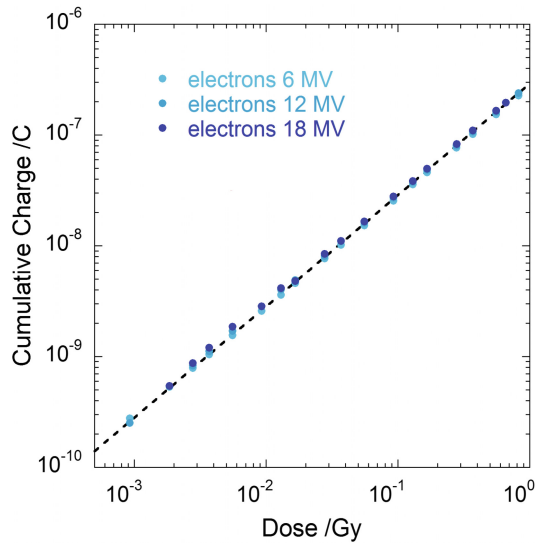
Fig. 5. Cumulative charge as a function of the dose of impinging electrons at 6, 12, and 18 MV (dots) and best-fit linear regression line of data with a slope of of (298 ± 4) nC/Gy (dotted line).

References

1. Lomax, M.E., Folkes, L.K., O'Neill, P.: Biological consequences of radiation-induced DNA damage: relevance to radiotherapy. Clin. Oncol. **25**, 578–585 (2013)
2. Favaudon, V., et al.: Time-resolved dosimetry of pulsed electron beams in very high dose-rate. Nucl. Inst. Meth. Phys. Res. A **944**, 162537 (2019)
3. Komlenok, M., et al.: Diamond detectors with laser induced surface graphite electrodes. Nucl. Inst. Methods Phys. Res. A **837**, 136–142 (2016)
4. Girolami, M., et al.: Investigation with β-particles and protons of buried graphite pillars in single-crystal CVD diamond. Diam. Relat. Mater. **84**, 1–10 (2018)
5. Girolami, M., et al.: CVD-diamond detectors for real-time beam profile measurements. In: Proceedings of IEEE Sensors, pp. 270–273. IEEE (2008)
6. Zahradnik, I.A., et al.: A diamond guard ring microdosimeter for ion beam therapy. Rev. Sci. Instrum. **91**, 054102 (2020)
7. PTW, microDiamond synthetic diamond detector for high-precision dosimetry https://www.ptwdosimetry.com/en/products/microdiamond/. Accessed 26 Sep 2022
8. Marinelli, M., et al.: Design, realization and characterization of a novel diamond detector prototype for flash radiotherapy dosimetry. Med. Phys. **49**(3), 1902–1910 (2022)
9. Pettinato, S., et al.: Compact embedded detection electronics for accurate dose measurements of MV pulsed x-rays and electrons. In: Proceedings of MeMeA, pp. 1–6. IEEE (2022)
10. Pettinato, S., et al.: Time-resolved dosimetry of pulsed photon beams for radiotherapy based on diamond detector. IEEE Sens. J. **22**(12), 12348–12356 (2022)
11. Pettinato, S., et al.: A high-precision gated integrator for repetitive pulsed signals acquisition. Electronics **8**(11), 1231 (2019)

Wireless Harmonic Transponder Based on Piezo-Varactor Direct Phase Modulation

G. Simoncini[✉], G. Cicioni, R. Salvati, V. Palazzi, G. Schiavolini,
G. Orecchini, F. Alimenti, P. Mezzanotte, and L. Roselli

University of Perugia, Perugia, Italy
guendalina.simoncini@studenti.unipg.it

Abstract. This paper presents a passive wireless harmonic transponder capable of transmitting information acquired by its vibration sensor. The system is equipped with a Schottky diode frequency doubler which converts the received signal from f_0 to its second harmonic $2f_0$. The sensed information is then encoded in the $2f_0$ carrier phase using a varactor phase-shifter (acting as the phase modulator) biased through a piezoelectric transducer (which senses the mechanical vibrations). The transponder operation is demonstrated with particular focus on piezoelectric transducer vibrating resonance frequency. The side-band amplitude of the backscattered signal increases by about 10 dB for an increment of the acceleration of the mechanical system under test of 1.5 g 128 Hz.

Keywords: IoT · Chipless harmonic tag · Phase shifter · Phase shifter sensor · Piezoelectric transducer · Wireless sensor system

1 Introduction

Wireless sensor networks (WSNs) have found applications in different areas such as environmental monitoring, healthcare, and many others. In this scenario, distributed sensing systems are employed to monitor one or more parameters (temperature, humidity, vibration, etc.). The increasing use of these sensing systems gets along well with battery-less sensors, [5]; For this reason, part of current research is focusing on energy harvesting techniques, among which harmonic transponders approaches are attracting growing attention [1]. These systems encode the sensor information in the backscattered signal, which is received at f_0 from the reader and sent back after a frequency conversion at $2f_0$. Among

them, there are the phase-based harmonic sensors that encode the information in the phase of the backscattered signal. Regarding the sensing device, piezoelectric materials are widely used for mechanical sensing applications due to their versatility, and in particular, they can be used to implement motion, force, or vibration sensors.

This contribution investigates the use of a piezoelectric cantilever as a vibration transducer, in conjunction with a harmonic transponder communication approach. The passive harmonic sensor encodes the vibration information in a phase variation by means of a varactor reflection-type phase shifter and a piezoelectric transducer. This particular combination of piezo-varactor, which was demonstrated for a frequency modulation in [2], is here combined with a reflection-type phase shifter which brings the modulation to a phase modulation. In the present work, the sensor, presented in [6], has been integrated and demonstrated to work as a harmonic transponder system. Wireless measurements are carried out, highlighting an interesting response when the sensor is stimulated with a vibration frequency equal to the piezoelectric resonant one.

2 System Overview and Circuit Design

The proposed harmonic transponder is shown in Fig. 1(a); it is composed by two antennas, a frequency doubler, and a vibration sensor. The passive transponder is interrogated by a sinusoidal signal at frequency f_0. The input antenna gathers part of the signal and sends it to a frequency doubler that converts the input signal from f_0 to its second harmonic $2f_0$, by means of a non-linearity (e.g. a diode). The signal is now passed to the sensor and it is then sent back to the receiver. The sensor modulates the phase of the backscattered signal as a function of the physical parameter which is designed to sense. In such a way, the sensor information is encoded in the phase difference between the signal received at f_0 and the one backscattered at $2f_0$. In the following, the frequency doubler and sensor will be described, with a particular focus on the developed sensor.

The frequency doubler used in our experiments is the Schottky diode doubler described in [4], here presented in its FR4 substrate implementation. It is designed to receive a signal at $f_0 = 1.04$ GHz and convert it to its second harmonic $2f_0 = 2.08$ GHz, thanks to the HSMS-2850-Agilent diode non-linearity.
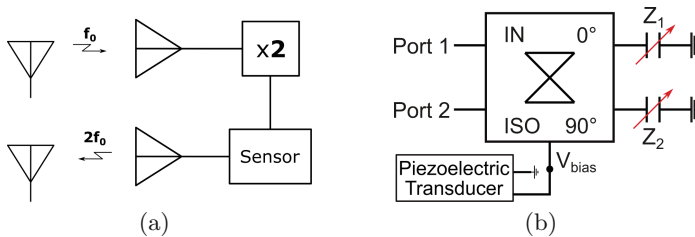
Fig. 1. (a) Scheme of the proposed passive harmonic transponder. (b) Schematic view of the implemented sensor.

The sensor presented in this work is the one reported in [6]. As visible from the schematic view of Fig. 1(b), it is made of a reflection-type phase shifter and a piezoelectric transducer. The phase shifter consists of a 90-degree hybrid junction in which the direct and coupled ports are closed onto two identical reactive impedances. The hybrid junction equally splits the input signal in two. These two signals arrive to the reactive load level with a mutual $90°$ phase shift. They are then reflected towards Port 1, where they combine in opposite phase, and Port 2, where they combine in phase. Since the reactive loads Z_1 and Z_2 are the same components $Z_1 = Z_2 = Z = jX$, the resulting reflection coefficients will be equal as well $\Gamma_1 = \Gamma_2 = \Gamma$. This gives a transmission coefficient

$$S_{21} = j \frac{\Gamma_1 + \Gamma_2}{2} = j\Gamma \qquad \angle S_{21} = \phi = \angle \Gamma + \frac{\pi}{2} \tag{1}$$

The choice of the reactive load jX allows to fix the desired phase shift. In our case, the direct and coupled ports of the phase shifter are connected to a capacitance C, for which the reflection and transmission coefficients are

$$\Gamma = \frac{1 - j2\pi f Z_0 C}{1 + j2\pi f Z_0 C} \qquad \phi = -2\tan^{-1}(2\pi f Z_0 C) + \frac{\pi}{2} \tag{2}$$

In the case of open circuit (C $\simeq$ 0 pF), the phase shift is no more than the one expected: $\phi = \pi/2$. When the terminations are comparable to short circuits (C $\geq$ 100 pF) a negative phase shift is established: $\phi = -\pi/2$. The load can therefore introduce a relative phase shift in the range of $0° \div 180°$, which can be widen introducing an inductor in series with the capacitance load [7].

Indeed, considering a reactive load made up of an inductance in series with a varactor, the reflection coefficient and its phase become

$$\Gamma \simeq \frac{(1 - \omega^2 L_{eq} C_{eq}) - j\omega Z_0 C_{eq}}{(1 - \omega^2 L_{eq} C_{eq}) + j\omega Z_0 C_{eq}} \qquad \angle \Gamma \simeq -2\tan^{-1}\left(\frac{\omega Z_0 C_{eq}}{1 - \omega^2 L_{eq} C_{eq}}\right) \tag{3}$$

with $C_{eq} = C_J + C_P$ and $L_{eq} = L + L_S$, where C_P, C_J, and L_S belongs to the equivalent circuit of the varactor [7], while L is the fixed inductor load.

Following the previous discussions, the layout of the phase shifter is implemented. The direct and coupled ports of the hybrid junction are closed on the series of a SMV1247-079LF varactor diode D_1 and the inductance $L_1 = 1.15\ nH$. This provides a measured phase shift dynamics in the range of $0° \div 160°$ for a sinusoidal voltage bias in the range of $-5 \div 5$ V, Fig. 2(a). Finally, the biasing voltage is delivered to the diodes through a proper network, like the one reported in [7]; the network is made of a resistor $R_1 = 100\ K\Omega$ and a parallel of two capacitances of 10 nF and 10 pF. The S129-H5FR-1803YB piezoelectric bending transducer from Mide is employed as a voltage source for the varactor biasing. Every time the transducer bends it generates the varactor voltage bias, which consequently defines the signal phase shift.

3   Experimental Results

A phase-shifter prototype has been manufactured and assembled, as shown in Fig. 2(b). The microstrip circuit is realized on an 0.8-mm-thick FR4 substrate
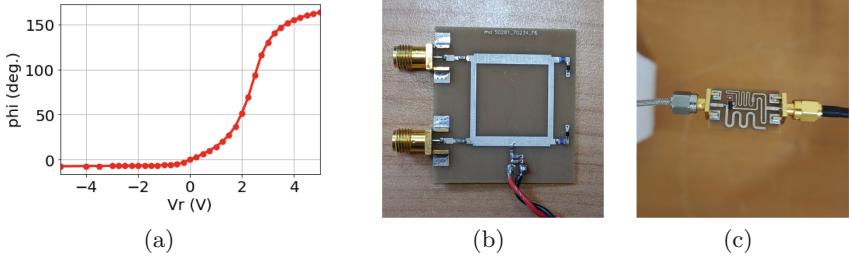
Fig. 2. (a) Measured phase shift of the backscattered signal as a function of the voltage V_R applied to the phase-shifter varactor. (b) Assembled reflection-type phase shifter. (c) Assembled frequency doubler based on low-barrier Schottky diode.

(relative permittivity 4.7, loss tangent 0.011). The frequency doubler employed for the experiment is the one displayed in Fig. 2(c).

To validate the operating principle of the proposed sensor the experimental setup displayed in Fig. 3 is employed. The piezoelectric bending transducer has a cantilever shape and it is screwed on top of a shaker (model DS-PM-20 from DEWESoft), whose vibration frequency f_s and acceleration a can be manually controlled. While the vibration frequency can be seen on the shaker display, the acceleration magnitude (expressed in g) is evaluated by the ADXL345 accelerometer module from Analog Devices, placed on top of the vibrating station and connected to an Arduino board. The interrogation signal at $f_0 = 1.04$ GHz is provided by an RF signal generator (HP8664A from HP) with a transmitted power of +15 dBm. The spectrum analyzer N9320B from Agilent is used as receiver and it is set with a measurement band of 2 kHz, centered at $2f_0 = 2.08$ GHz and a resolution bandwidth 10 Hz. The antenna system is composed of two helical antennas (G $\approx$ 5 dBi) and two patch antennas, placed at a distance of nearly 45 cm. To demonstrate the harmonic transponder behaviour, two different set of measurements are carried out.
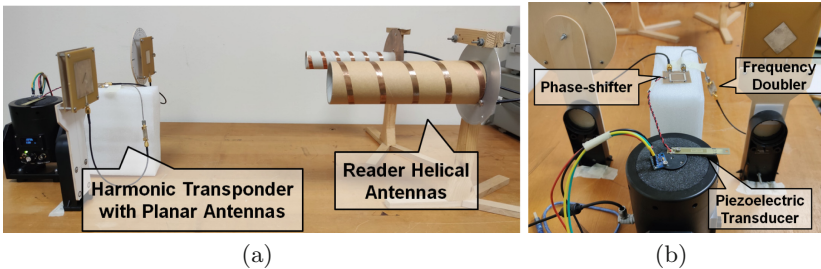
Fig. 3. (a) Measurement setup. (b) Passive harmonic transponder as arranged for the measurement session. The piezoelectric transducer is placed over the shaker.
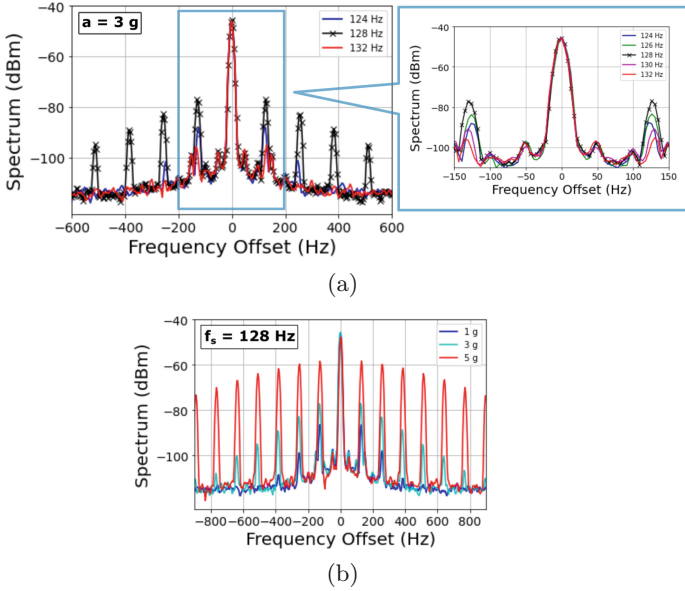
Fig. 4. Spectrum of the backscattered signal, centered at $2f_0 = 2.08\,\mathrm{GHz}$. (a) Results of the first experiment with fixed a and variable f_s. (b) Result of the second experiment with fixed f_s and variable a.

Figure 4 (a) shows the spectrum of the backscattered signal obtained from the first experiment, using a constant acceleration $a = 3\,\mathrm{g}$ while varying the vibration frequency of the shaker f_s 128 Hz; this frequency value is chosen considering that the piezoelectric transducer has a resonance frequency f_r that depends on the shape of the cantilever. Indeed, once the transducer is stimulated with a frequency $f_s = f_r$, the phase modulation is such that a higher number of side-bands shows up compared to the side-bands produced by other vibration frequencies. This is visible in the graph where a change in the vibration frequency of 4 Hz changes the side-lobe numbers from 8 at $f_s = f_r = 128\,\mathrm{Hz}$, to only 2 side-lobes at $f_s = 132\,\mathrm{Hz}$. In the closer-look image, we can also observe a frequency shift of the side-lobes accordingly to the variation of the vibration frequency f_s. This is a consequence of the phase modulation itself for which the distance, expressed in Hz, between lobes is equal to the modulation frequency, i.e., our vibration frequency. Moreover, the amplitude of the side-lobes varies with the vibration frequency and the maximum is achieved when the resonance frequency of the cantilever is considered. For the second experiment f_s is fixed 128 Hz, whereas the acceleration magnitude is varied between 1 and 5 g. Results of the experiment are reported in Fig. 4(b), showing that the spectrum significantly depends on the acceleration magnitude. Varying the acceleration from 1 g to 3 g produces a side-band amplitude increase from -87 dBm to -77 dBm below the carrier.

4   Conclusion

In this paper, a harmonic transponder capable of sensing vibrations is presented. The sensor is obtained by combining a variable reflection-type phase shifter with a piezoelectric transducer. A variation in the intensity and frequency of vibrations produces a change in the output voltage of the piezoelectric transducer, which in turn determines the biasing voltage applied to the varactor. As result, the vibration information can be encoded in the phase modulation of a single carrier signal. To increase the robustness of the transponder sensor, a Schottky frequency doubler is integrated into the system, so that the f_0 received signal is converted to its second harmonic $2f_0$.

The system appears to be particularly sensitive to acceleration magnitude when the vibration frequency approaches the resonance frequency of the cantilever, with an excursion of 10 dB of the re-transmitted signal for 2 g variation. Since the resonance frequency depends on the shape of the transducer and the way it is mounted on top of the shaker, this sensor seems to be particularly interesting as vibration detector for a specific frequency. When the shaker vibrates at the resonance frequency of the sensor, it can provide accurate information about the acceleration magnitude, thanks to its high sensitivity.

These promising results encourage further developments of the presented sensor which might be potentially implemented on paper substrate [3], thus resulting in a light sensor feasible to be mounted on mobile platform, such as drones, without interfering with its operation.

References

1. Gu, X., Srinaga, N.N., Guo, L., Hemour, S., Wu, K.: Diplexer-based fully passive harmonic transponder for sub-6-GHz 5G-compatible IoT applications. IEEE Trans. Microw. Theory Techn. **67**(5), 1675–1687 (2019)
2. Laskovski, A.N., Yuce, M.R., Moheimani, S.R.: Ultra low frequency FM sensing of piezoelectric strain voltage. In: SENSORS 2012, pp. 1–4. IEEE (2012)
3. Mariotti, C., Alimenti, F., Roselli, L., Tentzeris, M.M.: High-performance RF devices and components on flexible cellulose substrate by vertically integrated additive manufacturing technologies. IEEE Trans. Microw. Theory Techn. **65**(1), 62–71 (2016)
4. Palazzi, V., et al.: Low-power frequency doubler in cellulose-based materials for harmonic RFID applications. IEEE Microw. Wireless Compon. Lett. **24**(12), 896–898 (2014)
5. Palazzi, V., Gelati, F., Vaglioni, U., Alimenti, F., Mezzanotte, P., Roselli, L.: Leaf-compatible autonomous RFID-based wireless temperature sensors for precision agriculture. In: 2019 IEEE Topical Conference on Wireless Sensors and Sensor Networks (WiSNet). IEEE (2019)
6. Simoncini, G., et al.: Zero-power vibration sensor for wireless harmonic systems based on a reflection-type phase shifter and a piezoelectric transducer. In: 2022 IEEE Topical Conference on Wireless Sensors and Sensor Networks (WiSNeT), pp. 47–49. IEEE (2022)
7. Solutions, S.: A varactor controlled phase shifter for PCS base station applications. Application Note-Skyworks Solutions Inc. (2009)

A 0.8 mW TinyML-Based PDM-to-PCM Conversion for In-Sensor KWS Applications

Paola Vitolo[1]([✉]) , Rosalba Liguori[1] , Luigi Di Benedetto[1] ,
Alfredo Rubino[1] , Danilo Pau[2] , and Gian Domenico Licciardo[1]

[1] Department of Industrial Engineering, University of Salerno,
Via Giovanni Paolo II, 132, 84084 Fisciano, SA, Italy
{pvitolo,ldbenedetto,arubino,gdlicciardo}@unisa.it
[2] System Research and Application, STMicroelectronics,
20864 Agrate Brianza, MB, Italy
danilo.pau@st.com

Abstract. This paper proposes an ultra-low-power hardware architecture of a tiny machine learning (tinyML)-based conversion from Pulse Density Modulation (PDM) to Pulse Code Modulation (PCM). A hardware-aware efficient design of this conversion is essential to interface digital MEMS microphones, which outputs PDM signals, with audio processing systems, which takes PCM signals, in scenarios of in-sensor computing Keyword Spotting (KWS) applications. Neural network methods are used in a view to effectively combine the proposed converter with tinyML KWS systems, realizing an end-to-end KWS application. The proposed converter consists of a 1-D Convolutional Neural Network, which has been 8-bit quantized to reduce the computational complexity while preserving a 48 dB of Signal-to-Noise Ratio. The hardware accelerator has been implemented on a Xilinx Artix-7 FPGA, achieving a dynamic power consumption (DynP) of 182 µW, a utilization of 917 LUTs and 361 FFs. When the proposed converter is used in the KWS pipeline, the classification accuracy is 89% over 12 classes. Synthesis results in TSMC 0.13 µm CMOS report an area of $0.086\,\text{mm}^2$ and a DynP of 837 µW, making it possible to integrate the converter into the sensor integrated circuit.

Keywords: PDM-to-PCM conversion · In-Sensor Computing · tinyML · Keyword spotting · Neural networks

1 Introduction

With the rapid spread of the Internet-of-Things, more and more sensors are deployed, resulting in a sharp increase in the amount of generated data [1]. Shifting part of the data processing closer to the edge devices has become
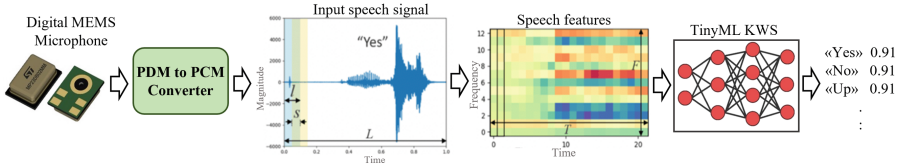
Fig. 1. Pipeline of a KWS system.

increasingly necessary to avoid redundant data transfers between sensing and processing units, reducing energy consumption, saving communication bandwidth, and improving data security and privacy. In-Sensor Computing (ISC) represents the extreme level of this shifting, where the processing is moved close\in the sensors [2–7]. However, the hardware (HW) constraints in terms of area and power are extremely severe. One of the applications for which this context is very attractive is KeyWord Spotting (KWS) [8]. It is becoming one of the most important building blocks in Human-Machine Interface (HMI) solutions, in several application fields, from domotics to automotive systems, to handheld devices. To be used in ISC, the entire KWS pipeline depicted in Fig. 1, from the sensor to the application's output, has to meet the HW ISC constraints. However, very few works in the literature deal with the design of the interface between KWS processing systems and the data source: the microphone. Output of digital Micro Electro-Mechanical System (MEMS) microphones is encoded with a Pulse Density Modulation (PDM), which has a sampling rate in the MHz range and uses 1-bit coding, while digital audio processing requires Pulse Code Modulation (PCM) signals, generally encoded with 8 bits and sampling range in the kHz range for KWS applications [9,10]. Nowadays, the most HW-aware efficient methods for this conversion are based on Cascaded Integrator-Comb (CIC) filters [11]. However, so far, in 130 nm CMOS technology, which is the most used technology node for MEMS fabrication, they are neither low power nor small enough to be integrated close to the sensor [12]. To overcome the above limitations and with a view to effectively combine the converter with tinyML KWS systems [13], this work proposes a new low-power PDM-to-PCM converter based on artificial neural network that meet the ISC constraints. The proposed system consists of a 1-D Convolutional Neural Network (1D-CNN), whose choice allows to easily implement the decimation through the stride parameter, to reduce the memory compared to dense networks, and to reduce area occupation in the HW design [14–16]. The model has been 8-bit quantized by using TensorFlow (TF) and QKeras frameworks to reduce the computational complexity while preserving its Signal-to-Noise Ratio (SNR). An optimized custom HW accelerator has been designed in VHDL to find a good trade-off between processing speed and the number of physical resources. Although quantized, the proposed system achieves a SNR of 48 dB while it shows a dynamic power consumption of 182 µW and a utilization of 917 LUTs and 361 FFs when implemented on a Xilinx Artix-7 FPGA. To demonstrate that the proposed converter can be used effectively in KWS system pipelines, it has been used as input block of a tinyML KWS system, obtaining 89% classification accuracy

Table 1. Number of recordings of each word of the created dataset

Word	Down	Up	Left	Right	Yes	No	Go	Stop	off	On	Silence	Unknown
# of Utterances	100	100	100	100	100	100	100	100	100	100	100	100

over 12 classes. To explore the suitability of in-sensor integration, the proposed converter has been synthesized with TSMC 0.13 µm CMOS standard cells. The results report an area occupation of $0.086\,mm^2$ and a DynP of 128.7 µW/MHz, making it possible to integrate the proposed design into the CMOS circuitry that equips digital MEMS microphones.

2   Proposed Model

Figure 2.a depicts the proposed PDM-to-PCM converter. It takes as input PDM signals from digital MEMS microphones and outputs PCM signals. PDM signals have a sampling rate of 2.048 MHz and encoded with 1-bit, while PCM signals have a bit depth of 8 bits and a sampling rate of 16 kHz. The proposed converter is based on a tiny CNN, chosen because it has fewer parameters than fully connected networks, thus requiring fewer parameters. Furthermore, the stride parameter can be exploited to implement decimation. The proposed model consists of: an input shape of 2,048,000 samples, encoded with 1 bit; a convolutional layer (CONV1D_1) with 1 channel, same padding, 64 kernel size, and 64 strides; a second convolutional layer (CONV1D_2) with 1 channel, same padding, 23 kernel size, 2 strides, and (1) as activation function. The output shape of CONV1D_1 is 32,000, encoded with 8 bits.

$$y = tanh(x) = \frac{e^x - e^{-x}}{e^x + e^{-x}}. \tag{1}$$

To train and evaluate the proposed models, a custom PDM-PCM dataset has been created. The Google Speech Commands Dataset (GSCD) shown in [17] has been used to extract the PCM values and labels. Then, the PCM values have been preprocessed and converted in PDM format by using the Delta Sigma Toolbox (DST) in Matlab [18], setting the order of sigma delta ADC to 4 and the OverSampling Ratio (OSR) to 128. As reported in Table 1, the resulting balanced dataset consists of 100 utterances of 1 s for each one of the twelve classes, for a total of 1200 recordings, in PCM and PDM formats. The dataset has been split into training (80%), validation (10%), and test (10%) partitions. The converter has been modeled and trained using TF and QKeras frameworks. The number of epochs has been set to 150. A custom function, Fast-Fourier-Transform Mean Absolute Error (FFT-MAE) described in (2), has been set as loss function.

$$FFT_{MAE} = \frac{1}{n} \sum_{i=0}^{n} ||FFT(Y_i)| - |FFT(\hat{Y}_i)|| \tag{2}$$

To evaluate the model, FFT-MAE and MAE have been calculated on the test dataset, achieving 0.16 and 0.005, respectively. The SNR achieved with a 1 kHz

Table 2. Classification model summary

	Layer	Filt.	Size/Ker	Strides	Padd	Act Funct	Output
	Input	–	49×10	–	–	–	–
	Conv2D+BN	64	10×4	2×2	Same	ReLU	$25 \times 5 \times 64$
DSConv2D	DWConv2D+BN	–	3×3	1×1	Same	ReLU	$25 \times 5 \times 64$
$\times 4$	Conv2D+BN	–	3×3	1×1	Same	ReLU	$25 \times 5 \times 64$
	MaxPool2D	–	25×5	None	Valid	–	64
	Dense	–	64	–	–	None	64
	Dense	–	12	–	–	Softmax	12

sinusoidal input is 48 dB, which is only 4% lower than the theoretical maximum SNR with 8-bits quantization. To evaluate the deployability of the proposed converter into the KWS pipeline described in Fig. 1, we have modeled a KWS model based on a Depthwise Separable CNN. As reported in Table 2, it is composed of one 2D Convolution layer (Conv2D), four Depthwise Separable 2D Convolution layers (DSConv2Ds), one 2D Max Pooling layer (MaxPool2D), and two FC layers. The test dataset has been input to the proposed converter. Then, the Mel Frequency Cepstrum Coefficients (MFCCs) have been extracted from the converter. Finally, the MFCCs have been input to the KWS model. The results show an average accuracy of 92% accuracy over the 12 classes in Table 1.
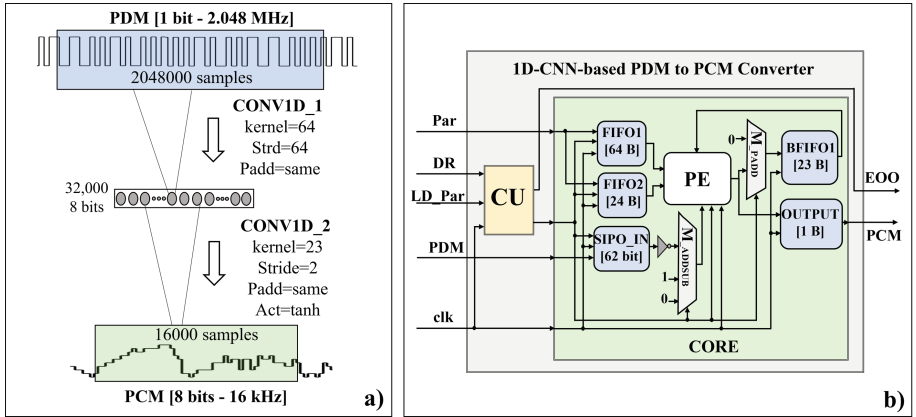
Fig. 2. Schema of the Proposed Converter: a) Proposed 1D-CNN model for the conversion; b) Block Diagram of the proposed HW accelerator.

3   Proposed HW Architecture

Figure 2b schematizes the HW architecture of the proposed converter. It consists of a processing block (CORE) and a Control Unit (CU). The CU is implemented

Table 3. FPGA and standard cells synthesis results.

–	FPGA	std cells
Platform	Xilinx Artix 7	TSMC 130 nm CMOS
FF	361	–
LUT	917	–
Area [mm^2]	–	0.086
Total Power [mW]	104.182	844.45×10^{-3}
Static Power [mW]	104	7.45×10^{-3}
Dynamic Power [mW]	0.182	837×10^{-3}
Maximum Clk Freq. [MHz]	45	200

by using a Finite State Machine and generates all the control signals necessary to manage the flow of the data. The CORE recursively performs all the operations necessary for the implementation of the network layers. It consists of one Processing Element (PE), which features arithmetic operations; multiplexers, to properly route the signals; and registers, to store the parameters of the network, partial results, and the incoming data. The total memory required is 958 bits.

4   Results

Table 3 reports the results of the implementation of the proposed HW architecture on a Xilinx Artix-7 (xc7a35tfgg484-1) FPGA and the synthesis with TSMC 130 nm CMOS. The clock frequency has been set to 6.5 MHz, which ensures the real-time processing. The FFs and LUTs mapped on the FPGA are 361 and 917, respectively. The total power on FPGA is 104.182 mW, with only 0.182 mW of dynamic power. The total power in standard cells, estimated through Cadence Joules RTL Power Solution using SAIF files, is 0.8 mW, with a marginal leakage power of 7.45 µW. The occupied area is 0.086 mm^2. These results enables a compact and ultra-low-power design that is well suited to the integration into the CMOS circuit that generally equips MEMS microphones.

5   Conclusions

A new decimation filter for audio PDM-to-PCM conversion by using a 1D-CNN and a custom HW accelerator synthetized in 130 nm CMOS technology have been presented. The accelerator shows very low energy and mapped physical resources compatible to be used in ISC scenarios for KWS applications. Future work will be aimed at optimizing the other blocks of the KWS pipeline, realizing an end-to-end KWS system for ISC applications.

References

1. Baccour, E., et al.: Pervasive AI for IoT applications: a survey on resource-efficient distributed artificial intelligence. IEEE Commun. Surv. Tutorials, 1 (2022)
2. Pan, W., Zheng, J., Wang, L., Luo, Y.: A future perspective on in-sensor computing. Engineering (2022). https://www.sciencedirect.com/science/article/pii/S2095809922001394
3. De Vita, A., et al.: A partially binarized hybrid neural network system for low-power and resource constrained human activity recognition. IEEE Trans. Circuits Syst. I Regul. Pap. **67**(11), 3893–3904 (2020)
4. Vitolo, P., et al.: Low-power anomaly detection and classification system based on a partially binarized autoencoder for in-sensor computing, pp. 1–5 (2021)
5. De Vita, A., et al.: Low power tiny binary neural network with improved accuracy in human recognition systems. In: 2020 23rd Euromicro Conference on Digital System Design (DSD), pp. 309–315. IEEE (2020)
6. Vitolo, P., et al.: Low-power detection and classification for in-sensor predictive maintenance based on vibration monitoring, pp. 6942–6951 (2022)
7. De Vita, A., et al.: Low-power HWAccelerator for AI edge-computing in human activity recognition systems. In: 2020 2nd IEEE International Conference on Artificial Intelligence Circuits and Systems (AICAS), pp. 291–295. IEEE (2020)
8. López-Espejo, I., Tan, Z.-H., Hansen, J.H.L., Jensen, J.: Deep spoken keyword spotting: an overview. IEEE Access **10**, 4169–4199 (2022)
9. Mishchenko, Y.: Low-bit quantization and quantization-aware training for small-footprint keyword spotting. In: 2019 18th IEEE International Conference On Machine Learning And Applications (ICMLA), pp. 706–711 (2019)
10. Vitolo, P., et al.: Quantized ID-CNN for a low-power PDM-to-PCM conversion in TinyML KWS applications. In: 2022 IEEE 4th International Conference on Artificial Intelligence Circuits and Systems (AICAS), pp. 154–157 (2022)
11. Da Silva, B., Segers, L., Braeken, A., Steenhaut, K., Touhafi, A.: Design exploration and performance strategies towards power-efficient FPGA-based architectures for sound source localization. J. Sens. (2019)
12. STMicroelectronics: Mems audio sensor omnidirectional digital microphone for industrial applications. IMP34DT05-Rev **4** (2021)
13. Mishchenko, Y.: Low-bit quantization and quantization-aware training for small-footprint keyword spotting. In: 2019 18th IEEE International Conference On Machine Learning And Applications (ICMLA), pp. 706–711 (2019)
14. De Vita, A., Pau, D., Di Benedetto, L., Rubino, A., Pétrot, F., Licciardo, G.D.: Highly-accurate binary tiny neural network for low-power human activity recognition. Microprocess. Microsyst. **87**, 104371 (2021)
15. Licciardo, G.D., Cappetta, C., Di Benedetto, L.: Design of a convolutional two-dimensional filter in FPGA for image processing applications. Computers **6**(2) (2017)
16. Licciardo, G.D., Cappetta, C., Di Benedetto, L.: FPGA optimization of convolution-based 2D filtering processor for image processing. In: 2016 8th Computer Science and Electronic Engineering (CEEC), Colchester, UK (2016)
17. Warden, P.: Speech commands: a dataset for limited-vocabulary speech recognition (2018). https://arxiv.org/abs/1804.03209
18. Schreier, R.: Delta sigma toolbox. MATLAB Cent. File Exch. https://www.mathworks.com/matlabcentral/leexchange/19deltasigmatoolbox

Optoelectronics and Photonics

Optical Power Screening Effects
in Ge-on-Si Vertical *Pin* Photodetectors

Matteo G. C. Alasio[1]([✉]) , Paolo Franco[1], Alberto Tibaldi[1,2] ,
Francesco Bertazzi[1,2] , Soha Namnabat[3], Donald Adams[3],
Prakash Gothoskar[3], Gianlorenzo Masini[3], Fabrizio Forghieri[3],
Giovanni Ghione[1] , and Michele Goano[1,2]

[1] Dipartimento di Elettronica e Telecomunicazioni, Politecnico di Torino, Corso Duca
degli Abruzzi 24, 10129 Turin, Italy
`matteo.alasio@polito.it`
[2] IEIIT-CNR, Corso Duca degli Abruzzi 24, 10129 Turin, Italy
[3] Cisco Systems, 7540 Windsor Drive, Suite 412, Allentown, PA 18195, USA

Abstract. We present an experimental and numerical study on the
effects of the input optical power on the electro-optic frequency response
of a Ge-on-Si vertical *pin* waveguide photodetector. Experimental results
were provided by Cisco Systems, which characterized several nominally
identical devices. Increasing the optical power from $-2\,$dBm to $3\,$dBm, a
significant decrease of the electro-optic frequency response was observed
in the O-band, from about $40\,$GHz down to approximately $32\,$GHz.
This trend is accurately predicted by our 3D multiphysics model, where
Maxwell's equations are solved with the FDTD method to evaluate the
spatial distribution of photogenerated carriers, which is then converted
in an optical generation rate included in the drift-diffusion solver. The
3D model provides a detailed explanation of the experiments by showing
the effects of carrier screening on the magnitude of the electric field pro-
file, which is reduced for high optical power, slowing the photogenerated
carriers and reducing the bandwidth.

Keywords: Silicon photonics · Device multiphysics modeling ·
Ge-on-Si waveguide photodetectors · Waveguide photodetectors ·
Germanium · 3D modeling

1 Introduction

We have investigated, both experimentally and through multiphysics numerical
simulation, the behavior of a Ge-on-Si waveguide photodetector with vertical
pin junction for increasing input optical power. A 3D perspective view and
a cross-section of the device are shown in Fig. 1, while the main geometrical
parameters are reported in Table 1. The metallic contacts are placed on top of
the Ge absorber and laterally on the Si substrate. High dopant densities are
present both in the substrate and at the metal/Ge interface, while most of Ge

is undoped. An optical waveguide is connected to the silicon substrate with a tapered transition, and the light is evanescently coupled in the Ge absorber [2].

This kind of photodetector, widely employed in silicon photonics [8], is commonly operated at input optical powers in the µW range. We have studied the extent of the performance drop when increasing the input optical power to the mW range, observing a reduction in the electro-optic frequency response bandwidth [4, Sec. 4.9] of more than 20 %.
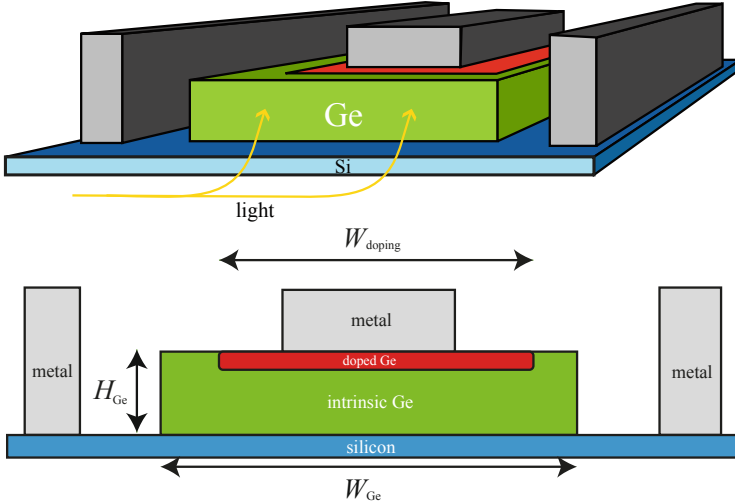
Fig. 1. Perspective view of the waveguide photodetector (top) and its transverse cross section (bottom). The Ge absorber, of length L_{Ge}, is grown over an highly doped Si substrate. The metallic contacts are placed laterally on Si and on top of the Ge absorber, where a highly doped region is present.

Table 1. Photodetector geometry.

W_{Ge}	H_{Ge}	L_{Ge}	W_{doping}
4 µm	0.8 µm	15 µm	3 µm

2 Methodology

We adopt a multiphysics approach to solve the optical and electrical problems with the finite-difference time-domain (FDTD) method and the drift-diffusion model, respectively, as implemented in Synopsys RSoft FullWAVE [11] and in the Synopsys TCAD Sentaurus suite [10]. The simulation process, whose flow is reported in Fig. 2, and the adopted model parameters are discussed in [7]. The optical generation rate G_{opt}, evaluated by solving Maxwell's equations, is

included as a source term in the electrical transport problem. Due to the evanescent coupling of the light in the absorber, this source term has a complex spatial distribution along the device, and a 3D representation is needed [1].

This work is focused on the O-band of optical communications, centered around $\lambda = 1.31\,\mu m$, where the absorption of Ge is higher [9] and the device performance is expected to be significantly more sensitive to the input optical power than in the C-band.

The experimental setup used in Cisco Systems is based on a Keysight LCA [6], which allows electro-optic measurements up to 50 GHz. Five nominally identical photodetectors, taken from different wafer regions, were characterized, determining mean value and standard deviation of the electro-optic cutoff frequency at different input optical powers for all the samples.
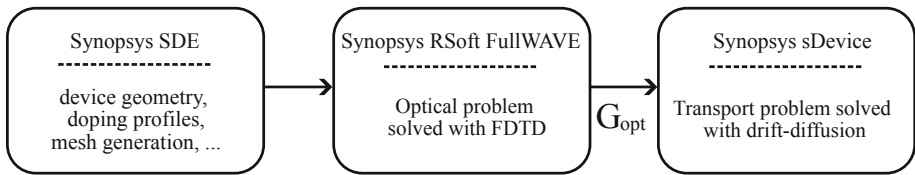
Fig. 2. Block diagram of the simulation flow in the modeling process. First, we define the device geometry, doping distributions and mesh. Then we use FDTD to extract the 3D spatial distribution of the optical generation rate G_{opt}. Finally, drift-diffusion provides a solution of the electrical problem by using G_{opt} as a source term.

3   Results

Figure 3 compares measurements and simulations of the electro-optic cutoff frequency at a reverse bias of 3 V and at different optical powers as measured at the laser output. (The optical power assigned in the simulations takes into account the losses between laser and detector due to fiber coupling and waveguide propagation, estimated to be 3 dB overall.)

In the figure, along with the simulation results (blue dots), are reported the mean values of the experimental electro-optic cutoff frequencies over five nominally identical devices (black dots), while the error bars represent the standard deviation of the measurements. An excellent match between measurements and simulations is observed for all the measured powers.

Increasing the optical power from -2 dBm to 3 dBm, the electro-optic cutoff frequency is reduced by more than 20%. This decrease can be explained in terms of a reduction of the carrier velocity due to a screening of the electric field in Ge by the photogenerated carriers. The magnitude of this effect is shown in Fig. 4, which reports the absolute value of the electric field evaluated along a 1D vertical cut, from metal to silicon substrate, near the beginning of the absorber. At low input optical power (10 μW) the electric field is coincident with its profile in dark. On the contrary, at an optical power of 500 μW, the peak value of the electric field is reduced by a factor 3. This drop affects the device performance
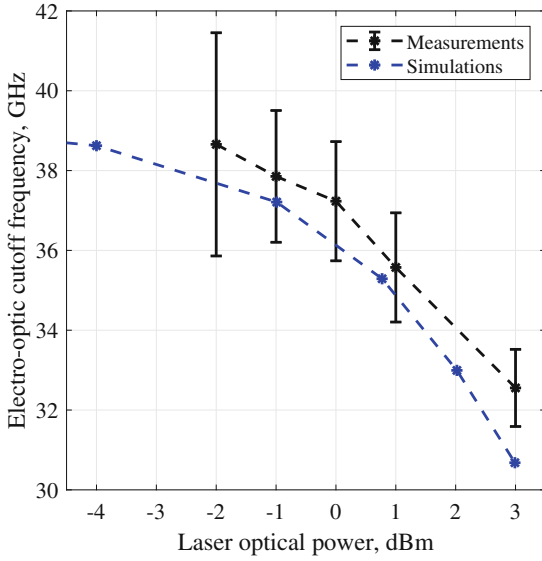
Fig. 3. Electro-optic cutoff frequency as a function of the optical power measured at the laser output.
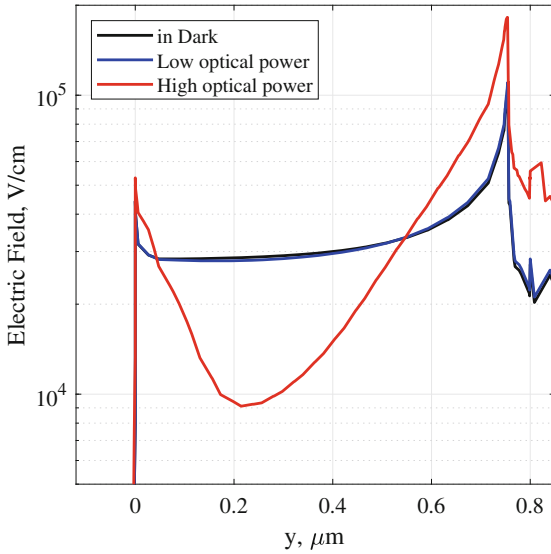
Fig. 4. Magnitude of the electric field in Ge along a 1D vertical cut between the center of the top metal contact and the silicon waveguide, at a distance of 1 μm from the front section of the absorber.

since the photogenerated carriers do not reach the saturation velocity, hence decreasing the electro-optic cutoff frequency.

4   Conclusions

The screening effect we have observed is a nonnegligible limitation to the performance of waveguide photodetectors in the O-band and should be taken into account in the device design. The excellent match demonstrated here between measurements and simulations suggest that the multiphysics 3D modeling approach provides a realistic description of this effect and can be used as an effective tool in the device optimization towards the new 200 Gbit/s applications [3,5].

References

1. Alasio, M.G.C., et al.: Modeling the frequency response of vertical and lateral Ge-on-Si waveguide photodetectors: Is 3D simulation unavoidable? In: 2022 Conference on Lasers and Electro-Optics (CLEO), San Jose, CA, May 2022. https://doi.org/10.1364/CLEO_AT.2022.JW3A.28
2. Beling, A., Campbell, J.C.: High-speed photodiodes. IEEE J. Select. Topics Quantum Electron. **20**(6), 3804507 (2014). https://doi.org/10.1109/JSTQE.2014.2341573
3. Chen, D., Zhang, H., Liu, M., Hu, X., Zhang, Y., Wu, D., Zhou, P., Chang, S., Wang, L., Xiao, X.: 67 GHz light-trapping-structure germanium photodetector supporting 240 Gb/s PAM-4 transmission. Photon. Res. **10**(9), 2165–2171 (2022). https://doi.org/10.1364/PRJ.455291
4. Ghione, G.: Semiconductor Devices for High-Speed Optoelectronics. Cambridge University Press, Cambridge (2009)
5. Hu, W., Xie, X., Xu, Q., Zhang, W., Song, H.: Research progress of SiGe heterojunction photodetectors. In: Seventh Symposium on Novel Photoelectronic Detection Technology and Applications, vol. 11763, Proceedings of the SPIE, p. 11763A4. Kunming, China, March 2021. https://doi.org/10.1117/12.2588373
6. Technologies, K.: Santa Rosa. Lightwave Component Analyzer application notes, CA (2017)
7. Palmieri, A., et al.: Heterostructure modeling considerations for Ge-on-Si waveguide photodetectors. Opt. Quantum Electron. **50**(2), 1–10 (2018). https://doi.org/10.1007/s11082-018-1338-y
8. Soref, R.: The past, present, and future of silicon photonics. IEEE J. Select. Topics Quantum Electron. **12**(6), 1678–1687 (2006). https://doi.org/10.1109/JSTQE.2006.883151
9. Sorianello, V., et al.: Low-temperature germanium thin films on silicon. Opt. Mater. Express **1**(5), 856–865 (2011). https://doi.org/10.1364/OME.1.000856
10. Synopsys Inc, Sentaurus Device User Guide. Version N-2017.09, Mountain View, CA, September 2017
11. Synopsys Inc, Optical Solutions Group, RSoft FullWAVE User Guide, Ossining, NY, v2019.09 (2019)

Silicone Embedded FBGs for Force Sensing

P. Di Palma, E. De Vita, A. Iadicicco, and S. Campopiano$^{(\boxtimes)}$

Department of Engineering, University of Naples "Parthenope", Naples, Italy
stefania.campopiano@uniparthenope.it

Abstract. Force sensing is spreading in many fields, spanning from biomedicine to robotics. Commercial and traditional solutions include strain gauges and micro-electro-mechanical systems, that however exhibit drawbacks related to their electrical nature, fragility, and not flexible structure. Therefore, in this work, a flexible force sensor based on the fiber Bragg grating (FBG) embedded in a silicone patch is proposed and characterized. Silicone embedding represents the solution for handling a soft, stretchable, safe, and skin-mountable force sensor suitable for human interactions. Force tests are reported and demonstrate the silicone patch capability to make the FBG sensitive to force variations with good linearity and a force sensitivity of 17.6 pm/N. Moreover, the performances of the developed patch in terms of temperature and strain are compared with respect to the more traditional FBGs embedded in 3D printed PLA patch. The comparison reveals the strong influence, and complementarity, of the patch materials employed for the embedding on the sensing potentialities of the final devices.

Keywords: Fiber Bragg grating · Fiber optic sensor · Force sensor · Silicone embedding

1 Introduction

Fiber Bragg gratings (FBGs) represent a sensing solution able to provide many advantageous features, from wavelength division multiplexing to immunity to electromagnetic interferences, non-toxicity, biocompatibility, and electrical safety. A peculiar aspect is given by their small size, which makes them suitable for easy installation and embedding procedures into a variety of materials and structures. FBG-embedding strategies can be implemented for several reasons: i) for sensing purposes, i.e., to make FBGs responsive to specific parameters, such as pressure [1], curvature [2], and 3D shape [3]; ii) to package the sensing element aiming to protect the fragile regions of the optical fiber, [4]; iii) to enable smart structures, by integrating them with FBGs for design validation and damage detection [5], or by sensorizing robotic fingers and skin [6].

One of the FBG embedding techniques is represented by the embedding during manufacturing, with which the optical fiber is directly integrated into the composite laminate during its manufacturing. For this reason, 3D printing based on the fused deposition method (FDM), which lies in a continuous stacking of physical layers, matches well with FBG embedding needs. By implementing this strategy, FBGs can be easily

embedded in patches made with resin and plastic materials like acrylonitrile butadiene styrene (ABS) and polylactic acid (PLA) [7, 8].

However, due to the arising interest in biomedical purposes, robotics applications and, more specifically, soft robots in domestic and healthcare environments, the demand for flexible, skin-mountable, and wearable electronic devices is increasing toward safer sensing systems able to smoothly interact with the human body as well as to handle fragile objects. Therefore, in this work, silicone matrix has been investigated and used as substrate material to realize a flexible FBG-based patch. Thanks to the embedding inside the silicone matrix, the FBG not only can be protected in a soft material able to adapt its shape to the environment but has proved also to be sensitive to the variations of transversal forces acting. Such sensor overcomes the typical disadvantages of traditional electrical force sensors, being flexible, stretchable, and with a moldable shape [9].

The aim of this work is to quantitatively describe the performances of the developed silicone FBG-based patch and to compare it with FBGs embedded in more traditional materials, such as 3D printed PLA patches. Results show that silicone embedding insulates the FBG from strain variations while allowing measurements of force variations acting on the patch.

2   Materials and Methods

The proposed sensor consists in a silicone flexible patch embedding an FBG having a length of 10 mm and positioned at the center of the patch.

An FBG is a periodic perturbation of the refractive index in the optical fiber core witch, in presence of a broadband light, reflects a very narrow band centered around the Bragg wavelength (i.e., λ_B), specific for that FBG [10]. Since both thermal and strain variations induce a λ_B shift, FBGs are sensitive to both these parameters by means of a thermal and strain sensitivity, which typical values are 10 pm/°C and 1.2 pm/$\mu\varepsilon$, respectively, for a bare FBG.

In a preliminary phase, the process to realize the sensing device involved the 3D printing technology to realize the mold in which the silicone patch has been obtained afterward. In particular, Renkforce RF500 3D printer and the FDM have been employed for manufacturing the mold in PLA filament, produced by Renkforce. Once printed the mold, the fabrication of the FBG embedded in the silicone matrix was performed in six stages, as described in Fig. 1.
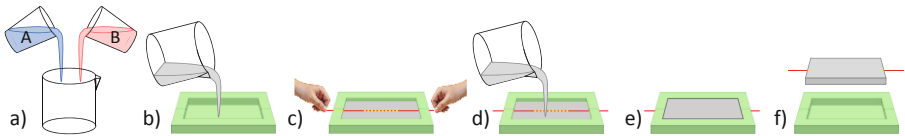
Fig. 1. Fabrication steps of the silicone patch embedding the FBG sensor: a) mixing of the two silicone components; b) pouring of half of the mixture in the mold; c) FBG positioning; d) pouring of the remaining half of the silicone; e) curing; f) patch extraction from the mold.

The process started with the preparation of the silicone matrix, i.e., Dragon Skin™ (DS) 10 Medium, by mixing its two components in equal amounts (Fig. 1a). Then, half

of the mixture was poured in the mold (Fig. 1b), in such a way that the optical fiber containing a bare FBG could be positioned in the center (Fig. 1c); subsequently, the remaining mixture was poured over (Fig. 1d). Finally, after a curing time of five hours (Fig. 1e), the device was removed from the mold, obtaining a silicone patch, 2.5 mm thick, ready to be used (Fig. 1f).

3   Results and Discussion

In this section, the results of the thermal and strain characterizations of the silicone patch are reported and compared with the ones obtained by a previously developed 3D printed PLA patch, 1.8 mm thick embedding an FBG having a length of 10 mm (as for the FBG embedded in the silicone patch) [11]. Moreover, the force characterization is reported, demonstrating the silicone embedding capability to make FBGs sensitive to force variations acting on the patch.

The results related to the thermal characterization are reported in Fig. 2. In particular, Fig. 2a shows the schematic of the experimental setup used during the thermal tests, whereas Fig. 2b reports the profiles of Bragg wavelength variation $\Delta\lambda$ as function of temperature T recorded by the silicone (in red) and the PLA (in blue) patches, each one compared with the profile recorded by the bare FBG (in black). Beyond optical interrogator, FBG patches, and PC to process sensor data, the experimental setup includes a thermal chamber to perform the tests from 5 °C to 40 °C.
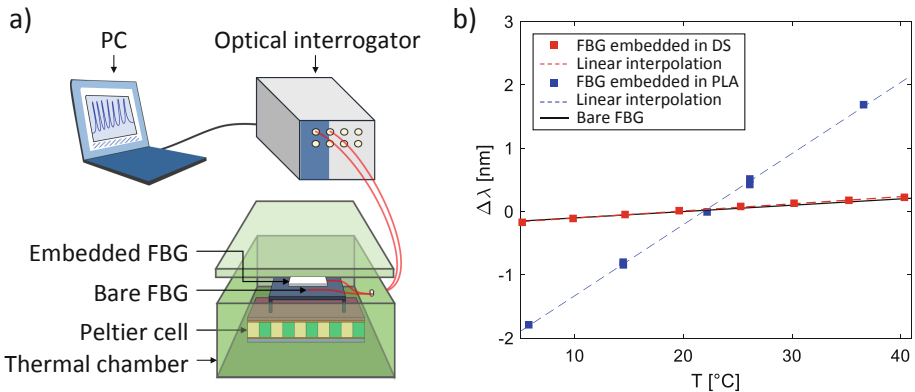
Fig. 2. Thermal characterization: sketch of the implemented experimental setup (a) trends of $\Delta\lambda$ as function of T recorded by the FBG embedded in the silicone patch, in red, and the one embedded in the PLA patch, in blue (b). Black profile corresponds to the bare FBG.

Trends reported in Fig. 2b show a linear behavior in temperature for both patches but with very different thermal sensitivities, i.e., 11.3 pm/°C for the silicone patch and 112.3 pm/°C for the PLA patch. Such results reveal that silicon matrix causes only a slight increase of the thermal sensitivity of the bare FBG, whereas the PLA is responsible for a noticeable thermal sensitivity increase of more than ten time, due to the higher thermal expansion coefficient of the PLA, which is around 80 μm·m^{-1}·°C^{-1} against

$6\ \mu m \cdot m^{-1} \cdot {}^\circ C^{-1}$ of the silica. Actually, the silicone thermal expansion coefficient is about four times higher than PLA one, but the measured sensitivity value is close to the bare FBG sensitivity due to the high elasticity of the silicone.

Concerning the tests for the strain characterization, the experimental setup shown in in Fig. 3a was used: to induce a strain variation in the embedded FBGs, both silicone and PLA patches were bonded on a beam together with a bare FBG as reference, and the beam was bent by means of loads ranging from 2 kg to 6 kg.
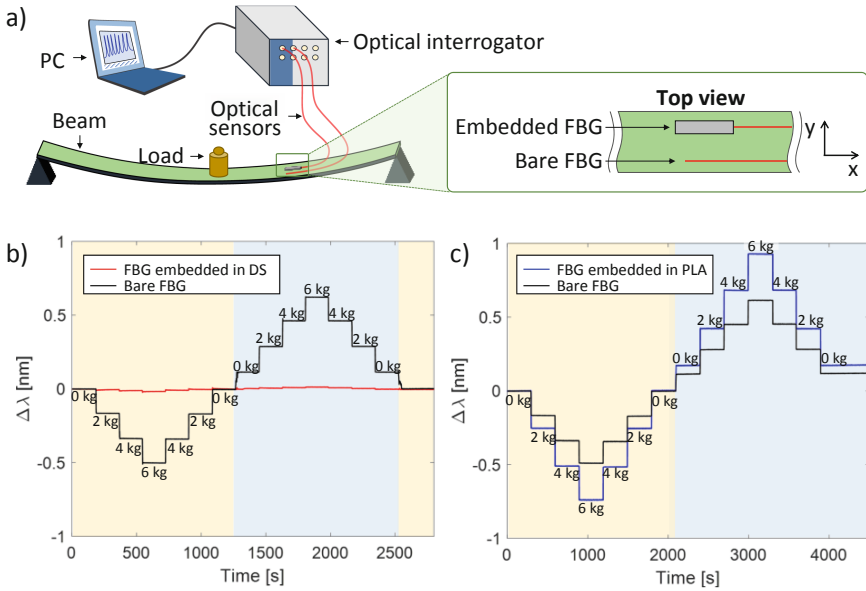
Fig. 3. Strain characterization: sketch of the implemented experimental setup (a) trends of $\Delta\lambda$ as function of time recorded by the FBG embedded in the silicone patch, in red (b) and the one embedded in the PLA patch, in blue (c). Profiles steps correspond to increasing and decreasing loads, whereas the profile recorded by the bare FBG is reported in black. The yellow and blue squares in (b) and (c) correspond to the test performed with the sensors on the upper and bottom sides of the beam, respectively.

Figure 3b and Fig. 3c report the $\Delta\lambda$ profiles as function of time recorded by the silicone (in red) and PLA (in blue) patches, respectively, whereas the profile recorded by the bare FBG is shown in black. These results demonstrate that, the PLA patch preserves the same strain sensitivity of the FBG bare (i.e., 1.2 pm/$\mu\varepsilon$), since the slight increase of the sensitivity value is not due to the plastic material, but rather to the higher distance of the embedded FBG from the neutral axis with respect to the bare one. On the contrary, silicone embedding does not transmit the strain solicitation from the external surface of the patch to the internal FBG, resulting in the insulation of the sensor from strain variations. Indeed, the strain sensitivity of the silicone patch is $3.1 \cdot 10^{-2}$ pm/$\mu\varepsilon$.

The measured thermal and strain sensitivities for the bare FBG and the FBGs embedded in silicone and PLA patches are summarized in Table 1.

Table 1. Silicone embedded, PLA embedded, and bare FBGs: comparison among their temperature and strain sensitivities.

	Temperature sensitivity [pm/°C]	Strain sensitivity [pm/με]
FBG in silicone patch	11.3	$3.1 \cdot 10^{-2}$
FBG in PLA patch	112.3	1.2
Bare FBG	10.0	1.2

Finally, force characterization proves the capability of the developed silicone patch to measure force variations exerted on the patch itself. The working principle is based on the expansion of the silicone matrix in the plane orthogonal with respect to the compression direction when a distributed load is applied to the upper surface of the patch, as shown in Fig. 4a.
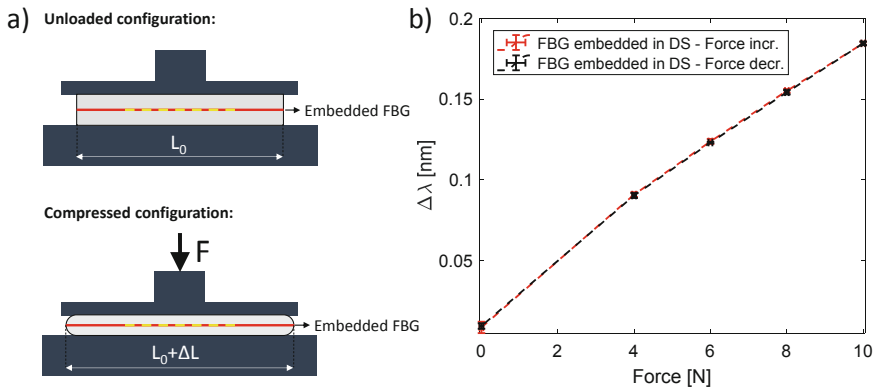
Fig. 4. Force characterization: sketch of the implemented experimental setup (a) and trend of $\Delta\lambda$ recorded by the FBG embedded during force increasing (in red) and decreasing (in black).

The force characterization result is reported in Fig. 4b. A force sensitivity of 17.6 pm/N was found, demonstrating good linearity, repeatability, and absence of hysteresis in the investigated range, i.e., from 0 to 10 N.

4   Conclusions

In conclusion, this work demonstrates the effectiveness of silicone embedded FBGs for force sensing, realizable by means of a simple fabrication process and a low-cost setup. Several novelties are worth to be highlighted in comparison to literature, such as the device flexibility due to the silicone material, allowing to obtain a sensing device easily adaptable to irregular supports. Moreover, the sensor is not affected by tensile strain, differently from the common embedded sensors reported in literature.

It is worth noting that the developed silicone patch shows complementary performances with respect to the previously developed 3D printed patch in PLA, as demonstrated by the experimental results reported in Fig. 2 and Fig. 3. Indeed, while PLA patch increases the temperature sensitivity of the FBG, keeping constant the strain sensitivity, the silicone patch desensitizes the FBG with respect to strain variations, keeping almost constant its thermal sensitivity and making the FBG sensitive to the force variations acting on the patch. These results lead to a flexible FBG-based patch with a strain sensitivity independent from the material where the patch is fixed and facilitating the temperature compensation operation.

References

1. Hong, C., Zhang, Y., Borana, L.: Design, fabrication and testing of a 3D printed FBG pressure sensor. IEEE Access. **7**, 38577–38583 (2019)
2. Di Palma, P., Iadicicco, A., Campopiano, S.: Curvature sensor based on FBGs embedded in 3D printed patches. IEEE Sens. J. **21**(16), 17868–17874 (2021)
3. Di Palma, P., De Vita, E., Iadicicco, A., Campopiano, S.: 3D shape sensing with FBG-based patch: from the idea to the device. IEEE Sens. J. **22**(2), 1338–1345 (2022)
4. Manzo, N. R., Callado, G.T., Cordeiro, C.M, Vieira Jr., L.C. M.: Embedding optical fiber Bragg grating (FBG) sensors in 3D printed casings. Opt. Fiber Technol. **53**, 102015 (2019)
5. Beukema, R.P.: Embedding technologies of FBG sensors in composites: technologies, applications and practical use. In: 6th European Workshop on Structural Health Monitoring, Dresden (EWSHM 2012), vol. 3 (2012)
6. Park, Y.-L., Chau, K., Black, R.J., Cutkosky, M.R.: Force sensing robot fingers using embedded fiber Bragg grating sensors and shape deposition manufacturing. In: Proceedings 2007 IEEE International Conference on Robotics and Automation, pp. 1510–1516. IEEE (2007)
7. Di Palma, P., Iadicicco, A., Campopiano, S.: FBGs in 3D printed objects monitoring. In: 2021 IEEE International Workshop on Metrology for Industry 4.0 IoT, pp. 182–186. IEEE (2021)
8. Lin, Y.K., Hsieh, T.S., Tsai, L., Wang, S.H., Chiang, C.C.: Using three-dimensional printing technology to produce a novel optical fiber Bragg grating pressure sensor. Sens. Mater. **28**(5), 389–394 (2016)
9. Tarchanidis, K.N., Lygouras, J.N.: Data glove with a force sensor. IEEE Trans. Instrum. Meas. **52**(3), 984–989 (2003)
10. Hill, K.O., Meltz, G.: Fiber Bragg grating technology fundamentals and overview. J. Lightwave Technol. **15**(8), 1263–1276 (1997)
11. Di Palma, P., Iadicicco, A., Campopiano, S.: Study of fiber Bragg gratings embedded in 3d-printed patches for deformation monitoring. IEEE Sens. J. **20**(22), 13379–13386 (2020)

A New Way of Using Plasmonic Phenomena in Optical Fibers to Realize Highly Sensitive Sensors: What Prospects?

Nunzio Cennamo[✉], Francesco Arcadio, Domenico Del Prete, and Luigi Zeni

Department of Engineering, University of Campania Luigi Vanvitelli, Aversa, Italy
`nunzio.cennamo@unicampania.it`

Abstract. A novel sensing approach has been presented. The Surface Plasmon Resonance (SPR) and the properties of multimodal plastic optical fibers (POFs) have been used to implement this novel approach. For instance, the proposed sensor systems harnessing this method have been designed, realized, and tested to detect a magnetic field, temperature, and force. More in detail, the physical quantity under test interacts with a sensitive patch (a modified multimode POF), changing the light mode profile at the input of an SPR-POF platform combined with a dielectric medium at a fixed refractive index. This method allowed to use of the SPR platform without any additive sensing layer, obtaining very interesting results compared to the traditional plasmonic sensing approach.

Keywords: Multimode optical fibers · Surface Plasmon Resonance (SPR) · Plastic optical fibers (POFs) · Optical sensors

1 Introduction

In the last years, great importance has been achieved from the Surface Plasmon Resonance (SPR) phenomenon. It is a very sensitive technique to detect a small variation of refractive index at the interface between a metallic nanofilm and a dielectric medium. When the resonance condition is satisfied, strong light absorption occurs, and a dip at a particular wavelength appears in the transmitted spectra, related to the refractive index at the interface. This phenomenon has been coupled with optical fiber probes, in order to obtain different sensor systems useful in several application fields [1, 2]. More specifically, the SPR sensors can be obtained by using both mono-mode or multimode fibers; in the case of multimode fibers, the SPR phenomenon can be more easily excited, and, for this reason, optical fiber sensors based on this type of fiber are widespread. In the multimodal fibers, the absorption caused by the SPR phenomenon is a result of a convolution of different resonance wavelengths, each related at a different incident angle [3, 4].

In this work, a new measurement approach has been used by exploiting the properties of the multimode fibers in SPR. In particular, a modified optical fiber patch sensitive to a specific physical quantity is used to trigger the SPR phenomenon into a cascaded

SPR D-shaped POF platform [4]. So, in the proposed sensors, the sensing layer is not present on the metal film in the plasmonic region. Different tests have been reported to characterize several sensor systems based on the proposed method. Moreover, for each sensor, a comparative analysis has been carried out in terms of sensitivity and resolution.

2 Principle of Sensing and Experimental Setup

The proposed sensor systems consist of two parts connected in a cascade: the first one is a patch of multimode POF sensitive to the quantity of interest, whereas the second one is an SPR D-shaped POF platform, extensively described in [4]. The refractive index of the dielectric medium on the plasmonic platform is kept fixed while the quantity of interest interacting with the sensitive patch varies. Thanks to the properties of multimode fibers, when the quantity of interest varies, there is a variation in the guided mode profile in the sensitive optical fiber patch used to launch the light into the SPR platform. In other words, the variation in the quantity of interest changes the incident angles associated with the propagated modes in the SPR D-shaped POF platform, varying the plasmonic resonance condition (e.g., the resonance wavelength). The tuning of the plasmonic phenomenon has been used to deploy different sensor systems, such as for measuring the magnetic field, temperature, and force.

For each sensor system presented in this work, the simple required equipment consists of a white light source, a spectrometer, and a laptop. In particular, the white light source (HL–2000–LL, manufactured by Ocean Insight, Orlando, FL, USA) has a wavelength emission range from 360 nm to 1700 nm. It is connected to an optical fiber patch sensitive to the quantity of interest. The sensitive patch is connected in input to an SPR D-shaped POF chip. In the end, the light in the output of the SPR sensor is collected by a spectrometer (FLAME-S-VIS-NIR-ES, Ocean Insight, Orlando, FL, USA) with a detection range between 350 nm and 1000 nm.

The spectrometer is connected to a laptop in order to acquire and process the experimental data.

Figure 1 shows an outline of the described sensor system (the experimental setup), valid for measuring different quantities by changing the sensitive patch.
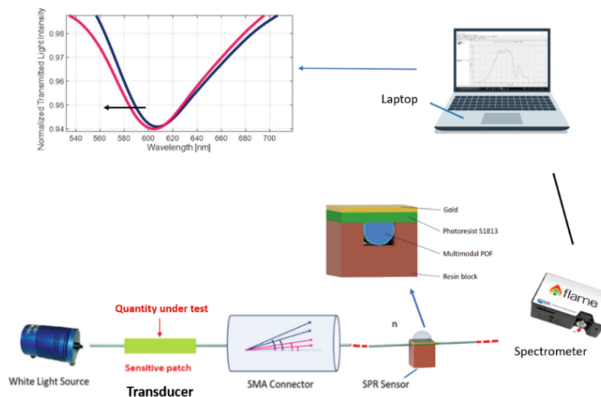
Fig. 1. Sensor system outline: the experimental setup.

3   The Developed Sensor Systems

3.1   Magnetic Field Sensor

In the proposed magnetic field sensor system, schematically reported in Fig. 2, the sensitive patch consists of a POF covered by ferrofluid. The used patch has a diameter of 500 µm and, in order to make it sensitive to the variation of the magnetic field, it has been covered by a ferrofluid layer for a length of 20 mm and a thickness of about 100 µm, as described in [5]. A magnet has been used to tune the magnetic field intensity, which exerts a bending force on the patch covered by ferrofluid. In such a way, the input light varies, producing a shift in the SPR wavelength. In particular, the sensor system has shown a linear behavior in the range between 0.28 and 0.75 mT, a sensitivity equal to about 6800 pm/mT and a resolution of 0.029 mT [5].
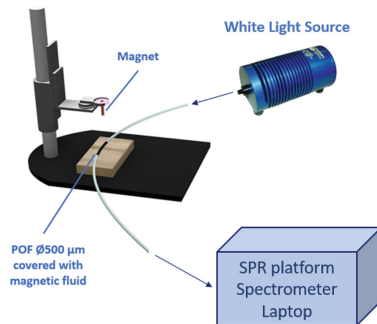
Fig. 2. Magnetic field sensor system: The experimental setup with the holder used to change the distance between the magnet and the POF covered with ferrofluid

In Table 1, a comparative analysis has been reported in order to compare the proposed magnetic field sensor with other SPR-based sensors.

Table 1. Comparative analysis between different types of magnetic field sensors.

Sensing approach	Sensitivity [pm/mT]	Resolution [mT]	Reference
Exploiting multimode SPR optical fiber	6800	0.29	[5]
Exploiting a magnetic fluid liquid in contact with an SPR optical fiber sensor	3000	–	[6]
Exploiting a magnetic fluid liquid in contact with an SPR optical fiber sensor	10000	0.5	[7]
Exploiting a magnetic fluid liquid in contact with an SPR optical fiber sensor	870	–	[8]

3.2 Temperature Sensor

The proposed temperature sensor consists of two D-shaped POF platforms connected in series. The first is characterized by a layer of thermosensitive material on the exposed core. The second is an SPR D-shaped POF sensor [4]. For both platforms, the used POF is a multimodal one with a core of 980 µm and a cladding diameter of 10 µm (total diameter of 1 mm). The production process to obtain the D-shaped POF sensing area of the thermosensitive platform is almost the same as the SPR platform. In particular, the POF is fixed in a resin block and then polished by two types of polishing papers (5 and 1 µm grits) to achieve the D-shaped POF region. Lastly, on the exposed core of the thermosensitive platform, a 70 µm thick silicone layer is deposited, acting as thermosensitive material [9]. Figure 3 shows the proposed temperature sensor system and a cross-section of the thermosensitive platform. In this case, the results have shown that the resonance wavelength decreases when the temperature of the liquid under test, in contact with the silicone, increases (blue shift) [9]. In particular, the sensor has denoted a good linear behaviour in the considered temperature range (20°–38°), a sensitivity of 0.158 nm/°C, with a resolution of about 1.2 °C [9].
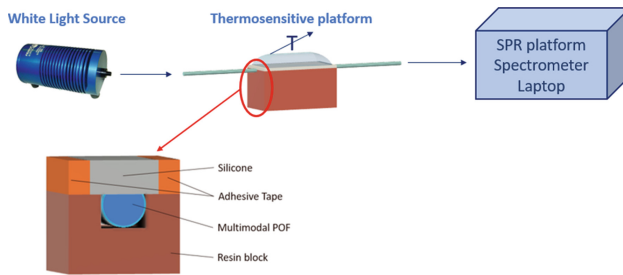
Fig. 3. Temperature sensor system and cross-section of the thermosensitive platform.

In Table 2, a comparative analysis has been reported in order to compare the proposed temperature sensor with other optical fiber sensors.

Table 2. Comparative analysis between different types of temperature sensors.

Sensing approach	Linear range [°C]	Resolution [°C]	Reference
Exploiting the mode profile variation in an SPR optical fiber sensor	20–38	1.2	[9]
Exploiting a fiber optic displacement sensor based on an intensity modulation technique	42–90	2.4	[10]
Exploiting a sourceless sapphire fiber extrinsic Fabry-Perot interferometer	–	1	[11]
Exploiting SPR in optical fibers	30–70	0.8	[12]

3.3   Force Sensor

The force sensor system proposed here consists of a POF patch fixed in a 3D printed holder and connected to an SPR D-shaped POF platform in a cascade. The used POF patch is a multimodal one with a total diameter of 1 mm (980 μm of core and 10 μm of cladding). It is fixed in the holder via two designed clamps and represents the force-sensing region, as shown in Fig. 4. The force values were changed by applying the different weights to the piece of the POF patch between the clamps [13]. As for before, the results have demonstrated that the SPR wavelength decreases when the applied force increases. In particular, in the range 0–0.5 N, the sensor has denoted a linear behaviour with a sensitivity of 4.4 nm/N and a resolution of about 22 mN [13].
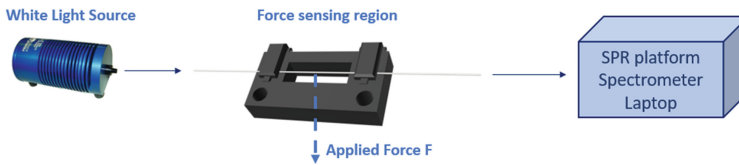
Fig. 4. The force sensor system with the 3D-printed holder.

Table 3 reports a comparative analysis of different types of force sensors based on different sensor configurations in terms of resolution.

Table 3. Comparative analysis between different types of force sensors.

Sensor configuration	Resolution	Reference
SPR-POF-based	~22 mN	[13]
Reflective measurements with optical fibers	~10 mN	[14]
Whispering gallery mode resonators based	~10 μN	[15]
Intensity-based POF beam	~0.1 N	[16]

4   Conclusion

This work presents a novel sensing approach exploiting the properties of multimodal POFs combined with the SPR phenomena. The presented sensor systems based on this approach exploit sensitive patches connected in series with an SPR D-shaped POF platform covered by water. In this work, it has been analyzed how relating the variation of the mode profile of the light to a physical quantity it is possible to detect variations of the physical quantity under tests, such as magnetic field, force, and temperature.

References

1. Gupta, B.D., Verma, R.K.: Surface plasmon resonance-based fiber optic sensors: principle, probe designs, and some applications. J. Sensors **2009**, 1–12 (2009)

2. Sharma, A.K., Jha, R., Gupta, B.D.: Fiber-optic sensors based on surface plasmon resonance: a comprehensive review. IEEE Sens. J. **7**(8), 1118–1129 (2007)
3. Dwivedi, Y.S., Sharma, A.K., Gupta, B.D.: Influence of design parameters on the performance of a surface plasmon sensor based fiber optic sensor. Plasmonics **3**(2–3), 79–86 (2008)
4. Cennamo, N., Massarotti, D., Conte, L., Zeni, L.: Low cost sensors based on SPR in a plastic optical fiber for biosensor implementation. Sensors **11**, 11752–11760 (2011)
5. Cennamo, N., Arcadio, F., Marletta, V., Baglio, S., Zeni, L., Ando, B.: A magnetic field sensor based on SPR-POF platforms and ferrofluids. IEEE T. Instrum. Meas. **70**, 1–10 (2021)
6. Zhou, X., Li, X., Li, S., An, G.-W., Cheng, T.: Magnetic field sensing based on SPR optical fiber sensor interacting with magnetic fluid. IEEE Trans. Instrum. Meas. **68**(1), 234–239 (2019)
7. Rodríguez-Schwendtner, E., Díaz-Herrera, N., Navarrete, M.C., González-Cano, A., Esteban, Ó.: Plasmonic sensor based on tapered optical fibers and magnetic fluids for measuring magnetic fields. Sens. Actuators A, Phys. **264**, 58–62 (2017)
8. Liu, H., et al.: Temperature-compensated magnetic field sensor based on surface plasmon resonance and directional resonance coupling in a D-shaped photonic crystal fiber. Optik **158**, 1402–1409 (2018)
9. Cennamo, N., Del Prete, D., Arcadio, F., Zeni, L.: A temperature sensor exploiting plasmonic phenomena changes in multimode POFs. IEEE Sens. J. **22**, 12900–12905 (2022)
10. Rahman, H.A., Harun, S.W., Saidin, N., Yasin, M., Ahmad, H.: Fiber optic displacement sensor for temperature measurement. IEEE Sens. J. **12**(5), 1361–1364 (2012)
11. Tian, Z., Yu, Z., Liu, B., Wang, A.: Sourceless optical fiber high temperature sensor. Opt. lett. **41**(2), 195–198 (2016)
12. Lu, L., et al.: A portable optical fiber SPR temperature sensor based on a smart-phone. Opt. express **27**(18), 25420–25427 (2019)
13. Arcadio, F., Zeni, L., Cennamo, N.: Exploiting plasmonic phenomena in polymer optical fibers to realize a force sensor. Sensors **22**, 2391 (2022)
14. Ioppolo, T., Kozhevnikov, M., Stepaniuk, V., Volkan Ötügen, M., Sheverev, V.: Micro-optical force sensor concept based on whispering gallery mode resonators. Appl. Opt. **47**, 3009–3014 (2008)
15. Kulkarni, A., Na, J., Kim, Y.J., Baik, S., Kim, T.: An evaluation of the optical fiber beam as a force sensor. Opt. Fiber Technol. **15**, 131–135 (2009)
16. Peirs, J., et al.: A micro optical force sensor for force feedback during minimally invasive robotic surgery. Sens. Actuators A **115**, 447–455 (2004)

Spaceborne LiDAR for Debris Detection and Tracking

M. Tagliente, G. Campiti, G. Brunetti, M. N. Armenise, and C. Ciminelli[✉]

Optoelectronics Laboratory, Politecnico di Bari, Bari, Italy
caterina.ciminelli@poliba.it

Abstract. The NewSpace paradigm is causing a significant growth of space debris, making the risk of catastrophic collisions increasingly high. Satellites in Low Earth Orbit (LEO) already perform two collision avoidance maneuvers on average each year, disrupting the nominal operations and consuming propellant. With a quickly growing space population, this will occur even more often in the future. However, maneuver rates are largely driven by the presence of uncertainties in debris measurements, which are currently performed mainly through ground-based sensors. The data accuracy can be improved by allowing spacecrafts to perform autonomous observations of debris through on-board sensors. Here, an Ultra-Long-Range LiDAR is proposed as a secondary payload for medium-sized or larger (>500 kg) satellites. A preliminary analysis led to the definition of the high-level requirements, such as a range and lateral resolution of 10 m, a Field of View (*FoV*) $\geq 0.12° \times 10°$ and the ability to scan, within 10 s, a frame of 90 m radius at 500 km. Following those results, a system-level analysis is conducted, to identify the best design choices regarding the method of target illumination, the detection scheme, and the source wavelength (λ). A beam scanning, Frequency Modulated Continuous Wave (FMCW)-based LiDAR architecture, operating in the optical C-band, is identified as the best solution for the proposed application. Then, the required performance for the LiDAR building blocks has been derived.

Keywords: LiDAR · FMCW · Space debris · Collision avoidance

1 Introduction

The number of man-made objects in Earth's orbit has increased dramatically in recent years. The risk of in-orbit collisions between active satellites and dangerous debris is already high enough that space operators deal daily with collision avoidance-related activities. Currently, the near-Earth environment is mainly surveilled through ground-based sensors. The tracking data is used to predict the future trajectories of space objects and identify potential hazards to operational spacecraft. As of today, satellites in congested orbital regions already perform two maneuvers per year on average, each time entailing the interruption of nominal activities as well as the consumption of some propellant. As space debris is constantly growing, the occurrence of risky conjunctions will increasingly become more common. Nevertheless, current maneuver rates are mainly

driven by the uncertainty in surveillance data more than by an actual risk of collision, whereby maneuver decisions are made in a rather conservative way to avoid any risk. Therefore, to avoid future scenarios in which satellites are constantly maneuvering to dodge debris, more accurate surveillance information is needed. A great improvement can be obtained by allowing satellites to autonomously acquire tracking data on potentially colliding debris. As space objects pass close to each other several times before a potential collision, an at-risk satellite has some unique opportunities to observe a secondary object and refine its trajectory estimation prior to the predicted event. In this article, we propose an Ultra-Long-Range LiDAR as a secondary payload for medium-to-large satellites, where it would only require a small percentage of the allocated resources in terms of power demand, mass, and volume. The operational concept of the proposed system is schematized in Fig. 1.

The orbital state of potentially dangerous objects is first estimated by ground infrastructure and is communicated to the at-risk satellite. The onboard data are used to predict when the secondary object will be visible during the orbits before the probable collision and thus to identify potential observing windows. At each planned observation, the estimated debris trajectory is used to narrow the search field of the sensor. The obtained measurements are processed together with the satellite's position and attitude data to reduce the uncertainties in the ephemerides of the secondary object. Based on the updated information, the satellite autonomously decides whether to perform a maneuver and eventually implements it briefly before the closest approach, e.g., half an orbit before. To define the desirable performance for the LiDAR sensor, the typical dynamics of conjuncting objects before potential collisions and the high-level system requirements have been reported in [1, 2]. A range of 500 km was identified as the best compromise for having the chance to observe most secondary objects, with an area > 8 cm $\times 8$ cm, prior to the closest approach, while maintaining limited usage of on-board resources. Other requirements are a range and lateral resolution ≤ 10 m, a *FoV* $\geq 0.12°$ x $10°$ and an observation time window ≤ 10 s to scan a frame with a radius ≥ 90 m at the maximum range.
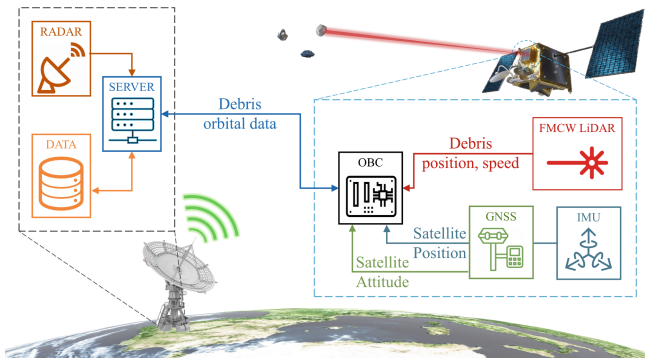
Fig. 1. Concept of operations of the proposed system

2 Spaceborne LiDAR System

2.1 System-Level Analysis

A spaceborne LiDAR sensor has to operate in a harsh environment, where interference caused by external light sources (e.g., the Sun) can reach higher power levels than the signal backscattered by the expected targets. In addition, the detection system proposed must work at an ultra-long distance. In this condition, the power of the reflected signal is very weak and the background represents an additional source of shot noise with a detrimental effect on the Signal to Noise Ratio (SNR). For these reasons, it is necessary to design a receiver architecture able to combine high immunity to interference with the greatest possible sensitivity.

The design of the LIDAR sensor has been addressed by choosing the proper illumination method, the detection architecture, and the operating wavelength (λ). Regarding the former, the most effective methods known are 1) illuminating the entire scene through a laser flash or 2) using progressive scanning through a laser beam. The first option is not viable, because of the large emitting power needed to illuminate a target at the required range of 500 km. In contrast, the progressive scanning illumination method allows the emitted power to be concentrated in a narrow beam. The detection scheme can be either a direct time-of-flight (ToF) or a coherent receiver. Although the sensitivity of ToF systems can be increased through digital signal processing (DSP) techniques, the coherent detection scheme has the inherent advantage of being able to distinguish between signals emitted from the sensor source and every other source. In addition, a heterodyne receiver allows to simultaneously measure target velocity as well as its position. The choice of λ can affect both the performance of the system and its implementation costs, depending on the availability of components capable of operating at the selected frequencies. The most widely used wavelength in contemporary LiDAR is 905 nm, due to the availability of low-cost components for the receiving subsystem. On the other hand, components operating in the optical C-band have reached a high degree of maturity due to their use in fiber-based communication systems and they are compatible with silicon photonics fabrication processes.

The result of this analysis is that a beam scanning, FMCW-based LiDAR, with a 1550 nm laser source, exhibits advantages that meet the needs of our application.

2.2 Hardware Performance Analysis

The proposed implementation is based on an optical coherent receiver (Fig. 2). The laser source emission frequency is chirped using a triangular wave. A part of the emitted light is used as a Local Oscillator (LO) in an interferometer, where it is compared to the light entering the device. Modulation makes it possible to measure the distance and velocity of the targets, discriminating the radiation backscattered by the intended targets from that emitted by external sources.

The modulation bandwidth (B_m) is defined by the max ($f_{m,max}$) and min ($f_{m,min}$) frequencies of the modulated signal.

In the hypothesis of an ideal linear modulation, the chirp rate (γ) is constant and related to the modulation period (T_m):

$$\gamma = B_m / T_m \qquad (1)$$
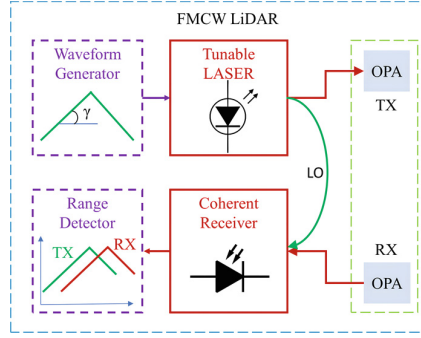
Fig. 2. FMCW LiDAR architecture

The analysis can be restricted to the up-chirp interval, without loss of generality. The frequency of the emitted signal (f_e) can be expressed as a function of time (t):

$$f_e(t) = \gamma\, t + f_{m,min} \tag{2}$$

The phase of the emitted signal (φ_e) can be expressed as a function of f_e, with the contribution of the initial phase (φ_0) and of the phase noise (φ_N):

$$\varphi_e = \int_0^t 2\pi f_e(\tau)d\tau + \varphi_0 + \varphi_N(t) \tag{3}$$

The phase of the reflected signal is cohent with that of the emitted signal, apart from a delay (t_f) that is related to the target distance (D), and the speed of light (c):

$$t_f = 2\,D\,/\,c \tag{4}$$

After the detection, the signal is converted to an electrical current whose phase (φ_r) is equal to the difference between φ_e and φ_r:

$$\varphi_r(t, t_f) = \int_{t-t_f}^t 2\pi f_e(\tau)d\tau + \varphi_N(t) - \varphi_N(t - t_f) \tag{5}$$

If the phase noise terms were negligible, the frequency of the baseband signal (f_r) could be derived directly from φ_r:

$$f_r(t, t_f) = \frac{1}{2\pi}\frac{d}{dt}\varphi_r(t, t_f) = f_e(t) - f_e(t - t_f) \tag{6}$$

Using Eq. (2), D can be estimated as:

$$D = \frac{c}{2}\frac{f_r}{\gamma} = \frac{c}{2}t_f \tag{7}$$

The hypothesis of negligible φ_N, made to derive Eq. (6), is clearly fundamental to obtain a useful estimation of D. The coherence distance (D_c) is the limit beyond which

the signal cannot extend, otherwise φ_N would reach an unacceptable level. Given the source linewidth ($\Delta\nu$), it can be expressed as:

$$D_c = \frac{c}{2\pi\,\Delta\nu} \tag{8}$$

From this, $\Delta\nu = 95$ Hz for the laser source has been derived to meet the requirement on the sensor range (R):

$$\Delta\nu \leq \frac{c}{2\pi R} \tag{9}$$

From the theory on line spectral estimation, it can be proved that the sensor range resolution (ΔR), which is the capacity to resolve multiple targets in the same direction, is related to the time needed to perform a proper measurement (T_{meas}), and to B_m [3], as:

$$\Delta R = c\frac{0.89}{T_{meas}}\frac{T_m}{B_m} \tag{10}$$

However, it is possible and convenient to choose T_m equal to T_{meas} in order to reduce discontinuities in the time domain, that could affect the spectral estimation. Therefore, the needed value for B_m can be estimated as:

$$B_m \geq c\frac{0.89}{\Delta R} \tag{11}$$

A $\Delta R < 10$ m can be attained by using chirped waveform generators with a large Time-Bandwidth Product (TBWP) $\geq 4.51 \times 10^5$ ($BW = 27$ MHz; time interval $=$ 16.7 ms) [4].

The requirement on lateral resolution (Δl) was used to define the performance of the emitted beam, in terms of Full Width Half Maximum Beamwidth ($FWHM_b$) [5]:

$$FWHM_b = 2asin\left(\frac{\Delta l}{2R}\right) \tag{12}$$

To achieve $FWHM_b = 0.0011°$, an Optical Phased Array (OPA) is the ideal solution for the transmitting stage. Its needed aperture ($W_{OPA,t}$) can be estimated as:

$$W_{OPA,t} = \frac{2.78\lambda}{\pi\,FWHM_b} \tag{13}$$

The spacing between two adjacent elements in the OPA (d_{OPA}) can be set starting from the requested FoV, and then by the beam steering angle requirement (θ_{max}), as:

$$d_{OPA} = \frac{\lambda}{2sin\frac{\theta_{max}}{2}} \tag{14}$$

The number of elements (NxN) necessary to form the OPA can be then estimated, as:

$$N = W_{OPA,t}/d_{OPA} \tag{15}$$

Therefore, an NxN OPA with $N > 7{,}712$ and $W_{OPA,t} = 7$ cm is required. However, an OPA with the aforementioned performance has not been demonstrated.

The receiver sensitivity (S_r) is limited by the SNR, that should be > 20 dB (SNR_{min}) to overcome the threshold effect in the frequency analysis [6]. Therefore, given the elementary charge (q), and the detector responsivity (E), S_r has to be [7]:

$$S_r \geq \frac{q}{E} \frac{SNR_{min}}{T_{meas}} \qquad (16)$$

A minimum threshold of -131.3 dB for S_r has been obtained by assuming an avalanche photodiode with $E = 13$ A/W. $T_{meas} = 16.7$ ms has been selected to fulfill observation time window and frame requirements [2].

The transmission optical power (P_t), required to illuminate a target of 8 cm $\times$ 8 cm area (A_t) at a distance equal to R, has been estimated by the RADAR range equation [5], selecting an OPA with a receiving aperture ($W_{OPA,r}$) of 48 cm and taking the following assumptions: 1) ideal transmission efficiency, 2) negligible internal losses, 3) a target with a Lambertian reflectance (ρ_t) of 0.9:

$$P_t = \frac{\pi^2 S_r FWHM_b^2 R^4}{\rho_t W_{OPA,r}^2 A_t} \qquad (17)$$

An optical power $P_t \geq 14$ W can be obtained using a laser diode in an array configuration as a source. The receiving OPA, in a tiled arrangement, can be folded to fit within size constraints.

The result of this analysis demonstrates the potential feasibility of a compact and lightweight FMCW-based silicon photonics LiDAR system. The adoption of a sensor with the described hardware performance would make a significant contribution in addressing the problem of the growing number of space debris.

References

1. Campiti, G., *et al.*: Observing opportunities of space conjuncting objects in the orbits prior to the closest approach. In: Space Debris Risk Assessment and Mitigation Analysis Workshop. ESA/ESOC (2022)
2. Campiti, G., *et al.*: Debris detection and tracking through on-board Lidar. In: International Conference on Applications in Electronics Pervading Industry, Environment and Society - APPLEPIES 2022, Genova, 26–27 September 2022
3. Hayes, M.: Statistical Digital Signal Processing and Modeling. John Wiley & Sons (1996)
4. Brunetti, G., *et al.:* High performance chirped microwave generator for space applications. In: International Conference on Space Optics—ICSO 2020, vol. 11852, pp. 1230–1239. SPIE (2021)
5. Balanis, C.: Antenna Theory: Analysis and Design. John Wiley & Sons, New York (2016)
6. Rife, D., et al.: Single tone parameter estimation from discrete-time observations. IEEE Trans. Inf. Theory **20**(5), 591–598 (1974)
7. Barry, J., et al.: Performance of coherent optical receivers. Proc. IEEE **78**(8), 1369–1394 (1990)

All-Optical Biophotonic and Microfluidic Circuits for Photo-Thermal Applications

Carlo Santini[1], Luciano De Sio[2], Francesca Petronella[3],
and Antonio d'Alessandro[1(✉)]

[1] Department of Information Engineering, Electronics and Telecommunications, Rome, Italy
antonio.dalessandro@uniroma1.it

[2] Department of Medico-Surgical Sciences and Biotechnologies, Center for Biophotonics, Sapienza University, Rome, Italy

[3] National Research Council of Italy Institute of Crystallography, Montelibretti (RM), Italy

Abstract. We propose a photonic biochip which combines optical and microfluidic channels to exploit the potential of gold nanorods (GNRs) in developing light-assisted antimicrobial therapies. The proposed chip is obtained by coupling two separately processed PolyDiMethylSiloxane (PDMS) substrates in which microfluidic channels, conveying biological fluid flow, and optical waveguides, confining near-infrared light, interact. The light activates the localized plasmonic resonance of GNRs dispersed in a film deposited on the functionalized PDMS substrates. This paper uses experimental measurements and numerical simulations based on Finite Element Method software tools to optimize the final design in terms of suitable GNRs irradiation, dimensions, aspect ratio, density, and distribution.

Keywords: Nanophotonics · Microfluidics · Nanoplasmonics · Integrated optics · Nanoparticles

1 Introduction

Nanotechnology offers, through the design and fabrication of functional nanomaterials, a powerful weapon against several diseases such as cancer [1] and pathogenic illnesses [2, 3]. Gold nanoparticles (NPs), upon irradiation at a suitable wavelength and the consequent triggering of localized plasmonic resonance (LPR), exhibit the remarkable intrinsic capability to confine an intense electromagnetic field at the nanoscale, realizing highly efficient nanosized sources of heat [4, 5]. Among NPs, colloidal gold nanorods (GNRs) possess unique chemical-physical characteristics, such as intrinsic non-toxicity, promptly processable surface, and a strong absorption band centered in the first biological window (700–900 nm). Plasmonic photo-thermal therapy (PPTT) combined with GNRs has also been proven very effective against bacterial strains resistant to standard antibiotic treatments [6]. Several plasmonic-based architectures have been made to inactivate heat-resistant bacteria [7] photothermally. Among the investigated plasmonic platforms, GNRs combined with microfluidic channels have not been investigated using confined guided laser beams as a photo-thermal activation technique. This manuscript shows that this compelling solution can open new routes in light-assisted thermal disinfection.

2 Proposed Design

2.1 PDMS Bulk Substrate

To combine microfluidic channels (MC) and optical waveguides (OW), PolyDiMethyl-Siloxane (PDMS) is used as a bulk substrate. PDMS has proved to be very effective and reliable for cheap soft lithographic fabrication of several microfluidic and micro-optical devices [8], being optically transparent, viscoelastic, chemically and thermally stable, hydrophobic, flexible and easily molded with high resolution and aspect ratio [9–11].

2.2 Microchip Structure

The proposed chip is obtained by coupling two separately processed PDMS substrates. The upper substrate contains a straight MC conveying biological fluid flow (a bacterial liquid solution) using inlet and outlet micropumps. The lower substrate includes the OW, confining near-infrared (NIR) light, supplied by a laser source and conveyed by an optical fiber coupled to the waveguide, operating at 810 nm. The light activates the plasmonic resonance in GNRs dispersed in a film deposited on the functionalized PDMS substrate. Figure 1 shows a representation of the proposed OW and MC design and an optical grating used to couple the incoming NIR light fed by an optical fiber.
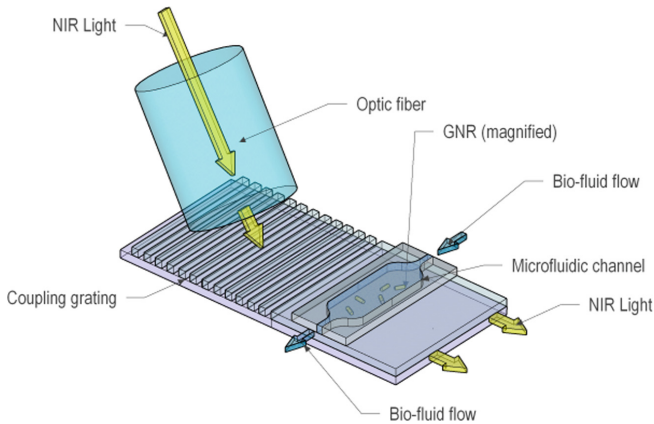
Fig. 1. Representation of the proposed bio-chip design. An optical grating is used to couple the incoming NIR light at a wavelength of 810 nm, fed by an optical fiber.

3 Experimental Results

A sample structure consisting of a single layer of randomly distributed GNRs, electrostatically immobilized on glass, has been fabricated to allow the investigation of GNR adsorption spectra and their consequent photo–thermal response. In Fig. 2, a photo of the sample of GNR-functionalized glass slab (a), used for experimental measurement, is

shown, along with a Scanning Electronic Microscope (SEM) micrograph of the sample showing well isolated and randomly oriented GNRs (b). The self-assembly methodology, reported in detail in [12], allows the deployment of monodispersed GNRs having a diameter, length, and average density of approx. 10 nm, 35 nm, and 500 GNR/μm^2, respectively. The spectral response of the sample, measured using a Uv-Vis spectrophotometer, evidences the presence of two absorption peaks centered at 520 nm (longitudinal) and 743 nm (transversal) (Fig. 3, black curve). By varying the refractive index surrounding the GNRs using water (n = 1.33) and nematic liquid crystal (n = 1.6), a well-evident red shift of the transversal plasmon band of about 143 nm is observed. This behavior can be explained using the Ganz theory [13], which predicts a monotonic red shift of the plasmon band for ellipsoidal nanoparticles as the refractive index increases. Noteworthy, the transversal absorption peak in the presence of water is centered at 810 nm, thus becoming very efficient for photo-thermal disinfection experiments.

4 Numerical Results

Finite Element Method (FEM) simulations of the proposed structure have been carried out, by means of COMSOL MULTIPHYSICS™ software, to investigate the properties of a GNR-functionalized glass or PDMS OW, surmounted by air or water cladding. Numerical results allow us to assess the role of OW thickness, refractive indexes, GNR dimensions, GNRs density, and orientation.

In Fig. 4(a), a portion of the top-surface GNR-functionalized OW is represented together with different configurations of GNRs: array or random distribution in insets (b) and (c), respectively.

In Fig. 5, the absorption cross-section, relevant to an array of GNR with parallel axes placed on top of a glass slab guide, conveying the fundamental TE0 mode, is plotted versus values of the angle α formed by the propagating direction and the axes of GNRs: showing maximum absorption when the axes of GNR are parallel to the direction of the guided TE0 field.

In Fig. 6, the GNRs absorption cross-section is plotted versus the wavelength of the guided radiation for a 0.25 μm^2 portion of glass slab OW, air-cladded and carrying an array of 25 GNRs (35 nm length, 10 nm diameter) having axes parallel to the guided electric field of the TE0 mode. The peak of the cross section in Fig. 6 is in agreement with the experimental results reported in Fig. 3 for n = 1.

In Fig. 7, the absorption cross-section of a distribution of GNR with random axes orientation is plotted versus the number of GNRs adsorbed on a 0.25 μm^2 portion of PDMS guide with air cladding, showing a linear regression between absorption cross-section and density of GNRs adsorbed on the OW surface.
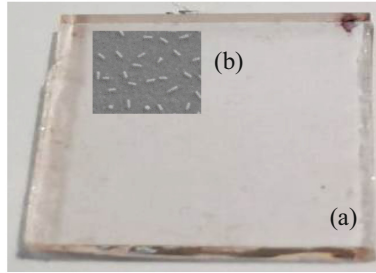
Fig. 2. GNR functionalized glass slide used for experimental measurements (a). Magnification of GNRs adsorbed on the upper surface of the glass slide (b). GNR length and diameter are approx. 35 nm and 10 nm, respectively. Average GNR density is approx. 500 GNRs/μm^2.
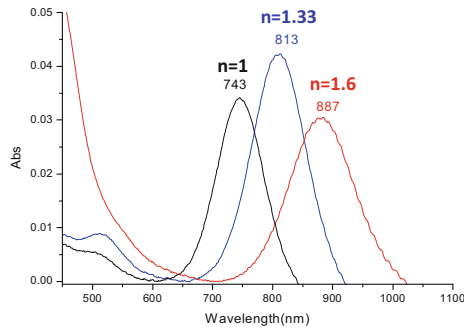
Fig. 3. Experimental plot of GNR absorption rate [a.u.] vs wavelength [nm] of incident radiation, for different media in which GNR are immersed (air refractive index n = 1, water n = 1.33, liquid crystal n = 1.6). Results are relevant to sample in Fig. 2.
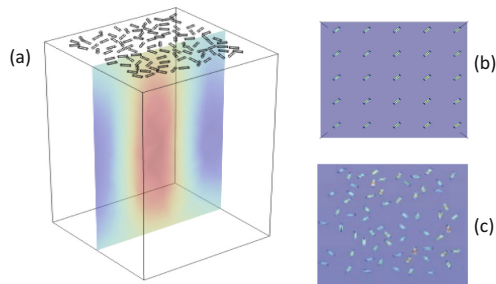
Fig. 4. Portion of a slab OW simulated by means of COMSOL MULTIPHYSICS™ FEM software (a). The OW GNR-functionalized top-surface, having a 0.25 μm^2 area, is shown for different configurations of GNRs: array (b) or random distribution (c). The fundamental modes TE0 and TM0 propagate in the 2 μm thick slab waveguide. GNR dimensions are the same as in Fig. 2.
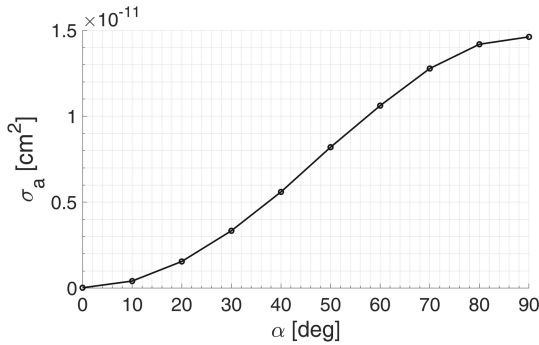
Fig. 5. Absorption cross-section σ_a [cm^2] of an array of 36 GNRs with parallel axes is plotted versus values of the angle α [deg] between the propagating direction and the axes of GNRs. GNR dimensions are the same as in Fig. 2.
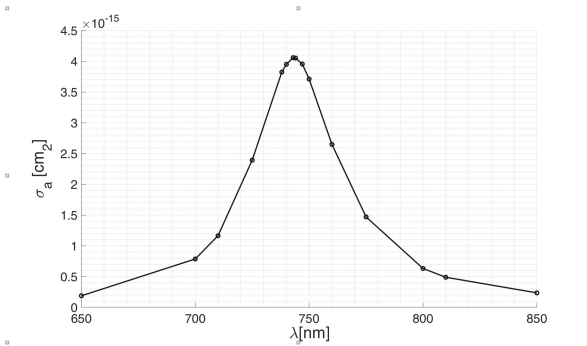
Fig. 6. Plot of GNR absorption cross-section σ_a [m^2] versus wavelength λ [nm] of the guided radiation. Simulations are relevant to a 0.25 μm^2 portion of air-cladded glass-slab OW, surmounted by an array of 25 GNRs with axes parallel to the guided electric field of the TE0 mode. The peak is in agreement with the experimental results reported in Fig. 3 for n = 1.
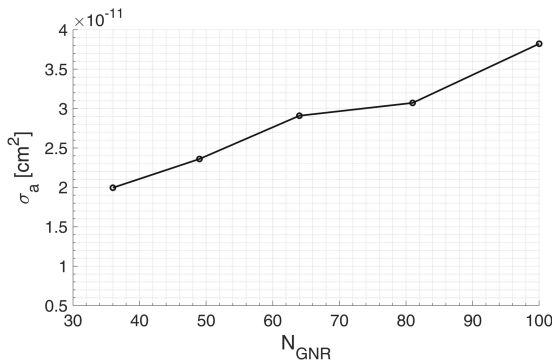
Fig. 7. Absorption cross-section σ_a (cm^2) of a distribution of GNR with random axes orientation plotted versus the number of GNRs adsorbed on a 0.25 μm^2 portion of PDMS guide with air cladding.

5   Conclusions

In this paper, we propose a simple and effective design that combines optical and microfluidic channels to allow the investigation of GNR in the development of light-assisted antimicrobial therapies in a portable and biocompatible microsystem. Our study represents a preliminary step for developing a compact, portable, biophotonic single-chip microsystem for bacterial killing or nanosensing. Further innovative evolution of the proposed approach could stem from its potential application to water purification from diluted bacteria. A proper design of a new kind of NP showing an absorption peak at visible wavelengths could allow the development of NP-assisted water purification by using daylight sources.

References

1. Lim, Z.Z., et al.: Gold nanoparticles in cancer therapy. Acta Pharmacol Sin. **32**(8), 983–990 (2011)
2. Annesi, F., et al.: Thermo-plasmonic killing of escherichia coli TG1 bacteria. Materials **12**(9), 1530 (2019)
3. Petronella, F., et al.: Uniform TiO2/In2O3 surface films effective in bacterial inactivation under visible light. J. Photochem. Photobiol., A **279**, 1–7 (2014)
4. Baffou, G., Quidant, R.: Thermo-plasmonics: using metallic nanostructures as nanosources of heat". Laser Photon. Rev. **7**(2), 171–187 (2013)
5. De Sio, L., et al.: Next-generation thermo-plasmonic technologies and plasmonic nanoparticles in optoelectronics. Prog. Quantum Electron. **41**, 23–70 (2015)
6. Norman, R.S., et al.: Targeted photothermal lysis of the pathogenic bacteria, Pseudomonas Aeruginosa, with gold nanorods". Nano Lett. **8**(1), 302–306 (2008)
7. Pihl, M., et al.: Bacterial biofilm elimination using gold nanorod localised surface plasmon resonance generated heat. Mater. Sci. Eng. **80**, 54–58 (2017)
8. Chang-Yen, D., et al.: A monolithic PDMS waveguide system fabricated using softlithography techniques". J. Lightwave Technol. **23**(6), 2088–2093 (2005)
9. Romeo, A., et al.: Elastomeric substrates with embedded stiff platforms for stretchable electronics. Appl. Phys. Lett. **102**(13), 131904 (2013)
10. Missinne, J., et al.: Stretchable optical waveguides. Opt. Express **22**(4), 4168–4179 (2014)
11. d'Alessandro, A., et al.: Polarization-independent nematic liquid crystal waveguides for optofluidic applications. IEEE Photonics Technol. Lett. **27**(16), 1709–1712 (2015)
12. Petronella, F., et al.: Label-free and reusable antibody-functionalized gold nanorod arrays for the rapid detection of Escherichia coli cells in a water dispersion. Environ. Sci.: Nano **9**(9), 3343–3360 (2022)
13. Gans, R.: Über die Form ultramikroskopischer Goldteilchen. Ann. Phys. **342**(5), 881–900 (1912)

Protein A Denaturation Sensing Through Surface Enhanced InfraRed Absorption (SEIRA) Spectroscopy

Valentina Di Meo[1], Massimo Moccia[2], Gennaro Sanità[1], Alessio Crescitelli[1], Annalisa Lamberti[3], Vincenzo Galdi[2], Ivo Rendina[1], and Emanuela Esposito[1(✉)]

[1] Institute of Applied Sciences and Intelligent Systems – Unit of Naples, National Research Council, Naples, Italy
`emanuela.esposito@cnr.it`
[2] Fields and Waves Lab, Department of Engineering, University of Sannio, Benevento, Italy
[3] Department of Molecular Medicine and Medical Biotechnology, University of Naples Federico II, Naples, Italy

Abstract. A pixeled plasmonic metasurface (MS) has been developed as a surface-enhanced infrared absorption (SEIRA) spectroscopy substrate to monitor the denaturation process of a protein A (PA) monolayer. The different pixels of the MS have been properly engineered to monitor different regions of the electromagnetic spectrum. Specifically, these pixels have their plasmonic resonances placed in the range 1500–2000 cm^{-1}, well matched with Amide I and Amide II vibrational bands. In particular, the SEIRA reflectance spectra of the native PA and the denatured PA have been compared, observing a redshift about 10 cm^{-1} for both Amide I and Amide II groups. Moreover, the evaluated enhancement factor (up to 7×10^4) allows to reveal both the presence and the denaturation process occurring to a very low amount of PA molecules (about 3 fmoles).

Keywords: SEIRA spectroscopy · Plasmonic metasurfaces · Pixeled sensing platform · Nanoplasmonics · Biosensors

1 Introduction

Biological samples sensing can be performed with several optical techniques [1–4]. Among these, mid-infrared (mid-IR) spectroscopy allows to powerfully solve the structural determination of molecules, since it enables the identification of the unique vibrational signatures of the chemical bonds occurring to the target analyte [5]. Among the mid-IR possible spectroscopic techniques, Fourier-Transform IR (FTIR) is one of the most routinely employed for the structural analysis of chemical and biological molecules, due to its capabilities to provide structural information on the target analyte, together with its dynamics, in a non-invasive and univocal way [6]. However, owing to the very low molecular absorption cross-section of IR radiations ($\sigma_{abs} \approx 10^{-20}$ cm^2) [7], a large

amount of material is required for accurate determinations. Surface-enhanced IR absorption (SEIRA) spectroscopy allows to overthrow this constraint thanks to the strong near-field enhancement offered by 2-D arrays of metallic nanoantennas (NAs) sustaining plasmonic resonances [8]. By varying the shape, size, and metal film thickness of each NA, as well as the array periodicity, it is possible to engineer the optical response of this metasurface (MS) through the whole electromagnetic spectrum [9]. This, in turn, enables spectroscopic analysis with a very huge sensitivity thanks to the high amplification of the vibrational modes of the molecules localized near the NAs [10–12].

In this study, we have monitored the denaturation process occurring to a protein A (PA) monolayer, by using a plasmonic MS (consisting of cross-shaped gold NAs fabricated on a silicon chip) as the substrate for SEIRA spectroscopy. Thanks to a multiresonant pixeled design, it has been possible to analyze the entire Amide spectral region (1500 $\div$ 2000 cm^{-1}). First, the identification of the PA layer binding has been performed, through the identification of the typical Amide I and Amide II vibrational bands. Then, the PA denaturation process has been induced and then monitored, observing a wavenumber red-shift of about 10 cm^{-1} for both Amide I and Amide II vibrational bands. The SEIRA enhancement factor has been estimated around 7×10^4, thereby enabling the detection of spectral variation in the vibrational bands even for a very small number of molecules (3 fmol in our experiment).

2 Material and Methods

The proposed plasmonic MS has been developed by following the subsequent research line, consisting of the device design, its fabrication, the functionalization and then the optical characterization.

2.1 Device Design

The modeling of the proposed platform has been carried out through the commercial software COMSOL Multiphysics v.5.1 [13]. Due to the polarization insensitivity offered by cross-shaped NAs and the high near field enhancement [14, 15], this geometry has been arranged in a 2-D periodic array positioned on a silicon substrate, as schematically shown in Fig. 1a. By taking fixed the NAs thickness t to 50 nm while varying the NAs geometrical parameters (cross arm length L, cross arm width W and the array period P), it has been possible to identify the parameters (summarized in Table 1) that locate the plasmonic resonance in the desired wavenumber range, i.e. 1500–2000 cm^{-1}, as shown in Fig. 1b.

Table 1. NAs geometrical parameters, together with their numerical and experimental resonances.

	Geometrical parameters			ν_{num}(cm^{-1})	ν_{exp}(cm^{-1})
	L [μm]	W [μm]	P [μm]		
Pixel 1	1.12	0.2	2.0	1500	1475
Pixel 2	1.25	0.27	1.5	1600	1601
Pixel 3	1.03	0.27	1.5	1737	1835
Pixel 4	0.84	0.25	1.5	2032	1945
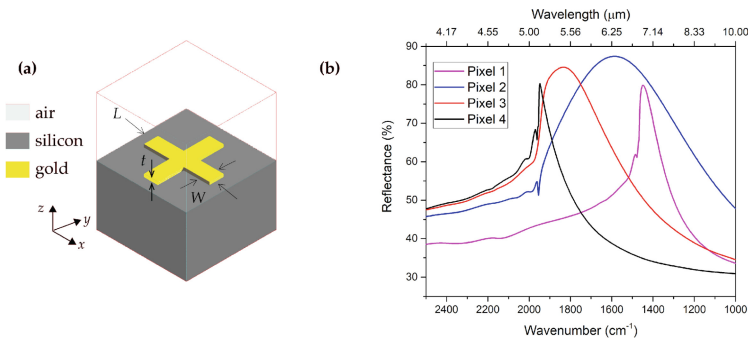
Fig. 1. Device modeling. (a) shows the schematization of the single unit cell. (b) shows the numerical optical responses of four pixels, whose parameters have been presented in Table 1.

2.2 Device Fabrication

The fabrication process of the proposed MS has been carried out through Electron Beam Lithography (EBL) and lift-off process. Indeed, to achieve a precise tuning of the plasmonic resonance to the desired range, the fabrication process should ensure an accurate control on NAs geometry. EBL offers high flexibility of use, high reproducibility and high reliability, therefore resulting as one of the most employed fabrication techniques for ordered arrays of NAs [16, 17]. The pixels, having an area of 0.5×0.5 mm^2, have been fabricated on a 1×1 cm^2 area float-zone silicon chip, as schematically shown in Fig. 2.

2.3 Device Functionalization

The developed MS functionalization protocol consists of the following steps: (i) chip surface cleaning and incubation with 2 mg/ml of dithiobis (succinimidiyl propionate) (DSP) in dimethyl sulfoxide (DMSO) for 1 h at room temperature; (ii) chip washing and incubation with PA (concentration 56.5 μM in phosphate buffered saline (PBS) solution) at 4 °C over night.

After the optical detection subsequent to the PA binding, a denaturation process has been performed, by inducing a pH jump by immersing the MS in a HCl solution (0.1 M) for 1 h, at room temperature.
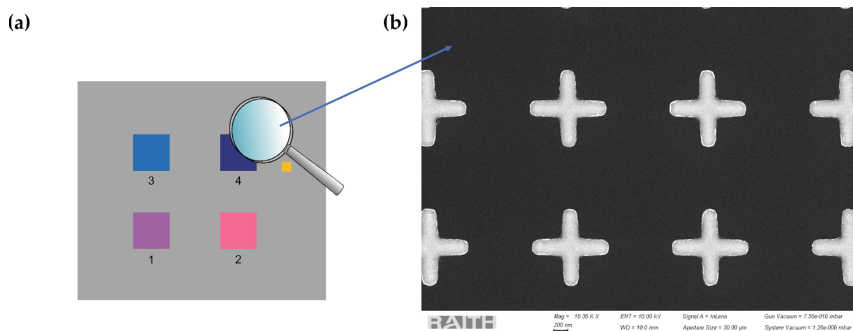
Fig. 2. (a) Schematization of the fabricated MS. (b) SEM image of a representative pixel.

3   Experimental Results

The proposed MS has been optically characterized at each step of the proposed experiment. The optical measurements have been performed with a Thermo-Nicholet NEXUS Continuum XL FTIR spectrometer, by collecting the reflection spectra of each pixel with a 4 cm^{-1} resolution over the range 4000–600 cm^{-1} for 128 scans.

The first characterization has been performed in air, to validate the numerical model. As reported in Table 1, a good agreement between the numerical and the experimental wavenumber resonance has been achieved, with a maximum discrepancy of about 6%, allowing an optical detection into the desired wavenumber range.

Once the validity of the numerical model has been confirmed, the MS has been functionalized with PA according to the protocol described in Sect. 2.3. After the PA binding, both a resonance peak wavenumber redshift of 8 cm^{-1} and the typical Amide I and Amide II vibrational bands appear, as shown in Fig. 3. In particular, Amide I bands, mainly attributable to the C $=$ O stretching vibrations, are placed in the spectral range 1700–1620 cm^{-1} [18]. On the other hand, Amide II vibrational modes are mainly due to the C-N stretching vibrations and to the in-plane N-H bend; these bands are placed in the range 1560–1500 cm^{-1} [19].

In order to validate the possibility to monitor conformational changes of a target analyte present on the proposed MS, the denaturation of the PA monolayer has been induced through a pH jump, as described in Sect. 2.3. As shown in Fig. 4, it is possible to observe a 9 cm^{-1} redshift for the Amide I band, and a redshift of 10 cm^{-1} for the Amide II band. These redshifts are attributable to the protein α-helical structures structural modifications and to the breaking of the hydrogen bonds that produce the unfolding of the protein chains [20].

The enhancement factor (EF) [10] of the proposed MS has also been estimated; in particular, EF values up to 7×10^4 have been evaluated, thus ensuring the capabilities to monitor the vibrational modes present even for extremely low amounts of molecules (3 fmoles in the proposed experiment).
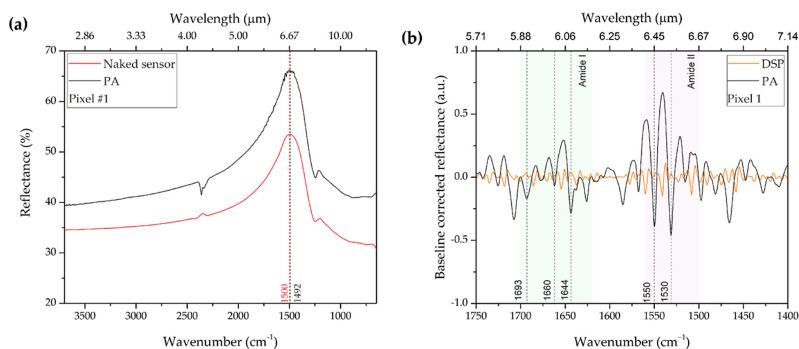
Fig. 3. Optical characterization of the MS after the PA binding. (a) shows an 8 cm^{-1} redshift of the plasmonic resonance peak. Red curve refers to the spectrum acquired with no molecules adsorbed on the MS, while black curve refers to the reflectance spectrum acquired after the PA binding. (b) shows the typical Amide I and Amide II vibrational bands appearing after the PA functionalization protocol. Orange curve refers to the reflectance spectrum acquired after the DSP incubation, while black curve refers to the reflectance response after the PA layer binding.
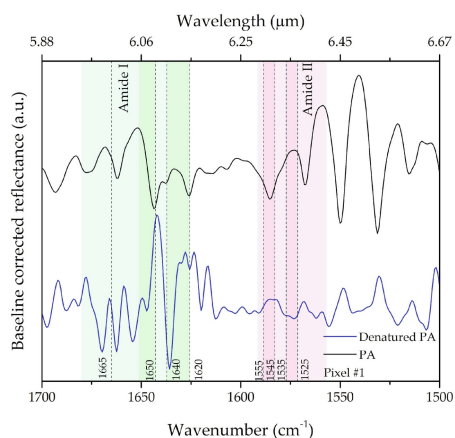
Fig. 4. Comparison between the baseline corrected SEIRA spectrum of native PA (black curve) and of the denatured PA (blue curve). A redshift of both Amide I bands (green area) and Amide II bands (pink area) appears.

4   Conclusions

In this work, a plasmonic MS suitable for SEIRA spectroscopy sensing has been employed to observe the denaturation process occurring to a PA monolayer. The proposed MS shows a pixeled design, with four different pixels able to cover the spectral region between 1500–2000 cm^{-1}. The MS is able to identify the typical Amide I and Amide II vibrational bands appearing after the PA layer binding, and also to monitor its conformational changes when a pH jump has been induced. This pH change has induced the denaturation of the PA monolayer, which can be observed in the SEIRA spectra as a

redshift of about 10 cm^{-1} for both Amide I and Amide II bands. Moreover, an EF up to 7×10^4 has been estimated, thus ensuring the SEIRA capabilities to monitor chemical changes in the target analyte even for small quantities of molecules.

References

1. Hu, H., et al.: Recent advances in two-dimensional transition metal dichalcogenides for biological sensing. Biosens. Bioelectron. **142**, 111573 (2019)
2. Wang, J., Lv, F., Liu, L., Ma, Y., Wang, S.: Strategies to design conjugated polymer based materials for biological sensing and imaging. Coord. Chem. Rev. **354**, 135–154 (2018)
3. Lovecchio, N., et al.: Integrated optoelectronic device for detection of fluorescent molecules. IEEE Trans. Biomed. Circuits Syst. **12**(6), 1337–1344 (2018)
4. Kumar, S., Singh, R.: Recent optical sensing technologies for the detection of various biomolecules. Opt. Laser Technol. **134**, 106620 (2021)
5. Stuart, B.H.: Infrared Spectroscopy: Fundamental and Application. Wiley, New York (2004)
6. Griffiths, P.R.: Fourier Transform Infrared Spectrometry. Wiley, Chichester (2007)
7. Mayerhöfer, T.G., Pahlow, S., Popp, J.: The Bouguer-Beer-Lambert Law: shining light on the obscure. ChemPhysChem **21**(18), 2029–2046 (2020)
8. Neubrech, F., Huck, C., Weber, K., Pucci, A., Giessen, H.: Surface-enhanced infrared spectroscopy using resonant nanoantennas. Chem. Rev. **117**, 5110–5145 (2017)
9. Vannini, G., Fernàndez-Dominguez, A.I., Heck, S.C., Maier, S.A.: Plasmonic nanoantennas: fundamentals and their use in controlling the radiative properties of nanoemitters. Chem. Rev. **111**(6), 3888–3912 (2011)
10. Di Meo, V., et al.: Metasurface based on cross-shaped plasmonic nanoantennas as chemical sensor for surface-enhanced infrared absorption spectroscopy. Sens. Actuators, B Chem. **286**, 600–607 (2019)
11. Di Meo, V., et al.: Pixeled metasurface for multiwavelength detection of vitamin D. Nanophotonics **9**(12), 3921–3930 (2020)
12. Di Meo, V., et al.: Advanced DNA detection via multispectral plasmonic metasurfaces. Front. Bioeng. Biotechnol. **9**, 666121 (2021)
13. COMSOL Multiphysics homepage. https://www.comsol.it. Accessed 28 Sept 2022
14. De Marcellis, A., Palange, E., Janneh, M., Rizza, C., Ciattoni, A., Mengali, S.: Design optimisation of plasmonic metasurfaces for mid-infrared high-sensitivity chemical sensing. Plasmonics **12**(2), 293–298 (2016). https://doi.org/10.1007/s11468-016-0263-9
15. Bagheri, S., Weber, K., Gissibl, T., Weiss, T., Neubrech, F., Giessen, H.: Fabrication of square-centimeter plasmonic nanoantenna arrays by femtosecond direct laser writing lithography: effects of collective excitations on SEIRA enhancement. ACS Photonics **2**, 779–786 (2015)
16. Vieu, C., et al.: Electron beam lithography: resolution limits and applications. Appl. Surf. Sci. **164**, 111–117 (2000)
17. Malara, P., et al.: Resonant enhancement of plasmonic nanostructured fiber optic sensors. Sens. Actuators, B Chem. **273**, 1587–1592 (2018)
18. Konermann, L., Pan, J., Liu, Y.H.: Hydrogen exchange mass spectrometry for studying protein structure and dynamics. Chem. Soc. Rev. **40**(3), 1224–1234 (2011)
19. Goormaghtigh, E., Cabiaux, V., Ruysschaert, J.M.: Determination of soluble and membrane protein structure by Fourier transform infrared spectroscopy. II. Experimental aspects, side chain structure, and H/D exchange. Subcell. Biochem. **23**, 363–403 (1994)
20. Lorenz-Fonfria, V.A.: Infrared difference spectroscopy of proteins: from bands to bonds. Chem. Rev. **120**(7), 3466–3576 (2020)

Multiscale and Multiphysics Solvers for AlGaAs TJ-VCSEL

Alberto Gullino[1(✉)] , Alberto Tibaldi[1,2] , Francesco Bertazzi[1,2] ,
Michele Goano[1,2] , and Pierluigi Debernardi[2]

[1] Dipartimento di Elettronica e Telecomunicazioni, Politecnico di Torino,
Corso Duca Degli Abruzzi 24, 10129 Torino, Italy
alberto.gullino@polito.it

[2] CNR-IEIIT, Corso Duca Degli Abruzzi 24, 10129 Torino, Italy

Abstract. Among possible strategies to improve the performance
of near infrared AlGaAs/GaAs vertical-cavity surface-emitting lasers
(VCSELs) for short-reach interconnects, current injection schemes based
on tunnel junctions (TJs) may be an enabling technology to meet the
high temperature requirements of data-center applications. To assess the
merits of TJs in this context, we perform a comparative simulation-based
study of a commercial *pin* VCSEL and a modified structure where holes
are injected into the active region through a TJ. Band-to-band tunneling
probabilities are computed within a multiband nonequilibrium Green's
function (NEGF) approach. The resulting generation rates are included
in a quantum-corrected drift-diffusion model for carrier transport. The
optical modes of the cavity are found with an electromagnetic solver, and
self-heating effects are studied with a thermal model. The comparative
multiphysical 1D and 3D simulations of *pin* and TJ-VCSELs predict that
the voltage penalty introduced by the reverse-biased TJ is compensated
by the higher output optical power.

Keywords: VCSEL · Optoelectronics · Physics-based · NEGF · TJ

1 Introduction

The staggering growth of intra-datacenter data traffic demands the improve-
ment of state-of-the-art AlGaAs/GaAs 850 and 980 nm vertical-cavity surface-
emitting lasers (VCSELs) performance, crucial for efficient and fast short-reach
interconnects [6]. Low production costs, array-oriented manufacturability, and
small power consumption determine the market dominance of VCSELs as reli-
able optical sources for on-chip communication.

At present, the commercial near-IR lasers are based on AlGaAs *pin* devices,
with an intrinsic active region including some quantum wells (QW) embed-
ded between two oppositely doped semiconductor distributed Bragg's reflectors
(DBRs). The *p*-doped top mirror (DBR) introduces higher free-carrier absorp-
tion (FCA) losses and larger electrical resistivity with respect to the *n*-doped

counterparts. This causes an earlier thermal roll-over due to self-heating, and a worse RC time constant, that limits the VCSEL bandwidth.

An alternative VCSEL design relies on the introduction of tunnel junctions (TJs) to obtain current injection inside the active region and limit lossy *p*-doped region to just few nanometers of the TJ. A TJ is a heavily doped *pn* junction working in reverse bias conditions where purely quantum direct band-to-band tunneling (BTBT) mechanism dominates transport.

The market pervasion of the *pin* VCSELs suggests that a technologically computer aided design (TCAD) approach should be preferred to avoid slow and expensive try-and-error prototyping campaigns. In this perspective, accurate and efficient physics-based tools should be developed. Therefore, here we follow the procedure presented in [5]: the same set of fitting parameters is used to calibrate our reduced dimensionality solver D1ANA to reproduce the results on a test TJ-VCSEL, characterized with our in-house multiphysics and multiscale solver VENUS [2,7,9]. In this way, we have a very accurate but time-consuming solver, and a faster one that provides reasonable predictions of TJ-VCSEL characteristics, and therefore is suited for extended parametric campaigns.

Further details about the VENUS and D1ANA will be provided in the next section. The structures are described in details in the third section. The results from VENUS and D1ANA are presented in the fourth section.

2   Adopted Methodology

The complexity of VCSELs operation requires that the electrical, optical and thermal problems should be addressed in a comprehensive self-consistent scheme. In this view, our group developed VENUS, a physics-based in-house 3D software able to describe accurately the operation of commercial *pin* VCSELs [2,7].

VENUS consists of three main building blocks. The electrical transport problem is treated by means of a quantum-correct drift-diffusion model (DD). Quantum corrections describe quantization effects in the nanostructured active region, needed to determine the optical gain/absorption features. The bound states are computed by solving a multiband k·p Schrödinger equation; gain is computed with the Fermi's golden rule. A capture/escape GR rate is introduced alongside other processes such as Auger and SRH recombinations to connect 2D and 3D populations. The optical problem is solved through our in-house electromagnetic solver VELM [1]. The optical modes are retrieved by imposing the resonance condition after a full round-trip. The corresponding eigenvalue problem is solved, returning the resonance wavelength and the modal losses. The computed eigenvectors represent the field expansion coefficients used to compute the optical field. This is used to extract a stimulated rate emission rate, connecting the optical and electrical problems. Eventually, the temperature variation due to self-heating processes is computed by solving the static heat equation.

The TJ modeling cannot be demanded to a semiclassical drift-diffusion model. BTBT is a purely quantum mechanical phenomenon that must be tackled with a genuine quantum approach. Therefore, the tunneling across the TJ is analyzed with a nonequilibrium Green's function (NEGF) model based on the same

electronic structure model used to compute the QW gain. NEGF extracts the interband spectral current by introducing fully nonlocal scattering self-energies computed in the self-consistent Born approximation (SCBA) [4,8]. A current density is obtained by integrating the spectral current. From this, a generation rate is computed and inserted in the DD alongside the other GR mechanisms.

However, the computational burden entailed by a 3D simulation limits the use of VENUS in extended parametric campaigns. Therefore, a reduced dimensionality (1D) solver called D1ANA is derived from VENUS. All the building blocks of the VENUS are converted into their 1D form and applied to a vertical cut taken from the center of the axisymmetric 3D structure. The steps required to calibrate D1ANA to reproduce the experimental results on the commercial *pin* VCSEL are discussed in depth in [5].

3   Investigated Structure

The test TJ-VCSEL is generated starting from a commercial *pin* VCSEL. The structure described in depth in [2,5,7]: here we report some details for the reader convenience. The active region embeds three 8 nm GaAs QWs in a 1λ-cavity. The bottom n-DBR is realized with 37 pairs with Al molar fraction concentration varying from 17% to 90%; the top outcoupling p-DBR is composed of 21 pairs with the same concentrations. The 30 nm thick oxide aperture with diameter 4.7 μm is placed in the first node of the optical standing wave (SW) to ensure modal stability [3]. This provides both optical and electrical lateral confinement. The top metallic contact consists of a metal ring (inner radius 6 μm), where an ohmic contact is realized with a heavily p-doped GaAs layer, which is afterwards etched by 60 nm after the contact ring is defined.

In the TJ-VCSEL, the TJ is placed in the same position of the oxide aperture (see Fig. 1a), to reduce the impact of the strong doping levels on the FCA losses of the structure. The TJ is extended across the whole VCSEL mesa; lateral confinement is demanded to the oxide aperture. Given the TJ position, in our test structure the oxide is placed between a node and an antinode of the SW. Different configurations will be investigated in future works. The presence of the TJ allows to switch the top mirror into a n-doped DBR. The consequent reduction of FCA losses (see Fig. 1b) allows to reduce the number of the outcoupling mirror pairs by two, to match the threshold gain of the *pin* VCSEL.

4   Results

In this section the results on the TJ-VCSEL are compared to the commercial *pin* device. These are obtained with VENUS and the calibrated D1ANA, starting with the same set of parameters used in [5]. In summary, they are: thermal conductivity and its temperature dependence, refractive index profile as a function of temperature dn/dT, carrier mobilities, and effective size of the oxide aperture.
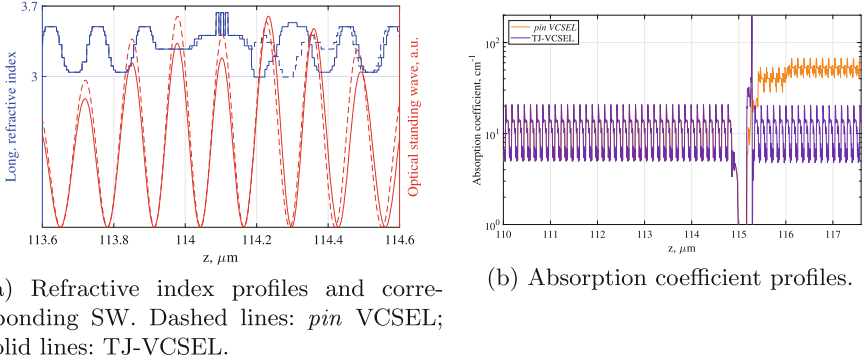
(a) Refractive index profiles and corresponding SW. Dashed lines: *pin* VCSEL; solid lines: TJ-VCSEL.

(b) Absorption coefficient profiles.

Fig. 1. (a) absorption coefficient levels. In the TJ-VCSEL there is a strong absorption in the TJ, whereas in the top DBR (right mirror) it is greatly reduced. In (b), the refractive index and the corresponding SW are reported for the two structures. The QWs are aligned, but the introduction of the TJ shifts the position of the oxide aperture in the TJ-VCSEL.

In Fig. 2, the light-current-voltage characteristics (LIV) of the two VCSELs are reported. The curves in purple represent the result of the calibration process realized in [5]. In Fig. 2a, D1ANA underestimates the current with respect to experimental and VENUS data at high bias levels. This is related to the current crowding effect in the oxide aperture proximity, and to the current flowing radially from the top annular contact, both neglected in a 1D framework. On the other hand, in Fig. 2b, D1ANA is more reliable in predicting the output optical power, and well reproduces the 3D results.

Moving to the TJ-VCSEL case (orange curves), the results remain consistent if two of the aforementioned parameters are further adjusted with respect to the *pin* case. In particular, the thermal dependence introduced on carrier mobilities and dn/dT are reduced. In Fig. 2a, there is the same issue encountered in the *pin* case at high applied bias, despite the mobility reduction. However, a remarkable difference arises at low bias, where D1ANA predicts larger values of current than VENUS. The discrepancy could be explained by the presence of the TJ, that is not radially limited. While the current crowding induced by the oxide aperture increases the current density, the TJ forces a large radial current that lowers the current density and cannot be predicted by D1ANA. In Fig. 2b, the LI curves are reported. As in the commercial VCSEL case, D1ANA reproduces the main features of the experimental curve, such as the threshold current at $\approx 0.5\,\mathrm{mA}$, the maximum output power of 4.5 mW at a current of 10 mA.

In Fig. 3, the emission wavelength is displayed as a function of the driving current $\lambda(I)$. This is useful to evaluate the VCSEL red-shift, caused by self-heating, and therefore the inner temperature variation. The results from VENUS

(a) I(V) characteristics.

(b) L(I) characteristics.
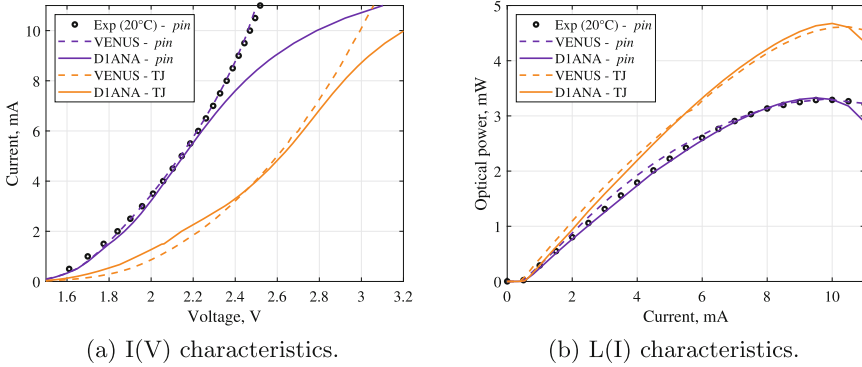
Fig. 2. Static characteristics of *pin* and TJ-VCSELs (purple and orange curves, respectively), computed with VENUS (dashed) and D1ANA (solid curves).

(dashed curves) are superimposed for the two structures, close to the experimental data. D1ANA provides good predictions on both the VCSELs. However, the dn/dT factor is reduced in the TJ-VCSEL case.
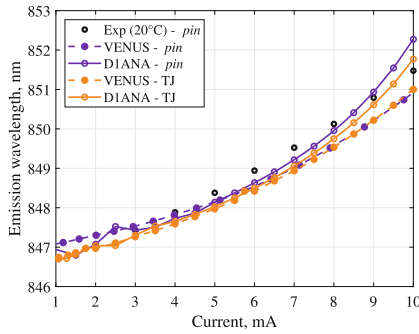
Fig. 3. $\lambda(I)$ curve for *pin* and TJ-VCSEL (purple and orange curves, respectively), computed with VENUS (dashed) and D1ANA (solid curves).

The variation of the two fitting parameters entails that in TJ-VCSEL the temperature rises more than in the *pin* structure. This appears to be in contrast with the prediction of a reduced self-heating induced by the *n*-doped DBR. However, TJ-VCSEL enables larger optical power, that in turn increase both the radiative and FCA losses, that play a main role in the self-heating process.

5   Conclusions

We have demonstrated that our calibrated one-dimensional solver is able to reproduce the main static characteristics of a TJ-VCSEL, within a NEGF-DD

model. The electrical characteristics show that the presence of the TJ causes an electrical penalty with respect to the *pin* device, related to the additional junction. At the same time, the TJ-VCSEL improves the output optical power at equal current values. The increased slope of the curve is induced by the out-coupling losses reduction, leading to a larger maximum optical power. Thermal roll-over makes the two VCSELs turn off at similar currents.

References

1. Debernardi, P., et al.: Anisotropic transverse confinement design for electrically pumped 850 nm VCSELs tuned by an intra cavity liquid-crystal cell. IEEE J. Select. Topics Quantum Electron. **28**(1), 1700111 (2022). https://doi.org/10.1109/JSTQE.2021.3089897

2. Debernardi, P., Tibaldi, A., Daubenschüz, M., Michalzik, R., Goano, M., Bertazzi, F.: Probing thermal effects in VCSELs by experiment-driven multiphysics modeling. IEEE J. Select. Topics Quantum Electron. **25**(6), 1700914 (2019). https://doi.org/10.1109/JSTQE.2019.2927580

3. Demeulenaere, B., Bienstman, P., Dhoedt, B., Baets, R.: Detailed study of alas-oxidized apertures in vcsel cavities for optimized modal performance. IEEE J. Quantum Electron. **35**(3), 358–367 (1999). https://doi.org/10.1109/3.748841

4. Gullino, A., Pecora, S., Tibaldi, A., Bertazzi, F., Goano, M., Debernardi, P.: A multiscale approach for BTJ-VCSEL electro-optical analysis. In: 21st International Conference on Numerical Simulation of Optoelectronic Devices (NUSOD 2021), pp. 79–80, September 2021. https://doi.org/10.1109/NUSOD52207.2021.9541423

5. Gullino, A., Tibaldi, A., Bertazzi, F., Goano, M., Debernardi, P.: Reduced dimensionality multiphysics model for efficient VCSEL optimization. MDPI Appl. Sci. **11**(15), 6908 (2021). https://doi.org/10.3390/app11156908

6. Larsson, A., Gustavsson, J.S., Fülöp, A., Haglund, E., Haglund, E.P., Kelkkanen, A.: The future of VCSELs: Dynamics and speed limitations. In: 2020 IEEE Photonics Conference (IPC), pp. 1–2 (2020). https://doi.org/10.1109/IPC47351.2020.9252236

7. Tibaldi, A., Bertazzi, F., Goano, M., Michalzik, R., Debernardi, P.: VENUS: a vertical-cavity surface-emitting laser Electro-opto-thermal NUmerical Simulator. IEEE J. Select. Topics Quantum Electron. **25**(6), 1500212 (2019). https://doi.org/10.1109/JSTQE.2019.2893755

8. Tibaldi, A., et al.: Analysis of carrier transport in tunnel-junction vertical-cavity surface-emitting lasers by a coupled nonequilibrium Green's function-drift-diffusion approach. Phys. Rev. Appl. **14**(2), 024037 (2020). https://doi.org/10.1103/PhysRevApplied.14.024037

9. Tibaldi, A., et al.: Bridging scales in multiphysics VCSEL modeling. Opt. Quantum Electron. **51**(7), 1–19 (2019). https://doi.org/10.1007/s11082-019-1931-8

Dynamic and High-Resolution Strain Measurements Using the Brillouin Optical Frequency-Domain Analysis

E. Catalano[1], R. Vallifuoco[1], R. Bernini[2], L. Zeni[1], and A. Minardo[1(✉)]

[1] Department of Engineering, Università Della Campania, Aversa, Italy
aldo.minardo@unicampania.it

[2] Consiglio Nazionale delle Ricerche, Istituto per il Rilevamento Elettromagnetico dell'Ambiente, Napoli, Italy

Abstract. In this work, we demonstrate a novel mechanism to localize the stimulated Brillouin interaction over a specific portion of an optical fiber, using a Brillouin Optical Frequency-Domain Analysis (BOFDA) interrogation system and an array of tapers. We show, both numerically and experimentally, that the frequency-domain fiber response, acquired over a narrow range by a vector network analyzer, can be uniquely associated to the multi-taper array whose period matches the swept spectral range. This opens the way to high-resolution (cm-scale) dynamic strain measurements, in addition to fully distributed static strain (or temperature) measurements over the same optical fiber and using the same apparatus.

Keywords: Stimulated Brillouin scattering · Distributed optical fiber sensors · Dynamic strain measurements

1 Introduction

Brillouin scattering offers a mechanism for distributed strain and temperature measurements in optical fibers. In the last decades, these sensors have been employed in various application fields, including geotechnical monitoring [1], pipeline monitoring [2], and so on. While these sensors typically rely on the estimation of the Brillouin frequency shift (BFS) of the fiber, different configurations exist which provide a spatial profile of the BFS with a given spatial resolution. In one of these configurations, referred to as Brillouin Optical Frequency-Domain Analysis [3, 4], the spatial distribution of the BFS along the fiber is retrieved by launching, into the fiber, a stationary probe field and a counterpropagating pump field with a small sine modulation impressed on it. The method relies on the acquisition, typically by means of a vector network analyzer (VNA), of the amplitude and phase of the modulation acquired by the probe field intensity, for a range of modulation frequencies. The frequency modulation range determines the maximum fiber length and the spatial resolution. For a maximum modulation frequency of 10 GHz, the spatial resolution is 1 cm. While offering a high spatial resolution, BOFDA sensors are inherently slow, because of two reasons: first, the number of modulation frequencies

to be swept increases with the ratio between the measurement range and the spatial resolution; second, such a sweep must be repeated for several frequency offsets between the pump and probe fields. These two factors lead to an acquisition time in the minutes range, typically. While the necessity of scanning multiple pump-probe frequency offsets can be overcome by adopting a slope-assisted configuration, i.e., biasing the pump-probe frequency offset along one of the two slopes of the Brillouin gain spectrum (BGS) [5, 6], the modulation frequency of the VNA must still be swept over a wide range, preventing the possibility to realize dynamic measurements. The objective of the technique proposed in this paper, is to enhance the BOFDA capabilities so that the sensor can retrieve the BFS changes in one or more positions of the fiber at a high sampling rate. This is achieved by realizing, in specific portions of the fiber, a spatial modulation of the Brillouin gain, which appears as a narrowband resonance in the frequency-domain fiber response. The amplitude of this resonance can be tracked at a high speed, and, under some circumstances, reproduces faithfully the BFS variations induced by strain. In the following, we demonstrate this approach by using an array of tapers realized along a short (a few cm) piece of fiber.

2   Principle of Operation

The operation principle is shown in Fig. 1 (from (a) to (d)). Let us suppose that the BFS is periodically modulated along a piece of fiber, with a modulation depth Δv and a modulation period ΔL. When the fiber is interrogated by a probe field tuned at the original BFS of the fiber, the Brillouin gain experienced by the probe field varies spatially with the same period (see Fig. 1(b)). In the frequency-domain, this gives rise to a narrow resonance centered at a frequency ω_{res} inversely proportional to ΔL (see Fig. 1(c)).
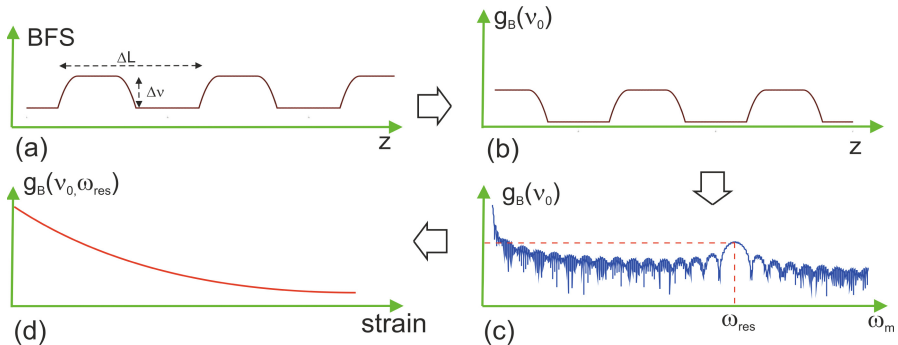
Fig. 1. (a) BFS profile. (c) Brillouin gain profile in the time-domain. (c) Brillouin gain profile in the frequency-domain; (d) Strain response.

Any strain (or temperature change) acting along the modulated fiber will result in a variation of the amplitude of this resonance, as shown in Fig. 1(d). From a practical point of view, the BFS modulation can be realized through fiber tapering [7], as we will describe in more detail in the experimental section.

3   Numerical Modeling

In order to analyze numerically the effect of a periodical modulation of the BFS on the stimulated Brillouin scattering (SBS) fiber response, we make use in this section of the frequency-domain model developed in Ref. [8]. According to this model, the modulation induced on the probe wave by SBS interaction with the pump, can be described through a baseband transfer function (TF) equal to:

$$TF(\omega_m) = \frac{I_{S1}(\omega_m)}{I_{P1}(\omega_m)} = E_{S0}(L)\int_0^L E_{S0}(z)g_{B,ac}(z,\omega_m)e^{-2j\omega_m n/c}dz \qquad (1)$$

where $I_{S1}(\omega_m)$ and $I_{P1}(\omega_m)$ are the complex ac intensities of the probe and pump field, respectively, ω_m is the modulation frequency, $E_{S0}(z)$ is the stationary probe field, L is the fiber length, n is the refractive index, c is the speed of light in the vacuum, z is the position along the fiber, and $g_{B,ac}$ is the small-signal Brillouin gain given by:

$$g_{B,ac}(z,\omega_m) = \frac{g_{B0}}{2}\left(\frac{1}{1-j\Delta'(z)} + \frac{1}{1+j\Delta'(z)} + \frac{1}{1-j(\Delta'(z)-\omega'(z))} + \frac{1}{1+j(\Delta'(z)+\omega'(z))}\right) \qquad (2)$$

In Eq. (2), g_{B0} is the SBS peak gain, $\Delta'(z)$ is a detuning parameter depending on the difference between the pump-probe frequency shift Δf_{pp} and the local BFS, i.e., $\Delta'(z) = 2\pi\left(\Delta f_{pp} - BFS(z)\right)/\Gamma$ (Γ is the acoustic damping rate), and $\omega' = \omega/\Gamma$.
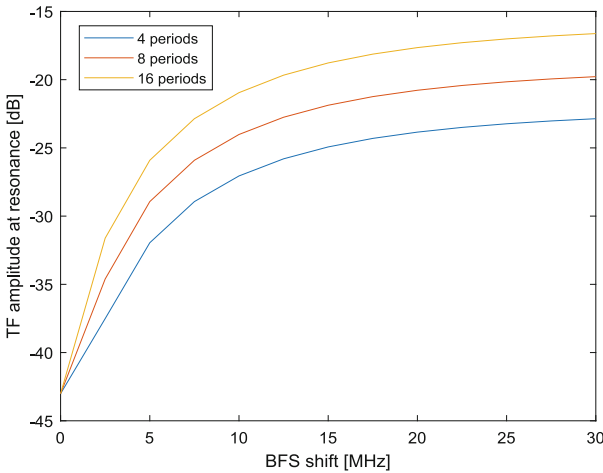
Fig. 2. Normalized amplitude of the TF at the resonance frequency, as a function of the BFS modulation amplitude.

The model described by Eqs. (1–2) has been employed to determine the amplitude of the TF at the resonance frequency ω_{res}, as a function of the modulation amplitude $\Delta\nu$. The results are shown in Fig. 2, which represents the TF amplitude at the resonance frequency ω_{res}, normalized to the TF amplitude at zero frequency, for a number of

periods equal to 4, 8 or 16. The figure reveals that the amplitude of the resonant peak saturates when the modulation amplitude approaches the BGS bandwidth (35 MHz in our simulations). Furthermore, it increases by 3 dB for each doubling in the number of periods. However, increasing the number of periods also results in a longer sensor, therefore a proper trade-off must be found between the amplitude of the signal and the extension of the sensing region for dynamic measurements.

Other simulations were performed to verify if the proposed method can be applied to more dynamic positions along the same fiber. To this aim, we suppose that a 16-periods BFS modulation is realized in 5 different positions of the fiber, each one with a different modulation period (17.2 mm, 12.9 mm, 10.3 mm, 8.6 mm, and 7.4 mm). These periods correspond to a resonance frequency of 6, 8, 10, 12 and 14 GHz, respectively. Figure 3 shows the fiber response simulated in case of no strain, or with a strain-induced BFS shift of 30 MHz applied sequentially to one of the 5 sensing positions. The figure reveals that the strain only modifies the TF amplitude at the resonance frequency corresponding to the strained position. We also note that, the BFS modulation with a period of 17.2 mm produces two resonances in the investigated spectral region (0–20 GHz), the first one at the fundamental frequency (6 GHz), and the second one at the first odd harmonic of the fundamental (18 GHz). Both resonances are affected by the strain acting on the corresponding sensing position. These results suggest that, to avoid crosstalk, the BFS modulation periods should not be integer multiples of each other.
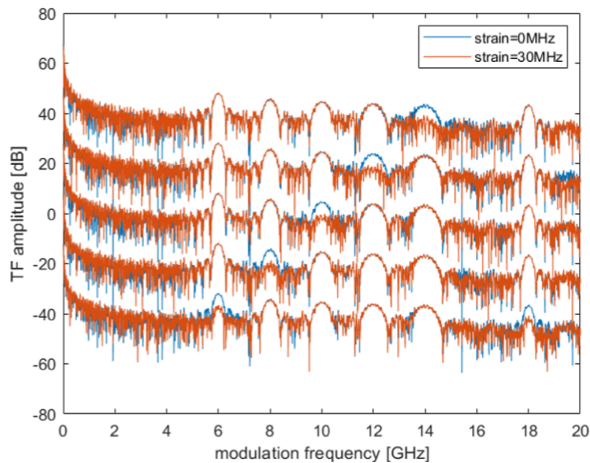
Fig. 3. TF amplitude simulated for a 5-m long fiber, comprising 5 dynamic sensing positions. The TF amplitude curves are vertically shifted by 20 dB each other for clarity purposes.

4   Experimental Results

For our experiments, the BFS spatial modulation was realized by tapering. In fact, tapering a standard SMF-28 single-mode fiber induces a blue-shift of its BFS [7]. Based

on the simulation results shown in Fig. 1, a 30 MHz modulation amplitude is sufficient to fully modulate the Brillouin gain. Such a BFS shift is realized adopting a taper diameter of 50 μm [7]. The tapers have been realized using a Vytran GPX3800 glass processor, which heats the glass up to its softening point, while simultaneously applying a tensile force. The glass processor was used to realize an array of 8 consecutive tapers with a nominal period of 8 mm. Each taper was realized with a downtaper and uptaper region of 3 mm, and a central waist region of 2 mm. The chosen parameters ensure an adiabatic transition across each taper. The BOFDA measurements were carried out using a conventional scheme, whose details can be found in Ref. [8]. In brief, the BOFDA sensor was used to acquire the baseband transfer function (TF) of the fiber in the frequency range 1.6 MHz–20 GHz, at the fixed pump-probe frequency shift of 10,866 MHz. The TF amplitude, reported in Fig. 4(a), reveals a resonance at around 11.4 GHz, which corresponds to a period of the array of ≈ 9.1 mm, thus slightly longer than the nominal value. This should be attributed to the fabrication tolerance of our glass processor. The resonance width is 2.6 GHz, approximately equal to twice the roundtrip time over the whole array. Figure 4(b) shows a segment of the inverse-Fourier-transformed signal, corresponding to a 15-cm fiber portion covering the multi-taper region. The modulation of the Brillouin gain induced by the tapers is clearly visible.

The dynamic sensing capabilities were tested by gluing the 72-mm long multi-taper onto the surface of a 70-cm cantilevered beam, close to its fixed end. The BOFDA sensor was used to acquire the transfer function over a narrow (200 MHz) modulation frequency range, chosen around the multi-taper resonance, while keeping the pump-probe frequency shift at a fixed value of 10,858 MHz, while putting the cantilever in free vibration. The IF bandwidth was set to 10 kHz.
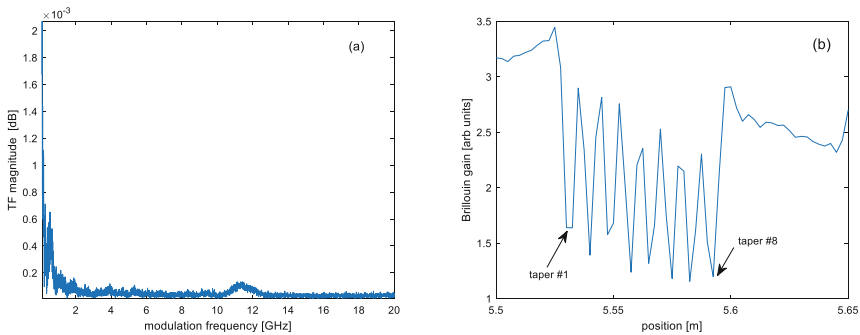
Fig. 4. (a) Transfer function amplitude measured at the pump-probe frequency shift of 10,866 MHz; (b) Portion of the inverse-Fourier-transformed data, for fiber positions close to the multi-taper structure.

Figure 5(a) shows the temporal series of the TF amplitude averaged over the acquired frequency range and acquired putting the cantilever in free oscillation. Finally, Fig. 5(b) shows the fast Fourier transform of the strain waveform in the time interval from 2.12 to 21.26 s, clearly revealing the first natural frequency of the cantilever at 3.6 Hz.
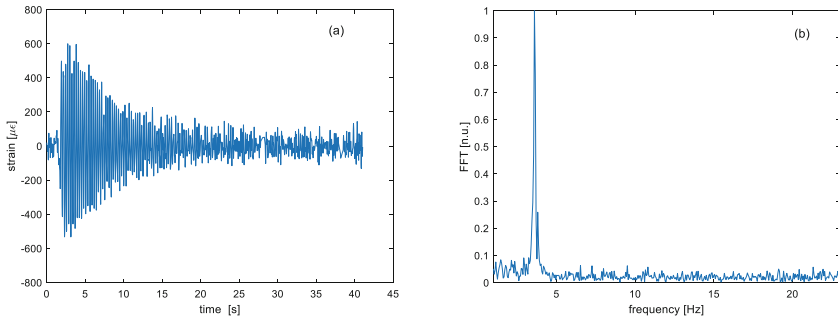
Fig. 5. (a) Dynamic strain measurement of the cantilever beam put in free vibration; (b) Corresponding fast Fourier transform (FFT) of the acquired strain waveform.

References

1. Damiano, E., Avolio, B., Minardo, A., Olivares, L., Picarelli, L., Zeni, L.: A laboratory study on the use of optical fibers for early detection of pre-failure slope movements in shallow granular soil deposits. Geotech. Test. J. **40**(4), 529–541 (2017)
2. Zou, L., Bao, X., Ravet, F., Chen, L.: Distributed Brillouin fiber sensor for detecting pipeline buckling in an energy pipe under internal pressure. Appl. Opt. **45**, 3372–3377 (2006)
3. Garus, D., Krebber, K., Schliep, F., Gogolla, T.: Distributed sensing technique based on Brillouin optical-fiber frequency-domain analysis. Opt. Lett. **21**, 1402 (1996)
4. Bernini, R., Crocco, L., Minardo, A., Soldovieri, F., Zeni, L.: All frequency domain distributed fiber-optic Brillouin sensing. IEEE Sens. J. **3**, 3R6 (2003)
5. Bernini, R., Minardo, A., Zeni, L.: Dynamic strain measurement in optical fibers by stimulated Brillouin scattering. Opt. Lett. **34**, 2613–2615 (2009)
6. Peled, Y., Motil, A., Yaron, L., Tur, M.: Slope-assisted fast distributed sensing in optical fibers with arbitrary Brillouin profile. Opt. Expr. **19**, 19845–19854 (2011)
7. Minardo, A., Zeni, L., Bernini, R., Catalano, E., Vallifuoco, R.: Quasi-distributed refractive index sensing by stimulated Brillouin scattering in tapered optical fibers. J. Light. Technol. **40**, 2619 (2022)
8. Minardo, A., Testa, G., Zeni, L., Bernini, R.: Theoretical and experimental analysis of Brillouin scattering in single-mode optical fiber excited by an intensity- and phase-modulated pump. J. Light. Technol. **28**, 193 (2010)

Power Electronics

2 MHz GaN-Based Isolated Resonant Converters: A Comparative Study

Stefano Cabizza$^{(\boxtimes)}$ and Giorgio Spiazzi

Department of Information Engineering (DEI), University of Padova, Padova, Italy
stefano.cabizza@phd.unipd.it, giorgio.spiazzi@dei.unipd.it

Abstract. This paper presents an initial analysis and comparison of two different 2 MHz GaN-based isolated resonant converters – named Active-Clamped Isolated SEPIC Converter (ACISC) and Active-Clamped Isolated Flyback Converter (ACIFC) – which support full ZVS throughout the 9 V–18 V automotive range and intended to provide isolation and power interface between the 12 V battery and the low-power subnet. Designed for resonant DCM operation and leveraging the high switching frequency enabled by GaN devices, the selected topologies lead to a strong reduction in total magnetic size and footprint. The analysis was verified through simulations as well as experimental measurements taken on two 7.2 W GaN-based prototypes employing planar transformers. Performance comparisons in terms of efficiency, conducted EMI and device stresses are also included.

Keywords: Resonant dc-dc converters · GaN devices · Zero Voltage Switching (ZVS) · Automotive power distribution

1 Introduction

Nowadays, in many low-power battery-connected automotive architectures there are a variety of 12 V low-power electronic loads – such as sensors, microcontrollers and communication transceivers – which are supplied by the 48 V main battery through an intermediate 12 V bus [1]. In case of failure of the latter, the entire system is sustained by a 12 V backup battery. The isolated converter interfacing the backup battery with the low-power 12 V intermediate bus must operate efficiently over the wide 9 V–18 V automotive input voltage range, while keeping magnetic size and overall footprint at a minimum. Presently adopted solutions at the industry level are based on the Flyback topology with Silicon devices, a poorly efficient solution mostly justified by its low component count and reduced footprint. In this paper, two GaN-based isolated resonant converters operating at 2 MHz − called *Active-Clamped Isolated SEPIC Converter* (ACISC) [2] and *Active-Clamped Isolated Flyback Converter* (ACIFC) [3,4] − are considered as viable substitutes for the application and, for this reason, compared in terms of *i)* efficiency, *ii)* conducted EMI, and *iii)* stresses across the switches.

2   Resonant DCM Operation of the Converters

In this paper, the two converters are operated in resonant DCM mode to ensure full ZVS operation for both switches throughout the operating range while simultaneously leading to small magnetics volume and footprint. Schematics of the converters are shown in Fig. 1a and Fig. 1b, where the adopted model for the high-frequency transformer T is also highlighted. As can be seen, the latter is modeled by an equivalent primary-side leakage inductance L_{pe}, an equivalent primary-side magnetizing inductance L_{me}, and an equivalent turns ratio n_e. The pictures of the two experimental prototypes are shown in Fig. 1c and Fig. 1d, where both of them are built around the EPC9055 development board which features the selected 100 V, 1.7 A EPC2106 half-bridge pair and the clamp capacitor. Figure 2 shows the main waveforms of the GaN-based converters in one of the possible resonant DCM modes, along with the information about when Q_1, Q_2 and D_r are ON or OFF during each of the three subintervals. The resonant operation − caused by the interaction between the resonant capacitor

(a)   (b)

(c)   (d)
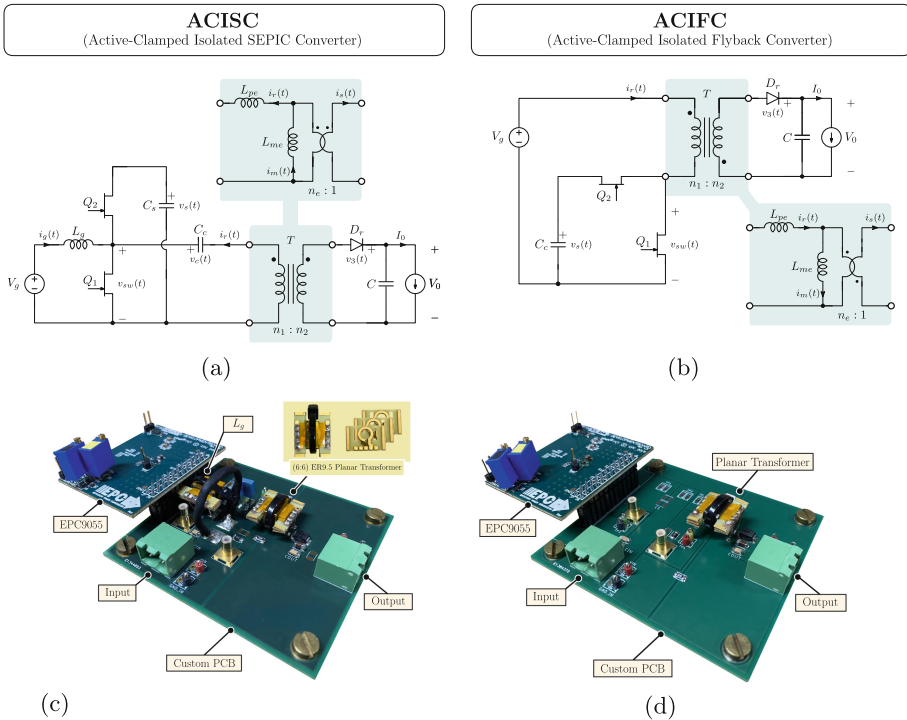
Fig. 1. (a) Schematic and (c) experimental prototype's photo of the GaN-based Active-Clamped Isolated SEPIC Converter (ACISC); (b) Schematic and (d) experimental prototype's picture of the GaN-based Active-Clamped Isolated Flyback Converter (ACIFC).
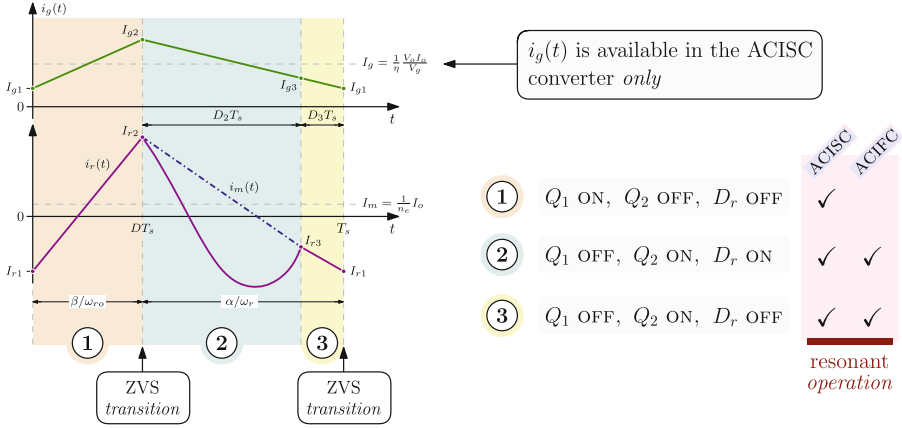
Fig. 2. Example of the main waveforms available in the two GaN-based isolated converters operated in resonant DCM mode.

C_c and the leakage inductance L_{pe} − can be easily seen by observing the trend of $i_r(t)$. Here DCM is defined by the output diode D_r being OFF during a fraction of the subinterval $(1-D)T_s$ (see interval D_3T_s in Fig. 2). Lastly, Fig. 2 also shows the ZVS transition for the switches which allows to turn Q_1 and Q_2 ON with zero-voltage at $t = DT_s$ and $t = T_s$, respectively, once a proper design of the magnetics is done.

3 Voltage Gain Analysis

An approximated closed-loop solution can be found for the particular operating point corresponding to the boundary between CCM and DCM operation, *i.e.* assuming subinterval $D_3T_s = 0$. The analytical expression for the voltage gain M yields values close to the simulated ones even when the converter enters the DCM. Thus, considering the boundary CCM/DCM operating point for the converters and assuming a negligible voltage ripple across the ACISC's resonant capacitor C_c (even if it doesn't reflect the reality for such application), the flux balance on the magnetizing inductance L_{me} yields

$$M \triangleq \frac{V_o}{V_g} = \frac{D}{(1-D)} \frac{1}{n_e(1+\lambda)} \tag{1}$$

either for the ACISC and ACIFC, where D is the duty-cycle of the low-side switch Q_1 and $\lambda \triangleq L_{pe}/L_{me}$ is the inductance ratio. The plot of M as a function of D predicted by (1) is shown in Fig. 3a, where n_e and λ are assumed to be equal to 1 and 10%, respectively. The simulated data points − which are also plotted in Fig. 3a − are obtained by varying the input voltage V_g from 9 V up to 18 V, with V_o fixed to 12 V since it represents the intermediate bus required by the battery-connected architecture. In this range of duty-cycle values, the two converters
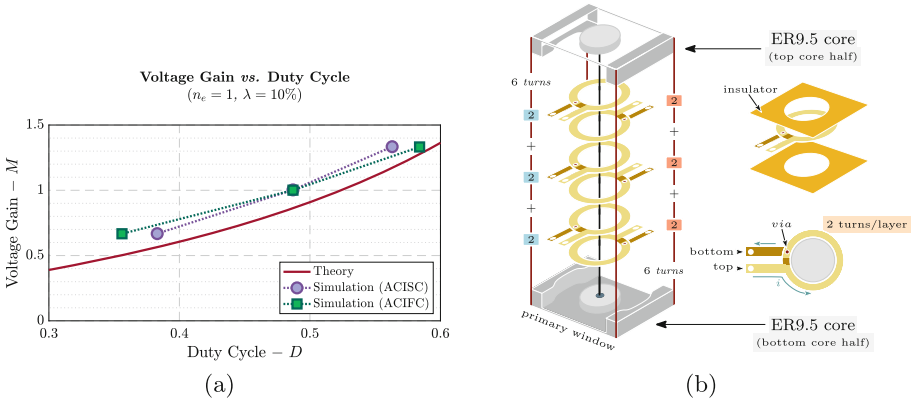
Fig. 3. (a) Voltage gain comparison between the theoretical model and simulated data points, and (b) exploded view of the realized planar transformers based on two ER9.5 half-cores and three two-turns layers per winding ($n_1 = n_2 = 6$).

are always operating in resonant DCM mode. As can be seen, (1) is close to the simulated data points either for the ACISC and ACIFC converter even if strong assumptions were previously made to obtain the expression. Looking at the simulated results obtained for the ACISC converter, a more precise analytical expression can be obtained – which perfectly fits with the data points – when the voltage ripple across C_c is taken into account (as shown in [2]). To obtain the right value for the magnetizing inductance L_{me} to satisfy the ZVS conditions in the ACIFC converter and, together with the input inductance value L_g for the ACISC, two high-frequency planar transformers having $n_1 = n_2 = 6$ turns on both primary and secondary windings are realized (to have an adequate compromise between core and winding losses). As can be noted by looking at the planar transformer structure shown in Fig. 3b, each 6-turn winding consists of three series-connected layers of two turns each. Each two-turn layer is hosted on a 440 µm-thick PCB module, with one turn on the top and the other one on the bottom. The transformers are based on two ER9.5 half-cores to reduce the overall footprint, with 380 µm and 640 µm air gaps between the central legs for the ACISC and ACIFC, respectively, to meet the desired magnetizing inductance value (see Tab. 1). Considering the design requirements summarized a few lines further down, and in particular the switching rate, the 3F4 high-frequency power material is chosen for the two half-cores.

The main specifications dictated by the considered application are as follows: $V_g = [9\,\text{V} \div 18\,\text{V}]$, $V_g^{nom} = 12\,\text{V}$, $V_o = 12\,\text{V}$, $I_o = 600\,\text{mA}$, $f_s = 2\,\text{MHz}$.

Table 1. Converter parameters

Parameter	Symbol	ACISC	ACIFC	
Input inductance	L_g	2.2	–	µH
Equivalent primary leakage inductance	L_{pe}	75.2	75.7	nH
Equivalent magnetizing inductance	L_{me}	1.2	0.6	µH
Inductance ratio	λ	6.3	12.6	%
Equivalent transformer turns ratio	n_e	0.97	0.95	
Resonant capacitor	C_c	47.8	20	nF
Clamp capacitor	C_s	1	–	µF
Output capacitor	C_o	10	10	µF

4   Experimental Results

The component values, measured at $f_s = 2\,\mathrm{MHz}$, are shown in Table 1. Figure 4a and Fig. 4b report the experimental waveforms for the ACISC and ACIFC, respectively, in nominal conditions ($V_g = V_o = 12\,\mathrm{V}$, $I_o = 600\,\mathrm{mA}$). The ZVS conditions are fully guaranteed for both converters: the switching-node voltage $v_{sw}(t)$ is capable of completing the entire transition before the end of the two dead times, resulting in the ZVS turn-ON of both switches. Figure 4 also shows – looking at $v_{sw}(t)$ – that the voltage stresses across the switches are considerably higher in the ACIFC converter due to a lower value for C_c required to operate the converter in resonant DCM mode. Figure 5a compares the efficiency of the two GaN-based prototypes as a function of the input voltage V_g and reveals a peak efficiency of the designed ACISC converter of 87.22 % at $V_o = 12\,\mathrm{V}$ and $I_o = 600\,\mathrm{mA}$, approximately 8 % better than the ACIFC converter. This signifi-cant difference is mainly due to the low value of L_{me} for the ACIFC required to
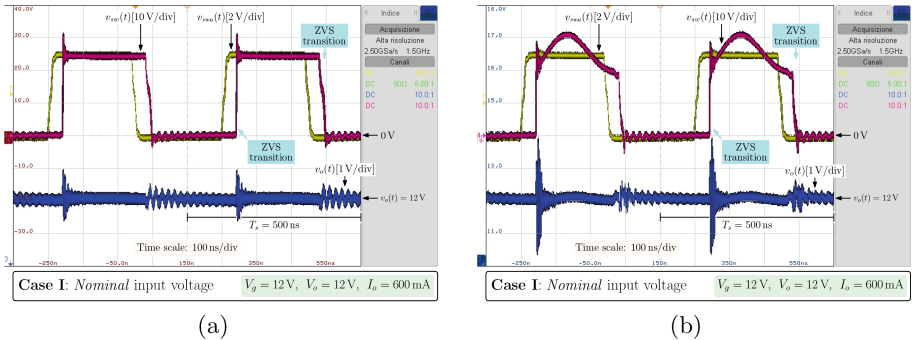

Fig. 4. Experimental screenshot of (a) the ACISC and (b) the ACIFC in nominal conditions. $v_o(t)$ (1 V/div, $v_{offset} = 14\,\mathrm{V}$) is the output voltage, $v_{PWM}(t)$ (2 V/div) is the input PWM used to drive the switches, and $v_{sw}(t)$ (10 V/div) is the switching node voltage. Time scale: 100 ns/div.
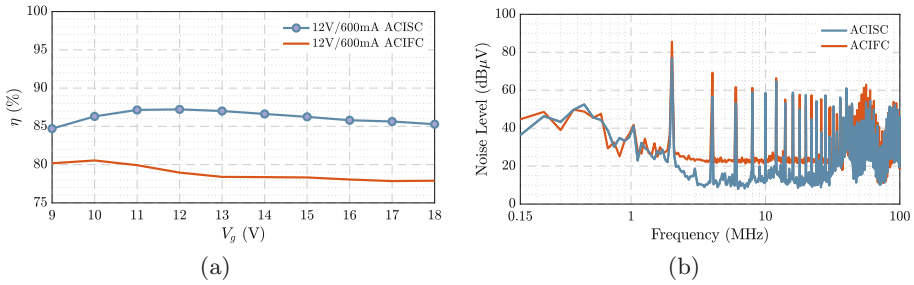
Fig. 5. (a) Efficiency comparison between the two GaN-based converters as a function of the input voltage V_g and (b) results in terms of conducted emission (measured at the input) in absence of any EMI filter.

guarantee the ZVS operation, which results in a significant increase in primary transformer winding losses. To conclude, Fig. 5b compares the two converters in terms of conducted emission (measured at the input using a noise separator and a LISN). Also here, the ACISC converter is better than the ACIFC one mainly due to the presence of the input inductor L_g which acts as a filter (looking *e.g.* at the first spectral line, the ACISC provides a reduction of almost $10\,\mathrm{dB\,\mu V}$).

5   Conclusions

This paper addresses an initial comparison between two GaN-based isolated resonant converters – named ACISC and ACIFC – operating in resonant DCM at $2\,\mathrm{MHz}$ with the aim of satisfying ZVS throughout the intended operating range and reducing the magnetic size and overall footprint. Reported experimental results confirm full ZVS operation of the converters and highlight better performances for the ACISC converter either in terms of efficiency (reaching a peak of $87.22\,\%$ in nominal condition) and electromagnetic interference noise.

References

1. Cabizza, S., Corradini, L., Spiazzi, G., Garbossa, C.: Comparative study of 48v-based low-power automotive architectures. In: 2020 IEEE 21st Workshop on Control and Modeling for Power Electronics (COMPEL), pp. 1–8 (2020)
2. Cabizza, S., Corradini, L., Spiazzi, G.: Analysis and design of a 2 MHz GaN-based active-clamped isolated Sepic converter for low-power automotive subnets. IEEE Appl. Power Electron. Conf. Exposition (APEC) **2022**, 2127–2134 (2022)
3. LaBella, T., York, B., Hutchens, C., Lai, J.-S.: Dead time optimization through loss analysis of an active-clamp flyback converter utilizing GaN devices. IEEE Energy Convers. Congr. Exposition (ECCE) **2012**, 3882–3889 (2012)
4. Perrin, R., Quentin, N., Allard, B., Martin, C., Ali, M.: High-temperature GaN Active-Clamp Flyback converter with resonant operation mode. In: IEEE Journal of Emerging and Selected Topics in Power Electronics, pp. 1077–1085 (2016)

Designing Power Systems to Charge Electrical Vehicle Fleets in the Industrial Environment

A. A. Nkembi, M. Simonazzi, D. Santoro, P. Cova, R. Menozzi, and N. Delmonte^(✉)

Department of Engineering and Architecture, University of Parma, Parma, Italy
nicola.delmonte@unipr.it

Abstract. The increased use of Electric Vehicles (EVs) in industrial environments (e.g., battery-powered forklifts) requires proper design of the grid architecture. The shift towards the use of Renewable Energy Sources (RES) and the need for efficient energy use are leading to promising solutions with Photovoltaic (PV) sources, Energy Storage Systems (ESSs), and small power electronic converters. However, the sizing of the facility power system, including the source nominal power and the capacity of the ESS, requires careful consideration of various parameters. In this work, we present a novel approach to define the most suitable grid architecture based on behavioral PLECS modeling and validated through tests carried out on a reduced-scale system; the model considers the number of EVs, initial investment costs, Power Grid (PG) consumption costs, CO_2 footprint, and EVs working time specifications. Through simulations, the optimum capacity of the PV and ESS installations can be determined by considering economic, technological, or environmental aspects.

Keywords: Electric vehicle · Renewable energy source · Battery energy storage system · Investment cost · Consumption costs · PLECS

1 Introduction

A proper grid architecture is needed in industrial environments where numerous EVs must be charged. Environmental and economic considerations encourage the use of RES [1]. From an environmental standpoint, increased self-sufficiency is mandatory to maximize the use of the green energy produced. However, if the primary energy source is a PV plant, maximizing self-sufficiency requires the installation of a suitably sized ESS, and increasing the ESS capacity is critical for reducing the exchange with the PG [2]. From an economic perspective, the optimum trade-off between the costs of initial investment (i.e., PV and ESS size), running costs and PG consumption must be determined [3]. Finally, the EV charging strategy, namely, timing, frequency, and duration, must be defined considering the electric grid characteristics to reduce the cost of PG power consumption, increase the battery lifetime, and maximize the operability time of the EV [4].

To define the most suitable grid architecture, this work presents a behavioral PLECS model, which we validated through experimental tests on a reduced-scale system. The

model of the whole grid architecture is described in Sect. 2, where the EV's behavioral model, the control algorithm, the power supply system, and a cost estimation analysis are highlighted. In Sect. 3 the reduced-scale prototype for the experimental validation is shown. Finally, in Sect. 4 the simulation results are presented, and conclusions are drawn in Sect. 5.

2 Description of the Model

Figure 1 shows the grid architecture of the simulation model considering a case study featuring a fleet of 10 EVs, each equipped with a 10.5 kWh battery, and 2 charging stations supplied by a PV plant supported by an ESS and by the PG. The EVs fleet is governed by a Job Scheduler (JS). The default schedule consists of working phases of about 2 h alternated with 5-minute charging phases. Work cycles and durations are assigned in a pseudo-random way.
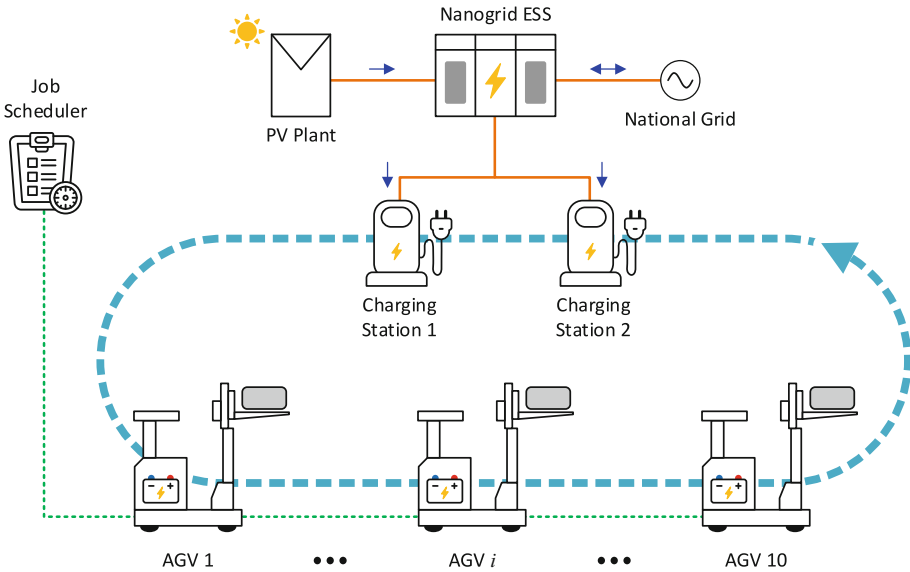
Fig. 1. Grid architecture of the simulation model.

We choose PLECS as simulation tool, in anticipation of carrying out Hardware in the Loop (HIL) simulations using a Plexim RT-BOX for model validation. The model consists of 5 main blocks (Fig. 2): a subsystem (*10 AGVs*) that runs the models of 10 EVs in parallel, a subsystem modelling the JS, the model of the PV plant with its perturb and observe Maximum Power Point Tracking (MPPT) controller [5], the Battery ESS (BESS) and an energy meter to estimate the global energy consumption from the PG and the operating costs.

2.1 Vehicles, Charging Stations and Job Scheduler

Vehicles are modelled by means of a Finite State Machine (FSM) coupled with the model of a battery. To simplify the model, each EV contains both the logic underlying the duration of the jobs and the one underlying the charging station. The two algorithms are mutually selected depending on the commands coming from the JS.

An EV can be in three different states. The initial one is the *off* state in which, the vehicle is parked, waiting to receive a *trigger* from the JS. If a *job trigger* is received the FSM sets the vehicle as *busy* and keeps it in this state for a random period of 2 ± 0.5 h. An exception is made if the vehicle reaches a SoC below 20% and it is unable to complete its work. When the job is completed successfully, the vehicle is ready to receive a new *trigger*. If a *charging trigger* is received, a flag is raised allowing the JS to count the number of free charging stations. Then the battery is fast-charged at constant current rate for 5 min. An extension on the charging time is allowed in case the SoC is still below the minimum threshold of 80%.

The JS is designed to monitor the global state of the system, namely the state of the vehicles and the number of available (or busy) charging stations. At each iteration of the simulation, the algorithm checks whether there are any free EVs. If at least one charging station is available, each free EV that has already carried out an assigned job will be triggered for the charging. Then the algorithm extracts a random number, limited to the total number of EVs, and if the corresponding EV is free, and its SoC is above a minimum safe value, it is triggered for a new job.
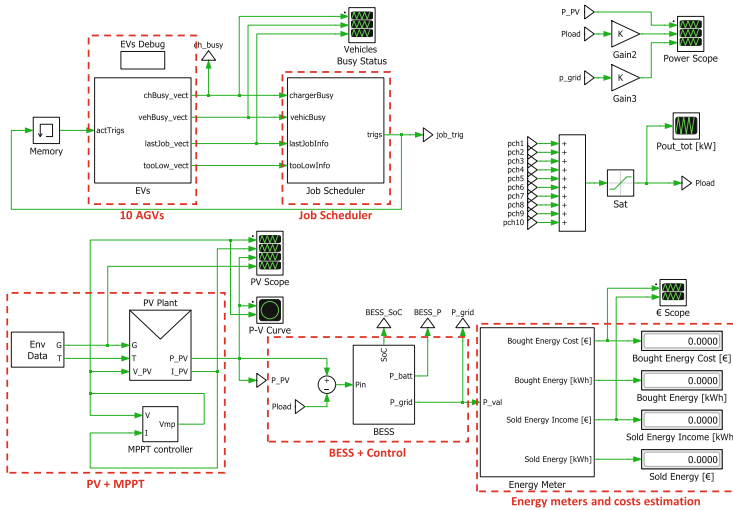

Fig. 2. Global view of the model implemented in PLECS simulation environment.

2.2 Power Supply System and Costs Estimation

The power required to charge the EVs is supplied by a PV plant supported by a BESS and by the connection with the PG. The PV array production is obtained by the 1-diode

equivalent circuit. The BESS is modelled starting from empirical equations representing the behaviour of a Li-ion battery unit, suitably scaled to obtain the entire storage unit.

The system is operated to try to minimize the amount of energy exchanged with the PG. The power entering (positive) or supplied by (negative) the BESS is computed by subtracting the value of power consumed by the loads from the PV power. If the BESS is in *full* SoC and there is an excess in energy production which is sold to the PG. Conversely, if the BESS is in *low* SoC and the PV production is not able to satisfy the load demand, the required energy is bought from the PG.

The total operating cost after one year ($C_{tot,1y}$) is obtained as in Eq. (1).

$$C_{tot,1y} = U_E^{bought} \int_0^{1y} P_{bought}\,dt - U_E^{sold} \int_0^{1y} P_{sold}\,dt + \frac{P_{PV}^{pk} \cdot U_{PV}}{20} + \frac{Q_{BSS}^{tot} \cdot U_{BESS}}{10}$$

(1)

The power exchanged with the PG is split in positive (P_{bought}) and negative (P_{sold}) components and integrated over time to obtain, the amount of energy sold and bought to/from the PG. Then, proper €/kWh prices (U_E^{bought} and U_E^{sold}) are applied to each component. Finally, we add the installation costs of the PV and of the BESS plants, computed from per-unit of peak-power (U_{PV}) and energy-capacity (U_{BESS}) costs, considering the actual size of each plant (P_{PV}^{pk} and Q_{BSS}^{tot}) and the typical plant lifetime (20 years for PV, 10 years for BESS). In addition, from an environmental standpoint, it is possible to estimate the amount of CO_2 produced due to the energy bought from the PG by applying a proper emission factor ($kgCO_2/kWh$) obtained from [6].

3   Reduced-Scale Prototype

Before performing yearlong simulations to find the optimum mix between PV and BESS size minimizing the system costs, we designed and setup a reduced-scale DC prototype to validate the behaviour of the model. To reduce the prototyping time, we deploy all the control logic of the system to the PLECS RT Box 1 HIL simulator.
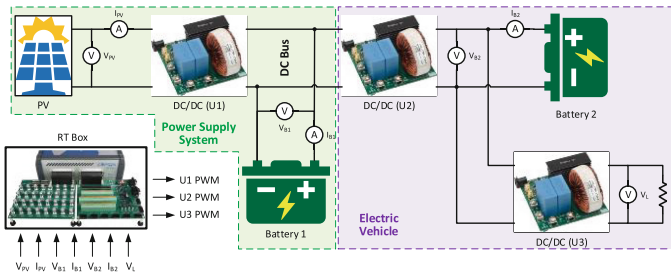
Fig. 3. Block diagram of the small-scale system prototype.

Figure 3 shows the block diagram of the prototype, while Fig. 4 shows the test bench implemented. The PV plant is emulated by means of a power generator with built-in solar
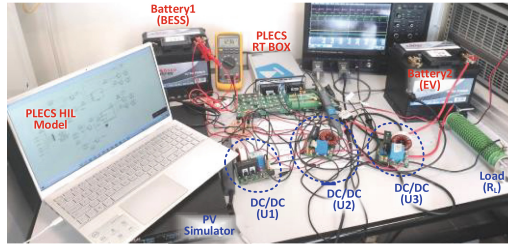
Fig. 4. Test bench setup of the small-scale system prototype.

array simulator which is interfaced with the BESS (emulated by *Battery 1*) by means of a DC/DC converter (*U1*). *Battery 1* also fixes the DC-bus voltage (V_{B1}). The behaviour of an EV is emulated by *Battery 2* which represents the onboard storage. It can be charged according to the JS via converter *U2* or discharged in a controlled manner (emulating a working cycle) by means of the converter *U3* closed on a power resistor (R_L). The HIL simulator controls *U1* by the MPPT, while *U2* and *U3* are mutually activated according to the JS and operated by a Proportional-Integrative controller.

4   Simulation Results

Figure 5 shows the simulated power profiles for three values of the PV plant capacity, with a working scenario of about 8 h per day. Parametric simulations estimate the optimal size for PV and BESS installations. For several PV-BESS combinations, we compute the total economic cost after one year of operation, including the installation and the energy balance costs. Table 1 shows the results obtained considering a scenario where the EVs are operated 24 h a day. The model allows the identification of the PV-ESS combination minimizing the system operational cost (green cells in Table 1).

Fig. 5. Power profiles: weekly simulation results for 8 h/day EVs operation scenario.

Table 1. Simulation results after 1 year for 24 h/day EVs operation scenario.

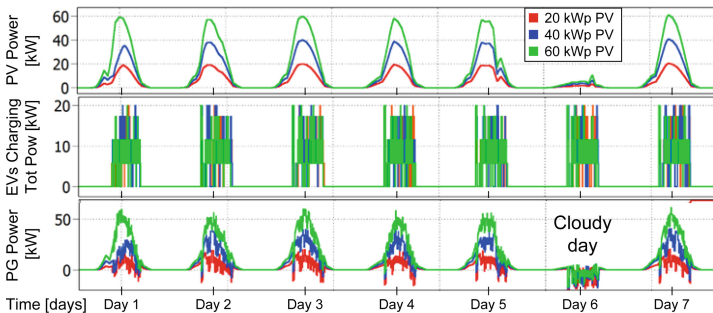| PV size [kWp]	ESS size [kWh]	$C_{PV}^{inst,1y}$ [10^3 €]	$C_{BESS}^{inst,1y}$ [10^3 €]	$C_{E,1y}$ [10^3 €]	$C_{tot,1y}$ [10^3 €]	CO_2 emissions [kg]
20	0	0.50	0.00	17.71	18.21	6.43
20	52	0.50	1.76	15.88	18.14	5.53
20	78	0.50	2.64	15.84	18.98	5.52
20	104	0.50	3.52	15.80	19.82	5.52
20	155	0.50	5.25	15.75	21.50	5.51
20	207	0.50	7.01	15.63	23.14	5.50
40	0	0.98	0.00	13.56	14.53	5.78
40	52	0.98	1.76	10.79	13.52	4.39
40	78	0.98	2.64	9.60	13.21	3.80
40	104	0.98	3.52	8.55	13.05	3.28
40	155	0.98	5.25	7.15	13.38	2.60
40	207	0.98	7.01	6.93	14.91	2.52
60	0	1.48	0.00	10.09	11.57	5.48
60	52	1.48	1.76	7.10	10.33	3.98
60	78	1.48	2.64	5.77	9.89	3.32
60	104	1.48	3.52	4.50	9.49	2.69
60	155	1.48	5.25	2.53	9.25	1.70
60	207	1.48	7.01	1.99	10.47	1.47

5 Conclusions

In this work, we have presented a novel approach to define the most suitable grid architecture to charge EV fleets in industrial environments. The design is based on a behavioural PLECS model, which we have validated through a reduced-scale system experimental test bench. Considering a 24 h/day scenario with 10 EVs and two charging stations supplied by a PV plant supported by an ESS and by the PG, the optimum grid architecture can be determined. The combination of PV sizes and ESS capacity that allows to minimize the system operational cost can be identified with the solution of a 60 kWp PV size and a 155 kWh ESS capacity. Instead, to minimize the environmental footprint, a solution with 207 kWh ESS capacity can be implemented.

Concluding, the proposed simulation model allows to define different EVs operation scenarios and to obtain the optimum capacity of the PV and ESS installations by considering economic, technological, or environmental aspects.

References

1. Vithayasrichareon, P., Mills, G., MacGill, I.F.: Impact of electric vehicles and solar PV on future generation portfolio investment. IEEE Trans. Sustain. Energy **6**(3), 899–908 (2015). https://doi.org/10.1109/TSTE.2015.2418338
2. Javaid, S., Kato, T., Matsuyama, T.: Power flow coloring system over a nanogrid with fluctuating power sources and loads. IEEE Trans. Industr. Inform. **13**(6), 3174–3184 (2017). https://doi.org/10.1109/TII.2017.2733550

3. Jiao, M., Pan, F., Huang, X., Yuan, X.: Evaluation on total cost of ownership of electric forklifts with lithium-ion battery. Proc. CIEEC **2021**, 1–5 (2021)
4. Aluisio, B., Dicorato, M., Ferrini, I., Forte, G., Sbrizzai, R., Trovato, M.: Optimal sizing procedure for electric vehicle supply infrastructure based on DC microgrid with station commitment. Energies **12**(10), 1–19 (2019)
5. Lyden, S., Haque, M.E.: Maximum power point tracking techniques for photovoltaic systems: a comprehensive review and comparative analysis. Renew. Sustain. Energy Rev. **52**, 1504–1518 (2015)
6. ElectricityMap|Live CO_2 emissions of electricity consumption, https://www.electricitymap.org/. Accessed 15 June 2022

FPGA HardWare Architecture for SVPWM Based on a Taylor Series Decomposition

Andrea Donisi[✉], Luigi Di Benedetto, Rosalba Liguori,
Gian Domenico Licciardo, and Alfredo Rubino

Department of Industrial Engineering, University of Salerno,
Fisciano, SA, Italy
adonisi@unsia.it, {ldibenedetto,rliguori,gdlicciardo,arubino}@unisa.it

Abstract. The parer illustrates a new FPGA hardware architecture for the Space Vector Pulse Width Modulation, which decompose the dwell-times expressions using the Taylor Series. The difference from the state of the arts is the disuse of other resources, like external reference signals or Digital Signal Processor, as well as specific architectures, like CORDIC core or Look Up Table-based approaches. All the calculations are done by a 32 bit fixed-point Arithmetic Logic Unit, which can perform a real time variation of the output amplitude.

The architecture has been implemented on a Xilinx Artix VII FPGA XC7A35T1CPG236C requiring 1967 LUTs and 492 Flip Flops, respectively, the 9.46% and 1.18% of the overall resources, and a dynamic power consumption of 1 mW.

Keywords: Space-vector pulsewidth modulation (SVPWM) · Field programmable gate array (FPGA) · Digital hardware design · Three-phase DC/AC power converter

1 Introduction

The advent of new technologies like silicon carbide [1,2] and gallium nitride [3,4] permits to increase the power density and the switching frequency of a power converter and the digital controllers became pervasive thanks to their performance and versatility [5–7]. Moreover, Field Programmable Gate Arrays, FPGA, are interesting for the possibility to reconfigure the controller and to have a real-time operation [5,8]. One of the more common techniques to control three-phase inverters is the Space Vector Pulse Width Modulation, SVPWM, and is exclusively managed through digital controllers, due to the high computational cost involved in the calculation of the dwell-times [9]. The computation of the trigonometric functions is a complex task for a HW processor and in literature several approaches are found, like the use of EPROM reference table [10] with the use of an external reference signal, of the CORDIC algorithm [11] or of the Look-Up Table, LUT [12].

In this paper we show a FPGA implementation of an open loop SVPWM controller used to drive a three-phase inverter and that can change the amplitude of the output voltage.

2   Theory of the Proposed SVPWM

The SVPWM is a modulation technique to generate the gate signals for the power transistors of a three-phase inverter. By keeping the transistors in certain configurations for a predetermined amount of time, named dwell-time, the modulation can define the desired frequency and amplitude of the three-phase output voltages. The problem of a FPGA implementation of such technique lies in the calculation of the dwell-times due to the computational costs of the trigonometric functions. This last constrain is solved through a Taylor Series [13] linearization of the dwell-time equations. Hence, after using the properties of the dwell-times highlighted in [14], we obtained the following equations:

$$T_{\mathrm{A}} = \frac{2V_{\mathrm{M}} f_{\mathrm{CLK}}}{V_{\mathrm{DC}} f_{\mathrm{SW}}^2} \left[0.75 f_{\mathrm{SW}} - 2.72 f_{\mathrm{C}} i - \frac{14.8 f_{\mathrm{C}}^2}{f_{\mathrm{SW}}} i^2 + \frac{17.9 f_{\mathrm{C}}^3 i^3}{f_{\mathrm{SW}}^2} \right] \tag{1a}$$

$$T_{\mathrm{B}} = \frac{2V_{\mathrm{M}} f_{\mathrm{CLK}}}{V_{\mathrm{DC}} f_{\mathrm{SW}}^2} \left[5.44 f_{\mathrm{C}} i - \frac{35.8 f_{\mathrm{C}}^3 i^3}{f_{\mathrm{SW}}^2} \right] \tag{1b}$$

$$T_0 = \frac{f_{\mathrm{CLK}}}{f_{\mathrm{SW}}} - T_{\mathrm{A}} - T_{\mathrm{B}} \tag{1c}$$

where i is from 0 to $(\frac{f_{\mathrm{SW}}}{6 f_{\mathrm{C}}} - 1) = i_{\mathrm{MAX}} - 1$, and f_{C}, f_{SW}, f_{CLK} are the carrier, the switching and the clock frequencies, respectively, V_{M} the output amplitude voltage and V_{DC} the DC-link voltage. The modulation index is defined as $m_{\mathrm{a}} = 2V_{\mathrm{M}}/V_{\mathrm{DC}} \leq 2/\sqrt{3}$.

3   HW Architecture

The architecture is built to work as an open loop control, but it can work as a closed loop controller as long as an external feedback network is added to the system. The block diagram of the proposed HW architecture is shown in Fig. 1, as it can be seen that the architecture is divided into three macro blocks:

– The TIME CALCULATOR is divided in two sub-blocks: the ALU is a 32 bit fixed point Arithmetic Logic Unit, which implements Eq. 1, meanwhile TIME DIVISOR divides the dwell-times calculated to obtain a sequence of dwell-times as: $\frac{T_0}{4}, \frac{T_{\mathrm{A}}}{2}, \frac{T_{\mathrm{B}}}{2}, T_7, \frac{T_{\mathrm{B}}}{2}, \frac{T_{\mathrm{A}}}{2}, \frac{T_0}{4}$.
– The CONTROL block is also divided in two sub-blocks: i-CALCULATOR keeps track of the actual sector and, also, manages i by changing its value at each switching period. COUNTER enables i-CALCULATOR to increment the value of i, chooses the MUX configuration and maintains it based on the actual dwell-time.

– INVERTER CONFIGURATION is composed by SECTOR SELECTOR, one
multiplexer and DEAD TIME. SECTOR SELECTOR is a look-up table con-
taining all the inverter configurations, which are selected by ACTUAL SEC-
TOR signal, and sends the four configurations to the multiplexer. DEAD
TIME generates the six gate control signals including the dead time.
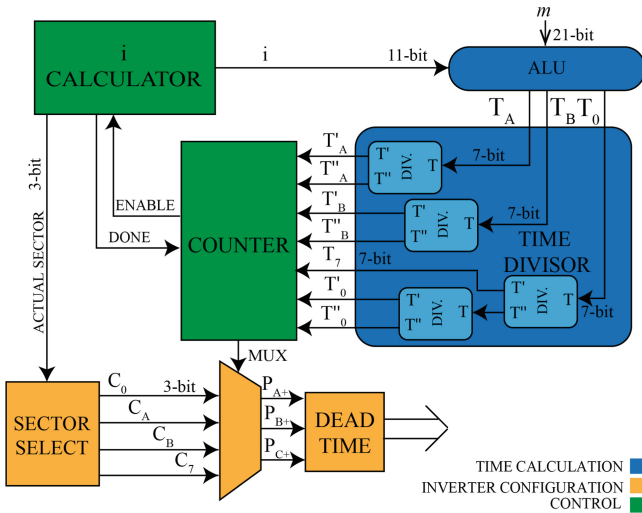
Fig. 1. Block diagram of the HW architecture

4 Experimental Results

The experimental setup is shown in Fig. 2. The proposed architecture is imple-
mented on a FPGA Xilinx Artix VII XC7A35T1CPG236C [15] and the three
top transistor control signals have been monitored with the Tektronix DPO 7254
oscilloscope. By using a sample frequency of the oscilloscope equal or lower than
the control switching frequency, the output waveforms are filtered and only the
fundamental harmonics are shown. In the implementation phase the carrier and
the switching frequencies are equal to $f_C = 10$ Hz and $f_{SW} = 100$ kHz, mean-
while the FPGA clock frequency is set to $f_{CLK} = 12$ MHz. The minimum angle
variation is $\Delta\theta = 2\pi f_C/f_{SW} = 2 \cdot 10^{-4}\pi$. It should be noted that the architecture
is fully described in VHDL.
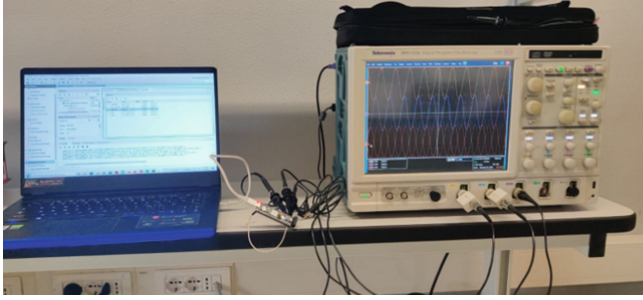
Fig. 2. Experimental setup

The experimental results are shown from Fig. 3 to Fig. 5. In Fig. 3 the top gate control signals are shown for multiple switching periods in the fifth sector, instead Fig. 4 shows the phase voltage amplitude variation in a time interval of 100 ms, with $0 \leq m_{\mathrm{a}} \leq 1$. In Fig. 5 the concatenate voltages, obtained thanks to the mat function of the oscilloscope, are shown for a $f_{\mathrm{C}} = 10\,\mathrm{Hz}$ and a $m_{\mathrm{a}} = 1$: it is clear the elimination of the third harmonic of the phase voltages in the concatenate ones.

Our architecture needs 1967 LUTs and 492 FFs, which are, respectively, the 9.46% and 1.18% of the total resources available on the device, and has a dynamic power consumption of 1 mW, which is been extracted by a saif power analysis performed on Vivado 2018.2. Table 1 shows the comparison between the proposed work and other architectures implemented on the same FPGA and with the same $\Delta\theta$ in terms of resources utilization. Although the CORDIC
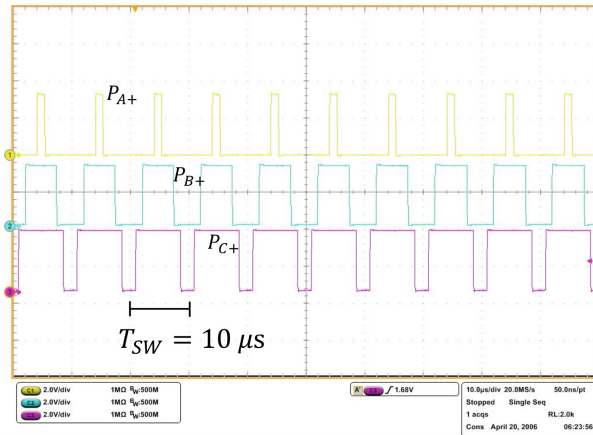
Fig. 3. Top gate control signal. Vertical axis: 2 V/div, time division: 5 μs/div.
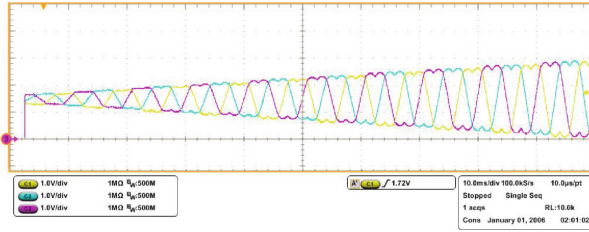
Fig. 4. Phase voltage with m_a variation from 0 to 1. Vertical axis: 1 V/div, time division: 10 ms/div, sampling rate: 100 kS/s
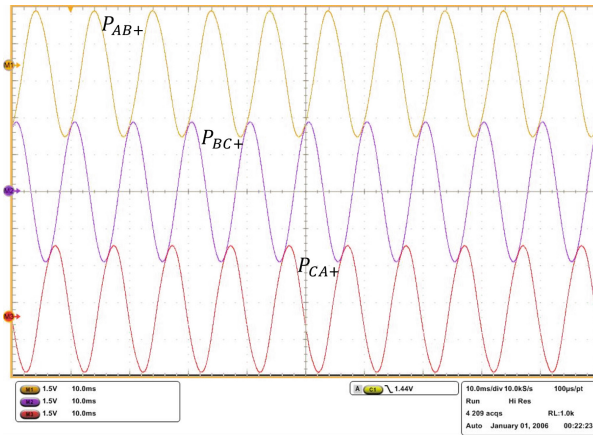
Fig. 5. Concatenate voltage with $m_a = 1$. $P_{AB+} = P_{A+} - P_{B+}$, $P_{BC+} = P_{B+} - P_{C+}$, $P_{CA+} = P_{C+} - P_{A+}$ Vertical axis: 1.5 V/div, time division: 10 ms/div, sampling rate: 10 kS/s

Iterative architecture requires the same dynamic power, 10.07% fewer LUT and 12.20% fewer FF than ours making it a good alternative, the number of iterations limits the possible maximum switching frequency, if the configuration of the system clock is unchanged. Instead, the CORDIC Cascade needs 31.37% more LUT, 22.36% fewer FF and a double dynamic power consumption than our architecture. Finally, the LUT architecture requires 363.08% more LUT and 78.45% more FF and has a dynamic power consumption seven times higher than ours, but can change the output switching and carrier frequencies, making it more flexible in terms of real-time configuration of the inverter.

Table 1. Comparison of resources utilization between CORDIC algorithm implemented in [15] and proposed architecture

	LUT [12]	CORDIC		Proposed HW
		Iterative	Cascade	
LUT	9108	1769	2584	1967
FF	878	432	382	492
Dyn.Pow [mW]	7	1	2.1	1
Clock Iteration	1	11	1	10

5 Conclusions

In this paper a novel hardware architecture shows promising results as an hardware accelerator to generate SVPWM control signals starting from the value of the desired amplitude without the requirement of an external signal reference. Its resource utilization is comparable with other architecture of the state of the art. The absence of DSP and BRAM also makes this work a good candidate for an ASIC implementation. By adding a feedback network to the system is also possible to utilize this HW to implement a closed loop control. Future development will focus on the optimization of the resources utilization, the possibility of a real time change of the output phase and of the switching and carrier frequency.

References

1. Di Benedetto, L., Licciardo, G., Erlbacher, T., Bauer, A., Rubino, A.: Optimized design for 4h-sic power dmosfet. IEEE Electron Device Lett. **37**(11), 1454–1457 (2016)
2. Di Benedetto, L., Licciardo, G.D., Erlbacher, T., Bauer, A.J., Liguori, R., Rubino, A.: A model of electric field distribution in gate oxide and JFET-region of 4h-sic DMOSFETS. IEEE Trans. Electron Devices **63**(9), 3795–3799 (2016)
3. Barth, C.B., et al.: Design, operation, and loss characterization of a 1-kw GAN-based three-level converter at cryogenic temperatures. IEEE Trans. Power Electron. **35**(11), 12040–12052 (2020)
4. Naradhipa, A.M., Kim, S., Yang, D., Choi, S., Yeo, I., Lee, Y.: Power density optimization of 700 KHZ GAN-based auxiliary power module for electric vehicles. IEEE Trans. Power Electron. **36**(5), 5610–5621 (2020)
5. Monmasson, E., Idkhajine, L., Cirstea, M.N., Bahri, I., Tisan, A., Naouar, M.W.: Fpgas in industrial control applications. IEEE Trans. Ind. inf. **7**(2), 224–243 (2011)
6. Rashid, M.H.: Power electronics handbook: devices, circuits and applications. Elsevier (2010)
7. Di Benedetto, L., Licciardo, G.D., Rubino, A., Lanzotti, E., Piccirilli, E.: Analysis of the performances of a fully 4h-sic insultated dc/ac converters. In: 2017 IEEE International Conference on Environment and Electrical Engineering and 2017 IEEE Industrial and Commercial Power Systems Europe (EEEIC/I&CPS Europe), pp. 1–4. IEEE (2017)

8. Licciardo, G.D., Cappetta, C., Di Benedetto, L.: Fpga optimization of convolution-based 2d filtering processor for image processing. In: 2016 8th Computer Science and Electronic Engineering (CEEC), pp. 180–185. IEEE (2016)
9. Li, Y., et al.: A 500kw forced-air-cooled silicon carbide (sic) 3-phase dc/ac converter with a power density of 1.246 mw/m 3 and efficiency> 98.5%. In: 2020 IEEE Energy Conversion Congress and Exposition (ECCE), pp. 209–216. IEEE (2020)
10. Neacşu, D.O., Kim, J.C., Lehman, B.: A three-phase multioptimal pwm implemented on 2-gbit flash memory integrated circuits. IEEE Trans. Power Electron. **32**(7), 5813–5826 (2017)
11. Wiśniewski, R., Bazydło, G., Szcześniak, P.: SVM algorithm oriented for implementation in a low-cost Xilinx FPGA. Integration **64**, 163–172 (2019)
12. Di Benedetto, L., Donisi, A., Licciardo, G.D., Liguori, R., Piccirilli, E., Lanzotti, E., Rubino, A.: Implementation of hardware architecture for svpwm with arbitrary parameters. IEEE Access **10**, 32381–32393 (2022)
13. In: Taylor expansions and applications. Springer Milan, Milano, pp. 223–255 (2008). https://doi.org/10.1007/978-88-470-0876-2_7
14. Di Benedetto, L., Donisi, A., Licciardo, G.D., Rubino, A.: A hardware architecture for svpwm digital control with variable carrier frequency and amplitude. IEEE Trans. Ind. Inf. **18**(8), 5330–5337 (2022)
15. Xilinx inc.: Artix 7. (2018) rev. 2018.02.27. https://www.xilinx.com/products/silicon-devices/fpga/artix-7.html

Average Modeling of DC-DC Converters Using Artificial Neural Networks

Andrea Zilio$^{(\boxtimes)}$, Davide Biadene , Tommaso Caldognetto ,
and Paolo Mattavelli

Department of Management and Engineering (DTG), University of Padova,
Vicenza, Italy
{andrea.zilio,davide.biadene,tommaso.caldognetto,
paolo.mattavelli}@unipd.it

Abstract. In this paper the use of artificial neural networks (ANNs) for the average modeling non-linearities in dc-dc converters is explored. The aim is to analyze the effectiveness of non-linear autoregressive exogenous NARX-ANN to realize an average black-box dynamic model of dc-dc converters that includes, within the same framework, converter non-linearities such as the operation in the discontinuous conduction mode (DCM) and the continuous conduction mode (CCM). Simulation results of buck dc-dc converter verify the validity of the proposed approach.

Keywords: Artificial neural network (ANN) · dc-dc converters · Average modeling · Black-box modeling

1 Introduction

Recently, broad interest is growing in the application of artificial intelligence (AI) in numerous scientific and industrial fields. Power electronic conversion circuits, and powerful digital controllers, present many compelling scenarios in which AI methods may unleash unprecedented performances, new features, and potential breakthrough applications [1]. Several approaches are available for power converters average modeling [2], but both the white-box and the grey-box methods require for their application some prior knowledge, which is not always available. Black-box modeling is a model-free approach that can potentially overcomes these limits.

Several approaches based on AI are described in the literature. In [3], a nonlinear autoregressive exogenous (NARX) artificial neural network (ANN) is used for modeling a boost converter in continuous conduction mode (CCM). A buck converter is modeled in [4] considering only the CCM operating mode. An approach for modeling the discontinuous conduction mode (DCM), in addition to the CCM, of a converter using long short-term memory (LSTM) networks is presented in [5]. However, compare to NARX-ANN, an LSTM network is more complex with a higher number of parameters [6]. Several black-box approaches to model non-linearities of power converters are found in the technical literature.

For example, in [7], a method based on polytopic models with dynamic weighting functions is presented to cope with the variation of the small-signal transfer function due to the variation of the operating points.

This paper proposes the average model of a buck converter using NARX-ANN able to precisely replicate the converter dynamic behaviour under different operating points. The buck converter is used as an example for a general black-box methodology that can be extended to any dc-dc converter average modeling.

2   CCM/DCM Buck Converter Non-linearity

The schematic of the buck converter is shown in Fig. 1. The goal is to address only the average modeling of the converter (i.e., only the state variables averaged over the switching period T_s). As any dc-dc converters, the buck converter presents a very large set of possible non-linearities, starting from the variation of the operating mode (i.e., CCM versus DCM), the variation of L versus the inductor DC current, switch S and diode D non-ideal switching transition, etc.. For the sake of understanding the potentials of adopting NARX-ANN for non-linear modeling in dc-dc converters, this paper considers the ideal operation and the only non-linearity due to the variation of the operating mode. Under these assumptions, in CCM, the transfer function between duty-cycle and output voltage is a second-order function independent on the operating point, while in DCM it is approximated by a first-order transfer function with a pole and a gain that depend on the operating point [8].

Following Fig. 1, in CCM operation the small-signal transfer function between the duty cycle $\delta(s)$ and the output voltage $v_o(s)$ is:

$$G_{\delta,v_o}(s) = \frac{v_o(s)}{\delta(s)} = V_{in}\frac{1+s\tau_c}{1+\frac{s}{Q\omega_o}+\frac{s^2}{\omega_o^2}} \tag{1}$$

being $\tau_c = r_cC$, $\omega_o = 1/\sqrt{LC}$ and $Q = \frac{1}{r_c+r_L}\sqrt{L/C}$. Instead, in DCM the small-signal transfer function, under first order approximation, is:

$$G_{\delta,v_o}(s) = \frac{v_o(s)}{\delta(s)} = k_o\frac{r_o}{1+sCr_o} \tag{2}$$

being k_o and r_o two variables depending on the operating point [8].

3   Basics of NARX-ANN

To take into account the dynamic behavior of dc-dc converters, an ANN with memory should be considered. In this work, this is achieved by using a NARX-ANN. NARX-ANN models can be used to model a wide variety of non-linear dynamic systems and they have been applied in various applications including time-series modeling [9]. Unlike other types of recurrent networks, such as the LSTM-ANN, in which the memory effect is implemented by the neurons, the
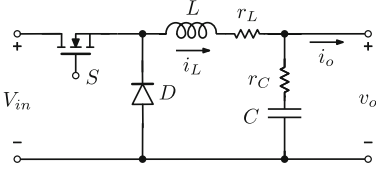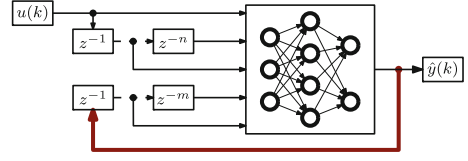
Fig. 1. Schematic of a buck converter.

Fig. 2. NARX-ANN model.

NARX-ANNs use delay-blocks at the network inputs to implement the memory effect. In particular, a multilayer perceptron (MLP)-ANN is used to map the correlations between inputs and outputs, while the outputs are fed back as inputs to the ANN via multiple delay blocks.

NARX models have two different architectures: the open-loop and the closed-loop architectures, also known as series-parallel and parallel architectures, respectively. The closed-loop configuration is displayed in Fig. 2. The system equation describing the behavior of the NARX-ANN in open-loop operation is:

$$\hat{y}_k = f\left(u_k, u_{k-1}, ..., u_{k-n}, y_{k-1}, ..., y_{k-m}\right) \tag{3}$$

where $\hat{y}_k$ is the estimated value at the k-th instant, u is the vector of inputs, y is the vector of outputs, and f is the non-linear function of the MLP-ANN with n and m the delays of the inputs and the outputs, respectively. While the system equation describing the behavior of the NARX-ANN in closed-loop operation is:

$$\hat{y}_k = f\left(u_k, u_{k-1}, ..., u_{k-n}, \hat{y}_{k-1}, ..., \hat{y}_{k-m}\right) \tag{4}$$

where $\hat{y}$ is the vector of values predicted by the ANN.

The choice of the ANN architecture depends on the specific problem to be solved. In this paper, the series-parallel architecture is used during the training processes and the error obtained from the comparison between the true value and the estimated one is used to update the ANN weights. Once the ANN is trained, it is converted into the closed-loop architecture to allow multi-step ahead prediction.

4   Case Study

In the proposed method there is no *a-priori* knowledge on the buck converter parameters, the only available signals are, as input, the duty-cycle δ and the output current i_o and, as output, the inductor current i_L and the output voltage v_o.

4.1   Simulation Model

The switching model of the buck converter reported in Fig. 1 is implemented in Simulink environment in order to collect the waveforms to build up the dataset. In Fig. 1, the converter parameters are $f_s = 30\,\text{kHz}$, $V_{in} = 24\,\text{V}$, $L = 34\,\mu\text{H}$, $r_L = 100\,\text{m}\Omega$, $C = 75\,\mu\text{F}$, $r_C = 300\,\text{m}\Omega$.

All the variables are acquired using a moving average filter with a window size equal to $T_s = 1/f_s$.

4.2   Dataset Definition

The ANN is developed using the library Tensorflow 2.8 on Python. The inputs are:

$$u(k) = [\delta(k), i_o(k), \delta(k-1), i_o(k-1), i_L(k-1), v_o(k-1), i_L(k-2), v_o(k-2)] \tag{5}$$

while the outputs are:

$$y(k) = [i_L(k), v_o(k)]. \tag{6}$$

The designed ANN is used for modeling the buck converter in its operating range, the δ varies between 10% and 50% while i_o between 0.8A and 4A. Within this range, the converter presents both the CCM and DCM operating modes.

In this work, several simulations has been carried out to understand the number of working points required for the dataset. A total amount of 75,000 operating conditions (in terms of δ and i_o) are used for the dataset, divided into training (70 %), validation (15%), and testing (15%). To cover the whole workspace during the training phase, the samples of the input signals are randomly chosen over the whole operating range. The system is stimulated by giving step signals between the different operating points being the duration of each step equal to 1.5 ms. Figure 3 shows an example of the signals used as inputs.
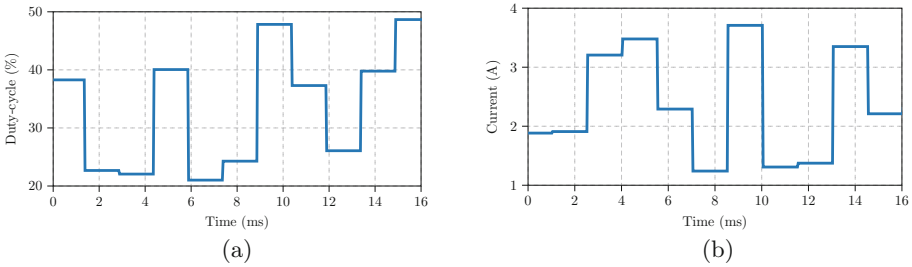

Fig. 3. Step signals used as input, in (a) the duty cycle δ, and in (b) the output current i_o.

To design the hyperparameters, in this paper the bayesian optimization algorithm [10] has been adopted and it is used to choose the learning rate, the number of hidden layers and neurons. The resulting ANN has 5 layers with 40, 20, 20, 15, 5 neurons, respectively, with a total number of parameters that amounts to 2,007. The learning rate is set equal to 0.01, and the Sigmoid activation function is used for the hidden layers while the ReLu for the output layer. In this paper, the input signals $u(k)$ are normalised between 0 and 1. The time required for the training phase with 5,000 epochs is 2,500 s in a NVIDIA GeForce RTX 3070 Ti. The training algorithm is the ADAM, the loss function is the mean-square error, and the metric is the root-mean-square error (RMSE).

To visualise the performance of the NARX-ANN, the test-set is evaluated obtaining an RMSE of 83mA for the inductor current and an error of 89mV for the output voltage.
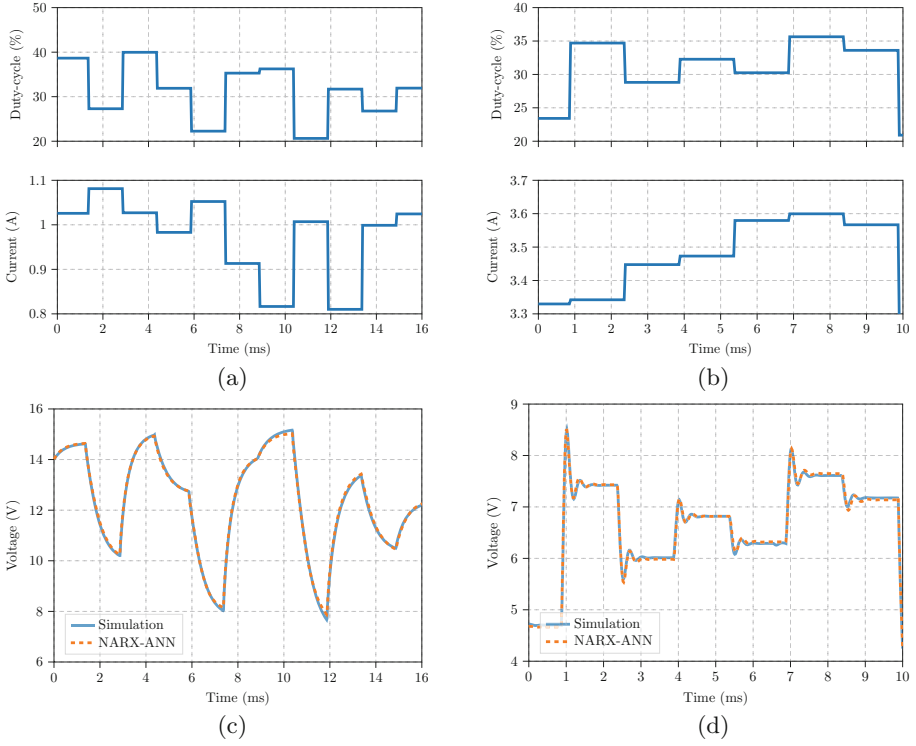
Fig. 4. Comparison between the v_o obtained with time-domain simulation and v_o estimated by the NARX-ANN. In (a) the input signals in DCM that generate the response in (c), and in (b) the input signals in CCM that generate the response in (d).

5   Simulation Results

In order to verify the validity of the NARX-ANN, a total amount of 18 working points out of the 11,250 that compose the test-set are chosen, and the response of the system is compared with ANN predictions. Figure 4 shows the time domain responses in DCM and CCM. It is noteworthy that the values predicted by ANN overlap with the true values even during transient phases both in DCM and CCM.

6   Conclusion

A black-box approach based on the application of NARX-ANN for modeling non-linearities in dc-dc converters is explored. The validity of the proposed model is verified in time domain by using the switching simulated model of the buck converter. The simulation results show good matching for both CCM and DCM operating modes of the converter. The proposed method is considered as an initial step

in black-box modeling of converters non-linearities using AI techniques. Further steps will address the modeling of other types of converters in the time and frequency domains, including the validation with experimental measurements.

References

1. Zhao, S., Blaabjerg, F., Wang, H.: An overview of artificial intelligence applications for power electronics. IEEE Trans. Power Electron. **36**(4), 4633–4658 (2020)
2. Wunderlich, A., Booth, K., Santi, E.: Hybrid analytical and data-driven modeling techniques for digital twin applications. In: IEEE Electric Ship Technologies Symposium (ESTS), vol. 2021, pp. 1–7. IEEE (2021)
3. Wunderlich, A., Santi, E.: Digital twin models of power electronic converters using dynamic neural networks. In: IEEE Applied Power Electronics Conference and Exposition (APEC), vol. 2021, pp. 2369–2376. IEEE (2021)
4. Rojas-Dueñas, G., Riba, J.-R., Kahalerras, K., Moreno-Eguilaz, M., Kadechkar, A., Gomez-Pau, A.: Black-box modelling of a DC-DC buck converter based on a recurrent neural network. In: 2020 IEEE International Conference on Industrial Technology (ICIT), pp. 456–461. IEEE (2020)
5. Rojas-Dueñas, G., Riba, J.-R., Moreno-Eguilaz, M.: a deep learning-based modeling of a 270 V-to-28 V DC-DC converter used in more electric aircrafts. IEEE Trans. Power Electron. **37**(1), 509–518 (2021)
6. Wang, S.-C.: Artificial neural network. In: Interdisciplinary Computing in Java Programming, pp. 81–100. Springer (2003). https://doi.org/10.1007/978-3-319-17885-1_100075
7. Frances, A., Asensi, R., Uceda, J.: Blackbox polytopic model with dynamic weighting functions for dc-dc converters IEEE Access **7**, 160 263–160 273 (2019)
8. Erickson, R.W., Maksimovic, D.: Fundamentals of Power Electronics, 3rd edn. Springer (2020). https://doi.org/10.1007/978-1-4615-7646-4
9. Boussaada, Z., Curea, O., Remaci, A., Camblong, H., Mrabet Bellaaj, N.: A nonlinear autoregressive exogenous (NARX) neural network model for the prediction of the daily direct solar radiation. Energies **11**(3), 620 (2018)
10. Feurer, M., Hutter, F.: Hyperparameter optimization. In: Automated Machine Learning, pp. 3–33. Springer, Cham (2019). https://doi.org/10.1007/978-1-4899-7687-1_100200

Electronic Systems and Applications

Improving SET Fault Resilience by Exploiting Buffered DMR Microarchitecture

Marcello Barbirotta(✉) , Antonio Mastrandrea , Abdallah Cheikh ,
Francesco Menichelli , and Mauro Olivieri

Sapienza University of Rome, Rome, Italy
{marcello.barbirotta,antonio.mastrandrea,abdallah.cheikh,
francesco.menichelli,mauro.olivieri}@uniroma1.it

Abstract. Over the past years, several complex redundant systems capable of executing safety applications were developed, with the common purpose of protecting circuits against Single Event Upset (SEU) in sequential logic and Single Event Transient (SET) in combinational logic. Single Event Transients in digital logic set up an ever-growing challenge in reliability design; understanding the SET sensitivity with scaling is necessary to estimate the logic failure and error probability in modern technology generations. The proposed approach uses an experimental Fault Injection campaign with signal glitching to identify SET vulnerability onto different voting strategies, showing how modified versions of N-Modular Redundancy (NMR) react to transient stimuli, using the Klessydra RISC-V processor family as the basis for all the experiments.

Keywords: Fault resilience · Single event transient · Fault injection

1 Introduction

The creation of gradually smaller and more performing devices in computing power is the goal of both the industry and research world, especially when technology scaling started to raise important design issues due to increased power density [10]. Complex systems, powerful microprocessors and vector coprocessors tailored for Machine learning (ML) and Digital Signal Processing (DSP) applications touched by CMOS scaling can be directly linked to safety [3]. Fault-Tolerant (FT) architectures are based on the combinational of several techniques. Functional redundancy is achieved using multi-core processors or Simultaneous Multi-Thread (SMT) processors, and it is used to detect and correct errors, with schemes like Triple Modular Redundancy (TMR) or Double Modular Redundancy (DMR) involving triplication or duplication of the basic module. Classical TMR protection against faults occurring in any bit of the core may be oversized for many applications, especially for low-cost implementations, and state-of-the-art is always looking for better-performing alternatives. TMR suffers from a

200% area overhead problem, and selective hardening methods were developed to solve that, such as Partial TMR, Selective TMR or Approximate TMR [1]. Protecting only the "selected" critical parts of a circuit makes it possible to save area maintaining the fault-masking. However, a faulty voter also represents a direct threat to the system's reliability in these optimized approaches. The majority-voting circuits are made from components of the same reliability as those used to construct the circuit modules, especially on commercial-off-the-shelf (COTS) devices where cost is a key feature in many embedded application domains for commercial sustainability. It has been proven that Interleaved Multi-Threading architecture (IMT) is effective for SEU fault tolerance with the Buffered TMR technique [3,4,6,9]. However, many FT implementations assume the voter is perfect and error-free [2,7], yet this may not be true in reality. This work leverages simulation-based Fault Injection approaches to analyze the SET faults vulnerabilities on different majority voter schemes. We also propose a specific voting circuit to reduce the failure rate when a transient pulse changes the output of a voter logic during the active clock edge, with performance and area overhead evaluations. The outline of the paper is as follows; Sect. 2 discusses the background on SET faults, while in Sect. 3 the specific Fault Injection setup is outlined, as long as the fault resilience comparisons between some voting mechanisms. Section 4 presents the simple idea of improving voting performances on DMR architectures, and finally, in Section V, we summarize our results in the conclusions.

2   Technology Background of Single Event Transients

Suppose a radioactive particle strikes the drain junction of a transistor. In that case, it generates electron-hole pairs through ionization processes, resulting in a transient current pulse, with amplitude and duration that determines whether the error propagates in the digital circuit, causing logic failure [12]. The transient interaction depends on the particle, its energy, and the material properties through which it travels. SETs in analogue ICs appear at very low threshold levels because any additional currents in the circuit will disturb the 'normal linear condition'. SETs in digital ICs generally require a minimum quantity of injected charge to be generated because they work in their saturated condition. For ON elements, in digital technology, adding charge to an already saturated condition has no effects, while in OFF elements, sufficient transient currents can temporally upset the stable condition generating a SET fault. The conversion of transients into erroneous data depends on the clock frequency and the duration of a SET which decreases in proportion to the square of the technology feature size. The range of SET durations for a given Linear Energy Transfer (LET), defined as energy deposition per mass thickness, on a 90nm technology can go from 300 to 1000 ps of pulse width [8]. In conclusion, as digital frequencies increase, SET faults may predominate over SEUs, creating growing challenges in protection methodologies.

3   Proposed Methodology

The different threads of an IMT round robin core [6][9] can be used to guarantee the repetition of three identical instructions in temporal and spatial redundancy. In that way, it is possible to obtain the Buffered TMR technique [4][3], which allows using the corresponding hardware support of the IMT core for maintaining each thread state and using them to execute the instructions with clock granularity. However, obtaining triple redundancy is very expensive, and DMR solutions can be easily applied in IMT structures. Exploiting two active threads that execute the same instruction in different clock cycles guarantees higher speed and hardware savings. It allows for activating software or hardware restore procedures in case of discrepancies between the results. This work aims to analyze the SET-type faults tolerance in Full TMR, Buffered TMR and Buffered DMR voting systems. Both majority voters from Full TMR or Buffered TMR systems are subjected to failure in case of errors in combinational logic (Fig. 1), while in the Buffered DMR system, restoring procedures can be activated or not according to where the fault falls.
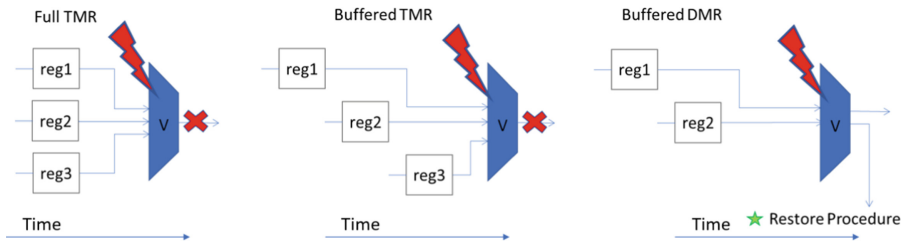

Fig. 1. Voting structures and corresponding timing conceptual scheme for different FT implementations.

3.1   Fault Injection Simulations

We applied all these methodologies to the same Write-Back register inside a 32-bit processor Klessydra-T03 [6,9], targeting its voting systems with SET Fault Injection simulations [5]. In order to simulate a strong SET pulse analysis, we decided to oversize the SET pulse width up to 10ns, which is more than the common one [8,11]. We applied an increasing failure rate from zero up to the unreachable limit of multiple consecutive faults in the order of 1 each 15 clock cycles, with a 5% error margin in a Monte Carlo scenario, setting up a UVM Fault Injection simulation environment [5] as a test bench for the T03 processor. By always running the same benchmark, it is possible to notice from Fig. 2 that the Buffered TMR architecture is better in terms of fault tolerance than a Full TMR system, thanks to its double redundancy (spatial and temporal). In comparison, the Buffered DMR architecture is always better than the others thanks to its dual redundancy combined with its recovery mechanism.
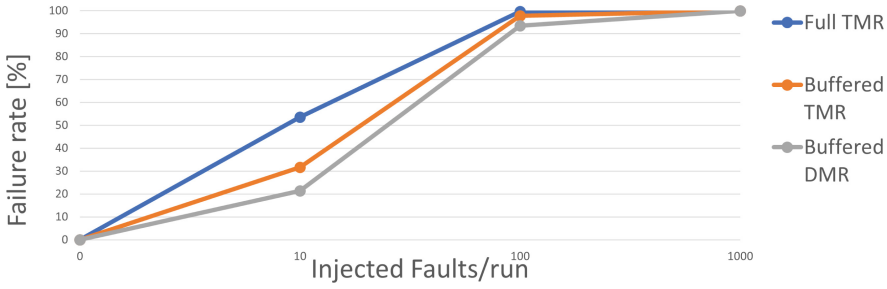
Fig. 2. 10ns SET random Fault Injection comparisons between different FT implementations, targeting the same benchmark under 5% error margin Montecarlo analysis.

3.2   Results Improvement and Comparisons

Evaluating the results in Fig. 2, the most promising architecture in terms of fault resilience is the Buffered DMR system. DMR architecture can have heavy software or hardware restore procedures that consume power and time in case of discrepancies between the results. However, they are more flexible from the fault tolerance point of view. We observe that by simply adding some logic gates (Fig. 3) capable of performing parity checks, it is possible to improve the standard voter fault resilience in the Buffered DMR architecture. As presented in Fig. 3, the recovery signal that returns the processor status to a correct previous checkpoint is always activated whatever SET occurs in the combinatorial logic, in the hypothesis of single faults and no faults fall during the restore procedures, considering the real event rates in Space applications. Replicating the same Fault Injection analysis and comparing the results with the previous test, we can observe in Fig. 4 a clear improvement in fault resilience at a low fault rate. By increasing the number of injected faults, the failure rate curve increases exponentially, remaining much lower than the others.
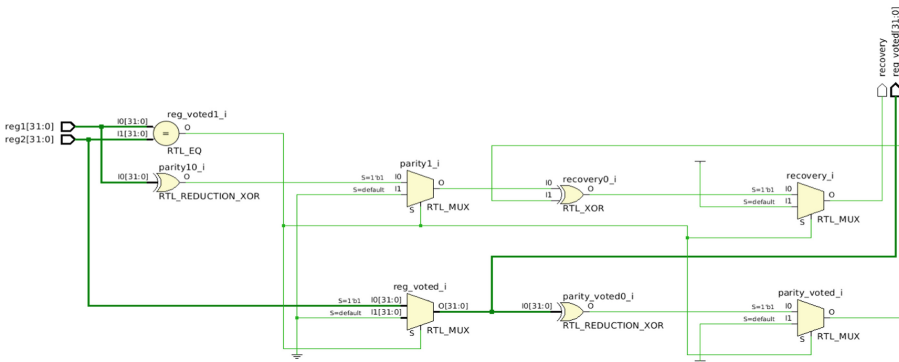

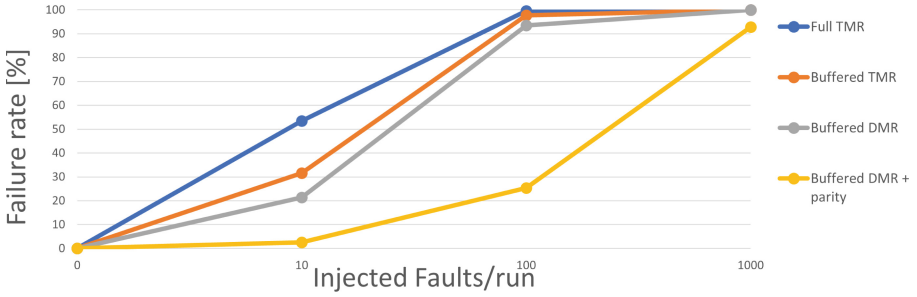**Fig. 3.** Logic Implementation of a DMR voter + parity checker.

Fig. 4. 10ns SET random Fault Injection comparisons between different FT implementations, targeting the same benchmark under 5% error margin Montecarlo analysis; the case of Buffered DMR + parity.

Comparing the hardware resource consumption for all the analyzed methodologies, the area overhead of the Buffered approaches turns out to be only 10% of the total number of FF. In contrast, the combinational overhead of voting logic remains around 20% rather than the standard Full TMR approach, which presents 200% and 100% in terms of sequential and voting logic. Only for the Buffered DMR voting system with parity additions, an increase in voter size can be seen around 20% compared to the standard majority voter.

Table 1. Overhead comparisons between different FT implementations.

	Full TMR	Buffered TMR	Buffered DMR	Buffered DMR + parity
$N°$FF	3x	$0,1$x	$0,1$x	$0,1$x
N° Voter	1x	$0,2$x	$0,2$x	$0,2$x+
Voter size	32 LUT	32 LUT	28 LUT	40 LUT

4   Conclusions

The results from our work prove that Buffered NMR architectures are better than the classical Full TMR approach, not only from the resource utilization point of view but also from the fault resilience point of view. In particular, in this work, we proved SETs fault resilience to an oversized transient pulse exploiting all the advantages of the DMR architecture compared to a Full or Buffered TMR system. By adding some logic gates able to perform parity checks, we found that it is possible to drastically improve Buffered DMR fault resilience, paying in a small logic overhead. The proposed approach can be effectively used for SETs FT improvement in DMR systems, which will also be evaluated on the whole architecture in future works.

References

1. Arifeen, T., Hassan, A.S., Lee, J.A.: A fault tolerant voter for approximate triple modular redundancy. Electronics **8**(3), 332 (2019)

2. Ban, T., de Barros Naviner, L.A.: A simple fault-tolerant digital voter circuit in tmr nanoarchitectures. In: Proceedings of the 8th IEEE International NEWCAS Conference 2010, pp. 269–272. IEEE (2010)

3. Barbirotta, M., Cheikh, A., Mastrandrea, A., Menichelli, F., Olivieri, M.: Analysis of a fault tolerant edge-computing microarchitecture exploiting vector acceleration. In: 2022 17th Conference on Ph. D Research in Microelectronics and Electronics (PRIME), pp. 237–240. IEEE (2022)

4. Barbirotta, M., Cheikh, A., Mastrandrea, A., Menichelli, F., Vigli, F., Olivieri, M.: A fault tolerant soft-core obtained from an interleaved-multi-threading risc-v microprocessor design. In: 2021 IEEE International Symposium on Defect and Fault Tolerance in VLSI and Nanotechnology Systems (DFT), pp. 1–4. IEEE (2021)

5. Barbirotta, M., et al.: Fault resilience analysis of a risc-v microprocessor design through a dedicated uvm environment. In: 2020 IEEE International Symposium on Defect and Fault Tolerance in VLSI and Nanotechnology Systems (DFT), pp. 1–6. IEEE (2020)

6. Cheikh, A., Cerutti, G., Mastrandrea, A., Menichelli, F., Olivieri, M.: The microarchitecture of a multi-threaded RISC-V compliant processing core family for IoT end-nodes. In: De Gloria, A. (ed.) ApplePies 2017. LNEE, vol. 512, pp. 89–97. Springer, Cham (2019). https://doi.org/10.1007/978-3-319-93082-4_12

7. Gomes, E.P., Saha, A., Beulet, A.S.: Optimized voter circuit for fault tolerant implementation in tmr. In: Proceedings of International Conference on Sustainable Computing in Science, Technology and Management (SUSCOM), Amity University Rajasthan, Jaipur-India (2019)

8. Narasimham, B., et al.: Neutron and alpha particle-induced transients in 90 nm technology. In: 2008 IEEE International Reliability Physics Symposium, pp. 478–481. IEEE (2008)

9. Olivieri, M., Cheikh, A., Cerutti, G., Mastrandrea, A., Menichelli, F.: Investigation on the optimal pipeline organization in risc-v multi-threaded soft processor cores. In: 2017 New Generation of CAS (NGCAS), pp. 45–48. IEEE (2017)

10. Stazi, G., Adani, L., Mastrandrea, A., Olivieri, M., Menichelli, F.: Impact of approximate memory data allocation on a H.264 software video encoder. In: Yokota, R., Weiland, M., Shalf, J., Alam, S. (eds.) ISC High Performance 2018. LNCS, vol. 11203, pp. 545–553. Springer, Cham (2018). https://doi.org/10.1007/978-3-030-02465-9_38

11. Veeravalli, V.S.: An infrastructure for accurate characterization of single-event transients in digital circuits. Microprocess. Microsyst. **37**(8), 772–791 (2013)

12. Velamala, J., LiVolsi, R., Torres, M., Cao, Y.: Design sensitivity of single event transients in scaled logic circuits. In: 2011 48th ACM/EDAC/IEEE Design Automation Conference (DAC), pp. 694–699. IEEE (2011)

Designing an Interpretability Analysis Framework for Deep Reinforcement Learning (DRL) Agents in Highway Automated Driving Simulation

Francesco Bellotti[(✉)], Luca Lazzaroni, Alessio Capello, Marianna Cossu, Alessandro De Gloria, and Riccardo Berta

Department of Electrical, Electronic and Telecommunication Engineering (DITEN), University of Genoa, Via Opera Pia 11a, 16145 Genoa, Italy
{franz,luca.lazzaroni}@elios.unige.it

Abstract. Explainability is a key requirement for users to effectively understand, trust, and manage artificial intelligence applications, especially those concerning safety. We present the design of a framework aimed at supporting a quantitative explanation of the behavioural planning performed in automated driving (AD) highway simulations by a high-level decision making agent trained through deep reinforcement learning (DRL). The framework relies on the computation of SHAP values and keeps into consideration a neural architecture featuring an attention layer. The framework is particularly devoted to study the relationship between attention and interpretability, and how to represent, analyze and compare attention and SHAP values in a 2D spatial highway environment. The framework features three main visualization areas, that are obtained by processing quantities such as attention, SHAP values, vehicular observations: Episode view, plotting quantities on an episode's timeline; Frame view, reporting the measurement values step by step; Aggregated view, showing, also on 2D maps, statistical values from the aggregation of several simulation episodes. To the best of our knowledge, this is the first in-depth explainability analysis of a DRL-based decision-making AD system, also including a statistical analysis. We hope that the upcoming open source release of the designed framework will be useful to further advance research in the field.

Keywords: Explainable artificial intelligence · Interpretability · Machine learning · Deep reinforcement learning · Graphical user interface

1 Introduction

Behavioural planning of automated driving (AD) vehicles has becoming a significant research area, given the continuous advancements in context perception and in advanced driving assistance systems (ADAS) [1]. Among the techniques being employed for the task, deep reinforcement learning (DRL) is emerging since it trains an agent which learns a decision making policy from data and simulations, through trial and error [2].

A key requirement for users to effectively understand, trust, and manage artificial intelligence applications, especially those concerning safety, has become explainability (e.g., [3]). There are two main types of explainable artificial intelligence (XAI) approaches in machine learning (ML). The first one relies on intrinsically explainable models, such as trees; the second one exploits techniques that process the inputs and the outputs of the model to gain insights into it. Among them, SHAP [4] estimates the importance of each feature for each output. Importance may be positive (i.e., the value of the feature is a motivator for the output), or negative (i.e., the value of the feature is a deterrent). In the context of a DRL system, the features are the observations provided by the environment. In the behavioural planning DRL case, the output is a decision taken by the agent (for instance, for a high-level decision system: accelerate, decelerate, turn right, turn left). At every decision step, SHAP values are computed on the DRL's value network, which outputs the Q value of each possible action, that is the overall expected reward assuming the agent is in the observed state and performs the action, and then continues playing until the end of the episode following some policy π. Thus, SHAP values are computed for each possible action, even those that are not selected. In a Deep Q-Network (DQN) algorithm [5], the action selected at each step is the one that maximizes the expected cumulative gain (Q value).

Liessner et al., [6], showed the effectiveness of a SHAP analysis on the 1D OpenAI Gym LongiControl environment, illustrating, through a car trip example, how different factors (i.e., features, such as velocity or speed limit) influenced the longitudinal acceleration/deceleration profile of a vehicle.

State of the art deep neural networks (DNN) frequently exploit the attention mechanism to achieve the best performance [7]. Leurent and Mercat, [8], designed an attention-based neural architecture to implement a DRL AD agent able to cross an intersection, and interpreted the vehicle behavior, particularly its interaction with the other vehicles around, by exploiting the values provided by the attention layer of the agent's DNN.

Taking inspiration from these two XAI works on SHAP [6] and attention [8], this paper presents the design of an operational interpretability framework aimed at supporting the work of designers and analysts of DRL-based AD high-level decision making. As the reference RL environment, we take the highway-env OpenAI Gym 2D environment [9], which is quite popular for research in AD decision making (e.g., [10]).

The underlying analysis methodology has been developed on the basis of literature study and field experience (e.g., [11]), and is particularly devoted to study:

- The relationship between attention and interpretability, which is still highly debated (e.g., [12, 13]). We use SHAP, given its solid foundation in game theory, and its wide adoption also in the AD research literature.
- How to represent, analyze and compare attention and SHAP values in a 2D spatial highway environment (limiting our analysis to single frames, thus ignoring temporal correlations, for simplicity).
- How to integrate abstract information from the neural model (i.e., attention and SHAP values) with domain-specific knowledge.

Building on the mentioned studies, our research aims at designing a tool able to support a more general and quantitative analysis, also moving from a single episode

(e.g., 60 s of an AD vehicle highway drive) to a statistical investigation of several episodes.

The next section presents the core features of the proposed interpretability framework, while Sect. 3 draws the conclusions on the work done and outlines next research steps.

2 Proposed Framework

Analyzing and interpreting the decision of an agent requires considering several aspects, at each decision step:

- Action taken among those selectable by the agent driving the ego vehicle (e.g., accelerate, decelerate, turn right, turn left, idle)
- Observations (e.g., the kinematic values of the ego and the close-by vehicles), that are features that the agent relies on to take the action
- Context (e.g., the road space ahead and behind the vehicle)
- XAI quantities, such as SHAP values and attention values.

For the attention values, we take the output of the attention layer, which is a probability distribution across vehicles, as we group the environment observations per vehicle, as in [8]. Thus, the sum is always equal to 1, and high max attention values indicate that the attention is focused on a single vehicle.

SHAP values, on the other hand, are per feature. So, in order to allow a comparison with attention values (that are per vehicle), we define the SHAP value of a vehicle as the SHAP value of its most important feature. This is a clear approximation, but could be reasonable, because explanations are typically given mentioning only the most important feature (e.g., [6]). Such per-vehicle SHAP values are then converted into probabilities through softmax.

In order to support the interpretability analysis, we propose a graphical user interface (GUI) with three main views, that correspond to different types of data visualization. Values reported in the GUI are computed at each step, which is the moment in time in which the agent takes a decision (e.g., at 10 Hz). The views, detailed in the following subsections, are:

- Episode View, a time-line representation of each episode's evolution in terms of the kinematic signals of the ego and close-by vehicles (i.e., the features), with SHAP values represented through a color code. A sketch is provided in Fig. 1 a) and b);
- Frame View, for a step by step display of all the feature values together with the attention values (per vehicle) and SHAP values (per feature) (Fig. 1 c));
- Aggregated View, for a statistical analysis of attention, SHAP and vehicular (i.e., feature) values over a set of episodes, also segmented by vehicle/traffic conditions (Fig. 1 d));
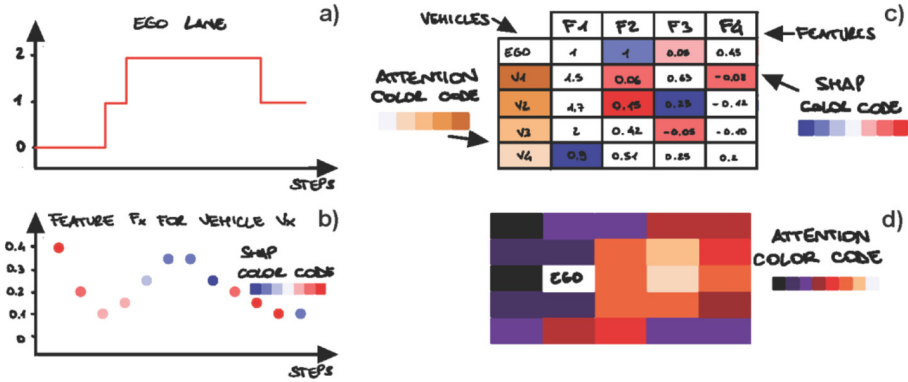
Fig. 1. Sketch of: Episode view a) and b); Frame view c); and Aggregated view d).

2.1 Episode View

The goal of this view is to provide an overview of the evolution in time of the quantities of an episode.

The view plots original and derived measurement timeseries on an episode's timeline. Relevant quantities (that are plotted, in homogeneous groups, on different axes) include: the chosen action, lane of the ego vehicle (e.g., Fig. 1 a)), speed of the ego and of close-by vehicles, time headway, space headway, vehicle id with max attention and with max SHAP value, distances from the ego of the max SHAP and max Attention, the max SHAP feature.

A second part of this view plots all the single observations color-coded according to their SHAP value (e.g., Fig. 1 b)), providing an overview of the time evolution of all the features, together with their importance.

The expected benefit of this view concerns the analysis and interpretation of examples of the time evolution of a whole episode, probably focusing on the most interesting parts of it (e.g., to see in which situation an agent behaves well and in which not). The limit, similarly to [6] and [8], is that this approach is anecdotal (i.e., single case only – even if the tool allows to study several different cases, of course).

2.2 Frame View

The goal of this view is to support a step-by-step analysis of the attention and SHAP values for each feature.

This view consists of a set of tables, one for each step (e.g., Fig. 1 c)). The rows represent the observed vehicles, the columns their observed features. The table cells report the numerical values of the observations, and their background is coloured according to a code based on the SHAP value of the feature. Similarly, the vehicle ID column is also colored based on the attention value.

This view considers reports SHAP values for the selected action only. However, it can be extended by adding, at each step, one table for all the possible actions. Extension

is useful to understand what the alternative suggested action is by a feature, that may have resulted as a deterrent for the selected action.

We argue that this view is useful to analyze in detail a timestep (or few consecutive ones) and is useful to compare attention and SHAP values. Similarly to the Episode View, the limit is that this approach focuses on single cases.

2.3 Aggregated View

The goal of this view is to provide an aggregated perspective across a number of episodes. Differently from the previous views, this one loses the notion of time, but puts an hyphen on space.

This view computes statistical values (average, standard deviation, histograms) for such quantities as the distances (in time and space) of the max SHAP and max attention vehicle(s) from the ego, attention and SHAP values, etc. Entropy of attention and SHAP is computed as well, together with correlations. Heatmaps are computed, capturing the position of the max attention and max SHAP vehicles in a bird-eye-view of the road space around the vehicle (e.g., Fig. 1 d)). Another heatmap reports the distribution of the max SHAP feature, as some features may be more relevant in some areas.

The statistical analysis is segmented according to different conditions based on traffic (e.g., low traffic around) and attention/SHAP values (e.g., low distance from the max attention vehicle).

This view has been designed as a complement to the previous ones, as the statistical analysis allows giving a quantitative overall weight to the various cases and situations. Important additional explanation hints are also provided (e.g., what are the statistical indicators in difficult action decisions).

3   Conclusions and Future Work

We have presented the design of a graphical framework aimed at supporting a quantitative explanation of the behavioural planning performed in AD highway simulations by a high-level decision making agent trained through DRL. We spotted three main visualization clusters, that are obtained by processing quantities such as attention, SHAP values, vehicular observations: Episode view, Frame view and Aggregated view.

To the best of our knowledge, this is the first in-depth explainability analysis of a DRL-based decision-making AD system, also including a statistical analysis. We hope that the upcoming open source release of the designed framework will be useful to further advance research in the field.

Concrete implementation and testing will be useful also to understand the degree to which abstract information from the neural model (i.e., attention and SHAP values) should be complemented with domain-specific analysis for a proper explanation of the how the system takes its decisions.

References

1. Claussmann, L., Revilloud, M., Gruyer, D., Glaser, S.: A review of motion planning for highway autonomous driving. IEEE Trans. Intell. Transp. Syst. **21**, 1826–1848 (2019). https://doi.org/10.1109/TITS.2019.2913998

2. Everett, M., Chen, Y.F., How, J.P.: Motion planning among dynamic, decision-making agents with deep reinforcement learning. arXiv, 4 May 2018. https://doi.org/10.48550/arXiv.1805.01956

3. Gunning, D., Stefik, M., Choi, J., Miller, T., Stumpf, S., Yang, G.-Z.: XAI—explainable artificial intelligence. Sci. Robot. **4**(37), eaay7120 (2019). https://doi.org/10.1126/scirobotics.aay7120

4. Lundberg, S.M., Lee, S.-I.: A unified approach to interpreting model predictions. In: Advances in Neural Information Processing Systems, vol. 30 (2017). https://papers.nips.cc/paper/2017/hash/8a20a8621978632d76c43dfd28b67767-Abstract.html. Accessed 11 July 2022

5. Mnih, V., et al.: Human-level control through deep reinforcement learning. Nature **518**(7540), 529–533 (2015). https://doi.org/10.1038/nature14236

6. Liessner, R., Dohmen, J., Wiering, M.: Explainable reinforcement learning for longitudinal control. In: 13th International Conference on Agents and Artificial Intelligence, ICAART 2021, Proceedings of the 13th International Conference on Agents and Artificial Intelligence, pp. 874–881 (2021)

7. Niu, Z., Zhong, G., Yu, H.: A review on the attention mechanism of deep learning. Neurocomputing **452**, 48–62 (2021). https://doi.org/10.1016/j.neucom.2021.03.091

8. Leurent, E., Mercat, J.: Social attention for autonomous decision-making in dense traffic. arXiv, 27 November 2019. https://doi.org/10.48550/arXiv.1911.12250

9. GitHub-eleurent/highway-env: A minimalist environment for decision-making in autonomous driving. https://github.com/eleurent/highway-env. Accessed 11 July 2022

10. Zhang, S., Wu, Y., Ogai, H., Inujima, H., Tateno, S.: Tactical decision-making for autonomous driving using dueling double deep Q network with double attention. IEEE Access **9**, 151983–151992 (2021). https://doi.org/10.1109/ACCESS.2021.3127105

11. Campodonico, G., et al.: Adapting autonomous agents for automotive driving games. In: de Rosa, F., Marfisi Schottman, I., Baalsrud Hauge, J., Bellotti, F., Dondio, P., Romero, M. (eds.) GALA 2021. LNCS, vol. 13134, pp. 101–110. Springer, Cham (2021). https://doi.org/10.1007/978-3-030-92182-8_10

12. Ghassemi, M., Oakden-Rayner, L., Beam, A.L.: The false hope of current approaches to explainable artificial intelligence in health care. Lancet Digital Health **3**(11), e745–e750 (2021). https://doi.org/10.1016/S2589-7500(21)00208-9

13. Rudin, C.: Stop explaining black box machine learning models for high stakes decisions and use interpretable models instead. Nat. Mach. Intell. **1**(5), 206–215 (2019). https://doi.org/10.1038/s42256-019-0048-x

Fast Learning Digital Twin with Reduced Dimensionality for Non-linear Dynamical Systems

D. Iero[1]([✉]), A. Bergamin[1], M. Merenda[2], F. G. Della Corte[3], and R. Carotenuto[1]

[1] Department of Information, Infrastructure and Sustainable Energy Engineering,
Università Degli Studi "Mediterranea" of Reggio Calabria, 89060 Reggio Calabria, Italy
demetrio.iero@unirc.it

[2] Center for Digital Safety and Security, Austrian Institute of Technology Gmbh, Vienna, Austria

[3] Department of Electrical Engineering and Information Technologies, Università Degli Studi di Napoli Federico II, 80125 Naples, Italy

Abstract. A black-box model of a nonlinear system can be obtained by observing the input-output pairs. We propose a reduced complexity modeling technique that, in many cases, represents the system sufficiently well for control applications. A real-time experimental setup based on an STM32 board is realized to model a nonlinear system and results are presented.

Keywords: Black-box model · Digital twin · Predictor · Non-linear dynamical systems

1 Introduction

Because a sufficiently accurate analytical description of a given process cannot be obtained in many cases, modeling and output prediction of complex dynamical systems play an important role in modern digital control techniques, particularly when aiming for virtual replication of a physical system, a digital twin.

In the domains of IoT and Industry 4.0 applications, a virtual model of a real physical system paves the way for cloud and distributed predictive maintenance, fault detection, and model drift avoidance. In many industry cases, controllers may incorporate black-box nonparametric models built from experimental input and output data sets.

This approach is similar to the one adopted by Machine Learning (ML) [1]; however, ML involves an often extremely expensive learning phase, the need for accurate datasets, and adequate labeling. Furthermore, the models obtained are also subject to drift and aging.

Instead, a black-box model can be seen as a static mapping function $f: \Re^n \to \Re$ from the input and the state spaces to the output space [2–6]. Further, black-box modelling can be applied to very complex systems in order to catch internal small changes [7–10]. Samples are usually provided by ADCs with M quantization levels, and the mapping to be represented is an n-dimensional matrix, consisting of M^n discrete points. The direct representation of the n-dimensional point set is a challenging problem because, in general, there is an exponential growth of the memory requirements.

Exponential memory growth can be avoided by using the technique presented in [11], where it was supported only by simulation data. It allows approximating the n-dimensional matrix, with a proper set of 1-dimensional arrays:

$$y(x_1, x_2, \ldots, x_n) = \sum_{j=1}^{n} g_j(x_j) = g_1(x_1) + g_2(x_2) + \ldots + g_n(x_n) \qquad (1)$$

The predicted outputs are calculated from the inputs x_j and the arrays g_j as:

$$y_p = g_1^i(x_1) + g_2^i(x_2) + \ldots + g_n^i(x_n). \qquad (2)$$

A learning algorithm computes the g_j arrays' values iteratively to minimize the mapping representation error $(y - y_p)$.

In this work, the technique is experimentally implemented for the first time using a microcontroller. An experimental black-box predictor is realized using a Nucleo board from STMicroelectronics. The non-linear system to be digitally replicated here consists of a non-linear second-order system.

The paper is organized as follows. Section 2 describes the system setup, whereas Sect. 3 reports the obtained results. Finally, Sect. 4 presents the conclusions.

2   System Setup

A proof-of-concept has been realized using a Nucleo-144 STM32L496ZG board from STMicroelectronics. The non-linear system to be digitally replicated here consists of a diode voltage limiter followed by a 2nd order low-pass filter with cut frequency 228 Hz and $Q = 7$. The circuit schematic is reported in Fig. 1. The non-linear system is excited with different signals and exhibits strong non-linearity and damped oscillations. Input and output are sampled at 1 kS/s by two on-chip 8-bit ADCs and four arrays are used, which are indexed by two past inputs and by two past outputs of the system.

Figure 2 shows the experimental setup with the microcontroller board and the non-linear circuit.
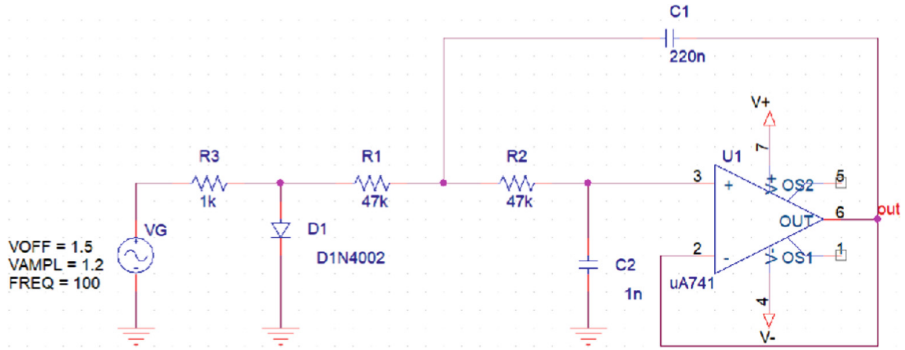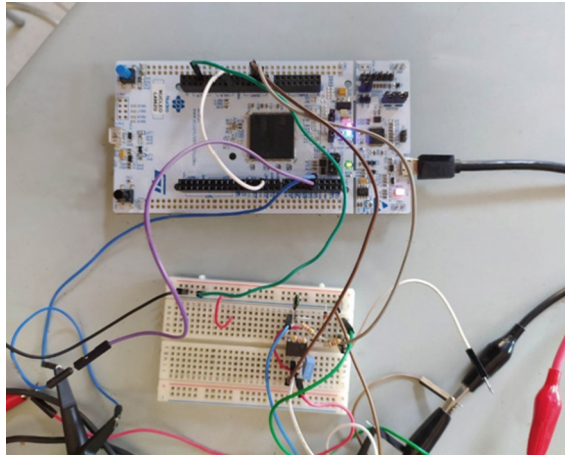
Fig. 1. Schematic of the non-linear circuit used.

Fig. 2. Experimental setup: the Nucleo-144 STM32L496 board acting as the predictor and the example non-linear electronic circuit system.
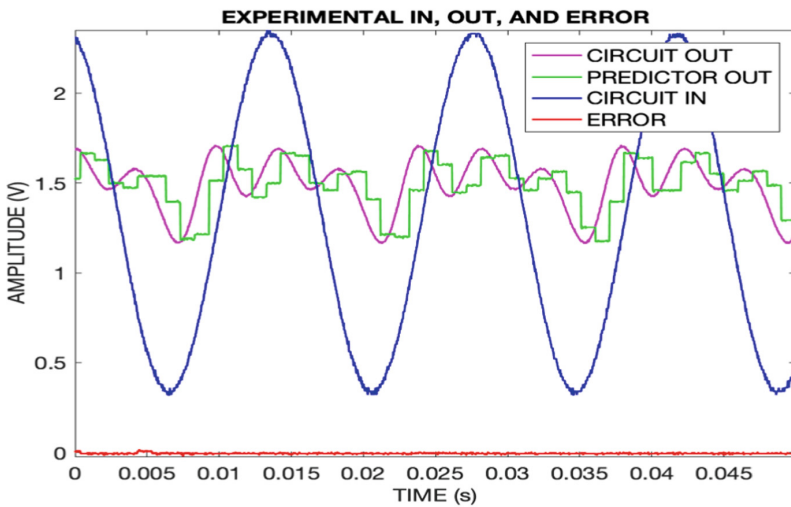
3   Results

The predicted output is compared with that of the real system during a learning phase and is provided for display by the on-chip 8-bit DAC. After the learning is complete, the predictor receives only the input from the real system, and the obtained "model" is able to reconstruct the correct output.

Figure 3 represents the input, the output, the predicted output, and the prediction error near the quantization approximation, for two different circuit inputs (ramp and sine). Figure 4 shows the four numeric arrays learned by the predictor which compactly represents the non-linear mapping.
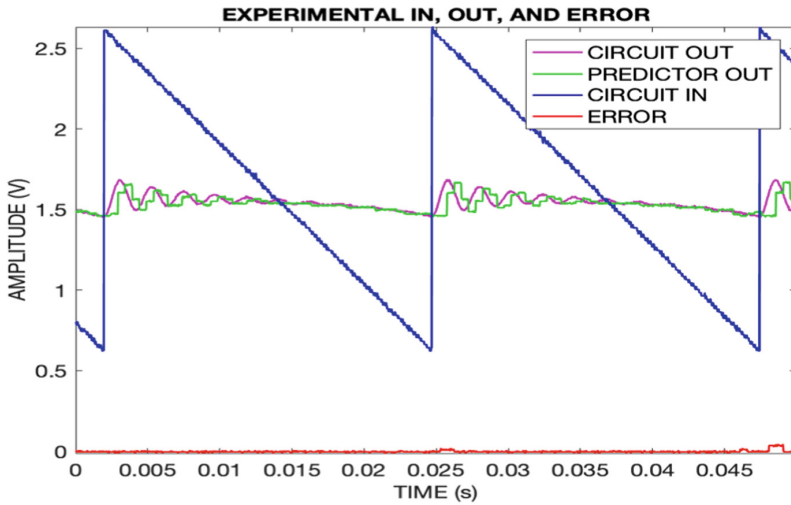
(a)

(b)

Fig. 3. Experimental results after learning is complete: non-linear circuit input (blu), circuit output (violet), predicted output (green), and prediction error (red) for two different circuit inputs: a) ramp, and b) sine.
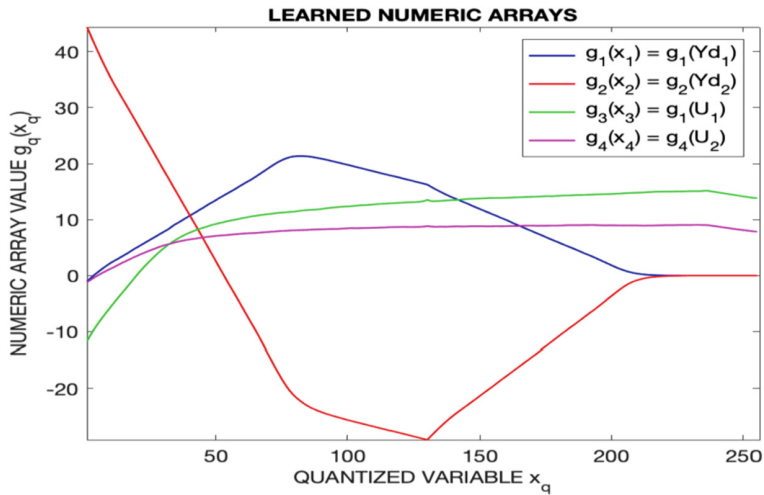
Fig. 4. Content of the four numeric arrays learned by the predictor that constitute the numerical representation of the nonlinear system after the learning has been completed.

4 Conclusion

The reduced dimensionality predictor theory was applied to the black box modeling of a nonlinear system. An experimental setup based on the STM32L496 Nucleo-144 board demonstrated online learning of 1 kS/s and operation with a low error, comparable to quantization error.

References

1. Merenda, M., Porcaro, C., Iero, D.: Edge machine learning for AI-enabled IoT devices: a review. Sensors **20**, 2533 (2020). https://doi.org/10.3390/s20092533
2. Kolmogorov, A.N.: On the representation of continuous functions of many variables by superposition of continuous functions of one variable and addition. Dokl. Akad. Nauk SSSR **114**, 953–956 (1957)
3. Sprecher, D.A.: An improvement in the superposition theorem of Kolmogorov. J. Math. Anal. Appl. **38**, 208–213 (1972). https://doi.org/10.1016/0022-247X(72)90129-1
4. Narendra, K.S., Parthasarathy, K.: Identification and control of dynamical systems using neural networks. IEEE Trans. Neural Networks **1**, 4–27 (1990). https://doi.org/10.1109/72.80202
5. Carotenuto, R.: A range estimation system using coded ultrasound. Sens. Actuators, A **238**, 104–111 (2016). https://doi.org/10.1016/j.sna.2015.12.006
6. Polar, A., Poluektov, M.: A deep machine learning algorithm for construction of the Kolmogorov-Arnold representation. Eng. Appl. Artif. Intell. **99**, 104137 (2021). https://doi.org/10.1016/j.engappai.2020.104137
7. Rosario, F., Filippo Giammaria, P., Riccardo, C., Della Corte, G.F.: Structural health monitoring of pavement assets through acoustic signature. In: Bearing Capacity of Roads, Railways and Airfields-Proceedings of the 10th International Conference on the Bearing Capacity of Roads, Railways and Airfields, BCRRA 2017, pp. 869–875 (2017)

8. Rosario, F., Della Corte, G.F., Riccardo, C., Filippo Giammaria, P.: Sensing road pavement health status through acoustic signals analysis. In: 2017 13th Conference on Ph.D. Research in Microelectronics and Electronics (PRIME), pp. 165–168. IEEE (2017)

9. Iero, D., Merenda, M., Polimeni, S., et al.: A technique for the direct measurement of the junction temperature in power light emitting diodes. IEEE Sens. J. **21**, 6293–6299 (2021). https://doi.org/10.1109/JSEN.2020.3037132

10. Della Corte, F., Pangallo, G., Carotenuto, R., et al.: Temperature sensing characteristics and long term stability of power LEDs used for voltage vs. junction temperature measurements and related procedure. IEEE Access **8**, 43057–43066 (2020). https://doi.org/10.1109/ACCESS.2020.2976516

11. Carotenuto, R.: A learning approximator for compact representation of experimental mappings. Int. J. Adapt. Control Signal Process. **17**, 353–361 (2003). https://doi.org/10.1002/acs.752

Food Waste Prevention System to Improve Smart Homes Sustainability

Giovanni Mezzina[(✉)] [ID], Dionisio Ciccarese, and Daniela De Venuto [ID]

Department of Electrical and Information Engineering, Politecnico di Bari, Bari, Italy
`giovanni.mezzina@poliba.it`

Abstract. The recent spread of smart homes is sparking corporates and research interest in residents' needs with a particular focus on reduced energy consumption and less stressful daily life. As seen in the literature, to the food waste, one of the most pressing problems of today, has not been given special attention. In this scenario, in order to curb poor consumer behavior and improper food storage, the proposed work leverages the close cooperation of a Wireless Sensor Network (WSN) and an actuation system enriching smart homes of pervasive capabilities. The sensor network is constituted by a fleet of sensor nodes each of which monitors the microclimate of a particular food item. The microclimate data is used to compute a dynamic expiration date and to evaluate the need for intervention by the actuation system. This last consists in a robotic platform with an assistive purpose. When prompted to act, the robot starts a series of routines to bring the good and move it to a place with better preservation conditions.

Keywords: Food waste · Robotic platform · Smart homes · Object manipulation · Smart sensors

1 Introduction

In recent years, with the help of smart home assistants and IoT devices, more and more emphasis has been placed on customer comfort and economic well-being. The latter, such as electronic shutters, smart thermostats, and RGB lights, can be controlled remotely or trigger automatic tasks to save energy and, consequently, the environment [1]. Nevertheless, few solutions to food waste have been proposed [2, 3]. These solutions still require active intervention by residents based on notifications or alarms generated by smart refrigerator management or habit analysis. The emergence of robotic platforms in the smart home concept [4–6] paves the way for new designs in which robots play the main role and can replace humans in the completion of certain tasks. To combat food waste, this work proposes a more proactive way based on the collaboration between a robotic platform and a wireless sensor network, offering a new and cost-effective solution.

This paper is structured as follows. Section 2 describes the proposed architecture. Section 3 presents experimental results collected by testing the architecture in a laboratory environment. Section 4 summarizes the results and leaves future developments.

2　The Proposed Architecture

Figure 1 shows the complete architecture that implements the mitigation chain for food waste reduction. When attached to a food item, the sensor node calculates its dynamic expiration date and calls the Actuation system for intervention if needed. In order to maximize the Shelf-Life of the item, the robotic platform finds the object and moves it to a place with better storage condition.
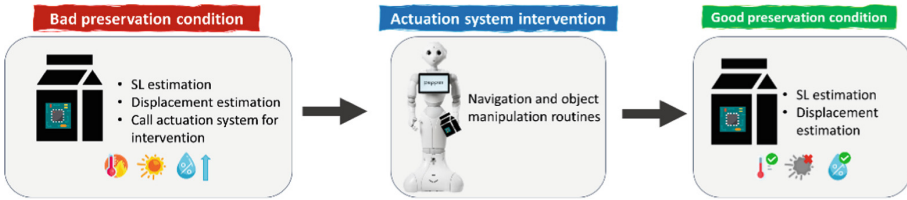

Fig. 1. Whole food waste reduction architecture

2.1　The Sensor Node

Each smart multisensor node has been fully customized. It is a low-power and battery-operated custom PCB. Many requirements were considered during development, such as firmware customization via *Over The Air* (OTA) updates, small footprint, ease of use, and component availability. Figure 2 shows a complete overview of the implemented board.
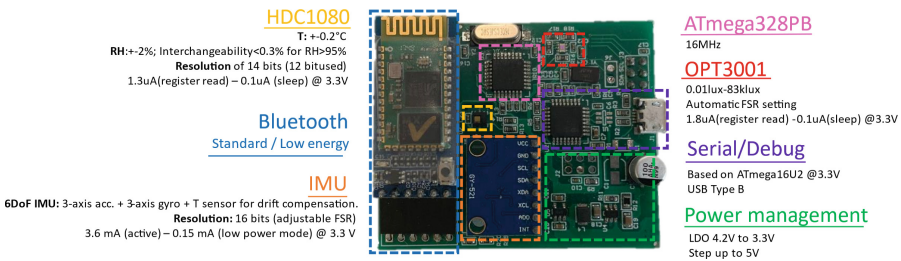
Fig. 2. Sensor node architecture and PCB implementation

The computational core is the ATmega328PB, a mainstream microcontroller by Microchip that interfaces through I2C a set of four sensors: temperature and relative humidity sensor, ambient light sensor, and an IMU. Every time the controller collects the data from the sensors, it performs the Shelf-Life computation. Moreover, based on IMU data, it computes the displacement estimation of the node so that the actuation system can find the item of interest. Assuming two data readings from the sensors and two wireless transmissions per minute, the sensor node can operate for at least 50 days on a single 2000 mAh LiPo battery.

2.2   The Robotic Platform

In this feasibility study, the robotic platform is the Pepper Y20 model manufactured by SoftBank Robotics. It is an assistive purpose robot equipped with an Intel ATOM Z530 processor running at 1.6 GHz. For the proposed use case, 1 GB of RAM and 2 GB of flash were reserved for navigation and object manipulation routines. To properly perform each task, the robot uses a set of cameras and 3 sets of 15 pulsed lasers whose main features are listed in Table 1. While the output of the RGB cameras has been set to 640*480px (kVGA) at a frame rate of 10 fps, the output of 3D sensor provides images of 320*240px (kQVGA) at 5 fps.

Table 1.   Cameras and laser technical specifications

Type	Model	Manufacturer	Resolution	HFOV	VFOV	DFOV
RGB	OV5640	Omnivision	5 Mp	55.2°	44.3°	68.2°
3D	Xtion	ASUS	0.3 Mp	58°	45°	70°
Laser	–	–	–	60°	40°	–

2.3   The Shelf-Life Estimation Model

The sensor node collects data periodically. at 30-s intervals, to predict the effective expiration date of a given food item. The Shelf-Life algorithm implemented on the embedded microcontroller is based on the 1st order Arrhenius kinetic model, an empirical model that describes temperature dependence in simple chemical reactions [11]. Equation 1 shows the full expression of the Shelf life as described in one of our previous papers [7].

$$SL(t) = \frac{1}{k} ln\left(\frac{c(k, t)}{C_{eq}} \right) \cdot \alpha_{RH} \cdot \alpha_{AL} \tag{1}$$

In the above formula, k is the decay rate of the good item, $c(k, t)$ is the food quality related to a specific metric, C_{eq} is the reference food quality while α_{RH} and α_{AL} are two correction factors related to relative humidity and ambient light, respectively. The empirical model can be enriched by adding the development time of bacterial organisms.

2.4   The Displacement Computation Model

When fixed over an object, the sensor node can detect motion and estimate its relative displacement using the inertial navigation algorithm whose block representation is shown in Figure. Based on the combination of accelerometer and gyroscope data, the algorithm is triggered by a sudden change in angular velocity. The data from IMU are processed by a Kalman filter, which has been chosen to offer the best performance in reducing accelerometer noise. Since the data processing is given by a recursive algorithm, it requires a small memory footprint for the microcontroller [8, 12–14]. Then, the Kalman

filter outcome is processed via the trapezoidal rule, saving power and even keeping the real-time signal processing requirement. If no change in angular velocity occurs for at least 5 s during the estimation, the object is considered motionless, and the sensor node stores the new relative coordinates locally (Fig. 3).
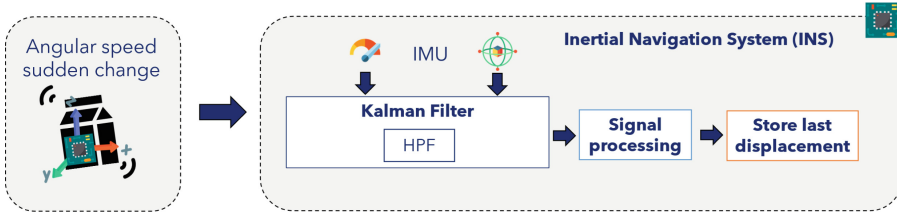

Fig. 3. The displacement computation method

2.5   Calling for Actuation System

Once the good is moved from its optimal preservation condition location, if a severe reduction in Shelf Life is detected, the node enables a timer with a timeout. If no residents' intervention occurs [15] within the timeout, the object is marked as "about to expire" and the robotic platform is called for action.

Actuation System Intervention. Once the actuation system is asked for intervention, the robot retrieves the good's relative coordinates from the sensor node and computes its absolute position. At this point, the object manipulation routine begins. It can be divided into three sub-routines: the navigation routine, the object detection routine, and the grab routine. Each of these it's crucial in order to establish the whole architecture success rate.

Object Detection and Grabbing Routines. During this routine, Pepper exploits its own set of cameras to find the object and move toward it. The RGB camera frames are sent to a pre-trained object detector based on the YOLO method. YOLO extracts a series of blobs giving each of these the probability of being the good of interest. Once an object is tagged as 'target', the robot moves toward it and exploits the YOLO Tag to extract the object distance from the 3D sensor's depth map and assign a specific color to the item.

The robot moves its hand close to the target object and partially covers it. During this process, the number of pixels in the 3D map identifying the object gradually decreases. Once it is between 40 and 45% of the original value, the robot stops adjusting its hand, locks the grasp and grabs the object to move it to a place with better preservation conditions.

3 Experimental Results

The whole architecture has been tested 50 times in a laboratory environment. For the proof of concept of this pilot study, a sensor node has been sticked to a common and easily manageable good while another has been placed near the window in order to trigger a sudden change in Shel Life and force the call for actuation system intervention.

Displacement Estimation and Scanning. Relating to the object scanning and finding, the system achieved a 74% success rate, completing 37 of 50 operations. An average error of about 20% was found between the estimated and actual coordinates along the x-axis and an error of about 15% along the y-axis was found between the estimated and actual coordinates. In 26% of cases, the experiment did not continue to the next step.

Navigation Routine. Concerning robot self-positioning, the robot's standard navigation system [9] has been enriched with a custom correction algorithm. During the calibration test, the robot performs three times three rotations on itself. First, it exploits only the built-in function, then it uses the built-in function and tolerance of 0.02 rad and 0.01 rad. The latter resulted in the best performance, also in terms of cumulative error during 30 min of navigation routine. In this step, the system achieves a 95% success rate taking 35 out of 37 operations to the next step.

Grasping Routine. The here implemented Grasping Routine resulted in 30/35 well-executed operations concluding the whole food waste reduction architecture with 60% of success rate. At this step, the robot has performed 11/30 operations with the left hand and the remaining with the right hand. Specifically, 4 errors concern the operations carried out with the left hand and only one relates to the right hand. More details about this routine are available in our previous work [10]. Figure 4 shows a complete overview of the success rate for the entire mitigation chain and for each routine.
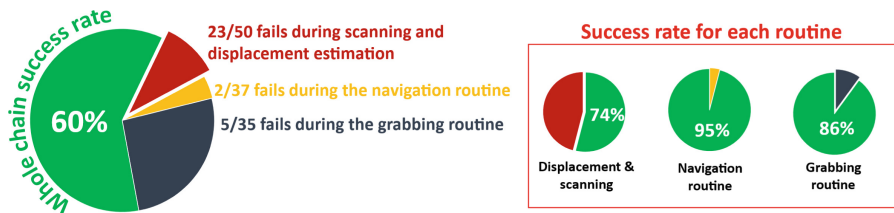

Fig. 4. Whole mitigation chain success rate and success rate for each routine

4 Conclusions

The proposed feasibility study exploits the cooperation of a sensor network and an actuation system to overcome one of the most urgent problems of modern times.

In this paper, we used a system of multisensory nodes to monitor various products to be stored correctly at home and a humanoid robot for moving food items if not stored at the right temperature or humidity.

This study has proven that adapting the pervasive capabilities of the robot-integrated smart home could lead to a significant food waste reduction. The entire architecture successfully completed 30 out of 50 scenarios with a final 60% success rate and paves the way for researchers focused on smart homes concept development.

References

1. Badar, A.Q.H., Anvari-Moghaddam, A.: Smart home energy management system–a review. Adv. Build. Energy Res. **16**(1), 118–143 (2022)

2. Cappelletti, F., et al.: Smart strategies for household food waste management. Procedia Comput. Sci. **200**, 887–895 (2022)

3. Roe, B.E., et al.: A randomized controlled trial to address consumer food waste with a technology-aided tailored sustainability intervention. Resour. Conserv. Recycl. **179**, 106121 (2022)

4. Khan, A.T., Li, S., Cao, X.: Human guided cooperative robotic agents in smart home using beetle antennae search. Sci Chin. Inf. Sci. **65**(2), 1–17 (2022). https://doi.org/10.1007/s11432-020-3073-5

5. Annese, V.F., De Venuto, D.: Fall-risk assessment by combined movement related potentials and co-contraction index monitoring. IEEE Biomed. Circuits Syst. Conf. (BioCAS) **2015**, 1–4 (2015). https://doi.org/10.1109/BioCAS.2015.7348366

6. Do, H.M., et al.: RiSH: a robot-integrated smart home for elderly care. Robot. Autonom. Syst. **101**, 74–92 (2018)

7. De Venuto, D., Mezzina, G.: Spatio-temporal optimization of perishable goods' shelf life by a pro-active WSN-based architecture. Sensors **18**, 2126 (2018). https://doi.org/10.3390/s18072126

8. Smyth, A., Wu, M.: Multi-rate Kalman filtering for the data fusion of displacement and acceleration response measurements in dynamic system monitoring. Mech. Syst. Signal Process. **21**(2), 706–723 (2007)

9. Pandey, A.K., Rodolphe, G.: A mass-produced sociable humanoid robot: pepper: the first machine of its kind. IEEE Robot. Autom. Mag. **25**(3), 40–48 (2018)

10. Mezzina, G., De Venuto, D.: RGB and 3D-segmentation data combination for the autonomous object manipulation in personal care robotics. In: 2021 16th International Conference on Design & Technology of Integrated Systems in Nanoscale Era (DTIS), pp. 1–6 (2021). https://doi.org/10.1109/DTIS53253.2021.9505128

11. Annese, V.F., De Venuto, D.: On-line shelf-life prediction in perishable goods chain through the integration of WSN technology with a 1st order kinetic model. In: 2015 IEEE 15th International Conference on Environment and Electrical Engineering (EEEIC), pp. 605–610 (2015). https://doi.org/10.1109/EEEIC.2015.7165232

12. De Venuto, D., Stikvoort, E., Tio Castro, D., Ponomarev, Y.: Ultra low-power 12-bit SAR ADC for RFID applications. In: 2010 Design, Automation & Test in Europe Conference & Exhibition (DATE 2010), pp. 1071–1075 (2010). https://doi.org/10.1109/DATE.2010.5456968

13. De Venuto, D., Castro, D.T., Ponomarev, Y., Stikvoort, E.: Low power 12-bit SAR ADC for autonomous wireless sensors network interface. In: 2009 3rd International Workshop on Advances in sensors and Interfaces, pp. 115–120 (2009). https://doi.org/10.1109/IWASI.2009.5184780

14. Blagojevic, M., Kayal, M., Gervais, M., De Venuto, D.: SOI hall-sensor front end for energy measurement. IEEE Sens. J. **6**(4), 1016–1021 (2006). https://doi.org/10.1109/JSEN.2006.877996

15. De Venuto, D., Annese, V.F., Mezzina, G., Ruta, M., Di Sciascio, E.: Brain-computer interface using P300: a gaming approach for neurocognitive impairment diagnosis. IEEE Int. High Level Des. Validation Test Workshop (HLDVT) **2016**, 93–99 (2016). https://doi.org/10.1109/HLDVT.2016.7748261

An Embeddable Object Manipulation Framework for Assistive Robotics

Giovanni Mezzina$^{(\boxtimes)}$ and Daniela De Venuto

Department of Electrical and Information Engineering, Politecnico di Bari, 70125 Bari, Italy
{giovanni.mezzina,daniela.venuto}@poliba.it

Abstract. Recently, robots' employment in the ambient assisted living framework is rapidly growing. Most of the employed robots fall within the category of social robots, i.e., automata able to interact verbally with the user to be assisted, supporting caregivers in patient's need comprehension. However, most of these, although equipped with arms for social interaction, lack manipulative abilities. In this context, the paper proposes an embeddable object manipulation framework, which consists of a set of low-complexity routines to expand functionalities on social robots, and specifically on Pepper by SoftBank Robotics, permitting its employment in assistive scenarios. Implemented routines exploit Pepper's built-in RGB cameras to (i) identify the object to be grabbed, (ii) estimate its coordinate in the three-dimensional frame; (iii) plan the arm movement sequence, and (iv) grab the object for final recognition. The routine is designed to be fully automatic (no internet connection), preserving sensitive data stored in the robot's memory. Experimental results demonstrated a grabbing accuracy of ~ 87% for different shelf heights, demonstrating the employability of improved social robotics for daily-life assistance and ambulatorial contexts.

Keywords: Object manipulation · Robotics · Personal care robots

1 Introduction

The automation of object and materials handling activities showed a high impact on efficiency and productivity increment in several sectors such as the healthcare and assistive ones, where most of these operations are still performed manually. Prolonged observation of US and European hospitals [1] during the pandemic emergency, highlighted that more than 40% of nurses' time is wasted in repetitive activities, such as drug selection and delivery. In this context, the employment of supporting robotics has been strongly reconsidered, aiming to lighten the medical staff effort and reduce complications related to erroneous drug delivery [2].

Due to the tradeoff between costs and provided services, the most used autonomous robot in healthcare facilities [3] and domestic assistance [4] is Pepper by SoftBank Robotics [5]. It is a social robot designed for verbal interactions. Thus, its main use in hospitals concerns reception tasks [6]. Also, Pepper has been successfully used to interface with people affected by dementia, as well as in a domestic assistance context

[7]. Although largely used, Pepper did not find application in most practical assistive situations, due to the missing manipulation capabilities.

In light of the great diffusion of Pepper in healthcare/assistive facilities, this paper proposes a robot capabilities expansion, by adding a low complexity object manipulation routine based on data from a built-in RGB camera. The paper is organized as follows. Sect. 2 reports the proposed framework. Sect. 3 provides and discusses some experimental results. Finally, Sect. 4 concludes the paper.

2   The Object Manipulation Framework

Figure 1 reports a schematic overview of the here-proposed framework. The workflow starts with the acquisition of frame sequences from the embedded top and bottom RGB cameras, proceeding with a shelf height extraction based on an edge detection approach. It allows the robot to plan proper arm segments movement to approach the object to be grabbed. A You-Only-Look-Once (YOLO) approach is then employed to adaptively drive the manipulation process.

2.1   The Hardware Platform

The framework is realized to improve the capabilities of Pepper Y20 by SoftBank Robotics. The implemented framework uses two RGB cameras (OV5640 by Omnivision). The first one, OV5640top in Fig. 1 is placed on the forehead at an angle of $90°$ with respect to the head frame axis. The OV5640bot camera is placed on the robot's mouth with an orientation of $-40°$. The maximum camera resolution is 5 Mp with $55.2°$ of the horizontal field of view (FOV) and $44.3°$ of vertical FOV. Frames are captured with a ratio kVGA (640*480 px) @ 10 fps. The system is supported by an ASUS Xtion 3D sensor with 0.3 Mp of resolution, $58°$ and $45°$ of horizontal and vertical FOV. Camera output has been set to be kQVGA (320*240 px) @ 5 fps [8, 9].

2.2   Working Principle: Preparation Steps

Shelf Height Estimation. The first preparation step consists of estimating the height of the shelf on which the object to be grabbed is placed. For this purpose, the system leverages top RGB camera and 3D sensor data.

Figure 2.a shows the shelf height estimation setup. In detail, the robot extracts the distance between the 3D camera and the NAO mark. Once extracted, the head frame pitch is increased to a known angle as per Fig. 2.a. The RGB top camera takes a picture that is analyzed via Laplacian edge detection algorithm with a 3×3 px convolution mask [10]. The robot body frame is adaptively moved to center the identified edges in the middle of the vertical FOV as per Figs. 2.b and c. Since the distance between the NAO mark and the shelf edge is set, the height of the shelf can geometrically estimate.

Object Scanning. Once the height is estimated, the RGB frames undergo an embedded version of YOLOv3 method: MiniYOLOv3 (MY3) [11]. It is offline pretrained to recognize specific objects of interest and the model weights are uploaded to the robot.
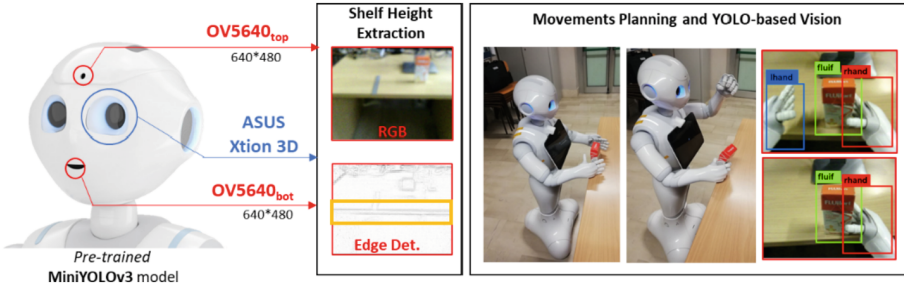
Fig. 1. Proposed framework workflow overview.

MY3 extracts a set of bounding boxes, returning the object label according to the highest probability of specific class belonging. The data collection phase for MY3 offline training consisted of 2496 images gathered for a total of 9984 annotations (4 per image) by using the bottom RGB camera from several different approach directions. The labeling has been manually realized via LabelImg software drawing bounding boxes that include the entirety of the object. Roboflow preprocessing has been also included through image auto orienting, and data augmentation to protect the model against overfitting [12].
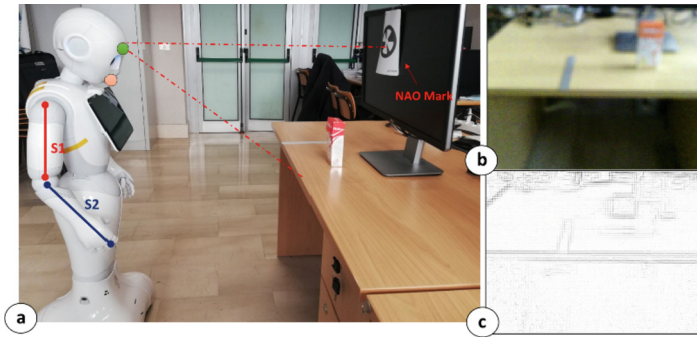
Fig. 2. Shelf Height Estimation. (a) Experimental setup; (b) RGB camera frame; (c) Laplacian edges detection.

2.3 Working Principle: Manipulation Routine

Arms Movement Planning. Once the shelf height is estimated and the object height is derived by the attributes linked to the MY3 record, the robot must position the arms segments (S1 and S2 – Fig. 2) to move toward the object without collisions. The positioning keeps into account the projection on the vertical axis of S1 and S2. The shoulder joint angle is the first to be moved, while the elbow one is used to adapt the height of the grab ensuring a perpendicular approach with the object.

Grabbing Approach. Pepper set S1 and S2 angles in a so-called safe area (with no collision), before starting moving toward the object, keeping the posture as per Fig. 3.

The movement considers the distance between the robot and the NAO mark and the preset distance between the object and the shelf edge. When the shelf is properly approached (a feedback check is realized via an embedded odometry algorithm), the proposed system runs an object position check step. It consists of taking a frame of the bottom RGB camera to be sent to MY3 for stable labeling. It ensures a correct robot-object alignment (object MY3 tag should be placed in the middle of the vertical FOV).

Hand Selection. When the object position check is completed (Fig. 3 – left), the framework evaluates the number of pixels involved in the overlap among hands bounding boxes (blue and red ones) and the recognized object one. The hand with the highest number of pixels overlapped with the object bounding box is selected for the grabbing procedure, while the other hand is raised to avoid interference in adjusting movements (Fig. 3 – middle). If the overlap involves less than 25% of the hand box, the robot is laterally moved to cover at least this limit.

Grab and Check. Once the alignment is completed, Pepper drives the hand closing completing the process. A successful grab check is carried out after the described procedure, by rotating the wrist and the elbow toward the camera as per the right panel in Fig. 3. It allows discriminating between an empty hand (grabbing procedure failed) or not (grabbing procedure completed).
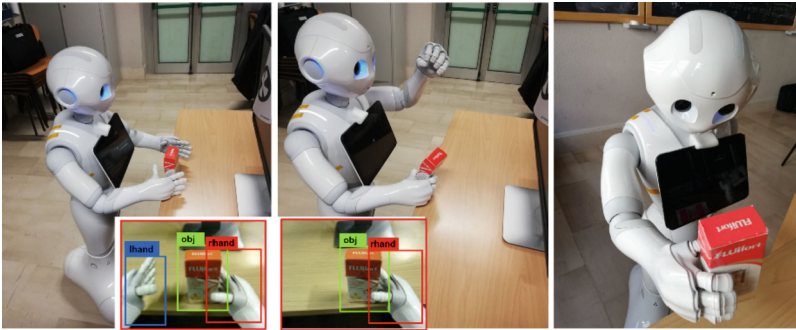
Fig. 3. Grabbing approach, Hand selection and Successfully grab check phases of the proposed framework

3   Experimental Results

All the proposed procedures have been implemented through Python 2.7 scripts and run in background on Pepper by means of NAOqi OS.

A total of 568 operations of object approaching and manipulation have been carried out to characterize the routine, covering all the phases explained in Sect. 2.2 and 2.3. In each analyzed operation, Pepper has been placed in front of the object to be grabbed at ~1.5 m. A lateral displacement between −25 cm and 25 cm from the center of the object and a horizontal angle orientation error ranging between −30° and 30° are also considered.

3.1   Object Manipulation Routine Success Rate

To characterize the improved capabilities of the Pepper robot, the present section analyzes the number of fails in the grabbing procedure over 568 operations constituting the observation set, dividing them per failing phase.

Figure 4.a summarizes the grabbing success rate of the carried-out operations. Results showed that 494 operations out of 568 (~87%) have been successfully completed without any errors. While 74/568 fails are recorded. Figure 4.b shows the occurrence rate of the failure causes. Results show that in 21.6% of cases the error can be related to an erroneous shelf height estimation. The operations have been stopped to avoid collisions. The arm movement planning is the phase that shows the highest failure rate. With 18/74 failures, the phase constitutes 24.32% of the erroneous operations.

The grabbing approach phase is responsible for 17.57% of errors. In most cases, it is due to unstable MY3 bounding boxes. Hand selection and Grab and Check steps show 10/74 unsuccessful operations (13.51%). Concerning the first routine (Hand Selection), the main cause of the error is the lateral adjustment to cover the 25% of overlap. Indeed, during adjustments, the robot moves lightweight envelopes, causing their fall. In the second case (Grab and Check), the main cause lies in the unstable recognition of the MY3 tag for the check and envelopes that shifted from the grab during wrist rotation. Object scanning is the best phase with 7/74 errors. This step is largely consolidated in terms of approach distance. More details are available in our previous work [13].

3.2   Bounding Boxes Overlap

To characterize the best bounding boxes overlap percentage, a package has been placed on the shelf. The shelf chosen for testing purposes was 76 cm tall, although shelves with a height between 68 and 82 cm still ensure the characterized grabbing accuracy. Then, different bounding boxes' overlap percentages have been evaluated in terms of grabbing accuracy. For the specific case, 11 different values of percentage have been assessed, starting from the 5%, up to 55% with a step of 5%. The arm segments were always set at specific and unaltered angles to ensure repeatability among different measurements. For every bounding box overlap percentage, ten identical runs have been carried out. Test results showed that the best overlap range moves from 20% (accuracy = 80%) and the 40% (accuracy = 80%), with a peak in 25% (accuracy = 100%).
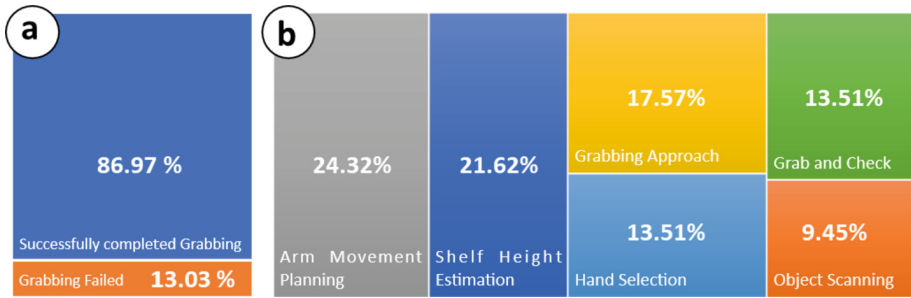
Fig. 4. Grabbing accuracy of the proposed framework. (a) Success rate, (b) Error occurrence versus involved phase.

4   Conclusions

In this paper, a novel, low-complexity framework to expand social robot Pepper capabilities and allow its employment in practical assistive contexts, has been proposed. The proposed system leverages data from Pepper RGB cameras to plan and actuate object handling procedures. Specifically, the proposed routine mainly exploits the bottom RGB camera of the robot and the MY3 tags to extract arms' segments trajectories. The grabbing procedure is entrusted to an overlap-based algorithm that analyzes the number of pixels mutually included by MY3 bounding boxes. The proposed routine, experimentally tested in a laboratory environment, demonstrated to be able in achieving a grabbing accuracy of 87%. The achieved promising results open to the possibility of updating the already employed Pepper by adding new and useful capabilities, aiming to lighten hospital staff or caregiver effort.

References

1. Khan, Z.H., et al.: Robotics utilization for healthcare digitization in global COVID-19 management. Int. J. Environ. Res. Public Health **17**(11), 3819 (2020). https://doi.org/10.3390/ijerph17113819
2. Yen, P.Y., et al.: Nurses' time allocation and multitasking of nursing activities: a time motion study. In: AMIA Annual Symposium Proceedings, vol. 2018, p. 1137. American Medical Informatics Association (2018)
3. Fragapane, G., Hvolby, H.-H., Sgarbossa, F., Strandhagen, J.O.: Autonomous mobile robots in hospital logistics. In: Lalic, B., Majstorovic, V., Marjanovic, U., von Cieminski, G., Romero, D. (eds.) APMS 2020. IAICT, vol. 591, pp. 672–679. Springer, Cham (2020). https://doi.org/10.1007/978-3-030-57993-7_76
4. Lestingi, L., Askarpour, M., Bersani, M.M., Rossi, M.: Formal verification of human-robot interaction in healthcare scenarios. In: de Boer, F., Cerone, A. (eds.) Software Engineering and Formal Methods: 18th International Conference, SEFM 2020, Amsterdam, The Netherlands, September 14–18, 2020, Proceedings, pp. 303–324. Springer International Publishing, Cham (2020). https://doi.org/10.1007/978-3-030-58768-0_17
5. Pandey, A.K., Gelin, R.: A mass-produced sociable humanoid robot: pepper: the first machine of its kind. IEEE Robot. Autom. Mag. **25**(3), 40–48 (2018)

6. Henschel, A., Laban, G., Cross, E.S.: What makes a robot social? a review of social robots from science fiction to a home or hospital near you. Current Robot. Rep. **2**(1), 9–19 (2021). https://doi.org/10.1007/s43154-020-00035-0

7. De Venuto, D., Annese, V.F., Mezzina, G., Ruta, M., Di Sciascio, E.: Brain-computer interface using P300: a gaming approach for neurocognitive impairment diagnosis. IEEE Int. High Level Des. Validation Test Workshop (HLDVT) **2016**, 93–99 (2016). https://doi.org/10.1109/HLDVT.2016.7748261

8. De Venuto, D., Stikvoort, E., Tio Castro, D., Ponomarev, Y.: Ultra low-power 12-bit SAR ADC for RFID applications. In: 2010 Design, Automation & Test in Europe Conference & Exhibition (DATE 2010), pp. 1071–1075 (2010). https://doi.org/10.1109/DATE.2010.5456968

9. De Venuto, D., Castro, D.T., Ponomarev, Y., Stikvoort, E.: Low power 12-bit SAR ADC for autonomous wireless sensors network interface. In: 2009 3rd International Workshop on Advances in sensors and Interfaces, pp. 115–120 (2009). https://doi.org/10.1109/IWASI.2009.5184780

10. Shrivakshan, G.T., Chandrasekar, C.: A comparison of various edge detection techniques used in image processing. Int. J. Comput. Sci. Issues **9**(5), 269 (2012)

11. Mao, Q-C., et al. : Mini-YOLOv3: real-time object detector for embedded applications. IEEE Access **7**, 133529–133538 (2019)

12. Blagojevic, M., Kayal, M., Gervais, M., De Venuto, D.: SOI hall-sensor front end for energy measurement. IEEE Sens. J. **6**(4), 1016–1021 (2006). https://doi.org/10.1109/JSEN.2006.877996

13. Mezzina, G., De Venuto, D.: RGB and 3D-segmentation data combination for the autonomous object manipulation in personal care robotics. In: 2021 16th International Conference on Design & Technology of Integrated Systems in Nanoscale Era (DTIS), pp. 1–6 (2021). https://doi.org/10.1109/DTIS53253.2021.9505128

Automatic Monitoring IoT System for Phytosanitary Products in Agricultural Machinery

Leandro Lucangeli[1,2], Emanuele D'Angelantonio[1,2], and Antonio Pallotti[1,3(✉)]

[1] Technoscience - Parco Scientifico e Tecnologico Pontino, 04100 Latina, Italy
{l.lucangeli,e.dangelantonio}@studenti.uniroma4.it,
leandro.lucangeli@technosceince.it, {emanuele.dangelantonio,
antonio.pallotti}@technoscience.it, antonio.pallotti@uniroma5.it
[2] University of Rome "Foro Italico", 00135 Rome, Italy
[3] University of Rome "San Raffaele", 00166 Rome, Italy

Abstract. In recent years, agricultural productivity depends on several factors: the demographic increase of the population, the climate changes, and the need for environmental sustainability. Increasing agricultural production capacity while respecting the environment is therefore necessary. Generally, substances that are potentially harmful both for the environment and for humans are used to satisfy the request. Monitoring of the production chain is a necessity of smart agriculture and technologies can ensure process optimization. This paper describes the automation of an agricultural machine for soil sterilization before sowing. This system is inserted in an IoT infrastructure, and it allows to monitor the quantity of sterilizing product dispensed on the ground and other soil parameters, such as temperature, pH and humidity. Quantification of the plant protection product dispensed is possible with the obtained system and it guarantees compliance with the current environmental laws in Europe. It also constitutes a safety system for operators, making the regulation of the plant protection product completely automatic and remotely controllable.

Keywords: Smart agriculture · Internet of things · Machine learning · Plant protection product · Remote monitoring

1 Introduction

Industrialization and intensification of agricultural services are increasingly necessary to ensure food in terms of quality and quantity that satisfy human needs [1]. Numerous pesticides and plant protection products are used to ensure the harvest in all seasons but often these have a negative impact on the ecosystem and, consequently, on human and animal health [2]. The monitoring of some processes, thanks to the use of the Internet of Things (IoT) and data analysis, allow the improvement of the productivity of the harvest [3] but also of the operational efficiency, for example with the supply of the right quantity of sterilizing or phytosanitary products (PP).

Technologies in agriculture include the automation of machines and the use of network infrastructures for data monitoring [4]. In fact, an essential element of modern agriculture is the adoption of Information and Communication Technology (ICT) [5], that connects sensorized systems, such as soil sensors, drones with cameras, automated guided vehicles to each other constituting complex IoT frameworks. Connected devices with integrated sensors produce a large amount of highly diversified data such as chemical physical parameters of air, soil and plants, that standard data processing techniques can struggle to process. Because of this, Artificial Intelligence (AI) and Machine Learning (ML) techniques are gaining ground in this field by leveraging their computing power. To give an example of the potential offered by artificial intelligence we can refer to works that use autonomous or semi-autonomous vehicle, robots and drones for analysing crop and detecting diseases in plants using computer vision techniques [6].

Nowadays, machine learning models are mainly used for soil analysis, crop recognition and yield prediction, but they are also used for water management [5]. Moreover, advanced artificial intelligence models allow to make immediate intelligent decisions such as determining the amount of water needed for irrigation [7]. The use of these modern technologies can control costs and guarantee more sustainable agriculture [8]. In fact, Internet of Things and Artificial Intelligence remove the randomness of some processes and assist farmer to better control and optimize each step of the agricultural process [9]. Therefore, the use of technologies to develop autonomous agricultural machinery has increased in recent years, which aim to improve the productivity of all agricultural processes in which conventional agricultural machines were inefficient [10]. Lastly, the use of technology and artificial intelligence is aimed at reducing human workload, enhancing safety, and generating real benefits for small and large companies alike.

This work will describe the automation of an agricultural machinery (Fig. 1) used for the sterilization of the land and the integration of the latter within an IoT infrastructure for remote monitoring and control. The machine to be automated allows soil sterilization
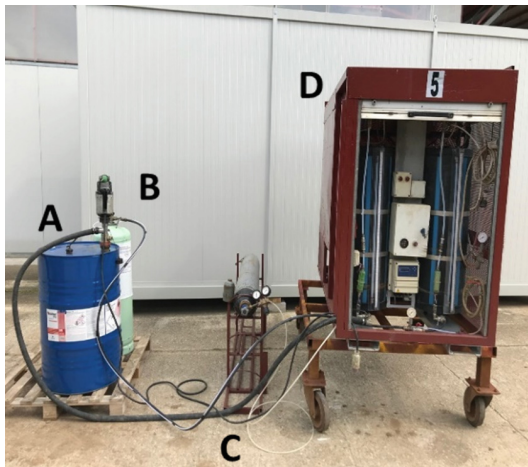
Fig. 1. The phytosanitary product (A-B), passing through a system of pipelines (C) are dispensed by a manual agricultural machine for the sterilization of the land (D).

thanks to a system capable of measuring the flow of water in the pipeline and injecting the right amount of phytosanitary product necessary for irrigation in the greenhouse. Currently, the operations described above are carried out manually by the operator. The main limitations of the machine are safety, as the operator who manages the machine is in the vicinity of high-pressure cylinders of plant protection product, and the absence of remote monitoring.

2 Materials and Methods

The system has been integrated with an Arduino Mega 2560 Rev3 board powered by a 12 V battery with a capacity of 74Ah. This microcontroller is suitable to be used with different actuators and sensors as it integrates several analogue and digital ports inside the board and to be powered with a wide range of voltages as required by the developed system. The board is capable of controlling an Arag Flowmeter (with an accuracy of $\pm$ 1% and a measuring range of 50 $\div$ 2500 l/min), for measuring the flow of water in the duct, a Raven proportional valve (with ball type of valve in stainless steel), for controlling the quantity of phytosanitary product to be injected, a SMC valve On/Off (normally closed (N.C.) type in stainless steel), for a safety check of the entire system, and a Biotech Flowmeter (with an accuracy of $\pm2,5\%$ and a measuring range of 0,1 $\div$ 10 l/min) for monitoring the amount of PP injected. All components included in the system were chosen because they met the requirements of measurement accuracy and chemical compatibility with respect to the requirements imposed by the application in the agricultural field.

The system is also integrated with a Bluetooth HC-05 module to allow remote control thanks to the use of an Android application developed in MIT App Inventor. With
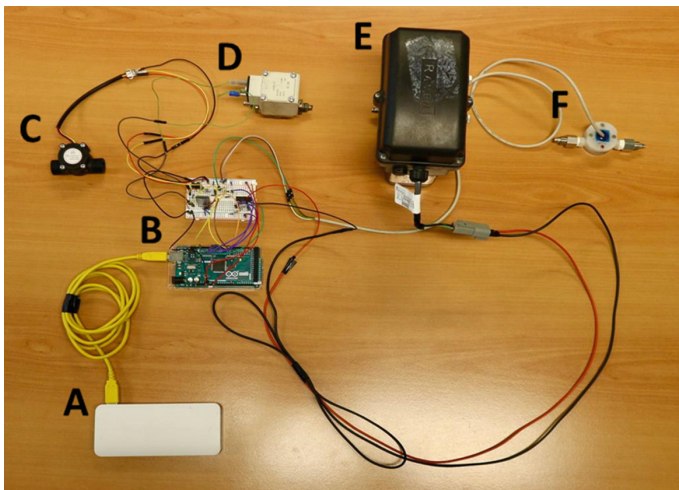
Fig. 2. The developed automatic prototype of the agricultural machine integrates a power supply (A), an Arduino Mega (B), an Arag flowmeter (C), an SMC valve (D), a Raven proportional valve (E) and a Biotech flowmeter (F).

this application it is possible to quantitatively monitor the flow of water in the pipeline and automatically define the right quantity of PP to be introduced controlling the Raven valve, according to the proportions that are established at the regulatory level. These operations can be carried out with the operator placed at a safe distance from the pressurized cylinders of plant protection product, which is particularly harmful to humans. Furthermore, the mobile application sends the data exchanged directly to a database (in compliance with EU legislation), the Google Firebase, to allow monitoring by other operators not involved in the sterilization operations in the field (Fig. 2).

3   Results and Discussion

The system, while still remaining in the prototype state, has been tested in the laboratory and provides satisfactory results in terms of measurement accuracy of the monitored physical quantities and control latency (less than 500 ms). Using the mobile application developed, it is possible to set the threshold values of the phytosanitary products used and measure the actual quantity of product and water mixed. The application communicates continuously in real time with the microcontroller board used in the system, thus allowing continuous remote monitoring of the solenoid valves.

Thus, in conclusion, the precise remote control of the valves that regulate the flow of plant protection product, harmful to humans, is an important result in the automation process of the agricultural machine and guarantees a greater level of safety for the worker. There are many possible future developments, starting with the miniaturization of the prototype for a more comfortable integration on agricultural machinery in motion. Furthermore, the use of wide-ranging communication protocols and finally the industrialization of the machine is planned for use on crops on large surfaces.

Finally, other developments concern the use of other sensors that can be integrated on the ground and on the agricultural machine for the creation of a complete monitoring system, not only of the supply of phytosanitary product but more generally of the state of the soil and plants, up to the harvest. As a latest development there is the possibility,
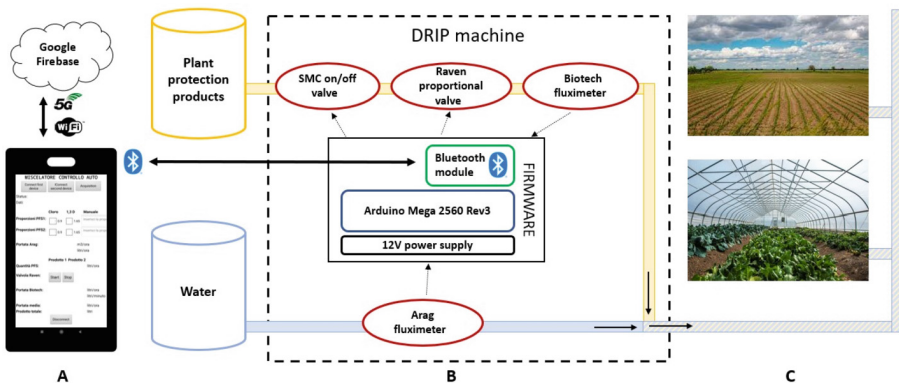
Fig. 3. Scheme of the developed automated drip machine (B) with the remote-control application (A) for the dispensing of phytosanitary products in greenhouse and in agricultural land (C).

through artificial intelligence that uses both data from integrated sensors and perhaps satellite images, to regulate the distribution of water and plant protection products on the ground automatically, with a level of safety for humans and very high environment (Fig. 3).

References

1. Farooq, M.S., et al.: Role of IoT technology in agriculture: a systematic literature review. Electronics **9**(2), 319 (2020)
2. Labite, H., et al.: A review and evaluation of plant protection product ranking tools used in agriculture. Hum. Ecol. Risk Assess. Int. J. **17**(2), 300–327 (2011)
3. Elijah, O., et al.: An overview of internet of things (IoT) and data analytics in agriculture: benefits and challenges. IEEE Internet Things J. **5**(5), 3758–3773 (2018)
4. Zhao, J., et al.: The study and application of the IOT technology in agriculture. In: 2010 3rd International Conference on Computer Science and Information Technology (2010)
5. Benos, L., Tagarakis, A.C., Dolias, G., Berruto, R., Kateris, D., Bochtis, D.: Machine learning in agriculture: a comprehensive updated review. Sensors **21**, 3758 (2021). https://doi.org/10.3390/s21113758
6. Nex, F., Remondino, F.: UAV for 3D mapping applications: a review. Appl. Geomatics **6**(1), 1–15 (2014)
7. Bu, F., et al.: A smart agriculture IoT system based on deep reinforcement learning. Future Gener. Comput. Syst. **99**, 500–507 (2019)
8. Mekala, M.S., et al.: A survey: smart agriculture IoT with cloud computing. In: 2017 International conference on Microelectronic Devices, Circuits and Systems (ICMDCS) (2017)
9. Sharma, A., Jain, A., Gupta, P., Chowdary, V.: Machine learning applications for precision agriculture: a comprehensive review. IEEE Access **9**, 4843–4873 (2020)
10. Talaviya, T., Shah, D., Patel, N., Yagnik, H., Shah, M.: Implementation of artificial intelligence in agriculture for optimization of irrigation and application of pesticides and herbicides. Artif. Intell. Agric. **4**, 58–73 (2020)

Scalable Design Space Exploration for the Synthesis of Redundant Architectures

Antonio Tierno[1(✉)] , Giuliano Turri[2], Alessandro Cimatti[2] ,
and Roberto Passerone[1]

[1] Dipartimento di Ingegneria e Scienza dell'Informazione,
University of Trento, Trento, Italy
{antonio.tierno,roberto.passerone}@unitn.it
[2] Embedded Systems, Fondazione Bruno Kessler, Trento, Italy
{gturri,cimatti}@fbk.eu

Abstract. Reliability is an essential quality requirement for Embedded Systems, especially for those that are life critical, which need to contain mechanisms to react properly to malfunctions of system parts. An approach that is usually applied to increase reliability consists in integrating additional *redundant* components that take over in case of failure of the primary ones. In this work, we face specifically the problem of optimally allocate redundancy to system components.

Keywords: Redundancy · Reliability · Optimization

1 Introduction

Given a (non-redundant) system defining the architecture and the behavior of a component-based system, and a finite set of available redundant patterns, we propose a fully automated approach for the assessment of reliability and other non-functional parameters of redundant alternatives for the given architecture, and therefore support the Design Space Exploration (DSE) for a Multi-Objective Optimization Problem (MOOP). We leverage the power of Satisfiability Modulo Theory (SMT) [1] techniques to express architectural constraints between components and their behaviors, and to find a satisfying assignment that optimizes the objective functions.

We build on our previous work [2–7] and introduce a novel assessment of reliability that combines symbolic search based on Binary Decision Diagrams (BDDs) with Depth First Search (DFS). The algorithm extracts a symbolic reliability function that expresses the reliability of a given system in terms of the reliability of individual components.

2 Proposed Method

We propose a *multi-objectives DSE* process that *automatically* selects the appropriate set of FT techniques (at the logical level) to be applied to the original,

non-redundant, system to obtain one that is redundant, optimizing simultaneously a collection of objective functions. This approach heavily relies on formal methods, and is based on the following phases.

2.1 Modeling the System Architecture

We model the system with a Directed Acyclic Graph (DAG) where nodes represent the computing elements (denoted by C_i) and edges describe the flow of data. We model the occurrence of faults with Boolean *fault variables* (denoted by F_i) that enable the component to have failures. Failure probabilities are given. Hence, each component has two behaviors, *nominal* and *faulty*, described using *uninterpreted functions*, which allow us to abstract from specific implementation.

A set of design patterns (denoted by P_j) is assigned to each component. We collect proven solutions in the field of ESs and use their abstract representation to evaluate their impact. Some patterns are illustrated in Fig. 1. The objectives are used as optimization goal of the overall system, and are not domain-specific (to be as general as possible). We assume that for each component of the given system a single Fault-Tolerant (FT) pattern can be allocated for redundancy. In addition, we assume that basic events are independent, and each component is critical, i.e., its failure triggers the system failure. For simplicity, we assume that all redundancy is active, i.e., redundant components operate simultaneously as soon as the mission starts.

We use the same approach to model the redundant components: the *behavior* of their computing modules can be abstracted by an uninterpreted function, while the behavior of the voters and comparators by logical formulae, as they have well defined implementations. The mapping between a component C_i of the basic system and a redundant pattern P_j of the library is defined by a *configuration variable* $cfg_i = (C_i, P_j)$. Leveraging this approach, we can model an entire redundant architecture using First-Order Logic (FOL), specifying the connections among the redundant components. As a result, the set of redundant alternatives for the given architecture can be modeled in a single SMT formula.

2.2 Reliability Assessment

Modeling nominal and faulty behaviors gives us the possibility to describe both reference and faulty systems. This system composition is known as *Miter* [8]. By providing the same inputs to the two architectures and comparing the outputs we detect a system level failure, also referred to as *Top Level Event* (TLE). A combination of component level failures (a.k.a. *basic event*) occurrences that leads to the TLE is referred to as *Cut-Set* (CS). Every CS can be represented as a conjunction of component faults, and the whole set of configurations as a disjunction of CSs. Hence, the Miter composition is an SMT formula over inputs, outputs, fault variables, and TLE, which represents the set of assignments to the fault variables F_i such that there exists an assignment to the inputs that leads the two architectures to provide different outputs. The problem of extracting
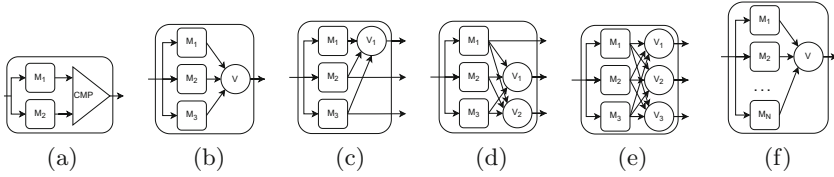
Fig. 1. Some redundant design patterns: (a) Comparator (*CMP*), (b) Triple Modular Redundancy (*TMR*), (c) *TMR* with one voter TMR_{100}, (d) *TMR* with two voters TMR_{012}, (e) *TMR* with three voters TMR_{123}, (f) *MooN*.

the CSs can be therefore encoded as an AllSMT [9] problem for the theory of Equality and Uninterpreted Functions (EUF).

Since the number of satisfiable assignments grows with the number of variables, we use *predicate abstraction* to abstract the behavior of a pattern and obtain a pure Boolean formula consisting of fault variables, and Boolean input and output ports. This translates into partitioning a global AllSMT(EUF) computation into a number of smaller and less complex AllSMT(EUF). To obtain a formula containing fault variables and configuration variables only, an additional quantifier elimination of Boolean inputs and outputs has to be performed on the global formula, by using BDD-based projection techniques. Finally, to extract a *symbolic function* that maps each configuration to its failure probability, a probability of failure is associated to each fault variable, and the formula of the CSs is converted into a BDD that is traversed to generate the reliability function by recursively applying the following formula to each node n:

$$\begin{cases} 1 & \text{if } n = \top \\ 0 & \text{if } n = \bot \\ F_i \cdot BddProb(n_\top) + \\ (1 - F_i) \cdot BddProb(n_\bot) & \text{if } n = ITE(F_i, n_\top, n_\bot) \end{cases} \quad (1)$$

Note that the formula (and the BDD) representing the CSs of the set of architectures contains two types of nodes: *configuration nodes* and *fault nodes*. In case of a configuration node, evaluation of 1 translates into a *ITE* (Fig. 2(a)) that basically selects the path to the TLE.

2.3   Optimization

We can generalize the approach used for reliability assessment to other non-functional parameters, like cost, weight, and power consumption, facing therefore a MOOP. As a result, we have three alternative approaches for optimization.

The simplest one is the *enumerative approach*: parameters are made explicit before the search. We iterate over each candidate design point and compute the costs of every architecture. The second is a *symbolic approach*, in which we parametrize the system and obtain a single symbolic representation of the problem. This approach produces a compact function, but since the number of
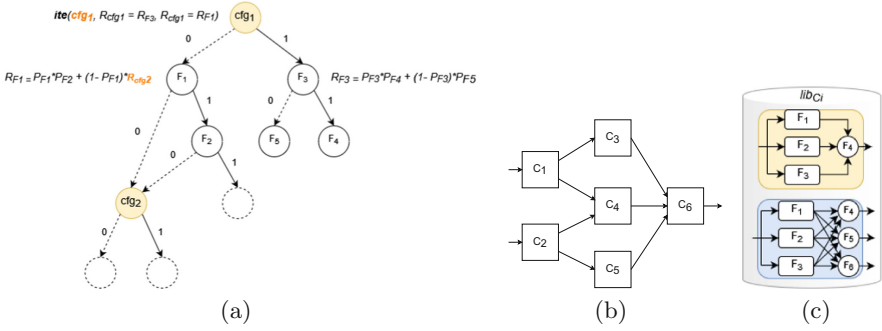
Fig. 2. (a) BDDs representing the CSs of an architecture are composed of configuration nodes and fault nodes. (b) Example system. (c) A library made of two redundant patters (TMR_{111} and TMR_{123}) is associated to each component.

configurations rapidly grows with the size of the architecture, the resulting function defining the space of the design alternatives is very complex. The third is a *hybrid approach*. First, we extract the symbolic function of each parameter, and then use this function to obtain the precise parameter values for each configuration, in order to build a function that explicitly defines all the design points of the space. To sum up, we can range from a fully explicit to a fully symbolic approach. In order to find the allocations that optimize the objective functions of the redundant system, we can rely on an existing SMT solver.

3   Experimental Evaluation

To help illustrate the method, consider an example system made of six components, each with two suitable redundant patterns, as illustrated in Fig. 2. The optimization problem involves a Reliability function to be maximized (which is equivalent to minimizing the fault probability) and a Cost function to be minimized. We assign arbitrary values of fault probability and cost to modules and voters. Our method produced eight solutions illustrated in Fig. 3.

More in general, the overall performance of the method has two main contributions: assessment of non-functional parameters and optimization. The more burdensome parameter is reliability, as for simplicity we choose the other parameters as cumulative, and their assessment translates therefore in a simple addition. The overall performance of reliability assessment takes into account three main tasks: abstraction (AllSMT computation), BDD-based quantifier elimination, and BDD traversing. Thanks to predicate abstraction, the first task is negligible. The results indicate that the time for the BDD-based quantifier elimination grows with the number of components, the size of the pattern library, and on how components are connected, as illustrated in Fig. 4(a), in which the labels on the bars represent the different fan-out of the TMR patterns employed in the library. Hence, the performance is proportional to the BDD complexity.
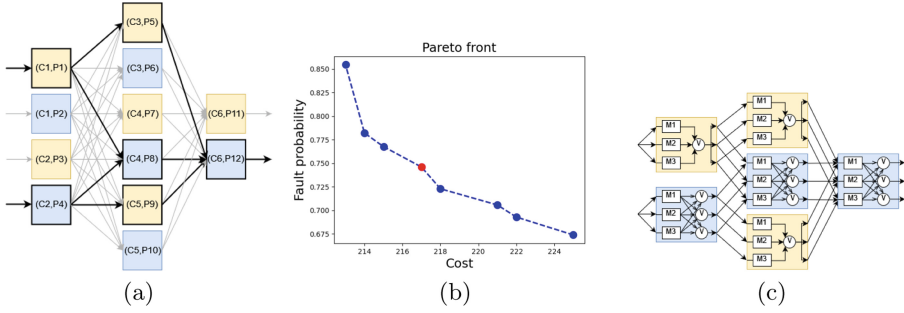
Fig. 3. (a) Set of redundant architectures. (b) Exact solutions. (c) One of the optimal redundant architectures (the one highlighted in Fig. 4(a) and in red color in Fig. 4(b)).
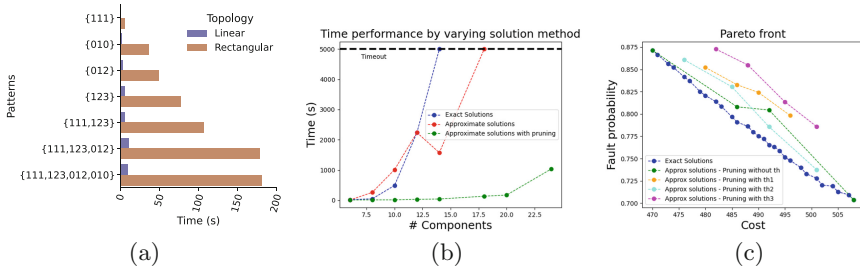
Fig. 4. (a) Time performance for extraction of non-functional parameters using a library of different redundant patterns for serial architecture of 100 components and rectangular (repeating pairs) architecture of 100 components, organized in 50 levels (b) Comparison between solution methods for a complex architecture. (c) Example of a complex system composed of fourteen components with a library of twenty-eight patterns: approximate solutions move away from exact solutions as the pruning threshold is tightened up (th1 < th2 < th3).

For reliability extraction via BDD traversing, time performance on linear and rectangular architectures is linear with respect to the size of the BDD. For complex architectures (i.e., systems that cannot be broken down to groups of series and parallel components), both BDD-based quantifier elimination and reliability are more burdensome, since the topology has no periodicity. As far as the optimization is concerned, the results indicate that the hybrid approach outperforms the others, as reported in Table 1.

The main challenge of the symbolic encoding arises with very complex systems because of the sheer size of the design space. The computation time increases quickly with the size of the instance, as well as memory consumption. For the above reason, we investigated an approximated method based on the partitioning of the systems into smaller sub-systems. Partitions are dealt with individually, and subsequently recombined. Each sub-problem is exponentially more efficient, but fine grained partitions require recombining too many

Table 1. Optimization: symbolic vs hybrid approach

Topology	Linear			Rectangular		
Approach	Enumerative	Symbolic	Hybrid	Enumerative	Symbolic	Hybrid
Length 1	>5000 s	0.05 s	0.04 s	>5000 s	5.85 s	0.07 s
Length 2	>5000 s	4.09 s	0.15 s	>5000 s	645 s	0.43 s
Length 3	>5000 s	153 s	0.32 s	>5000 s	>5000 s	2.67 s

solutions. We therefore prune the design space by retaining only those solutions whose parameters come within a chosen threshold. By adjusting the threshold, we can strike the desired balance between optimality and run-time (Fig. 4(c)).

4   Conclusion

The symbolic approach proposed enables the analysis of the effect of component failures on various system configurations, it is capable of exploring the design space in an efficient way, and scales very well, easing the way to architecture synthesis. In future work, we will investigate the case where faults are associated with dynamics, going beyond combinatorial problems.

References

1. Barrett.C., Tinelli, C.: Satisfiability modulo theories. In: Handbook of Model Checking, pp. 305–343. Springer (2018). https://doi.org/10.1007/978-3-319-10575-8_11
2. Tierno, A., Turri, G., Cimatti, A., Passerone, R.: Symbolic encoding of reliability for the design of redundant architectures. In: Proceedings of the 5th International Conference on Industrial Cyber-Physical Systems, Coventry, UK, 24–26 May (2022)
3. Bozzano, M., Cimatti, A., Mattarei, C.: Formal reliability analysis of redundancy architectures. Formal Aspects Comput. **31**(1), 59–94 (2019). https://doi.org/10.1007/s00165-018-0475-1
4. Tierno, A., Turri, G., Cimatti, A., Passerone, R.: Automatic design space exploration of redundant architectures. In: Proceedings of the International Conference on Applications in Electronics Pervading Industry, Environment and Society, ApplePies 2021, Pisa, Italy, 21–22 September (2021)
5. Dal Lago, L., Ferrante, O., Passerone, R., Ferrari, A.: Dependability assessment of SOA-based CPS with contracts and model-based fault injection. IEEE Trans. Industr. Inf. **14**(1), 360–369 (2018)
6. Nuzzo, P., Bajaj, N., Masin, M., Kirov, D., Passerone, R., Sangiovanni-Vincentelli, A.L.: Optimized selection of reliable and cost-effective safety-critical system architectures. IEEE Trans. Comput. Aided Des. Integr. Circuits Syst. **39**(10), 2109–2123 (2020)
7. Kirov, D., Nuzzo, P., Passerone, R., Sangiovanni-Vincentelli, A.L.: An extensible framework for the exploration of cyber-physical system architectures. In Proceedings of the 54th Design Automation Conference, Austin, TX, 18–22 June (2017)

8. Brand, D.: Verification of large synthesized designs. In: Proceedings of International Conference on Computer Aided Design (ICCAD), pp. 534–537 (1993)
9. Phan, Q.-S., Malacaria, P.: All-solution satisfiability modulo theories: applications, algorithms and benchmarks. In: 2015 10th International Conference on Availability, Reliability and Security, pp. 100–109. IEEE (2015)

Batteryless Soil EIS Sensor Powered by Microbial Fuel Cell

Alessandro Torrisi$^{(\boxtimes)}$, Maria Doglioni, Luca Gemma, Andrea Albanese,
Luca Santoro, Matteo Nardello, and Davide Brunelli

Department of Industrial Engineering (DII), University of Trento, Trento, Italy
{alessandro.torrisi,maria.doglioni,luca.gemma,andrea.albanese,
luca.santoro,matteo.nardello,davide.brunelli}@unitn.it

Abstract. Batteryless devices are becoming fundamental to fostering self-sustainable and environmentally friendly Internet of Things (IoT) growth. In precision agriculture and, more broadly, for environmental monitoring, battery-less IoT systems are particularly effective due to their low environmental impact and maintenance cost. In this paper, we present the study of a battery-less Plant-Microbial Fuel Cells based IoT architecture for plant growth and health monitoring by exploiting electrochemical impedance spectroscopy. Plant-Microbial Fuel Cells – and, in turn, the plant itself – health and status can be assessed starting from specific features extracted from Electrochemical Impedance Spectroscopy (EIS) data. The proposed system exploits an ultra-low-power integrated electrochemical sensor analog front-end providing both DC polarization and EIS measurements. The system can self-sustain its operations by exploiting the same energy harvested from the monitored PMFC. Finally, a LoRa transceiver is in charge of transmitting status updates remotely. Results show that for a sweep of 19 points from 21.3 mHz to 21.8 kHz the overall required energy consumption is equal to 4.38 J.

Keywords: Energy harvesting · PMFC · EIS · Fuel cell · Battery-less-electronics

1 Introduction

IoT device shrinkage, maintenance, and environmental impact pose severe challenges in maximizing IoT applications' lifetime and even more when dealing with remote and wide areas monitoring. IoT device networks are constantly growing, making battery supply prohibitive, both in terms of costs, effort, and correct disposal. Using only batteries is costly, environmentally harmful, and needs periodic maintenance. In past years, researchers have thus proposed exploiting different Energy Harvesting (EH) [6] solutions as a power source. EH is proven to be a feasible solution to avoid polluting batteries in many applications [1,7,8] and a fundamental advantage in decreasing related maintenance costs. This paradigm shift is made possible also thanks to the development of

state-of-the-art hardware/software solutions, encompassing low-power accelerators, non-volatile memories, long-range low-power communication techniques, and innovative energy storage solutions [10].

With the introduction of these technologies, the IoT revolution is becoming affordable even in those harsh applications that require exchanging information over large distances with sensors installed in hard-to-reach areas. The so-called Plant-Microbial Fuel Cells (PMFC) represent a promising energy harvesting solution. A PMFC is a subclass of MFCs that uses a symbiotic plant-bacteria relationship to obtain rhizodeposition generation as a result of plant photosynthesis. PMFCs can provide a power density up to 18 times greater than MFCs as they can benefit from continuous substrate enrichment thanks to the presence of the plant, allowing long-term operation without specific maintenance for a long time. Generally, the healthier the plant and its photosynthesis activity, the higher will be the power generated by the PMFC.

The potential of PMFC as the energy source for powering low-power IoT devices has been deeply explored in recent years [4]. In [2,3], Brunelli et al. developed a system where the MFC is used both for powering a sensor node and as a biosensor for flora health monitoring. Other examples discuss how PMFCs can be exploited to implement long-range sensor nodes like the LoRa barometric and temperature sensor developed by Osorio-de-la-Rosa [9]. The proposed application exploits the PMFC to harvest electricity to power the sensing board and as a biosensor. Generally, the uses of MFC as biosensors involve monitoring its voltage which can be linked to a change in its working conditions (e.g., toxicity, CO2 levels, and water quality).

As discussed in [5], plants and fuel cells health can be correlated to specific features in the resulting Electrochemical Impedance Spectroscopy curves (EIS). It is a powerful non-destructive technique used to measure impedance as a function of frequency in electrochemical bioreactors. Understanding internal MFC impedance is key, as it is one of the main limiting factors in cell power output and can be exploited to comprehend the electro-bio-chemical phenomena ruling the functioning of MFCs. EIS measurements are realized through a potentiostat: a small (5–10 mV) AC signal is superimposed on the DC working voltage of the cell or of the electrode. The small AC signal does not disturb the cell's working point, and by measuring the current, we can estimate the impedance of the system under test. Fitting EIS data to an equivalent physical-based circuit allows us to model the electrical behavior of the bioreactor, find power production bottlenecks, and track cell maximum power points. EIS data can also be used to understand plant health, root growth, frost hardening, sensitivity to salinity, crop production, and plant stress. As the same PMFC under monitoring can also be exploited to provide the energy, creating a complete self-sustainable device is possible.

This paper presents an IoT battery-less PMFC-based architecture for plant growth and health monitoring exploiting EIS measurements. The proposed system's architecture is presented in Fig. 1 and was evaluated and tested against a reference potentiostat. Results highlight how the same EIS measurements can

be achieved by exploiting MAX30134 ultra-low power analog front end requiring only 4.38 J harvested from the same PMFC under monitoring. The rest of this paper is organized as follows: System's implementation is presented in Sect. 2 while results are discussed in 3. Section 4 close this work with final remarks and future works.
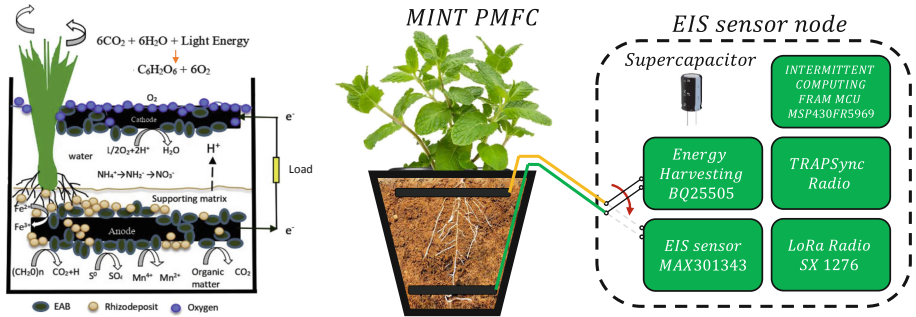
Fig. 1. On the left, the working principle of a P-MFC [4]. On the right, the PMFC battery-less sensor block diagram including the application sensor node.

2 System Implementation

This system uses the PMFCs both for harvesting electricity and as a biosensor. We gather in-depth information on the PMFC state through measurements such as EIS. EIS is primarily used as a steady state method to estimate impedance to investigate bio-film formation, anode and cathode electrochemical reactions, electrode coating, and material performance through appropriate physical-based circuit models.

2.1 System Design

The design of the sensor node used in this study is shown in Fig. 1. It aims to intermittently harvest energy from a PMFC reactor and store it in an appropriately sized supercapacitor, using a BQ25505 energy conditioning IC. Whenever energy is sufficient, the MSP430FR5969 triggers the MAX30134 analog front-end to execute an EIS measurement sweep. Results are communicated through a low-power long-range radio, using a backscatter channel for energy level communication and the Semtech SX1276 LoRa radio for data exchange. The reactor evaluated presents a volume of $1044\,cm^3$, composed of carbon brush electrodes and soil from our campus gardens. We chose *Mentha Piperita* as plant. It is a fast-growing and robust plant that can tolerate a damp environment. The cathode was slightly oversized with respect to the anode to compensate for slower cathodic reaction kinetics. Cell startup was done by flooding the PMFC reactor with water and leaving it undisturbed for up to two weeks. Subsequently, the
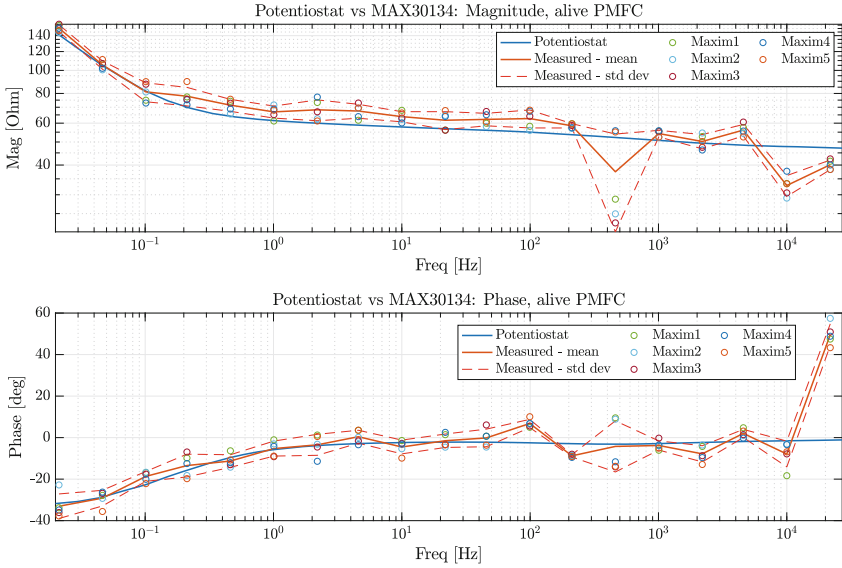
Fig. 2. Bode plots of an active PMFC obtained with the MAX30134 on the third day of tests, compared with the results obtained with the potentiostat Autolab PGSTAT302N.

reactor was provided common plant fertilizer and 137 cl of water each week. After the initial two weeks of startup, the Open Cell Voltage (OCV) started growing by about 100 mV daily, reaching 840 mV. Different capacitors and supercapacitors were used to test the feasibility of harvesting energy from the PMFC, as larger storage elements require higher startup power limiting the application scenarios. At its peak activity, our cell can cold-start a $470\,\mu\text{F}$ capacitor.

2.2 EIS Measurement

EIS measurements aim to enable online estimation of cell state from electrochemical properties so that appropriate actions can be taken to reach or maintain the cell's desired power output for as long as possible. This is achieved by fitting EIS data to physical-based circuit models. This allows to represent electrochemical phenomena with equivalent circuit elements making up the cell's overall impedance spectrum (i.e., solution resistance, Warburg impedance, and CPE), so that limiting factors can be identified and appropriate design choices can be taken. The EIS measurement is carried out with MAX30134 ultra-low-power integrated electrochemical sensor.

3   Results and Discussion

The experimental results are focused on the capabilities of our harvester to execute reliable low-power EIS measurements with MAX30134 IC.

3.1   PMFC Analysis

To validate the MAX30134s ability to measure the impedance spectra of our PMFC in all conditions, we executed EIS measurements at open-circuit voltage with the Autolab PGSTAT302N as a reference instrument. We chose two-terminal EIS measurements in the optics of a cost-effective application, which does not involve reference electrodes, which are bulky and expensive. Results obtained with MAX30134 were validated with a set of repeated measurements done with the potentiostat PGSTAT302N during various days of the experiment. Then, we selected a set of 19 logarithmically spaced frequency points for our MAX30134 EIS measurement sweep, ranging from 213 mHz up to 21.8 kHz, covering most of the MAX30134 range.

The Bode plot in Fig. 2 shows that the mean of the MAX30134 measurements closely matches those of the reference potentiostat, confirming the reliability of the EIS measurement through MAX30134.

3.2   EIS Sweep Energy Consumption

The energy needed to execute one EIS measurement depends on multiple factors, such as the chosen number of settle sine cycles and measurement sine cycles.
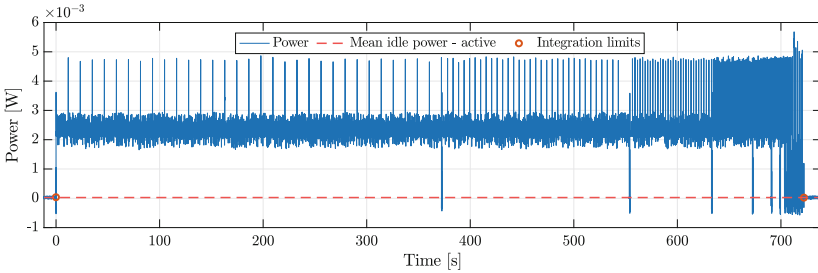
Fig. 3. Power profile during EIS measurement.

Figure 3 shows the power consumption profile during EIS measurement. For the complete sweep cycle of 19 points from 213 mHz to 21.8 kHz, considering active MCU during the measurement time, the overall required energy consumption is 4.38 J.

4   Conclusion

Plant-Microbial Fuel Cells is a promising technology for providing energy to low-power sensing devices. This paper presented an ultra-low-power sensing architecture based on EIS measurements for plant/MFC health assessment. The system can self-sustain its operation by harvesting energy from the same PMFC under

monitoring. We measured the energy needed for a complete EIS sweep of 19 logarithmically spaced frequency points, obtaining a total of 4.38 J, and we assessed the importance of a proper start-up phase for the PMFC power output stability. Future works will encompass the study of intermittent harvesting on PMFCs by experimenting with persistent timekeepers for controlling the cell harvester.

References

1. Albanese, A., Nardello, M., Brunelli, D.: Automated pest detection with DNN on the edge for precision agriculture. IEEE J. Emerg. Selected Topics Circ. Syst. **11**(3), 458–467 (2021). https://doi.org/10.1109/JETCAS.2021.3101740
2. Brunelli, D., Tosato, P., Rossi, M.: Flora health wireless monitoring with plant-microbial fuel cell. Proc. Eng. **168**, 1646–1650 (2016). https://doi.org/10.1016/j.proeng.2016.11.481
3. Brunelli, D., Tosato, P., Rossi, M.: Microbial fuel cell as a biosensor and a power source for flora health monitoring. In: 2016 IEEE SENSORS, pp. 1–3 (2016). https://doi.org/10.1109/ICSENS.2016.7808831
4. Kabutey, F.T., et al.: An overview of plant microbial fuel cells (pmfcs): Configurations and applications. Renew. Sustain. Energy Rev. **110**, 402–414 (2019). https://doi.org/10.1016/j.rser.2019.05.016
5. Kashyap, D., et al.: Application of electrochemical impedance spectroscopy in biofuel cell characterization: A review. Int. J. Hydrogen Energy **39**(35), 20159–20170 (2014). https://doi.org/10.1016/j.ijhydene.2014.10.003
6. Liu, L., Guo, X., Liu, W., Lee, C.: Recent progress in the energy harvesting technology-from self-powered sensors to self-sustained iot, and new applications. Nanomaterials **11**(11) (2021). https://doi.org/10.3390/nano11112975
7. Nardello, M., Desai, H., Brunelli, D., Lucia, B.: Camaroptera: A batteryless long-range remote visual sensing system. In: ENSsys 2019, pp. 8-14. Association for Computing Machinery, New York (2019). https://doi.org/10.1145/3362053.3363491
8. Nardello, M., Rossi, M., Brunelli, D.: A low-cost smart sensor for non intrusive load monitoring applications. In: 2017 IEEE 26th International Symposium on Industrial Electronics (ISIE), pp. 1362–1368 (2017). https://doi.org/10.1109/ISIE.2017.8001444
9. Osorio-de-la Rosa, E., et al.: Arrays of plant microbial fuel cells for implementing self-sustainable wireless sensor networks. IEEE Sens. J. **21**(2), 1965–1974 (2021). https://doi.org/10.1109/JSEN.2020.3019986
10. Torrisi, A., Yıldırım, K.S., Brunelli, D.: Reliable transiently-powered communication. IEEE Sens. J. **22**(9), 9124–9134 (2022). https://doi.org/10.1109/JSEN.2022.3158736

Author Index